NUMERICAL INVESTIGATION OF FLOW BEHAVIOUR AND SCOUR AROUND OFFSHORE PILES AND BRIDGE PIERS WITH DIFFERENT CROSS-SECTIONAL SHAPES

By

AMIR BORDBAR

A thesis submitted to the University of Birmingham for the degree of
DOCTOR OF PHILOSOPHY

School of Engineering
College of Engineering and Physical Sciences
University of Birmingham
March 2021

UNIVERSITY OF
BIRMINGHAM

University of Birmingham Research Archive

e-theses repository

This unpublished thesis/dissertation is copyright of the author and/or third parties. The intellectual property rights of the author or third parties in respect of this work are as defined by The Copyright Designs and Patents Act 1988 or as modified by any successor legislation.

Any use made of information contained in this thesis/dissertation must be in accordance with that legislation and must be properly acknowledged. Further distribution or reproduction in any format is prohibited without the permission of the copyright holder.

Abstract

The main aim of this study was to gain a deeper knowledge of flow behaviour and scour formation adjacent to bridge piers and offshore wind turbine foundations in shallow water using numerical modelling. Based on the literature, the capability of the previous models in the prediction of scour around the piers was attached to the pier shapes and its orientation angle to the flow. Hence, in this study, a coupled approach between a hydrodynamic and a morphodynamic model was implemented. The model was validated against eight different test cases for flow and sediment transport modelling. Overall, the results confirmed that the developed model has an acceptable capability in predicting local scour independent of the pier cross-section shapes.

Furthermore, the model was applied to predict the flow field, bed shear stress and the development of local scour around a square-shaped pier with 45˚ (diamond) and 90˚ (square) orientation angle to the flow, a hexagon-shaped pier with 30˚ and 60˚ orientation angle to the flow and a group of two identical side-by-side circular cylinders with different spacing ratios G/D= 1, 2 and 3 under current flow and live-bed condition, where D represents the pile diameter and G is the distance between the piles.

In the case of modelling a single pier, it was found that the maximum and minimum normalized quasi-equilibrium local scour depth occur for the square-shaped piers with 90° and 45° orientation angles to the flow, respectively. The normalized scour depth in quasi-equilibrium condition for the square pier was found to be almost twice (1.94) of that for the diamond pier. This ratio in the case of the hexagon-shaped pier for 60° and 30° orientation angles to the flow decreased to a value of 1.09. From these results, it was realized that an increase in the number of sides of the piers cross-section decrease the impact of the change in orientation angle to the

flow in terms of normalized scour depth. It was also inferred that with an increase in the number of sides of the pier's cross-section the resultant normalized scour depth in equilibrium condition tend to get closer to that of the circular pier regardless of pier orientation angle to the flow.

In the case of the local scour simulation around a group of two identical side-by-side piles, it was noticed that a deeper scour hole was observed in the area between the piles in all cases. However, due to the stronger turbulent structures and higher contraction of streamlines in the case of G/D=1, a deeper hole was observed adjacent to the piles in comparison to that of two other cases. The effect mitigated with an increase in spacing between the piles. The results showed that for $G/D \geq 3$ the pile group effect gradually vanishes, while it is assumed that the pile group effects are completely negligible for $G/D \geq 5$. An equation was fitted for the computed equilibrium scour depths for different spacing ratios which can be used for the prediction of the maximum scour depth adjacent to two side-by-side piles under steady current flow and live-bed condition for a specific range ($G/D \geq 1$).

Acknowledgements

I would firstly like to thank my supervisors Dr Soroosh Sharifi and Dr Hassan Hemida for their help and supports and sharing their expertise and insights during this research.

Thanks also go to

- Dr Mehdi Jangi for sharing his valuable experience in working with OpenFOAM.

- Dr Asaad Faramarzi for providing me with his thoughts and feedbacks.

- My dear friends and colleagues, Dr Koohyar Faizi, Dr Nikolina Kovacev, Dr Mehran Eskandari Torbaghan, and Dr Ali Monzer for their supports.

Table of Contents

1 INTRODUCTION 1

1.1 Problem of scour around structures 1

1.2 Gaps in knowledge 4

1.3 Aim and objectives 5

1.4 Outline of the thesis 7

1.5 Publication of research 8

2 REVIEW OF THE PREVIOUS RESEARCH 9

2.1 Introduction 9

2.2 Underlying physics of fluid flow around the mounted pile/pier and governing equations of fluid flow 9

2.2.1 Hydrodynamic model 11

2.2.2 Unsteady-RANS equations for a single-phase flow 14

2.2.3 The k-ω *SST* turbulence closure model 15

2.2.4 Boundary layer over a flat plate 17

2.2.5 Near-wall treatment methods (Wall-functions) 22

2.2.6 Bed shear stress 25

2.3 Underlying physics and governing equations of sediment transport 27

2.3.1 Cohesive and non-cohesive sands 27

2.3.2 Sediment transport modes in classical approach 28

2.3.3 Critical bed shear stress for the initiation of motion 32

2.3.4 Slope-dependent critical shear stress 34

2.3.5 Bedload transportation 34

2.3.6 Settling velocity (Fall velocity) 39

2.3.7 Suspended load transportation 40

2.3.8 Sediment continuity equation 43

2.3.9 Live-bed and clear-water conditions 45

2.4 Experimental studies 45

2.4.1 Experimental studies of flow behaviour around piles/piers on rigid bed 46

2.4.2 Experimental studies of scour on sandy mobile bed 51

2.5 Numerical studies 57

2.5.1 Numerical studies of flow behaviour around piles/piers on rigid bed 57

2.5.2 Numerical studies of scour on sandy mobile bed 59

2.6 Summary 66
3 METHODOLOGY 68
3.1 Introduction 68
3.2 Hydrodynamic model justification 69
3.2.1 Hydrodynamic model boundary conditions 69
3.3 Bed shear stress 75
3.4 Morphodynamic model setup 75
3.4.1 Bedload model 77
3.4.2 Suspended load model 78
3.4.3 Entrainment and deposition 78
3.4.4 Fall velocity 79
3.4.5 Mass-balance equation for sediment 79
3.4.6 Filtration of bed elevation 80
3.4.7 Sand sliding model 82
3.4.8 Coupling procedure 82
3.4.9 Mesh motion method 84
3.5 OpenFOAM® CFD toolbox 84
3.5.1 File structure of a test case in OpenFOAM® 85
3.6 Summary 86
4 VALIDATION OF THE PROPOSED MODEL 88
4.1 Introduction 88
4.2 Test case 1: homogenous bed model 89
4.3 Test case 2: flow around a vertical circular pile mounted on a smooth rigid bed 92
4.3.1 Experimental details 92
4.3.2 Numerical details and results 93
4.4 Test case 3: flow around a circular pile mounted on a rough rigid bed 100
4.4.1 Experimental details 100
4.4.2 Numerical details and results 101
4.5 Test case 4: net entrainment 104
4.5.1 Experimental details 104
4.5.2 Numerical details and results 105
4.6 Test case 5: submerged horizontal jet 106
4.6.1 Experimental details 106
4.6.2 Numerical details and results 107
4.7 Test case 6: scouring around a circular pile in live-bed condition 110
4.7.1 Experimental details 110

4.7.2 Numerical details and results 111
4.8 Test case 7 & 8: scour around a square shaped pier with different orientation angle to the flow in clear-water condition 115
4.8.1 Experimental details 115
4.8.2 Numerical details and results 115
4.9 Summary 118
5 FLOW BEHAVIOUR AND SCOUR AROUND SINGLE PIERS WITH DIFFERENT CROSS-SECTION SHAPES 120
5.1 Introduction 120
5.2 Square-shaped piers 121
5.2.1 Generated meshes and boundary conditions 121
5.2.2 Numerical modelling on a rigid bed 122
5.2.3 Numerical modelling on a mobile bed 129
5.3 Hexagon-shaped piers 133
5.3.1 Generated meshes and boundary conditions 133
5.3.2 Numerical modelling on a rigid bed 134
5.3.3 Numerical modelling on a mobile bed 138
5.4 Temporal development of Scour around single piers 142
5.5 Summary 144
6 FLOW BEHAVIOUR AND SCOUR AROUND A GROUP OF TWO IDENTICAL SIDE-BY-SIDE CIRCULAR PILES 145
6.1 Introduction 145
6.2 Generated meshes and boundary conditions 146
6.3 Numerical modelling on a rigid bed 148
6.4 Numerical modelling on a mobile bed 157
6.5 Summary 164
7 SUMMARY AND CONCLUSIONS 165
7.1 Numerical model development 165
7.2 Flow and scour around single piles with different cross-sections and a group of two side-by-side circular piles 167
7.3 Perspectives and future work 169
APPENDIX I 171
APPENDIX II 184
APPENDIX III 199
REFERENCES 206

Table of figures

Figure (1-1) Bridge failures due to scouring and flooding (a) Failure of Oat Ditch Bridge on I-15 in California in 2003 (Bojanowski and Kulak, 2010) (b) Schoharie Creek bridge collapse in 1987 (Craswell and Akib, 2020). 2
Figure (1-2) (a) solid concrete block as a bed armouring (Conteches, 2020) and (b) pier group as a flow-altering countermeasures (Wang et al., 2019). 3
Figure (2-1) Definition sketch of the junction flow and formation of HSV and lee-wake vortices from Roulund et al. (2005). 10
Figure (2-2) In and out flow for a fluid element (Versteeg and Malalasekera, 2007) 12
Figure (2-3) Turbulence boundary layer (Bakker, 2006). 18
Figure (2-4) Semi-logarithmic plot of the velocity profile for turbulence flow over smooth and rough wall (Driest, 1956). 22
Figure (2-5) Fluid and sediment flow of mass in and out of a volume element. 29
Figure (2-6) Definition sketch of the sediment transport model (Rijn, 1987). 32
Figure (2-7) Drag and lift forces acting on a grain resting on the bed (Fredsoe and Deigaard, 1992). 32
Figure (2-8) The critical Shields $\theta c, 0$ as a function of Reg (Fredsoe and Deigaard, 1992). 33
Figure (2-9) Sketch of forces acting on the particle on a sloping bed (Stahlmann, 2013c). 38
Figure (2-10) Numerical results of scouring around a 2D pipeline (a) without and (b) with sand sliding method from (Liang et al., 2005). 44
Figure (2-11) Variation of local scour depth with flow velocity and time (Melville and Chiew, 1999). 45
Figure (2-12) Flow pattern and formation of 4 horseshoe systems upstream of the mounted cylinder (Baker, 1980). 47
Figure (2-13) The sequence of formation of horseshoe vortices upstream of the cylinder in a plane of symmetry at ReD=20000 (Dargahi, 1989). 48
Figure (2-14) Schematic diagram of the vortex systems around a square-shaped cylinder with 90° orientation angle to the flow (Lin et al., 2008). 50
Figure (2-15) The layout of the piles in Qi et al. (2019). 57
Figure (2-16) Computational domain and the complex bridge pier structure in Alemi et al. (2019). 58
Figure (2-17) Schematic of a wing and corresponding variables in calculation of bluntness factor. 62
Figure (2-18) The tripod structures and generated computational grid for flow and scour simulations from Stahlmann (2013a) 63
Figure (3-1) Computational domain and boundaries. 70
Figure (3-2) Schematic of the change on free-surface due to presence of the pile in high Froude number. 72
Figure (3-3) Schematic of the mesh grids, centre of first layer of cells close to bed and acceptable area for suspended load reference height from the bed. 77
Figure (3-4) The 3D computational domain and corresponding 2D bed mesh to solve Exner equation. 80

Figure (3-5) Flow chart of the hydrodynamic and sediment transport coupling procedure in each time step of the scouring modelling. 83
Figure (3-6) Typical structure of a test case in OpenFOAM®. 86
Figure (4-1) Generated mesh for the homogenous bed test. 90
Figure (4-2) Comparison between simulation results and Cebeci and Bradshaw (1977) wall function equations. 91
Figure (4-3) Velocity profiles for different applied ks. 92
Figure (4-4) (a) 3D computational mesh and boundaries, (b) Generated mesh (Mesh1 in Table 4-1) for flow around a cylinder with a smooth bed test case (top view). 94
Figure (4-5) Formation of horseshoe and lee-wake vortices around the circular pile using the Q-criterion technique. 96
Figure (4-6) The velocity components in the x- and z- direction for flow around the cylinder with a smooth bed along the symmetry line on plane y=0 for different heights from the bed. 98
Figure (4-7)(a) Comparison of $BSSA$ between the unsteady-RANS model and numerical and experimental results reported by Roulund et al. (2005) (b) distribution of the absolute value of $BSSA$ on the bed around the cylinder pile. 100
Figure (4-8) The velocity components in the x- and z-direction for flow around a cylinder with the rough bed along the symmetry line on plane y=0 for different heights from the bed. 103
Figure (4-9) A schematic illustration of Rijn (1986) net entrainment test. 104
Figure (4-10) Concentration distribution along the sandy bed. 106
Figure (4-11) A schematic illustration of Chatterjee et al. (1994) submerged horizontal jet test. 107
Figure (4-12) (a) Generated mesh for Chatterjee et al. (1994) test, (b) area of rigid and movable bed contact and assumed pit and dune. 108
Figure (4-13) The velocity contour and deformed bed at 4 different times (a) $t = T/60,\ bt = 2T/15, ct = T/3\ and\ dt = T$ 109
Figure (4-14) Comparison of the formation of pit and dune on the bed between the numerical results and experimental data for different times. 110
Figure (4-15) Test conditions of scour around a cylinder test (Roulund et al., 2005). 110
Figure (4-16) Top view of generated mesh for scour around a cylinder test case. 112
Figure (4-17) Undisturbed mean flow velocity profile (Roulund et al., 2005). 112
Figure (4-18) Simulated bed displacement at 4 different times of the simulation $t = T/60,\ T/12,\ T/4$ and T 114
Figure (4-19) Changes in maximum scour depth with time (a) upstream and (b) downstream of the pile. 114
Figure (4-20) Changes in scour depth with time in case of (a) square and (b) diamond pier. 117
Figure (4-21) Comparison of measured (bottom) and computed (top) bed topography at equilibrium condition for (a) square pier, (b) diamond pier (the measurement unit is centimetre) 118
Figure (5-1) 3D view of the computational domain and boundaries for the square pier. 122
Figure (5-2) Top view of the generated meshes for (a) square and (b) diamond piers. 123
Figure (5-3) Turbulence structures around (a) square and (b) diamond piers using the Q-criterion concept at time T=70 s. 124
Figure (5-4) (a, b) Mean flow velocity and its component in (c, d) x-direction and (e, f) y-direction at plane z= 0.2 m around the square and diamond piers. 125
Figure (5-5) Variations of the lift force coefficient for (a) square and (b) diamond piers. 127
Figure (5-6) Formation of HSVs upstream of (a) square pier and (b) diamond pier. 128

Figure (5-7) Distribution of the absolute value of $BSSA$ on the bed around the square (top) and diamond (bottom) pier. 129
Figure (5-8) Bed deformation at 4 different times of the simulation t =30, 120, 900, 3600 s for the square and diamond piers. 130
Figure (5-9) Instantaneous flow velocity vector field in symmetry plane (y=0) for (a) the square and (b) diamond piers. 131
Figure (5-10) bed displacement contour around the (a) circular, (b) square and (c) diamond pier. 132
Figure (5-11) Top view of the generated meshes for regular hexagon pier with (a) 30° and (b) 60° orientation angles to the flow. 134
Figure (5-12) Turbulence structures around a hexagon pier with (a) 30° and (b) 60° orientation angles to the flow using the Q-criterion concept at time T=70 s. 135
Figure (5-13) (a, b) Mean flow velocity and its component in (c, d) x-direction and (e, f) y-direction at plane z= 0.2 m around the hexagon pier with different orientation angles. 137
Figure (5-14) Distribution of the absolute value of $BSSA$ on the bed around the hexagon pier with (Top) 30° and (Bottom) 60° orientation angles to the flow. 138
Figure (5-15) Bed deformation at 4 different times of the simulation t =30, 120, 900, 3600 s for the hexagon pier with different orientation angles. 140
Figure (5-16) Flow velocity vector field in symmetry plane (y=0) for the hexagon pier with (a) 30° and (b) 60° orientation angles to the flow. 141
Figure (5-17) Bed displacement contour in quasi-equilibrium condition for hexagon pier with (a) 30° and (b) 60° orientation angles to the flow. 142
Figure (5-18) Changes in scour depth in time for square-shaped, hexagon-shaped and circular piers. 143
Figure (6-1) (a) 3D view of the computational domain and boundaries and (b) top view for a group of two side-by-side piles. 146
Figure (6-2) The generated meshes for the bed boundary of the computational domains for (a) G=1D, (b) G=2D, (c) G=3D. 147
Figure (6-3) Mean flow field adjacent to two side-by-side piles with (a) G=1D, (b) G=2D, (c) G=3D and (d) a single pile in plane x=0. 149
Figure (6-4) Mean flow velocity in plane y=0 for different spacing ratios between the piles with (a) G=1D, (b) G=2D, and (c) G=3D. 150
Figure (6-5) Mean flow velocity in plane z= 20 cm for different spacing ratios between the piles with (a) G=1D, (b) G=2D, and (c) G=3D. 151
Figure (6-6) The traced streamlines from lines at z=0.5 cm and z=10 cm upstream of the pile groups with different arrangements. 154
Figure (6-7) Formation of turbulent structures with applying iso-surfaces for Q= 0.1 1/s2 at t =100 s for the pile groups with (a) G=1D, (b) G=2D, and (c) G=3D. 155
Figure (6-8) Distribution of the absolute value of BSSA on the bed around the pile groups with (a) G=1D, (b) G=2D, and (c) G=3D. 156
Figure (6-9) Scoured bed at 4 different times of the simulation (a) t =30 s, (b) t=60 s, (c) t=900 s, and (d) t=3600s for two side-by-side piles with G = 1D. 158
Figure (6-10) Scoured bed at 4 different times of the simulation (a) t =30 s, (b) t=60 s, (c) t=900 s, and (d) t=3600s for two side-by-side piles with G = 2D. 158
Figure (6-11) Scoured bed at 4 different times of the simulation (a) t =30 s, (b) t=60 s, (c) t=900 s, and (d) t=3600s for two side-by-side piles with G = 3D. 159

Figure (6-12) Instantaneous flow field adjacent to two side-by-side piles mounted in equilibrium scoured bed with (a) G=1D, (b) G=2D, (c) G=3D at plane x=0 and t =3600 s. 160
Figure (6-13) Comparison of the computed bed topography at quasi-equilibrium condition around the pile groups with (a) G=1D, (b) G=2D, and (c) G=3D. 161
Figure (6-14) Evolution of scour depth for two side-by-side piles with G=1D, 2D and 3D and a single pile. 162
Figure (6-15) Equilibrium scour depth for two side-by-side piles with different spacing ratios. 163

Nomenclature

Roman Symbols

A	Drist damping factor constant [-]
A_c	Cross-section area of the flume [L^2]
a	Angle between the near-bed flow velocity vector and direction of the steepest slope [-]
a_1, a_2	Lower and upper limits of integration [-]
B	Additive constant Eq. (2-21) [-]
BF	Bluntness Factor [-]
$BSSA$	Bed shear stress amplification [-]
b	Bed slope [-]
C, C_1	Constant [-]
$CD_{k\omega}$	Variable in the blending function Eq. (2-12) [-]
Co	Courant number [-]
C_s	Roughness constant [-]
C_μ	Constant [-]
c	Local sediment volume concentration [ML^{-3}]
c_D	Drag coefficient for the particle [-]
c_f	Friction coefficient [-]
c_Δ	Concentration at the reference level [ML^{-3}]
D	Circular pile/pier diameter [L]
D_w	Maximum width of the wing [L]
D_Δ	Deposition fluxes [$ML^{-2}T^{-1}$]
D_s, D_v	Diffusivity in advection-diffusion equation (Eqs. (2-46) and (2-71)) [L^2T^{-1}]
D_*	Dimensionless particle diameter [-]
d	Grain diameter [L]
d_s	Sieve particle diameter [L]
d_{xy}	Average distance of the face *i*, from neighbour cells in xy surface [L]
E_Δ	Entrainment fluxes [$ML^{-2}T^{-1}$]

$e_{f,i}$, $e_{s,i}$	Turbulence-induced transport components for fluid and sediment $[LT^{-1}]$
F	Variable in mass-balance equation $[LT^{-1}]$
Fr	Froude number [-]
F_{drag}	Agitating force for a sediment particle $[MLT^{-2}]$
F_g	Gravity force $[MLT^{-2}]$
F_N	Normal force $[MLT^{-2}]$
F_f	Stabilizing force for the sediment particle $[MLT^{-2}]$
F_1, F_2	Blending functions [-]
f	Vortex shedding frequency $[T^{-1}]$
G	Distance between two adjacent piles $[L]$
g	Acceleration of gravity $[LT^{-2}]$
H	Mean flow depth $[L]$
H_b	Bed-form height $[L]$
h	Local bed level height $[L]$
I	Bed slope of a flume [-]
K	Function of dimensionless roughness height [-]
KC	Keulegan-Carpenter's number [-]
k	Turbulent kinematic energy per unit mass $[L^2T^{-2}]$
k_s	Equivalent roughness height [-]
$k_{s,f}$	Wall or bed form roughness [-]
$k_{s,g}$	Single grain roughness [-]
L	Pier/pile height $[L]$
$\vec{N}$	Normal vector of the wall or bed [-]
n	Bed porosity [-]
P	Pressure $[ML^{-1}T^{-2}]$
P_k	Production term of k $[L^2T^{-3}]$
P_w	Wetted perimeter $[L]$
P_ω	Production term of ω $[T^{-2}]$
p	Pressure $[ML^{-1}T^{-2}]$ and Probability of the transport of the particles in a single layer [-]
Q	Q-criterion concept $[T^{-2}]$

$Q(x)$ Sample function Eq. (2-32) [-]

q_B Rate of bedload transport in volume of material per unit time and width $[L^2T^{-1}]$

R Radius of the leading-edge of a wing $[L]$

R_h Hydraulic radius $[L]$

Re_D Reynolds number for pile diameter D [-]

Re_g Reynolds number for the grain [-]

$Re_{g,w_{so}}$ Grain fall velocity Reynolds number [-]

Re_t Turbulence Reynolds number [-]

Re_z Local Reynolds number for distance z from a wall [-]

S Strain rate tensor $[T^{-1}]$

S Scour depth $[L]$

St Strouhal number [-]

S_D Distance from the leading edge along the structure surface to the maximum width of the wing $[L]$

S_c Source/sink term for entrainment and deposition $[ML^{-2}T^{-1}]$

S_m Equilibrium (maximum) scour depth $[L]$

S_M Body force $[MLT^{-2}]$

S_r Tuning parameter [-]

s Relative density (specific gravity) [-]

s_{ij} Strain rate tensor $[T^{-1}]$

T Inner product of the stress tensor $[ML^{-1}T^{-2}]$

T Time scale of scour process to reach equilibrium condition $[T]$

TKE Turbulent kinetic energy $[L^2T^{-2}]$

T_w Wave period $[T]$

t Time $[T]$

U_c Mean critical flow velocity for the initiation of motion for the bed materials $[LT^{-1}]$

U_m Maximum value of the outer oscillatory flow velocity $[LT^{-1}]$

U_0 Potential flow velocity at the top of the pile boundary layer at the point of separation $[LT^{-1}]$

U_∞ Mean velocity of the undisturbed approach flow $[LT^{-1}]$

u, v, w Local velocities in x, y, z directions $[LT^{-1}]$

u_B	Mean transport velocity of moving particles $[LT^{-1}]$
u_{center}	Velocity on the centre of the first layer of cells closest to the bed $[LT^{-1}]$
u_f	Friction velocity (shear velocity) $[LT^{-1}]$
u_{fm}	Maximum value of undisturbed bed shear velocity $[LT^{-1}]$
u_{fc}	Threshold friction velocity of particle motion (critical flow velocity) $[LT^{-1}]$
u_{max}	Undisturbed velocity over a boundary layer $[LT^{-1}]$
u_{nw}	Near-wall flow velocity $[LT^{-1}]$
u_r	Relative velocity $[LT^{-1}]$
u_s	Local sediment velocity $[LT^{-1}]$
u_{wall}	Velocity on the wall $[LT^{-1}]$
V_z	Vertical motion for cell $[LT^{-1}]$
w_F	Flume width $[L]$
w_p	Pier/pile width$[L]$
w_s	Grain settling velocity $[LT^{-1}]$
w_{s0}	Single grain settling (fall) velocity $[LT^{-1}]$
X	Length of the chordwise position of the nose from maximum width of the wing $[L]$
z	Vectorial direction and distance from a wall $[L]$

Greek Symbols

α	Non-dimensional coefficient [-]
α	Blending function constant [-]
α_s	Skew angle [-]
β	Blending function constant [-]
β^*	Model constant [-]
Γ	Strength of the shed vortices exposed to steady current flow $[L^2T^{-1}]$
γ_m	Diffusion coefficient [-]
Δ	Reference level height from the bed $[L]$
ΔB	Function of dimensionless roughness height [-]
δ	Boundary layer thickness $[L]$
δ_{ij}	Kronecker delta [-]

ε	Dissipation rate of turbulence energy $[L^2T^{-3}]$
η	Variable in the blending function [-]
θ	Shields parameter [-]
θ_c	Critical Shields parameter [-]
$\theta_{c,0}$	Critical Shields parameter for horizontal bed [-]
θ_0	Critical Shields Parameter for particles lying on the bed [-]
κ	von Karman's constant [-]
μ	Dynamic viscosity of the fluid $[ML^{-1}T^{-1}]$
μ_d	Coefficient of dynamic friction for a sediment [-]
μ_s	Coefficient of static friction between the grain and the surrounding grains [-]
ν	Molecular kinematic viscosity of the fluid $[L^2T^{-1}]$
ν_t	Kinematic turbulent viscosity (eddy viscosity) $[L^2T^{-1}]$
ν_{new}	$\nu+\nu_t$ $[L^2T^{-1}]$
ξ	Variable in the blending function [-]
ρ	Fluid density $[ML^{-3}]$
ρ_s	Sediment density $[ML^{-3}]$
σ_k, σ_ω	Blending function constants [-]
τ	Shear stress in flow $[ML^{-1}T^{-2}]$
τ_b	Skin friction shear stress
τ_f	Bed form-drag component of total bed shear stress $[ML^{-1}T^{-2}]$
τ_{Tot}	Total bed shear stress $[ML^{-1}T^{-2}]$
τ_w	Wall (bed) shear stress $[ML^{-1}T^{-2}]$
τ_∞	Wall Shear stress of the undisturbed flow $[ML^{-1}T^{-2}]$
Φ_B	Non-dimensional bedload discharge [-]
φ_r	Angle of repose [-]
Ω_{ij}	Vorticity $[T^{-1}]$
ω	Turbulence frequency or specific dissipation rate $[T^{-1}]$
ω_a	Angular frequency of the motion $[T^{-1}]$

Superscripts

$\vec{\square}$	Vectorial form

$\square'$	Turbulent fluctuation
$\square^+$	Normalized value
$\widetilde{\square}$	Filtered Value
$\widehat{\square}$	Bed elevation change after filtration

Subscripts

$\square_\tau$	Tangential to the bed
$\square_i$	In x_i direction
$\square_{in}$	Mean values for neighbour faces

1 INTRODUCTION

1.1 PROBLEM OF SCOUR AROUND STRUCTURES

The presence of bottom-mounted flow obstructing structures, such as bridge piers, abutments, offshore wind turbine foundations and oil/gas platforms in riverine and marine environments, changes the flow patterns and generates vortex flow structures in their vicinity (Yagci et al., 2017; Kim et al., 2017; Sumer, 2002). These changes increase the local bed shear stress near the structures, which consequently, in unprotected bed conditions, intensify the local sediment mobility. This often leads to the erosion of bed sediments adjacent to the structures, a phenomenon which is termed local scour (Zhang et al., 2017). Local scour lessens the insertion depth of the structures and weakens the foundation's bearing capacity which may result in the structure's failure and financial and life losses (Wang, 2020; Mahmoud, 2020).

Local scour around bridge piers is the major concern in bridge failure (Hong et al., 2012). Monitoring and studying bridge failures in the United States over a 30 years span, Briaud et al. (1999) concluded that 60% of total bridge failure cases were due to local scour which imposes an annual cost of about $30 million in maintenance and repair (Holnbeck and Parrett, 1997). Figure (1-1) illustrates examples of bridge failure due to scouring and flooding around piers. Likewise, in the offshore wind industry, scouring around the piles of offshore wind turbines has a significant effect on the stability of the superstructures. Observations show that the maximum possible scour depth around a pile in an unprotected bed can be up to twice the size of the pile diameter (Sumer and Fredsøe, 2001a), which means that a typical pile foundation length has to be overdesigned (Hansen et al., 2007). This imposes a huge extra cost considering that the

construction and installation of the foundation counts for 25-30% of the total wind farm development cost (Windeurope, 2018).



(a) (b)

Figure (1-1) Bridge failures due to scouring and flooding (a) Failure of Oat Ditch Bridge on I-15 in California in 2003 (Bojanowski and Kulak, 2010) (b) Schoharie Creek bridge collapse in 1987 (Craswell and Akib, 2020).

Different methods have been proposed and discussed in the literature for preventing local scour. These can generally be categorised into two groups of bed armouring and flow-altering countermeasures (Singh et al., 2020). Bed armouring countermeasures work as a shield to keep the vulnerable bed particles safe from movement. Riprap stones, articulating block, concrete armour units, etc. are different types of bed armouring devices. On the other hand, flow-altering countermeasures include methods to reduce the strength of the turbulent flow around the pile/pier foundations. Slot in the pier, collar plate attached to the pier, threaded pier, splitter plate, internal connecting tubes, pier group, and caisson are common flow altering measures (Singh et al., 2020). Figure (1-2) demonstrates two different types of scour countermeasure methods.



(a) (b)

Figure (1-2) (a) solid concrete block as a bed armouring (Conteches, 2020) and (b) pier group as a flow-altering countermeasures (Wang et al., 2019).

Countermeasure methods can be very expensive. For instance, Zaaijer and Van der Tempel (2004) estimated a cost of around $ 420,000 per turbine for a three-rock layer scour protection on the seabed for a 3MW offshore wind turbine with a 3.5 m diameter monopile which is more than 10% of the total cost of the offshore wind turbine excluding transmission.

The huge cost associated with installation, maintenance, protection and repair of the foundations in river and seabed, as mentioned in the few examples above, necessitates a true understanding of the flow behaviour and scour around structures and development of effective tools and methods for optimum design and selection of appropriate countermeasure.

In the literature, the study of the scouring has been investigated by both physical and numerical modelling approaches. Physical modelling can be divided into small- and large-scale modelling approaches. Small scale models tend to over-estimate the scour depth around foundation due to the scaling effect and lack of accuracy in the similitude of large-scale turbulent structures, while large-scale models are very time- and cost-consuming (Ettema et al., 1998; Huang et al., 2009; Lee and Sturm, 2008; Zhang et al., 2017). On the other hand, with the fast increase in the computational and storage of computers, numerical modelling is becoming more popular option

in scour investigation. The focus of this study is on the numerical investigation of temporal evolution of local scour around pile/pier foundations with different cross-section shapes under steady-current flow.

1.2 GAPS IN KNOWLEDGE

Despite the significant number of studies that have investigated scour around piles/piers in marine and riverine conditions, the spectrum of involved parameters in the development of local scour brings a high level of uncertainty for safe and economic designs. These factors generally consist of the geometry of pile/pier, approaching fluid flow attributes and bed material characteristics (Akhlaghi et al., 2020; Mir et al., 2019; Mir et al., 2018; Miyab et al., 2017).

The geometry of pile/pier contains a wide range of shapes and configurations from a simple cylinder (e.g. monopile or a bridge pier) to a complex geometry (e.g. tripod) or a pile group. Under a defined approaching flow and bed material conditions, the geometry controls the flow pattern in its vicinity (Mir et al., 2019). A change in shape and configuration (e.g. the cross-section shape of a single pier or arrangement of a pile group) changes the flow deformation and consequently local scour patterns around it. Therefore, a guideline for the prediction of scour around one geometry is not suitable for other shapes or configurations.

In the literature, singular cylinders with circular, rectangular, and hexagonal cross-section shapes have been introduced as the most common applied bridge pier shapes (Zhang et al., 2019). There are a significant number of studies on local scour around a single circular cylinder, while the study on cylinders with other cross-section shapes is rare. Among those, the experimental studies of Sumer et al. (1993); Diab et al. (2010); Yao et al. (2018), and Omara et al. (2020) on scour around square-shaped cylinders can be mentioned. Recently, attempts on numerical modelling of local scour around cylinders with different cross-sectional shapes has

also been carried out in works of Khosronejad et al. (2012) and Omara et al. (2019). However, it was found that the prediction capability of their models was dependent upon the pier shapes and its orientation angle to the flow and they were unsuccessful in prediction of local scour around pier with different cross-section shapes. This gap in knowledge can be bridged by developing a numerical model which can provide independent results for different pier shapes and configurations.

Apart from the impact of the geometry, local scour in terms of approaching flow field and bed material parameters can be divided into two basic categories of clear-water and live-bed conditions (Najafzadeh et al., 2014). In clear-water conditions, the mean velocity of the undisturbed approaching flow is less than the mean critical flow velocity for the initiation of motion for the bed materials ($U_\infty < U_c$), while in live-bed condition $U_\infty > U_c$. The mechanism of scour under these conditions is quite different. To the author's best knowledge, most of the studies in numerical modelling of scour have been conducted in clear-water condition (e.g. Khosronejad et al., 2012; Kim et al., 2014; Zhang et al., 2017; Omara et al., 2019), while very limited studies have been accomplished in live-bed (e.g. Roulund et al., 2005). Therefore, studying the scour evolution around different geometries of pile/pier in live-bed condition can elucidate the corresponding mechanism under scrutiny and add to the knowledge of scour problem.

1.3 AIM AND OBJECTIVES

The main aim of this study is to numerically investigate the flow behaviour and evolution of scour around vertical cylinders (e.g. offshore piles and bridge piers) with different cross-sectional shapes and configurations in shallow water under live-bed conditions. This aim will be achieved through the following objectives:

Obj 1) To develop and validate a numerical hydro-morphodynamic model to predict the flow field and scour around piles/piers in steady-current flow.

Obj 2) To evaluate the effect of single square-shaped and regular hexagon-shaped piers with different orientation angle to the flow on the flow field and local scour pattern in live-bed conditions using the developed model.

Obj 3) To predict the flow field and scour pattern around a group of two identical side-by-side circular piles with three different spacing ratios in live-bed conditions using the developed model.

For the purpose of this study, a numerical model which is able to predict the temporal scour development around the piles/piers is developed. A coupled hydro- and morphodynamic approach is applied and a code is implemented in the framework of OpenFOAM-Extend 4.0. The hydrodynamic part of the model solves the unsteady Reynolds Averaged Navier-Stokes (RANS) equation where the Reynolds stress tensors are modelled with *k-ω SST* turbulence closure. The morphodynamic part of the model includes the full-sediment transport modelling which is carried out by employing two sediment transport models, bedload and suspended load models. The model benefits from a modification on height of the reference level which is a hypothetical layer between the bedload and suspended load sediment transport modes. The developed model is validated against a wide range of well-documented experimental studies such as Roulund et al. (2005) and Khosronejad et al. (2012). The results illustrate that the model has promising capability in reproducing scour results around different pile geometries. The model is applied to better understand the flow behaviour and temporal scour development in live-bed conditions around piles/piers with different geometries. First, the model is applied for cases of single square-shaped and regular hexagon-shaped piers with different orientation

angles to the flow. Then, the model is used for cases of two identical side-by-side circular piles with three different spacing ratios 1D, 2D, and 3D, where D is the pile diameter.

1.4 OUTLINE OF THE THESIS

In the next chapter, Chapter 2, the characteristics of flow around the mounted pile/pier and an introduction to the pertinent mechanisms and governing equations on flow behaviour and sediment transport models are briefly described. Furthermore, a summary of the previous experimental and numerical research on local scour with a focus on notable works is provided.

Chapter 3 is dedicated to the proposed hydro-morphodynamic model and the description of its details including the governing equations, the model's constraints and boundary conditions, and applied filtration of bed elevation and sand sliding procedures.

Chapter 4 includes the validation of the proposed model against a set of eight test cases from the literature. The details of the laboratory setups and numerical simulations are provided. For each test case, the numerical results are compared with experimental measurements to validate the proposed model.

Chapter 5 contains the numerical results of the proposed model on the simulation of the flow field and scour progression around square and regular hexagon piers with two different orientation angles to the flow in live-bed conditions. The model's results are compared in terms of the flow field, bed shear stress, and local scour.

Chapter 6 presents the numerical results of the proposed model on the simulation of the flow field and scour development adjacent to a group of two identical side-by-side circular piles with different spacing ratios in live bed conditions. The results are compared in terms of the progression of scour pattern and maximum scour depth around them. Finally, an equation is developed for maximum scour hole depth as a function of the spacing ratio.

Chapter 7 summarizes the key findings and conclusions of this research and offers perspectives for future studies and suggestions to improve the proposed model.

1.5 PUBLICATION OF RESEARCH

Several journal and conference papers are prepared for publication from this thesis. Three of them are published in refereed journals and conference proceedings and the remaining are in process. The following papers can be found in appendices:

Appendix I: Bordbar A, Sharifi S, Hemida H (2021) Numerical Investigation of Different Sand Sliding Methods for Morphodynamic Modelling. Proceedings of the Institution of Civil Engineers- Maritime Engineering. (Under review)

Appendix II: Bordbar A, Sharifi S, Hemida H (2021) Prediction of Scour Around Single Vertical Piers with Different Cross-Section Shapes. Ocean System Engineering. Vol. 11, No. 1 (2021) DOI: https:// doi.org/10.12989/ose.2021.11.1.

Appendix III: Bordbar A, Sharifi S, Hemida H (2021) Investigation of Scour around Two Side-by-Side Piles with Different Spacing Ratios in Live-bed. The second Vietnam Symposium on Advances in Offshore Engineering (VSOE2021). (In press)

2 REVIEW OF THE PREVIOUS RESEARCH

2.1 INTRODUCTION

This chapter provides a brief introduction to underlying mechanism of local scour and its numerical modelling. First, in section 2.2, the underlying physics of fluid flow adjacent to the mounted pile/pier and governing equations on flow are described. Then, in section 2.3 underlying physics and governing equations of sediment transport is illustrated. Finally, in section 2.4 and 2.5, a literature review of previous experimental and numerical studies of scour around piles/piers under different flow conditions is provided, respectively. It is to be noted that the provided literature includes pertinent works with a focus on the aim and objectives of this study.

2.2 UNDERLYING PHYSICS OF FLUID FLOW AROUND THE MOUNTED PILE/PIER AND GOVERNING EQUATIONS OF FLUID FLOW

Flow around piles/piers mounted in a riverbed or seabed is an examples of junction flow. Junction flow is a complex 3-dimensional (3D) flow phenomenon that occurs when a boundary layer flow over a surface meets an obstacle attached to the surface as shown in Figure (2-1) (Simpson, 2001). A boundary layer is defined as a region of the flow where the velocity of a moving viscous fluid is distributed due to its interactions with a solid surface. Figure (2-1) illustrates formation of a junction flow around a circular cylinder. Junction flow includes the formation of horseshoe vortices at upstream, Kármán vortex street at downstream and contraction of streamlines at the sides of the obstacle (Sumer, 2002; Sumer and Fredsøe, 2001a). Due to the impact of the pier nose on flow, down-flow is formed upstream of the pier. The

down-flow impinges the bed and produces a complex vortex system known as a horseshoe vortex (HSV). HSVs are the 3D vortices that wrap around the obstacle due to producing an adverse pressure gradient and separation upstream of the obstacle. HSV structures can be of different forms, from a single steady primary vortex in laminar junction flow to multiple unsteady vortices in turbulent junction flow (Simpson, 2001). Kármán vortex shedding (lee-wake vortices), on the other hand, is an oscillating flow that forms downstream of the obstacle. Vortex shedding produces alternating low-pressure turbulent vortices downstream of the obstacle. These time-varying flow structures around the obstacle increase the local bed shear stress, and consequently, the sediment transport capacity. This increase in local sediment mobility unbalances the local sediment flux and leads to local scour.

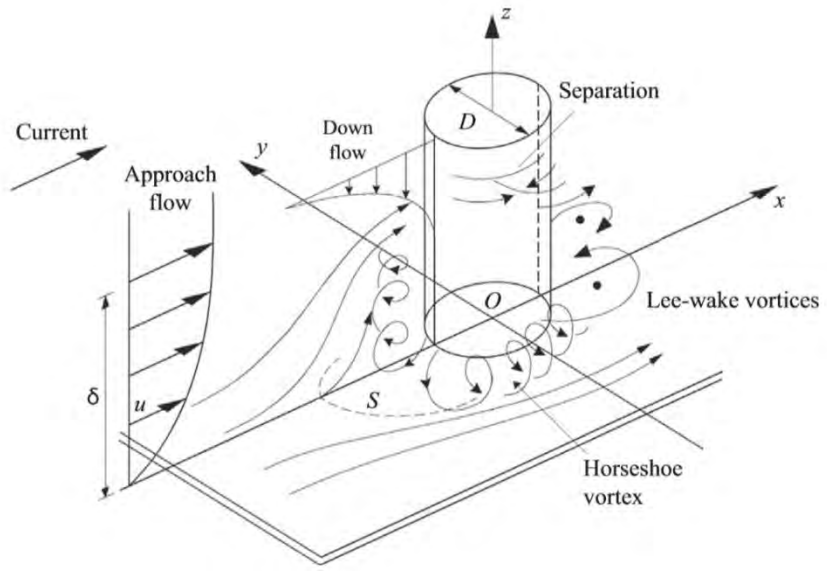


Figure (2-1) Definition sketch of the junction flow and formation of HSV and lee-wake vortices from Roulund et al. (2005).

Numerical modelling of scour can be divided into two groups of single- and two-phase flow modelling approaches. In single-phase approach, the flow field governing equations are solved only for fluid phase while in two-phase flow approaches, the flow field is solved for both

sediment and fluid phases. The single-phase model, which is known as classical approach, has been widely used for sediment transport modelling due to its simplicity and computational efficiency. In this approach, the bottom boundary of the computational domain is determined as a sandy bed. The model employs a coupled hydro- and morphodynamic system. The hydrodynamic part of the model solves the motion of the fluid substances. The results of the hydrodynamic model are applied to solve the semi-empirical sediment transport models and the results of the sediment transport are reflected as a deformation of the sandy bed. On the other hand, two-phase flow models have been conducted in an Eulerian-Eulerian or Eulerian-Lagrangian approach, while considering the sediment phase as a continuous or discrete phase, respectively.

In the present study, the classical approach is followed for modelling sediment transport and local scour. Therefore, the main focus of the following sub-sections is reviewing the literature and governing equations of the classical approach. A summary of the studies on two-phase flow modelling of sediment transport is also briefly provided at the end of this chapter.

2.2.1 Hydrodynamic model

In the classical approach for modelling scouring, the hydrodynamic and morphodynamic models are coupled. Solving the hydrodynamic model provides bed shear stress which is the primary parameter for the sediment transport model (Stahlmann, 2013b). Hence, the accuracy of the computed flow field has a direct impact on the results of sediment transport models and ultimate scour patterns. Mathematical description of a general-purpose model for fluid flow can be achieved by derivation of mass conservation and momentum equations. To be able to solve the flow field on the computational domain using the governing equations, the domain needs to be discretized into finite number of elements at which the variables will be calculated. In a

general form, writing down a mass-balance for a fluid element, as shown in Figure (2-2), states that the rate of increase of mass in the element is equal to the net rate of flow of mass into the element (Versteeg and Malalasekera, 2007). In Cartesian coordinate system, this yields an unsteady continuity equation for a compressible fluid in the convention of Einstein's summation as follows:

$$\frac{\partial \rho}{\partial t} + \frac{\partial \rho U_i}{\partial x_i} = 0 \qquad (2\text{-}1)$$

where t is time, ρ is the fluid density and U_i is instantaneous velocity in the x_i direction.

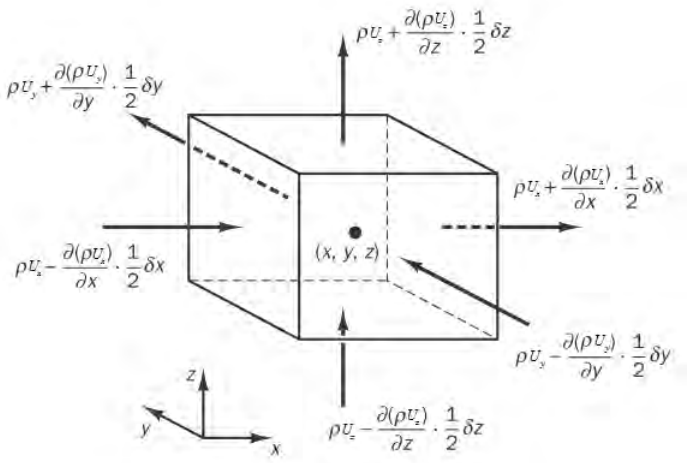


Figure (2-2) In and out flow for a fluid element (Versteeg and Malalasekera, 2007)

On the other hand, momentum equation for the fluid element states that the rate of change of momentum of a fluid elements is equal to the sum of the forces on the fluid elements (Versteeg and Malalasekera, 2007). Writing down the momentum equations (Newton's second low) for the fluid element and applying Newton's law of viscosity provides the Navier-Stokes equations. The Navier-Stokes equations in Cartesian coordinate system for a compressible flow are as follows:

$$\frac{\partial(\rho U_i)}{\partial t} + \frac{\partial(\rho U_i U_j)}{\partial x_j} = S_{M,i} - \frac{\partial P}{\partial x_i} + \mu \frac{\partial^2 U_i}{\partial x_i \partial x_j} \qquad (2\text{-}2)$$

where P is the instantaneous pressure, μ is fluid dynamic viscosity, and $S_{M,i}$ is the body force in the x_i direction.

In fluid dynamics, the fluid flow can generally be divided into two fluid regimes of laminar and turbulent flows. laminar flow is characterized by fluid particles following smooth paths in layers, with each layer moving smoothly past the adjacent layers with little or no mixing and its behaviour can be described by equation (2-1) and (2-2) (Versteeg and Malalasekera, 2007). On the other hand, in turbulent flow, a chaotic state of motion develops in which the flow attributes change continuously with time within substantial regions of flow (Versteeg and Malalasekera, 2007). In most practical cases, simulation of the flow behaviour is carried out by the means of turbulence modelling. Different approaches such as Large Eddy Simulation (LES), Reynolds Averaged Navier-Stokes (RANS) or a combined approach like Detached Eddy Simulation (DES) are defined for the purpose of turbulence modelling using the Navier-Stokes equations in 3D turbulent flow field. A general description of these approaches can be found in Rodi (1997), Rodi et al. (1997) and Wilcox et al. (2006). The accuracy of the models in capturing the behaviour of the turbulent structures near the junction and computational expenses are the main factors in selecting a suitable hydrodynamic model in the classical approach. Although LES model generally attains higher accuracy in simulation of turbulent quantities, it needs high mesh resolution and small-time steps which lead to high computational loads. Due to the large period of the physical process of scouring, e.g. few hours, LES model could not be chosen in the present study. On the other hand, for a case of RANS and DES, Paik et al. (2007) conducted a comparison between the unsteady-Reynolds Averaged Navier-Stokes (RANS), Detached Eddy Simulation (DES), and adjusted DES model in predicting HSVs upstream of a

wing mounted on a flat plate (wing-body junction). The results showed the acceptable capability of the unsteady-RANS model for modelling time-averaged vortices in junction flow, which is one of the main physical factors responsible for scour formation around a pile. In the next section a brief description of unsteady-RANS model in combination with the *k-ω SST* model as a turbulence closure is provided.

2.2.2 Unsteady-RANS equations for a single-phase flow

In order to model the random nature of the turbulent flow in Reynolds-averaged approach, the instantaneous flow variables U and P are replaced by:

$$U(t) = u + u'(t); P(t) = p + p'(t) \tag{2-3}$$

which is known as Reynolds decomposition, where u and p are mean (ensemble average) values and a u' and p' are fluctuation components. Substituting the Reynolds decomposition in Eq. (2-1) and Eq. (2-2) for an incompressible flow and some rearranging for the stress terms yields:

$$\frac{\partial u_i}{\partial x_i} = 0 \tag{2-4}$$

$$\frac{\partial u_i}{\partial t} + u_j \frac{\partial u_i}{\partial x_j} = s_{M,i} - \frac{1}{\rho}\frac{\partial p}{\partial x_i} + \nu \frac{\partial^2 u_i}{\partial x_i \partial x_j} + \frac{1}{\rho}\frac{\partial \tau_{ij}}{\partial x_j} \tag{2-5}$$

where u_i and $s_{M,i}$ are the ensemble average velocity and the body force in the x_i direction respectively, τ_{ij} is the Reynolds stress component, and ν is the kinematic viscosity of the fluid. The set of Eq. (2-4) and Eq. (2-5) is called unsteady-RANS equations. Boussinesq (1877) suggested that Reynolds stresses are proportional to the mean rate of deformation and can be presented in the form of:

$$\frac{\tau_{ij}}{\rho} = \nu_t \left(\frac{\partial u_i}{\partial x_j} + \frac{\partial u_j}{\partial x_i} \right) - \frac{2}{3} k \delta_{ij} \tag{2-6}$$

Where ν_t is kinematic turbulent viscosity (eddy viscosity), k is turbulent kinematic energy per unit mass, and δ_{ij} is Kronecker delta which is given as ($\delta_{ij} = 1\ if\ i = j\ and\ \delta_{ij} = 0\ if\ i \neq j$). In order to model eddy viscosity, different turbulence models, e.g. *k–ε*, *RNG k–ε*, *k-ω*, *Spalart-Allmaras*, *k-ω SST*, are developed. The *k-ω SST* turbulence closure model has a proven capability in predicting adverse pressure gradients and separation flow (Menter, 1992a). In the next sub-section, a robust two-equation eddy-viscosity turbulence model, the *k-ω SST* model, is explained.

2.2.3 The *k-ω SST* turbulence closure model

The *k-ω SST* model includes a combination of *k–ε* and *k-ω* turbulence closures. The model is able to switch between these two models. As Menter (1992a) pointed out, however, the *k–ε* model indicates a satisfactory performance on free stream flow, its performance in boundary layer flow with adverse pressure gradients is controversial. Thus, he suggested a hybrid model. The model uses the standard *k–ε* model in the fully turbulent region far from the wall and transformation of the *k–ε* model into a *k–ω* model in the near-wall region (Menter (1992a), Menter (1992b), Menter (1994), Menter (1997), Menter et al. (2003) and Wilcox et al. (2006)). The *k-ω SST* turbulence closure model has a good capability in predicting adverse pressure gradients and separating flow (Menter, 1992a).

The transport equation for turbulence kinematic energy, k, is described as:

$$\frac{\partial k}{\partial t} + \frac{\partial (u_i k)}{\partial x_i} - \frac{\partial}{\partial x_i}\left[(\nu + \sigma_k \nu_t)\ \frac{\partial k}{\partial x_i}\right] = P_k - \beta^* \omega k \qquad (2\text{-}7)$$

where P_k is the production term of k which is calculated as:

$$P_k = min\left\{\nu_t \left(\frac{\partial u_i}{\partial x_j} + \frac{\partial u_j}{\partial x_i}\right)\frac{\partial u_i}{\partial x_j}, 10\beta^* k\omega\right\} \qquad (2\text{-}8)$$

and β^* is a model constant with a value of 0.09. The turbulent viscosity, ν_t, is calculated from:

$$\nu_t = \frac{a_1 k}{max(a_1\omega, SF_2)} \tag{2-9}$$

Where $S = \sqrt{2s_{ij}s_{ij}}$ and

$$s_{ij} = \frac{1}{2}\left(\frac{\partial u_i}{\partial x_j} + \frac{\partial u_j}{\partial x_i}\right) \tag{2-10}$$

is the strain-rate tensor of the velocity field.

The turbulence frequency or specific dissipation rate, ω, is defined as a ratio of $\varepsilon/\beta^* k$, where ε is the dissipation rate of turbulence energy. The transport equation for turbulence frequency is (Davidson, 2006; Menter et al., 2003):

$$\begin{aligned} &\frac{\partial \omega}{\partial t} + \frac{\partial (u_i \omega)}{\partial x_i} - \frac{\partial}{\partial x_i}\left[(\nu + \sigma_\omega \nu_t)\ \frac{\partial \omega}{\partial x_i}\right] \\ &\qquad = P_\omega - \beta\omega^2 - 2(F_1 - 1)\frac{\sigma_{\omega 2}}{\omega}\frac{\partial k}{\partial x_i}\frac{\partial \omega}{\partial x_i} \end{aligned} \tag{2-11}$$

where $P_\omega = \alpha S^2$ is the production term of ω. The blending functions F_1 and F_2 are evaluated from:

$$F_1 = tanh(\xi^4), \qquad \xi = min\left[max\left(\frac{\sqrt{k}}{\beta^*\omega y}, \frac{500\nu}{y^2\omega}\right), \frac{4\sigma_{\omega 2} k}{CD_{k\omega} y^2}\right] \tag{2-12}$$

$$F_2 = tanh(\eta^2), \qquad \eta = max\left(\frac{2\sqrt{k}}{\beta^*\omega y}, \frac{500\nu}{y^2\omega}\right) \tag{2-13}$$

where $CD_{k\omega}$ is,

$$CD_{k\omega} = \max\left(2\frac{\sigma_{\omega 2}}{\omega}\frac{\partial k}{\partial x_i}\frac{\partial \omega}{\partial x_i}, 10^{-10}\right) \tag{2-14}$$

As mentioned earlier, the advantage of the *k-ω SST* model is the capability to switch between the *k–ε* and *k-ω* turbulence closures. This aim is met by the last term in Eq. (2-11). When this

term goes to 0, the model turns into *k–ε* model (Davidson, 2006; Menter et al., 2003). The model constants σ_k, σ_ω, α and β are also calculated by the meaning of blending function where,

$$\phi = F_1\phi_1 + (1 - F_1)\phi_2 \tag{2-15}$$

when ϕ should be substituted with one of σ_k, σ_ω, α and β when the other required constants are,

$$\alpha_1 = 5/9, \qquad \alpha_2 = 0.44$$

$$\beta_1 = 3/40, \qquad \beta_2 = 0.0828$$

$$\sigma_{k1} = 0.85, \qquad \sigma_{k2} = 1$$

$$\sigma_{\omega1} = 0.5, \qquad \sigma_{\omega2} = 0.856.$$

2.2.4 Boundary layer over a flat plate

As mentioned earlier at the beginning of section 2.2, a hydrodynamic boundary layer is defined as a region of the flow where the velocity of a moving viscous fluid is distributed due to its interactions with a solid surface. The behaviour of this layer can be explained with the definition of boundary layer theory. In this section, the boundary layer theory for smooth and rough walls is described in detail. According to Zanke (1982), the boundary layer thickness, δ, is measured from the solid surface, where the velocity is zero, to the point where the fluid's velocity reaches ~99% of undisturbed flow velocity (u_{max}). This boundary layer thickness is controlled by the surface roughness and the fluid and flow attributes. Generally, there are two types of laminar and turbulent boundary layer flows. In laminar flow, the fluid moves in layers where each layer gradually passes the adjacent layers. In turbulent boundary layer, in contrast, fluid moves in unsteady and random patterns. The turbulent boundary layer adjacent to a solid surface includes

inner and outer regions, as shown in Figure (2-3). The inner region has an approximate thickness of 10–20% of the total boundary layer and can be divided into three sub-layers:

- The linear sub-layer where the flow is dominated with viscous stresses.
- The buffer layer where both viscous and turbulent stresses are important.
- The log-law layer where the flow is dominated by turbulent (Reynolds) stresses.

The outer region or law of the wake layer is the region where the flow is dominated with inertia forces far from the wall, and free from direct viscous effects (Versteeg and Malalasekera, 2007).

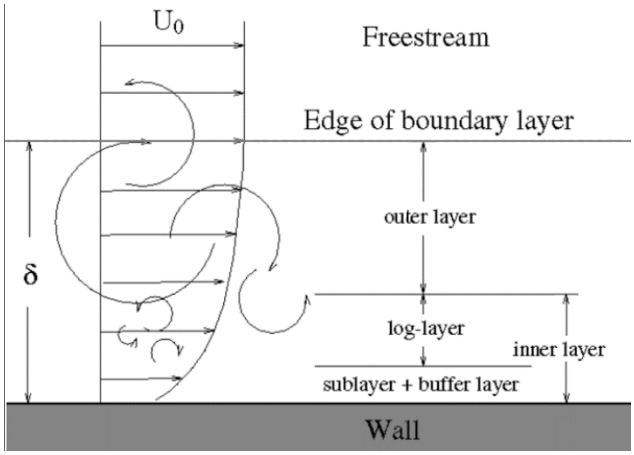


Figure (2-3) Turbulence boundary layer (Bakker, 2006).

Generally, surfaces can be categorised in two groups of smooth and rough surfaces. The roughness of a surface is measured by a parameter named equivalent roughness height k_s. When the roughness height k_s is smaller than the thickness of viscous sub-layer, the surface is smooth. In contrast, when the wall or bed roughness element exceeds the viscous sub-layer into the logarithmic layer, the surface is rough.

2.2.4.1 Smooth wall boundary layer

To better explain the flow behaviour in the boundary layer, a Reynolds number which represents the ratio of inertial force to viscous force within the fluid is defined. Re_z can be

defined as uz/ν on a distance z away from the wall, where u is the flow velocity at the point. On the wall, where $z \to 0$, $Re_z \to 0$ and the viscous forces dominate the flow. In contrast, far away from the wall ($Re_z \gg 1$), the inertia forces dominate the flow.

Inner layer

In the area very close to the wall, just before z reaches zero and where Re_z is of the order of 1, the viscous forces and the inertia forces will be in the same order of magnitude. In this thin layer close to the wall (inner region), flow is affected by viscous forces. In this layer, the mean flow velocity can be expressed as a function of distance z from the wall, fluid density ρ and dynamic viscosity μ and the wall shear stress τ_w (Versteeg and Malalasekera, 2007):

$$u = f(z, \rho, \mu, \tau_w) \tag{2-16}$$

For the inner region, dimensional analysis reveals that (Versteeg and Malalasekera, 2007):

$$u^+ = \frac{u}{u_f} = f(z^+), \qquad where\ z^+ = \frac{\rho u_f z}{\mu}. \tag{2-17}$$

Eq. (2-17) is called the law of the wall, and u^+ and z^+ are non-dimensional velocity and distance, respectively, and u_f is the friction velocity (shear velocity) defined as:

$$u_f = \sqrt{(\tau_w / \rho)}. \tag{2-18}$$

For calculating the velocity in the inner region, the analytical approximation functions for viscous sub-layer and the log-law layer are available, but for the buffer layer typically a blending function is used.

Linear or viscous sub-layer

In the case of smooth wall, very close to the wall ($z^+ < 5$) where the turbulent eddies do not exist, fluid behaviour is defined by viscous effects. In this layer, the shear stress is almost constant and equal to the wall shear stress τ_w. Hence:

$$\tau(z) = \mu \frac{\partial u}{\partial z} \cong \tau_w \tag{2-19}$$

with integration, and applying the corresponding boundary conditions, a linear relationship between the mean velocity and the distance from the wall is obtained:

$$u = \frac{\tau_w z}{\mu} \tag{2-20}$$

which is why viscous sublayer is also known as the linear sub-layer (Versteeg and Malalasekera, 2007).

Log-law layer

In the log-law layer (logarithmic layer) which is the region where $30 < z^+ < 500$ both viscous and turbulent effects are important. In this layer, shear stress changes with distance from the wall. In this region, based on the work of Schlichting (1979), a relationship between u^+ and z^+ is given:

$$u^+ = \frac{1}{\kappa} \ln(z^+) + B \tag{2-21}$$

where $\kappa \approx 0.4$ is von Karman's constant and $B \approx 5.5$ is the additive constant.

Outer layer

The inner layer only covers a small part of the turbulent boundary layer $z/\delta < 0.2$. For further distances from the wall in the boundary layer, $0.2 < z/\delta < 1$, the velocity at a point is affected by distance z, boundary layer thickness δ, viscosity μ and the wall shear stress τ_w (Versteeg and Malalasekera, 2007):

$$u = g(z, \delta, \mu, \tau_w). \tag{2-22}$$

Dimensional analysis for the outer region determines that (Versteeg and Malalasekera, 2007):

$$u^+ = \frac{u}{u_f} = g\left(\frac{z}{\delta}\right). \tag{2-23}$$

Tennekes and Lumley (1972) suggested a logarithmic formula for this region:

$$\frac{u_{max} - u}{u_f} = -\frac{1}{\kappa}\ln(\frac{z}{\delta}) + C \tag{2-24}$$

where C is a constant. Eq. (2-24) is called the velocity-defect law or law of the wake.

2.2.4.2 Rough wall boundary layer (Sandy bed boundary layer)

For the case of a sand-covered wall or bed, the calculation of roughness height entails two factors. 1) a single grain roughness ($k_{s,g}$) which is directly related to the single sediment particle diameter size, and 2) wall or bedform roughness ($k_{s,f}$) which is obtained from formation of sand ripples and dunes (Nikuradse, 1933). As mentioned earlier in section 2.2.4, when the wall or bed roughness element exceeds the viscous sub-layer into the logarithmic layer, the surface is rough. In this case, the viscous sub-layer does not exist. In one of the most well-known studies, Schlichting (1979) described the three regimes of hydraulically smooth, transition and completely rough surface by considering a dimensionless roughness height (normalized sand roughness) $k_s^+ = k_s u_f/\nu$ as below:

hydraulically smoot	$k_s^+ < 5$	
transition	$5 < k_s^+ < 70$	(2-25)
completely rough	$k_s^+ > 70$	

According to Schlichting (1979), the relationship which describes the velocity distribution for the logarithmic layer of a smooth wall, Eq. (2-21), remains valid for a rough wall, however, the

additive constant B in the equation is modified with adding a negative constant term ΔB which is a function of roughness height, k_s^+. Thus, Eq. (2-21) becomes:

$$u^+ = \frac{1}{\kappa}\ln(z^+) + B - \Delta B. \qquad (2\text{-}26)$$

Figure (2-4) from Driest (1956) provides a semi-logarithmic plot which illustrates velocity profiles for turbulent boundary layer flow near smooth and rough walls. For different values of dimensionless roughness height k_s^+ a different curve is drawn, however the provided range for each regime is a bit different from that of Schlichting (1979).

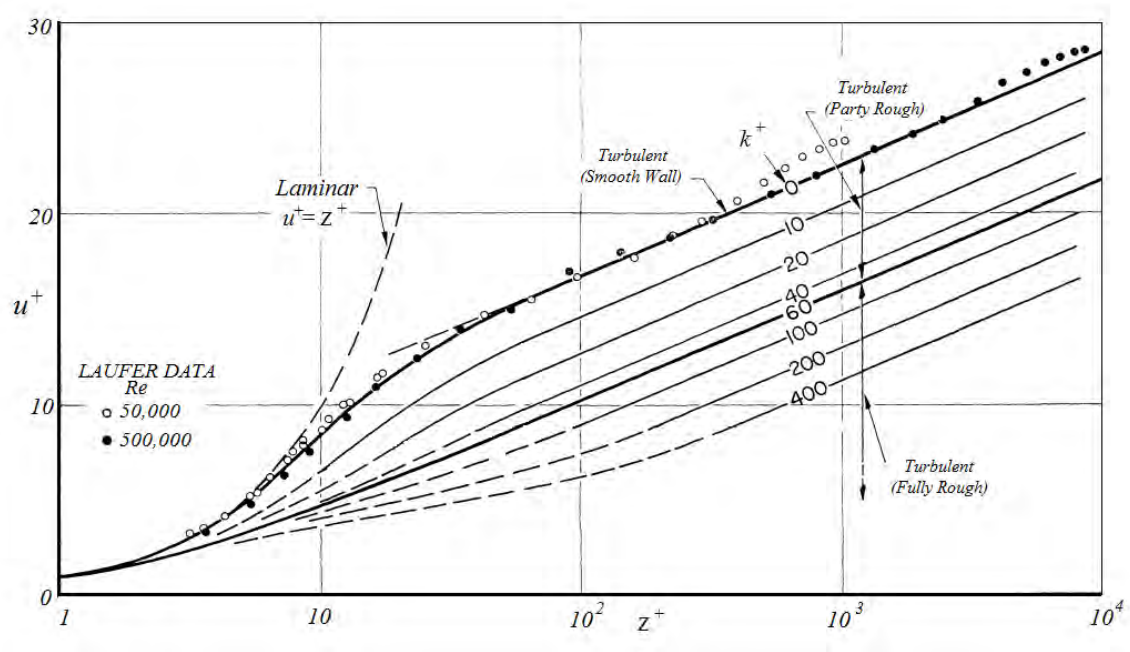


Figure (2-4) Semi-logarithmic plot of the velocity profile for turbulence flow over smooth and rough wall (Driest, 1956).

2.2.5 Near-wall treatment methods (Wall-functions)

In Computational Fluid Dynamics (CFD) modelling, generally, there are two approaches to satisfy the boundary conditions for the turbulence model attributes on the walls. These approaches are called low-Re and high-Re approaches. The difference between these

approaches is the way they treat the boundary layer region of the flow. In the low-Re approach, the resolution of the generated mesh near the wall is fine enough to enable the model to resolve the viscous sublayer near the wall where the turbulence Reynolds number ($Re_t = k^2/\varepsilon\nu$) is very small (Menter, 2009). Thereby, turbulent parameters can be described in a rather simple way by turbulent kinematic energy $k = 0$ (Schlichting and Gersten, 2006), and turbulent frequency $\omega = 6\nu/\beta_1 y^2$, where $\beta_1 = 0.075$ and y is the orthogonal distance of the first layer of mesh to the wall.

On the other hand, in the high-Re approach (known as the wall function approach), the resolution of the mesh near the wall is highly reduced to decrease the computational expenses (Launder and Spalding, 1972). In this case, the solution of the model for turbulent parameters around the boundary layer is invalid. So, wall functions are used to bridge the unresolved region between the wall and the turbulent flow. Therefore, near-wall values are provided by empirical functional relations (wall-functions) which provide rather similar values for turbulence properties (Schlichting and Gersten, 2006 and Menter, 2009). These equations are valid for different regions of the boundary layer and different wall conditions (smooth or rough wall).

2.2.5.1 Logarithmic wall function

In this method, where the roughness of the surface is known, the near-wall velocity distribution for the logarithmic region of the boundary layer can be defined by the logarithmic profile provided in Eq. (2-26). This method is widely used to calculate friction velocity in open channels and rivers (Nakagawa, 2017). As mentioned, ΔB in Eq. (2-26) depends on the wall roughness. Cebeci and Bradshaw (1977) proposed a method to calculate the value of ΔB based on the value of the dimensionless (normalized) roughness height:

Hydrodynamically smooth surface:

$(k_s^+ < 2.25)$: $$\Delta B = 0 \quad (2\text{-}27)$$

Transitional surface:

$(2.25 \leq k_s^+ \leq 90)$: $$\Delta B = \frac{1}{\kappa}\ln\left[\frac{k_s^+ - 2.25}{87.75} + C_s k_s^+\right]\sin\left[0.4258\,(\ln k_s^+ - 0.811)\right] \quad (2\text{-}28)$$

Fully rough surface:

$(k_s^+ > 90)$: $$\Delta B = \frac{1}{\kappa}\ln\left[1 + C_s k_s^+\right] \quad (2\text{-}29)$$

where C_s is the roughness constant.

2.2.5.2 Global (Continuous) wall function

Cebeci and Chang (1978) proposed a method to approximate the flow behaviour near rough walls in turbulent flow. This method is the expansion of the work of Driest (1956) which was valid for smooth walls. The original model, Driest (1956), proposed a global function for estimation of flow velocity in turbulent flow near smooth wall which was proven to be valid for all viscous, buffer and logarithmic layers. Cebeci and Chang (1978) added a coordinate shift method to the model to introduce a global function for the rough surfaces. Therefore the dimensionless near-wall flow velocity in Cebeci and Chang (1978) can be calculated from:

$$u^+ = \int_0^{z^+} \frac{2dz^+}{1 + \sqrt{1 + 4\kappa^2(z^+ + K)^2\left[1 - exp\left(-\frac{z^+ + K}{A}\right)\right]^2}} \quad (2\text{-}30)$$

where $A = 25$ is the Driest damping factor, and K is a function of dimensionless roughness height, as below:

$$K = \begin{cases} 0 & k_s^+ \leq 5 \\ 0.9\left[\sqrt{k_s^+} - k_s^+ exp\left(-\frac{k_s^+}{6}\right)\right] & 5 < k_s^+ < 2000. \end{cases} \quad (2\text{-}31)$$

In numerical modelling, the calculation of the integration, Eq. (2-30), follows by applying a trapezoidal rule, which in general form is as:

$$\int_{a_1}^{a_2} Q(x)dx \approx (a_2 - a_1)\frac{Q(a_1) + Q(a_2)}{2}. \quad (2\text{-}32)$$

where a_1 and a_2 are lower and upper limits of integration and $Q(x)$ is a sample function.

2.2.6 Bed shear stress

In sediment transport modelling using the classical approach, bed shear stress is a key parameter which connects the fluid flow outcomes to the sediment motion. The accuracy in calculating the local bed shear stress directly impacts the validity of calculated sediment transport capacity and ultimate sandy bed morphology results. According to Eq. (2-18), local bed shear stress is related to the friction velocity (shear velocity). In the literature, the calculation of the friction velocity can be achieved using different methods. The provided wall functions in section 2.2.5 can be used to calculate friction velocity in the boundary layer region. Apart from them, in the following sub-sections, a few other methods which are applicable to calculate friction velocity in open-channel flow with rough walls is presented.

2.2.6.1 Reach-averaged method

In the simplest method, based on a force balance approach and in two-dimensional uniform flow, shear velocity can be estimated by:

$$u_f = \sqrt{gR_hI} \quad (2\text{-}33)$$

where g is the acceleration of gravity, R_h is the hydraulic radius and I is the bed slope. Hydraulic radius R_h is equal to (A_c/P_w), where A_c is the cross-section area and P_w is the wetted perimeter.

2.2.6.2 Reynolds stress method

When turbulence property measurements are available, Kim et al. (2000) suggested applying the measured Reynolds stress distribution to calculate the local mean friction velocity. This method provides the direct calculation of friction velocity and ideally is independent of the distance from the wall. This idea can be expressed as:

$$u_f = \sqrt{\left(-\overline{u'w'}\right)} \tag{2-34}$$

where u' and w' are turbulent longitudinal and vertical velocity fluctuations, respectively, and the over bar denotes time averaged values.

2.2.6.3 Turbulent kinetic energy (TKE) method

Friction velocity can also be obtained from TKE calculations (Kim et al., 2000) where TKE is defined as:

$$TKE = \frac{1}{2}\left(\overline{u'^2} + \overline{v'^2} + \overline{w'^2}\right) \tag{2-35}$$

Where u', v', and w are turbulence velocity fluctuation in x, y, and z direction, respectively. Townsend (1976) mentioned linear relationships between TKE and shear stress, and Soulsby and Dyer (1981) pointed out the constant average ratio of shear stress to TKE, which leads to:

$$u_f = \sqrt{C_1\, TKE} \tag{2-36}$$

in which C_1 is a constant.

Other methods for calculating friction velocity are the wall similarity and spectral methods, which both are based on the definition of turbulent energy production and dissipation. For more information on different methods for estimating shear velocity in rough bed open-channel flow, the reader is referred to Bagherimiyab and Lemmin (2013) and Kim et al. (2000).

2.3 UNDERLYING PHYSICS AND GOVERNING EQUATIONS OF SEDIMENT TRANSPORT

2.3.1 Cohesive and non-cohesive sands

The sediment transported in river and seabed contains particles with different sizes, ranging from gravel or sand down to very small particles classified as silt or clay. Table (2-1) shows an accepted system of classification of sediment size by the American Geophysical Union (AGU). Based on Table (2-1), the cohesive soil particles are finer than 0.06 mm, and non-cohesive soil particles are in ranges from 0.06 mm to 64 mm. The provided sediment transport mechanism in this section is only valid for non-cohesive soils (sands and gravels). The behaviour of cohesive soils is different from non-cohesive soils, and thus, their behaviour cannot be explained by the same principles.

Since natural sediments include a heterogeneous mixture of particles, different approaches have been proposed to represent the particle size distribution. Sieve analysis is one of the most convenient methods for the analysis of particle size distribution, which is applicable for particle sizes larger than 0.06 mm. Based on sieve analysis, sieve diameter, d_s, is introduced to represent the sand particles. In which s is the percentage of the particles finer than a spherical particle with diameter d by weight.

Table (2-1) AGU's soil technology classification of particles (Mehta, 2013).

	Name	Particle size (mm)	Designation
Non-cohesive Soil	Gravel	64-32	Very coarse
		32-16	Coarse
		16-8	Medium
		8-4	Fine
		4-2	Very fine
	Sand	2-1	Very coarse
		1-0.5	Coarse
		0.5-0.25	Medium
		0.25-0.125	Fine
		0.125-0.062	Very fine
Cohesive Soil	Silt	0.062-0.031	Coarse
		0.031-0.016	Medium
		0.016-0.008	Fine
		0.008-0.004	Very fine
	Clay	0.004-0.002	Coarse
		0.002-0.001	Medium
		0.001-0.0005	Fine
		0.0005-0.0002	Very fine

2.3.2 Sediment transport modes in classical approach

In a very general case, to develop a mathematical basis for fluid and sediment flow, the governing equations are considered for a small element (Figure (2-5)). In this manner, mass-balance equations of a unit volume for a two-phase fluid-sediment flow can be written where the rate of increase of mass in the volume is equal to the net rate of flow of mass into the volume element, as given by:

$$\frac{\partial}{\partial t}\big(\rho(1-C)\big)+\frac{\partial}{\partial x_i}(\rho(1-C)\,U_i)=0 \qquad fluid \qquad (2\text{-}37)$$

$$\frac{\partial}{\partial t}(\rho_s C)+\frac{\partial}{\partial x_i}\big(\rho_s C\,U_{s,i}\big)=0 \qquad sediment \qquad (2\text{-}38)$$

In which C is the local sediment volume concentration, U_i and $U_{s,i}$ are local fluid and sediment velocity in x_i direction, respectively, ρ is fluid density, ρ_s is sediment density, and t is time.

Fundamentally, these equations must be solved concurrently for the fluid and sediment phases. The effect of turbulence can be considered by time averaging as follows:

$$U = u + u', \qquad C = c + c' \tag{2-39}$$

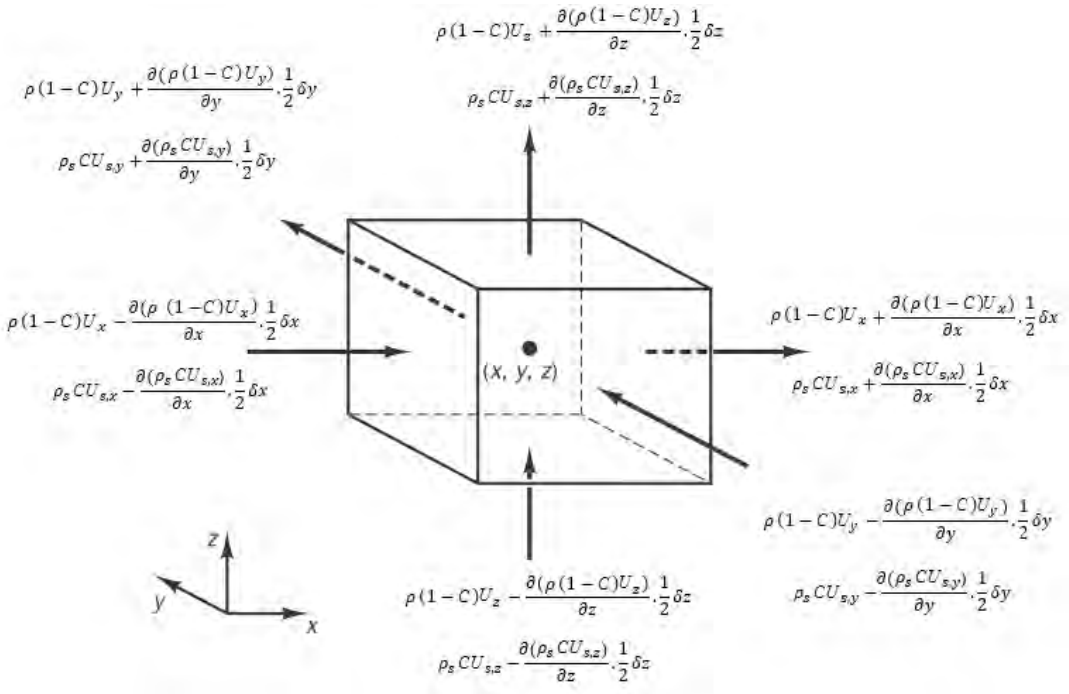


Figure (2-5) Fluid and sediment flow of mass in and out of a volume element.

in which, c and u represent the ensemble averaged and c' and u' represent the fluctuating components of sediment concentration and velocity. Substituting Eq. (2-39) in Eq. (2-37) and Eq. (2-38), averaging over time, and assuming constant fluid and sediment density leads to:

$$\frac{\partial}{\partial t}(1-c) + \frac{\partial}{\partial x_i}\Big((1-c)\,u_i - e_{f,i}\Big) = 0 \qquad fluid \tag{2-40}$$

$$\frac{\partial}{\partial t}(c) + \frac{\partial}{\partial x_i}\big(c\,u_{s,i} + e_{s,i}\big) = 0 \qquad sediment \tag{2-41}$$

Where $e_{f,i}$ and $e_{s,i}$ are turbulence-induced transport components for fluid and sediment, respectively. To represent turbulence-induced transport components, the eddy-viscosity concept (Boussinesq, 1877) is applied:

$$e_{f,i} = -D_f \frac{\partial c}{\partial x_i} \tag{2-42}$$

$$e_{s,i} = -D_s \frac{\partial c}{\partial x_i} \tag{2-43}$$

in which D_f and D_s are the fluid and sediment mixing coefficients (diffusivity), respectively.

Generally, it is a valid assumption that sediment velocities in the horizontal and lateral directions are the same as the fluid's velocity, but for the vertical component of sediment velocity, a term equal to particle fall velocity of sediments is added in the negative direction to the fluid's vertical velocity as:

$$u_{s,i} = u_i - w_s \delta_i \,, \qquad \delta_x = \delta_y = 0, \qquad \delta_z = 1. \tag{2-44}$$

Substituting equations (2-42), (2-43), and (2-44), in Eq. (2-40) and Eq. (2-41) provides:

$$\frac{\partial}{\partial t}(1-c) + \frac{\partial}{\partial x_i}\left((1-c)\, u_i + D_f \frac{\partial c}{\partial x_i}\right) = 0 \qquad fluid \tag{2-45}$$

$$\frac{\partial}{\partial t}(c) + \frac{\partial}{\partial x_i}\left(c\,(u_i - w_s \delta_i) - D_s \frac{\partial c}{\partial x_i}\right) = 0, \qquad sediment$$
$$\delta_x = \delta_y = 0, \qquad \delta_z = 1 \tag{2-46}$$

which is the general form of the mass-balance equation for two phase fluid-sediment flow. Rijn (1987) stated that generally in rivers and estuaries sediment concentrations are considerably small (around 5 kg/m^3), and for these conditions, the effects of sediment particles on the fluid phase are negligible. In this case, it is assumed to be accurate enough to only solve the mass-

balance equation for the sediment phase, Eq. (2-46) (also called scalar transport equation or convection-diffusion equation), in a passive manner and neglect the effect of sediments on fluid flow. However, in a very thin layer close to the bed where the sediment concentration is high (the sediment concentration can reach values as high as 60% in volume fraction) this assumption is not correct. Therefore, solving the convection-diffusion equation cannot satisfy sediment continuity adjacent to the bed. To deal with this problem, it is common to split the sediment transport modes into two main parts: Bedload and suspended load. The bedload part which is a thin layer very close to bed, includes grains that roll, slide, or jump along the bed, and can be determined by the skin friction shear stress, τ_b, which is the part of the bed shear stress acting directly on the sand grains. The suspended load, which transfer sediment over the bedload, includes grains without continuous contact with the bed, and is dominated by fluid turbulence (Fredsoe and Deigaard, 1992; Amoudry et al., 2005). Based on this explanation, for the purpose of sediment transport modelling in the classical approach, the numerical sediment transport model is divided into two modes: bedload (near-bottom transport) and suspended load (transport in the water column) where the edge between this two need to be accurately defined for mathematical representation (Rijn, 1987). A simple sketch of these sediment transport modes in the classical model is given in Figure (2-6). As shown, the reference level (dash-line) represents a hypothetical layer which splits the bedload and suspended load. The height of the reference level from the bed is in order of magnitude of a few particle diameters.

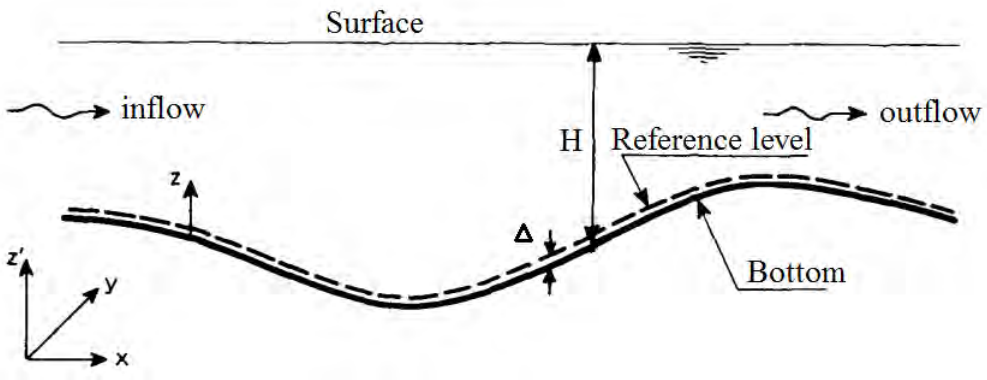


Figure (2-6) Definition sketch of the sediment transport model (Rijn, 1987).

In the next sub-sections the mathematical models for calculating both bedload and suspended load in the classical scour approach are explained in detail.

2.3.3 Critical bed shear stress for the initiation of motion

For the stationary sediment particles on the seabed/riverbed under steady current flow (time-independent flow) as shown in Figure (2-7), a certain threshold value has to be exceeded in order to initiate particle motion. This threshold value is commonly referred to as the critical bed shear stress. At very small flow velocities, particles stably rest on the bed, but with increase in velocity, when the driving forces exceed the resisting forces on the particles, the sediments will start to move. This flow velocity is called the critical flow velocity. Shields (1936) considered that the threshold of particle motion is obtained from the ratio between driving and resisting forces.

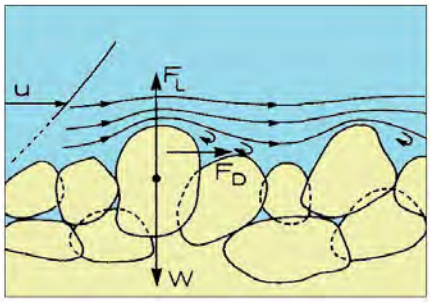


Figure (2-7) Drag and lift forces acting on a grain resting on the bed (Fredsoe and Deigaard, 1992).

In the simplest circumstance, for a particle resting on other particles on a plane horizontal bed, the critical flow velocity can be calculated by the critical Shields parameter:

$$\theta_{c,0} = \frac{u_{fc}^2}{(s-1)gd} = \frac{4\mu_s}{3c_D\alpha^2} \tag{2-47}$$

where u_{fc} is the threshold friction velocity of particle motion (critical flow velocity), d is the grain diameter, s is relative density (specific gravity), μ_s is the coefficient of static friction between the grain and the surrounding grains, c_D is the drag coefficient for the particle which can be calculated from Stokes' law for small local Reynolds number ($c_D = 24/Re_z$), and α is a non-dimensional coefficient which is in the order of 10 (Fredsoe and Deigaard, 1992). The dimensionless Shields parameter is also defined as:

$$\theta = \frac{\tau_b}{\rho g(s-1)d} = \frac{u_f^2}{g(s-1)d} \tag{2-48}$$

where τ_b is skin friction shear stress. The critical Shields parameter is a weak function of Reynolds number for the grain $Re_g = u_f d/\nu$ as shown in Figure (2-8).

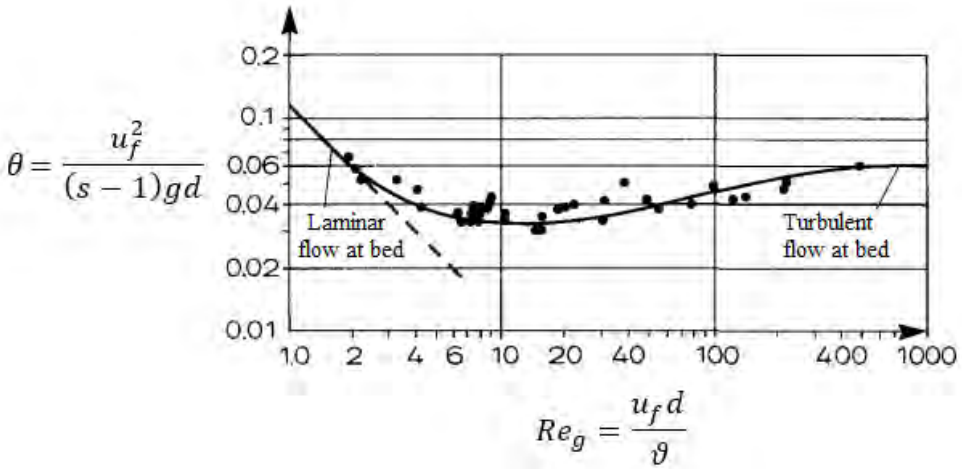


Figure (2-8) The critical Shields $\theta_{c,0}$ as a function of Re_g (Fredsoe and Deigaard, 1992).

Based on Shields experimental results as well as newer experimental data such as data compiled by Yalin and Karahan (1979), Soulsby (1997), an equation to calculate the critical Shields parameter is suggested:

$$\theta_{c,0} = \frac{0.3}{1 + 1.2D_*} + 0.055(1 - \exp(-0.02D_*)) \quad (2\text{-}49)$$

where the dimensionless particle diameter D_* is calculated as:

$$D_* = d\left[\frac{(s-1)g}{\nu^2}\right]^{1/3} \quad (2\text{-}50)$$

2.3.4 Slope-dependent critical shear stress

As mentioned in sub-section 2.3.3, θ_c is the critical value of θ for the initiation of sediment motion on the bed. The measured value for θ_c by Engelund and Fredsøe (1976) is applicable only for a horizontal bed. Based on the general case provided in Dey (2003), Roulund et al. (2005) modified the slope-dependent critical bed shear stress for cases where the bed surface has a slope in two directions (i.e. longitudinal and transverse directions):

$$\theta_c = \theta_{c,0}\left(cosb\sqrt{1 - \frac{sin^2a\,.\,tan^2b}{\mu_s^2}} - \frac{\cos a\,.\,\sin b}{\mu_s}\right) \quad (2\text{-}51)$$

where a is the angle between the near-bed flow velocity vector and direction of the steepest slope, b is the bed slope and the $\theta_{c,0}$ is the critical Shields parameter for horizontal bed.

2.3.5 Bedload transportation

Bedload occurs directly at or slightly above the bed surface. Einstein (1950) introduced one of the first theoretical approaches for the prediction of bedload transport. He used the theory of

probability to develop a bedload transport model. Based on Einstein's assumption, the mean distance travelled by a particle in the bedload is only proportional to the particle diameter. Based on the theory of probability, the principles used in his analysis were that deposition depends on the number of particles in motion in the area and on the probability that the dynamical forces on these grains let them to deposit; on the other hand, erosion depends on the number of particles within the area and on the probability that the hydrodynamic forces on these grains are strong enough to move them. Based on his work, the equilibrium condition will be achieved when the number of deposited and eroded particles are equal. This way, a non-dimensional quantity, namely bedload discharge is defined:

$$\Phi_B = \frac{q_B}{\sqrt{(s-1)gd^3}} \tag{2-52}$$

where q_B is the rate of bedload transport in a volume of material per unit time and width. The work of Einstein (1950) was modified by Bagnold (1954) and Luque (1974). Finally, Engelund and Fredsøe (1976) created a relatively simple formula for measuring the bedload transport rate on a plane bed, which is discussed in the next section. There are also different formulas and theories to calculate the bedload sediment transport rate. In this case, the works of Grass (1981) and Rijn (1993) can be noted.

2.3.5.1 Bedload transportation on a plane bed

Engelund and Fredsøe (1976) created a relatively simple formula for measuring bedload transport rate on a plane bed. They expressed the ratio of the mean transport velocity of moving particles in the bedload to friction velocity (u_B/u_f) from equilibrium of agitating (drag and lift) and stabilizing (dynamic friction) forces for moving particles. The agitating force for a sediment particle can be computed from:

$$F_{drag} = \frac{1}{2}\rho c_D(\alpha u_f - u_B)^2 \frac{\pi}{4} d^2 \tag{2-53}$$

where c_D is the drag and lift coefficient for the particle, u_B is the mean transport velocity of moving particles in the bedload and αu_f is the near-bed flow velocity at a distance of one particle diameter from the bed (Fredsoe and Deigaard, 1992) where α=10. The stabilizing force is obtained from:

$$F_f = F_N \mu_d = \frac{\pi}{6}\rho g(s-1) d^3 \mu_d \tag{2-54}$$

where F_N is the normal force and μ_d is coefficient of dynamic friction. In equilibrium conditions:

$$F_f = F_{drag} \tag{2-55}$$

substituting Eq. (2-53) and Eq. (2-54) in Eq. (2-55) and rearranging yields:

$$\frac{u_B}{u_f} = \alpha \left[1 - \sqrt{\frac{\theta_0}{\theta}}\right] \tag{2-56}$$

$$\theta_0 = \frac{4\mu_d}{3\alpha^2 c_D} \tag{2-57}$$

Luque (1974) found θ_0 to be $\frac{1}{2}\theta_c$ based on his observations. Therefore Eq. (2-56) may be re-written as:

$$\frac{u_B}{u_f} = 10 \left[1 - 0.7\sqrt{\frac{\theta_c}{\theta}}\right]. \tag{2-58}$$

Engelund and Fredsøe (1976) assumed that the bedload is the probability of the transport of the particles p that may be in a single layer. Therefore, when the total number of grains per unit

area of a surface is $1/d^2$, p/d^2 gives the number of moving particles on the bed. Hence, q_B can be written as:

$$q_B = \frac{\pi}{6} d^3 \frac{p}{d^2} u_B \tag{2-59}$$

where based on the measured value of p by Luque (1974) and Guy et al. (1966), p is given as:

$$p = \left[1 + \left(\frac{\frac{\pi}{6}\mu_d}{\theta - \theta_c} \right)^4 \right]^{-\frac{1}{4}} \tag{2-60}$$

2.3.5.2 Bedload transportation on sloping bed

Engelund and Fredsøe (1976) developed bedload transport formulations in a two-dimensional horizontal bed where Eq. (2-56) is used to calculate the mean particles transport velocity u_B. The same methodology is applied for the sloping bed, while the only difference is in the calculation of the mean particles transport velocity on the sloping bed. Roulund et al. (2005) expanded the formula of calculation of u_B for three-dimensional space of a sloping bed with the vectorial approach given in Kovacs and Parker (1994). Stahlmann (2013c) used the same approach as Jacobsen (2011) and decreased the problem of originally four non-linear coupled algebraic equations in Roulund et al. (2005) to a set of three equations. Here, a brief explanation of Stahlmann (2013c) is presented. Figure (2-9) shows the several forces acting on a single bed grain on a sloping bed.

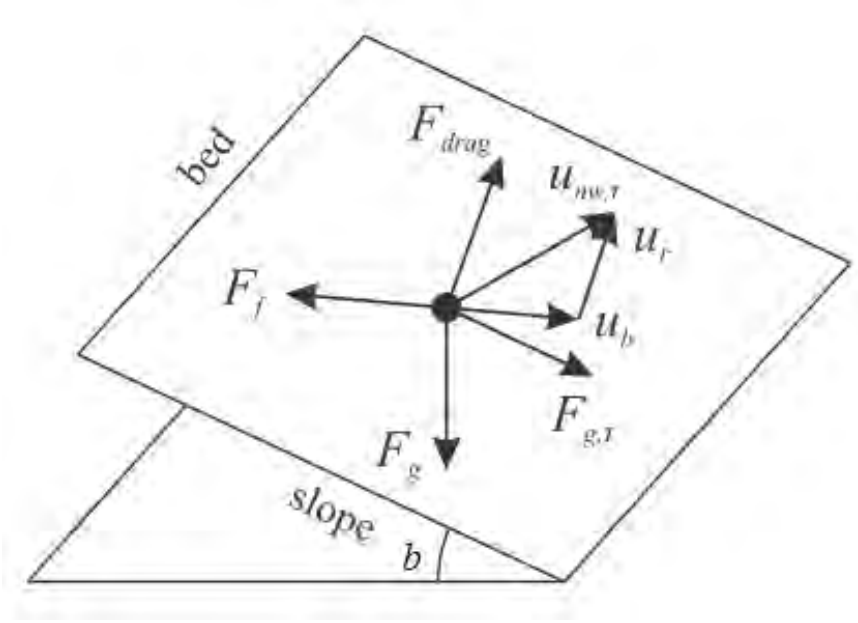


Figure (2-9) Sketch of forces acting on the particle on a sloping bed (Stahlmann, 2013c).

In Figure (2-9), $\overrightarrow{F_g}$ is the gravity force, $\overrightarrow{F_{drag}}$ is the combined lift and drag force due to relative velocity of the gains to fluid flow field, $\overrightarrow{F_f}$ is the friction force trying to resist the sediment grain movement which is given by:

$$\overrightarrow{F_f} = -\left|\overrightarrow{F_g}\right| \cos b \,.\, \mu_d \frac{\overrightarrow{u_B}}{|\overrightarrow{u_B}|} \tag{2-61}$$

in which $\overrightarrow{u_B}$ is the mean particles transport velocity vector, b is the bed slope. $\overrightarrow{F_{g,\tau}}$ is the part of $\overrightarrow{F_g}$ which works as an acting force in the direction of the steepest point of local bed slope which is given by:

$$\overrightarrow{F_{g,\tau}} = \vec{N} \times \left(\overrightarrow{F_g} \times \frac{\vec{N}}{|\vec{N}|}\right) / |\vec{N}| \tag{2-62}$$

where $\vec{N}$ is the normal vector of the sloping bed. $\overrightarrow{F_{drag}}$ is calculated by:

$$\overrightarrow{F_{drag}} = \frac{1}{2}\rho c_D \frac{\pi}{4} d^2 |\overrightarrow{u_r}| \overrightarrow{u_r} \tag{2-63}$$

Where the relative velocity $\overrightarrow{u_r}$ as shown in Figure (2-9) is related to the near-wall flow velocity $\overrightarrow{u_{nw}}$ and $\overrightarrow{u_B}$ by:

$$\overrightarrow{u_r} = \overrightarrow{u_{nw,\tau}} - \overrightarrow{u_B} \tag{2-64}$$

where $\overrightarrow{u_{nw,\tau}}$ is the near-wall flow velocity that is measured from the friction velocity:

$$\overrightarrow{u_{nw}} = a u_f \frac{\vec{u}}{|\vec{u}|}. \tag{2-65}$$

As $\overrightarrow{u_{nw}}$ may have a normal part relative to the bed surface, a mapping to the bed is required:

$$\overrightarrow{u_{nw,\tau}} = \vec{N} \times \left(\overrightarrow{u_{nw}} \times \frac{\vec{N}}{|\vec{N}|} \right) / |\vec{N}| \tag{2-66}$$

For the steady motion of the sediments, the bedload transport velocity $\overrightarrow{u_B}$ can be found from equilibrium of external forces:

$$\overrightarrow{F_f} + \overrightarrow{F_{drag}} + \overrightarrow{F_{g,\tau}} = 0. \tag{2-67}$$

Substituting equations (2-61), (2-62), and (2-63) in Eq. (2-67) creates a nonlinear system of coupled equations that are used to solve for the three components of the vector $\overrightarrow{u_B}$. The new measured value for $\overrightarrow{u_B}$ in a sloping bed is replaced with the calculated value for horizontal bed in Eq. (2-59) for measuring the vectorial form of bedload transport rate $\overrightarrow{q_B}$.

2.3.6 Settling velocity (Fall velocity)

The grain settling or fall velocity, w_{s0}, is defined as the final velocity of a grain settling in an extended fluid under the effect of gravity. A wrong estimation of the settling velocity may result in a complete infeasible result of the suspended load transport. Therefore, choosing a reasonable

value of the settling velocity is very important. A number of researchers in the past have derived equations to describe and quantify particles' settling velocity, e.g. Rijn (1984), Soulsby (1997), Jiménez and Madsen (2003), Camenen (2007). The calculated fall velocities from these studies are for a single particle, however, when the particle is one of many particles settling simultaneously, fall velocity, w_s, will be smaller than what is considered for a single particle. In this circumstance, the ratio w_s/w_{s0} is a function of the volume concentration c. A simplified equation from the experiments of Richardson and Zaki (1997), for $c << 1$, can be expressed as:

$$\begin{aligned} w_s &= w_{s0}(1-c)^n \\ n &= 4.35\, Re_{g,w_{s0}}^{-0.03} \qquad 0.2 < Re_{g,w_{s0}} < 1 \\ n &= 4.45\, Re_{g,w_{s0}}^{-0.10} \qquad 1 < Re_{g,w_{s0}} < 500 \\ n &= 2.39 \qquad\qquad\qquad 500 < Re_{g,w_{s0}} \end{aligned} \tag{2-68}$$

where $Re_{g,w_{s0}}$ is the grain fall velocity Reynolds number,

$$Re_{g,w_{s0}} = \frac{w_{s0}\, d}{\nu}. \tag{2-69}$$

2.3.7 Suspended load transportation

Over the reference level, where the turbulence is high and inter-granular interaction between the sediments is low, the sediment transport can be described by suspended load mode. In this region, with increase in distance from the bed, the sediment concentration, c, sharply decreases. Rouse (1938) proposed an equation to describe the sediment concentration distribution profile for a case of a uniform flow where the upward-directed sediment fluxes due to turbulence and downward directed sediment settling are equal:

$$c = c_{\Delta}\left[\left(\frac{H-z}{z}\right)\left(\frac{\Delta}{H-\Delta}\right)\right]^{\frac{w_s}{\kappa u_f}} \quad (2\text{-}70)$$

where c_{Δ} is the concentration at the reference level Δ above the bed, H is the water depth and z is the vertical coordinate. Nevertheless, this approach is not effective for the case of non-uniform flow such as disturbed flow around a structure. In these cases, suspended load transport and concentration have to be modelled by a transient concentration-balance equation resulting from mass conservation law for sediment concentration similar to equation (2-46) or in a more notable form,

$$\frac{\partial c}{\partial t} + \nabla.[(\vec{u} + \vec{w}_s)c] = \nabla.(D_v \nabla c) + S_c \quad (2\text{-}71)$$

where $\vec{u}$ and $\vec{w}_s$ are fluid velocity and sediment settling velocity vectors, respectively. D_v is the diffusivity and S_c is a source/sink term for entrainment and deposition. Eq. (2-71) is known as an advection-diffusion equation which is a scalar transport equation. This equation is passively solved using the resultant flow field but without any further interaction. This assumption is valid as the suspended sediment concentration is typically low and the development of the flow field itself is not affected by the suspended sediment particles in the water column (Wu, 2004; Rijn, 1987).

2.3.7.1 Entrainment and deposition

As two different models are used for calculating different parts of the sediment transport (bedload and suspended load), it is necessary to apply an interface between them (a reference level) to determine quantities of the total flux of suspended sediments from the bed into the fluid domain and vice versa. Different approaches have been recommended in the literature for calculating entrainment and deposition of particles. While they mainly describe the sediment exchanges as fluxes over the reference level, in a number of studies such as Lesser et al. (2004),

Wu (2004), Warner et al. (2008), and Stahlmann (2013c) the sediment exchanges are considered as a source/sink term. The last term in the right-hand-side of Eq. (2-71) indicates the source/sink term S_c which is applied just above the reference level. This term specifies a difference between the rate of sediment transport to the suspended sediments from the bed (entrainment fluxes E_Δ) and vice versa (deposition fluxes D_Δ) as:

$$S_c = E_\Delta - D_\Delta \tag{2-72}$$

In computing sediment transport loads, proper attention needs to be given to specifying the reference level height from the bed and the reference level concentration, since wrong estimations may result in large errors for the concentration profile (Rijn, 1984). Almost in all studies, the reference level height is assumed to be constant, however Wilson (1966) and Wilson (1987) showed that it may not be completely correct as the reference level height may change with the Shields parameter. Nevertheless, with assuming a constant height for the reference level, two different approaches are pursued in implementation of suspended sediment entrainment. A group of these approaches, e.g. Brørs (1999), Liang et al. (2005) and Jacobsen (2011) used the concept of turbulence diffusivity to calculate entrainment flux from:

$$E_\Delta = \nu_t \frac{\partial c}{\partial z} \tag{2-73}$$

On the other hand, a group of other researchers, worked with empirical equations to estimate the concentration at the reference level and applied it to calculate the entrainment flux. Different methods have been introduced for this purpose e.g. Rijn (1984), Zyserman and Fredsøe (1994), Garcia and Parker (1991), Smith and McLean (1977) and Engelund and Fredsøe (1976). The reference level height in each of these methods is defined in different ways related to the mean flow depth, bed-form height and sand roughness height. For example in Rijn (1984):

$$c_\Delta = 0.015 \frac{d_{50} \left(\frac{\theta - \theta_c}{\theta_c}\right)^{1.5}}{\Delta D_*^{0.3}} \quad (2\text{-}74)$$

where Δ is equal to $0.5H_b \; or \; k_s \; with \; \Delta_{min} = \; 0.01H$ where H_b is bed-form height.

Or in Zyserman and Fredsøe (1994) c_Δ is calculated by:

$$c_\Delta = \frac{0.331(\theta - \theta_c)^{1.75}}{1 + \frac{0.331}{0.46}(\theta - \theta_c)^{1.75}} \quad (2\text{-}75)$$

where $\Delta = 2d_{50}$.

2.3.8 Sediment continuity equation

Two factors of erosion and deposition of materials change the morphology of the bed level in case of non-equilibrium conditions. In numerical modelling using the classical approach, the sandy bed deformation or in fact, the changes in the morphology of the bed boundary of the computational domain are carried out by solving the sediment continuity equation over the bottom domain using the results of the sediment transport models. For this purpose, the Exner (1925) equation is applied:

$$\frac{\partial h}{\partial t} = \frac{-1}{1-n}[\nabla . \overrightarrow{q_B} - E_\Delta + D_\Delta] \quad (2\text{-}76)$$

where h is the local bed level height and n is the bed porosity taken as 0.4. Eq. (2-76) is in the form of a hyperbolic equation which takes into account the deformation of the bed boundary of the computational domain according to the sediment transport loads.

The sediment continuity equation (Exner's equation) has the wave-like nature. Therefore, numerical instability may occur during the solution as discussed in Jensen et al. (1999), Johnson and Zyserman (2002), and Callaghan et al. (2006). In order to limit this deviation due to numerical instability, filtration methods may be used to suppress spurious oscillations.

2.3.8.1 Sand sliding

Observation from the nature of the granular materials shows that when the slope of a heap of granular materials exceeds a critical angle relative to a horizontal plane, the gravity force overcomes the frictional forces for the materials. As a result, a bulk of materials from the upper layers shifts downwards. This critical angle and this phenomenon are known as the angle of repose φ_r and granular (sand) sliding process, respectively. In numerical modelling using the classical approach, to avoid unrealistic slopes on mobile sandy bed, a similar procedure of sand sliding has to be applied numerically in a way that the angle of repose is considered as a threshold of the sliding mechanism. The sliding mechanism includes an iterative procedure which takes place instantaneously in a pseudo time step. Figure (2-10) displays the results of a 2D numerical modelling of scour below a horizontal pipeline with and without sand sliding procedure, where x/D and z/D are the dimensionless horizontal and vertical axis, respectively, and D is the diameter of the pipe. The results show that in the case without sand sliding procedure during the development of the bed morphology, the bed slope angle may surpass the angle of repose to an invalid slope, as shown for the area in the red circle in Figure (2-10b).

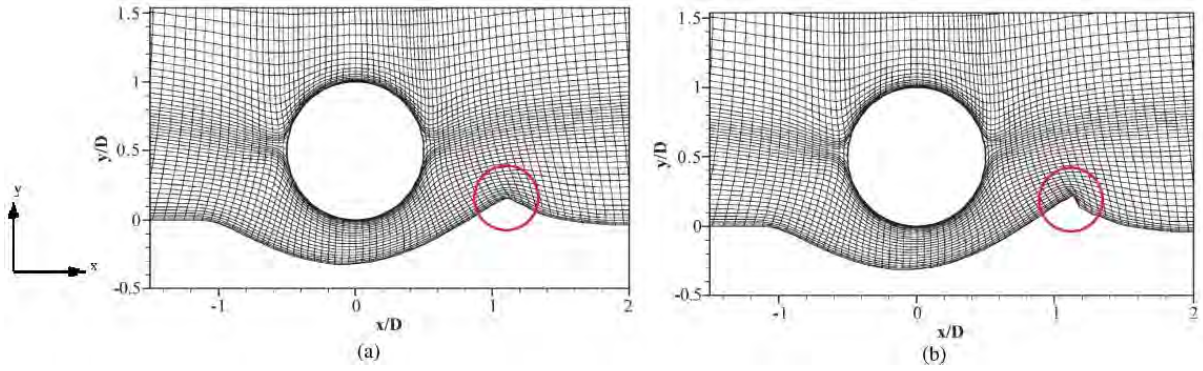


Figure (2-10) Numerical results of scouring around a 2D pipeline (a) without and (b) with sand sliding method from (Liang et al., 2005).

2.3.9 Live-bed and clear-water conditions

In the literature of scour, the flow conditions are divided into live-bed and clear-water conditions. The flow conditions are split up into these categories since the mechanism of scour under these conditions is quite different (Najafzadeh et al., 2014). In clear-water conditions, the mean velocity of the undisturbed approach flow, U_∞, is less than the mean critical flow velocity, U_c, for the initiation of motion for the bed materials ($U_\infty < U_c$), while in live-bed conditions $U_\infty > U_c$. It is to be noted that maximum equilibrium scour occurs in the case of $U_\infty = U_c$. Figure (2-11) displays the difference between scouring in clear-water and live-bed conditions using a threshold velocity for bed sediment entrainment U_c.

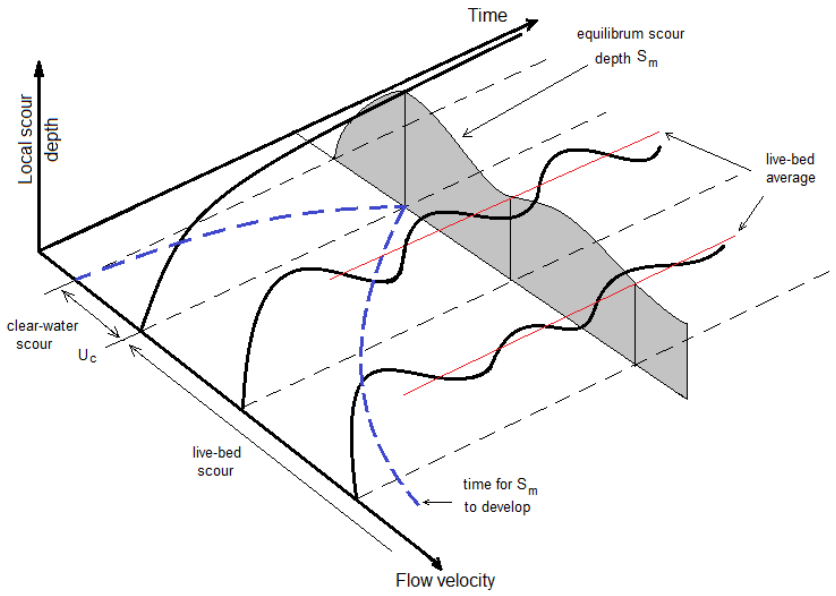


Figure (2-11) Variation of local scour depth with flow velocity and time (Melville and Chiew, 1999).

2.4 EXPERIMENTAL STUDIES

The pioneer experimental investigation of the turbulent structures and scour around piles/piers dates back to the 20th century when various studies were devoted to understanding the underlying mechanisms of local induced-scour around piles/piers. A summary of previous

experimental works can be found in many remarkable books and papers such as Kraus (1988), Whitehouse (1998), Melville and Coleman (2000), Sumer and Fredsoe (2002), and more recently Roulund et al. (2005), Sumer (2007), and Sumer et al. (2007). Here, a summary of notable experimental works on studying of flow behaviour and scouring in junction flow is provided. The experimental studies are divided into two groups. 1) studies on rigid beds to understand the flow structures around different pile/pier configurations, and 2) studies on scour development on sandy mobile beds.

2.4.1 Experimental studies of flow behaviour around piles/piers on rigid bed

A group of experimental studies was dedicated to the understanding of the characteristics of turbulent structures such as horseshoe and lee-wake vortices as described in section 2.2. In this section, the most well-known studies on the behaviour of flow around a mounted cylinder are noted and the details of the formation of turbulent vortices are explained.

Baker (1980) is one of the first studies that tried to understand the HSV structures and tried to correlate the variation of HSV and boundary layer separation position with flow parameters such as U_∞ and δ. He carried out a series of experiments for circular cylinders in a wind tunnel at Cambridge University. The tests were conducted for cylinders with different diameters between D=2.5 cm and D =10.1 cm and height of L=30.5 cm. The cylinders were placed on 0.5 m downstream of a leading edge of a false floor within the tunnel with a cross-section of 71 cm by 51 cm. The experiments were conducted for 4000< Re_D=$U_\infty D/\nu$ <9000, and 4< D/δ <30. Using an oil-flow visualization technique, Baker was able to confirm the formation of four vortices as shown in Figure (2-12). Also, as part of his work, he specified the variation in the position of the centre of the main HSV on the plane of symmetry upstream of the cylinder

(horseshoe system number 1 in Figure (2-12) with flow parameters $U_\infty \delta/\nu$ and D/δ, although Baker mentioned considerable errors involved in the measurements.

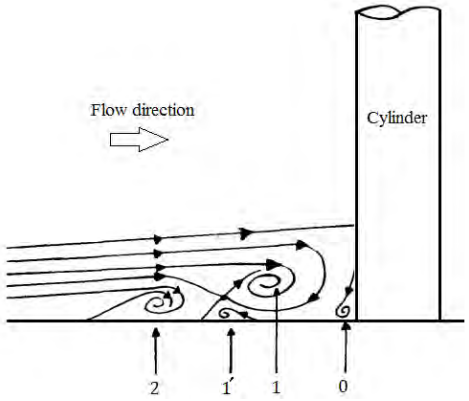


Figure (2-12) Flow pattern and formation of 4 horseshoe systems upstream of the mounted cylinder (Baker, 1980).

Dargahi (1989) studied the flow field around a circular cylinder mounted on a flat rigid bed experimentally for Re_D ranging from 8400 to 46000. His experiments were conducted in a 22 m long, and 1.5 m wide flume. A circular cylinder with a diameter of $D = 0.15$ cm was mounted at a distance of 18 m from the inlet. The bed of the flume was covered with the sand with D_{50}= 0.36 mm which was glued to the bed surface. The flow was visualized using a hydrogen bubble technique using a gold wire of diameter 0.05 mm. The turbulent characteristics of the flow were studied using a hot-film anemometry. Dargahi described the shed quasi-periodic characteristic of horseshoe vortices in the separated region upstream of the cylinder and noted that the number of vortices increases with increase in Reynolds number. It was also reported that the vortex system upstream of the cylinder is independent of the lee-wake vortices downstream of the cylinder. The work also demonstrated the sequence of formation of quasi-periodic HSVs as shown in Figure (2-13), however the author failed to provide a complete description for all horseshoe structures. The flow behaviour in the wake region downstream of the cylinder was three-dimensional due to the effect of the rigid bed. Dargahi (1989) implied that for the

investigated case studies, the behaviour of the wake vortices downstream of the cylinder in the region of $0.1 < y/H < 0.9$, where y was the distance from the bed and H was the mean depth of the flow, can be predicted with good agreement by the standard Strouhal number St:

$$St = \frac{f w_p}{U_\infty} \tag{2-77}$$

where f is the vortex shedding frequency and w_p is the pier/pile width. However, near the bed and in the region $x/D < 8$, where x was the distance downstream of the cylinder from its centre, observation showed that the turbulent character of the wake was amplified and the width of the wake decreased.

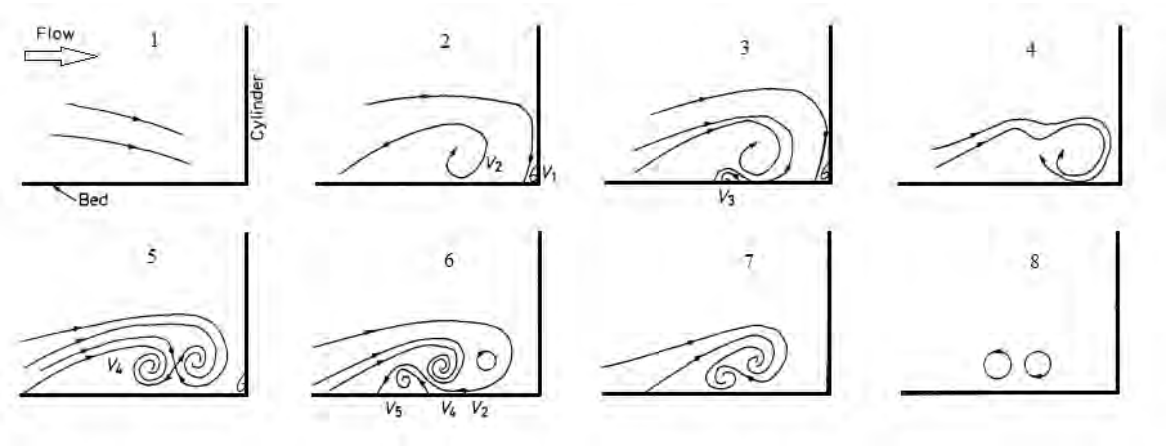


Figure (2-13) The sequence of formation of horseshoe vortices upstream of the cylinder in a plane of symmetry at Re_D=20000 (Dargahi, 1989).

Agui and Andreopoulos (1992) pointed out that most of the works before them on junction flow had been restricted to time-average measurements of pressure or flow fields. Their experiments were conducted in a large-scale wind tunnel with the cross-section of 1.42 m by 1.42 m for two different Reynolds numbers $Re_D = 1.0 \times 10^5$ and 2.2×10^5 for a circular cylinder with a diameter D= 30.5 cm and height of L=61 cm. Flow visualization was carried out using a laser sheet to illuminate the flow structures. Based on the obtained results, they concluded that

upstream of the cylinder a primary vortex is always present which is quasi-periodic unsteady. In contrast, a secondary vortex upstream of the primary one was occasionally observed. Their results indicated that the instantaneous flow structures upstream of the cylinder are significantly different from that of the time average. The $St = 0.135 \pm 0.016$ was found for the vortex shedding off the cylinder in their experiments which is different from the Strouhal number for a two-dimensional cylinder with the same Reynolds number (St = 0.2). The difference was assumed to be due to the low aspect ratio of the cylinder ($L/D = 2$) and the presence of the flat plate.

A few years later, in another study, Lin et al. (2008) studied the flow behaviour around the square-shaped cylinder with 90° orientation angle to the flow mounted on a flat plate as depicted in Figure (2-14). The experiments were run in a water channel with the test section dimensions of 0.5 m wide, 0.54 high, and 3.05 m long. Square cylinders with different sizes used for the test where the Re_D was in a range of 2.0×10^5 to 6.0×10^5. Particle Image Velocimetry (PIV) and particle trajectory photography were used for velocity measurements and flow visualization, respectively. As a result, they found the formation of four major horseshoe systems upstream of the square cylinder, while the number of vortices increases with increase in Re_D.

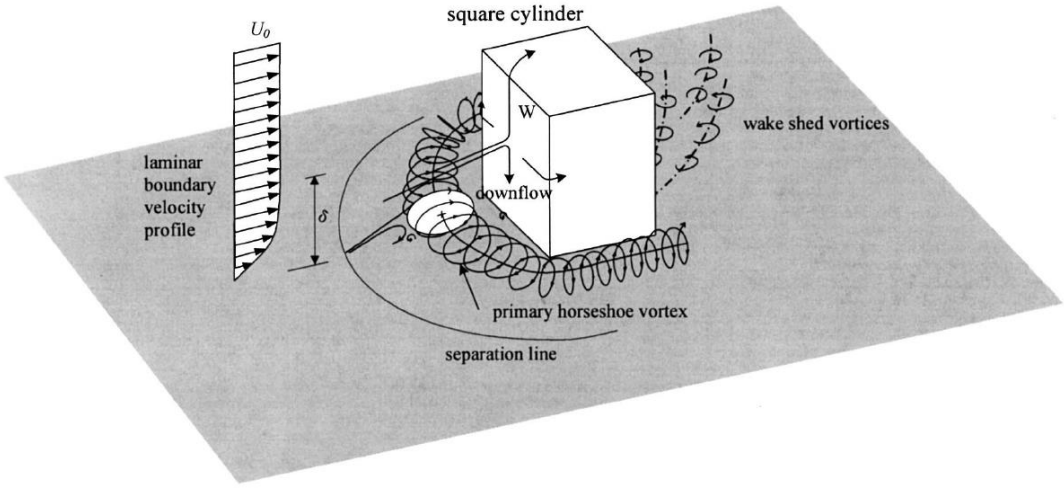


Figure (2-14) Schematic diagram of the vortex systems around a square-shaped cylinder with 90° orientation angle to the flow (Lin et al., 2008).

All of the above-mentioned studies investigated the flow behaviour around a cylinder over a flat rigid bed. Another group of experimental studies such as Shen et al. (1965), Dey et al. (1995), Kobayashi et al. (1997), Ahmed and Rajaratnam (1998), Graf and Istiarto (2002) and Jaman et al. (2017) followed a different approach where the flow field around the cylinder on an scoured bed was investigated. In one of the most detailed studies in this group, Dey et al. (1995) experimentally investigated a three-dimensional flow behaviour around a circular cylinder mounted in a quasi-equilibrium scour hole under a clear-water regime. In their study, the model was run for a period of 12 hours to attain the equilibrium condition. After carefully draining out the water, to stabilize the bed, a synthetic resin was sprayed over the bed. They measured the three-dimensional velocity vector using a five-hole pitot sphere. Individual equations for each component of flow velocity were developed which made the prediction of flow velocity adjacent to the pile possible.

2.4.2 Experimental studies of scour on sandy mobile bed

The studies of flow behaviour around cylinders mounted on a rigid bed was followed with a wide range of works focused on experimentally studying the evolution of scour around riverine and marine structures on a mobile bed.

Dargahi (1990) noted that most of the previous experimental works on scouring around circular cylinder had emphasized on the formulation of the scour-depth equation, rather than the mechanism of local scouring. Therefore, some efforts were made to understand the underlying mechanisms. Scour around a circular cylinder was examined in a 22 m long, 1.5 m wide and 0.65 m deep flume. A cylindrical pile of 0.15 m diameter was located vertically on the flume centreline, 18 m from the inlet on the bed flume. The water flow with a mean flow depth of 0.2 m and a mean flow velocity of 0.26 m/s was conducted for the test, which provided Re_D= 39000. The study defined three different stages of the scouring process: initiation, primary scouring and gradual reduction. The initial stage is the delay before the beginning of the scouring and formation of HSVs upstream of the pile which lasted about 20 seconds in the test and corresponds to the time of the expansion of the boundary layer over the bed. The formation of the scour profile around the cylinder starts at stage two and continues at stage three. It was mentioned that scour first takes place in the wake side of the cylinder in the results of wake vortices. In addition, the influence of the attached collars with different shapes to a cylinder as a method of local scour countermeasure was investigated. It was found that the collars can effectively reduce the strength of the horseshoe vortices when placed within the separated boundary layer.

In another experimental work, Melville and Chiew (1999) conducted a wide range of tests for clear-water local scour around circular bridge piers in four different flumes at the University of

Auckland and Nanyang Technological University. As a result of their work, equations for prediction of local scour depth at any stage of the scour hole evolution and the time taken for equilibrium scour was provided for a given pier diameter, sediment size, approach flow velocity (U_∞) and flow shallowness (H/D). It was also pointed out that in the first 10% of the time to equilibrium, the scour depth may reach between about 50% and 80% of the equilibrium depth depending on the flow intensity.

Roulund et al. (2005) experimentally studied scour development around a 10 cm diameter circular cylinder mounted in a bed covered with sand with a particle diameter of $d_{50} = 0.26$ mm. The experiment was conducted in a flume, 10 m long and 4 m wide where cylinder was fixed at 6.6 m downstream of the inlet section. The test was conducted on a mobile bed and under steady current flow. The water depth in the experiment was maintained at 0.4 m and the depth average velocity was 0.46 m/s. Scour depth measurements were carried out upstream and downstream of the cylinder during the scour development process where they found that the scour depth increased as the process continued. It was also figured out that the maximum scour depth at upstream of the cylinder was $S_{eq}/w_p \approx 1.2$ in equilibrium condition.

Ataie-Ashtiani and Beheshti (2006) experimentally investigated local scour around pile groups including two to eight circular piles with different arrangements and spacing ratios in clear-water steady current conditions. In total, 112 tests were carried out. It was found that scour around a pile group can be different from that of a single pile depending on pile spacing. In their study, for the case of two side-by-side piles, the maximum scour depth happened for the $G/D \approx 0.25$, where G represents the distance between the piles and D is the pile diameter. In this case, the maximum scour depth was 50% more than that for a single pile.

More recently, in a notable experimental work, Diab et al. (2010) conducted experimental tests on scouring around circular and square piers under clear-water conditions where the bed shear stress in undisturbed flow was 95% of the critical value for the initiation of the sediment motion. The test was performed in a flume 26 m long, 2 m wide, and 1 m depth. Circular and square piers with the same width of 0.2 m to the flow direction were considered for the tests. The flume bed was covered with grains with d_{50}= 3.25 mm and the hydraulic condition U_{∞}=0.62 m/s and water depth of H=0.3 m was applied. Their results illustrated that in equilibrium condition, the scour hole in the square pier case was 35% deeper than the circular pier.

Khosronejad et al. (2012) experimentally investigated local scour around a circular, square and diamond piers. The experimental test was conducted in a flume with 10 m long and 1.21 m wide. In all tests, the piers were mounted at 4 m downstream of the flume inlet. Tests were conducted for a circular pier with diameter 16.51 cm and a square-shaped piers with edge length of 16.51 cm but with two different orientation angles, 90°(square pier) and 45° (diamond pier), to the flow. Hence in the case of the square pier, the pier width to the flow direction was 16.51 cm and for the diamond pier, 23.35 cm. All tests were carried out under clear-water scour condition and the bed was covered with sand particles with mean diameter of $d_{50} = 0.85$ mm, while different flow condition was applied for the tests. They provided bed topography at equilibrium scored bed condition for each case which has been used in different numerical studies as a validation test case.

Vaghefi (2018) experimentally studied the scour pattern around three side-by-side and tandem arrangements of circular cylinders in a 180° bend under clear-water and steady current flow conditions. Circular cylinders with constant G/D =2 were placed at the positions of 60°, 90° and 120° of the bend. In their study, the maximum scouring depth occurred in the side-by-side arrangement at the position of 90° of the bend and around the pier closer to the outer bank.

Yao et al. (2018) carried out a set of experiments for submerged circular, diamond and square piers under steady currents and live-bed condition in a fully enclosed circulating water channel. A wide range of cylinder height to width ratios (0.1–8) was considered in the experiments. They mentioned that for height to width ratios larger than 4 the changes in equilibrium scour depth was almost negligible. From their results for height to width ratios larger than 4, the S_{eq}/w_pvalue for local scour around square and diamond piers was found to be around 2 and 1.5 respectively.

In another study, Omara et al. (2020) conducted scour experiments around a vertical and inclined circular, square and rectangular piers with different length to width ratios in clear-water condition. In their work, the bed shear stress in undisturbed flow was equal to the critical value for the initiation of the sediment motion. Their results for vertical circular and square piers revealed that the scour hole was deeper for square pier than circular in the range of 6% to 29%. Other studies such as Talib et al. (2016), Al-Shukur et al. (2016), Helmy et al. (2017) and Mir et al. (2019) can be mentioned on experimental investigation of scour around piers with different cross-section shapes, as well.

All previously mentioned scour studies were subjected to steady-current flow, while various studies (e.g. Das, 1970; Kawata and Tsuchiya (1989), Wang and Herbich (1983), Eadie and Herbich (1987), Sumer and Fredsøe (2001a), Sumer and Fredsøe (2001b), Ataie-Ashtiani et al. (2010), Chen and Li (2018), Chen and Li (2019), Yang et al. (2020)) have investigated scour around structures exposed to wave-induced flow or combination of steady-current and wave. Sumer et al. (1992) investigated the flow behaviour and scour around a vertical circular pile exposed to waves in a systematic manner. An extensive series of laboratory scour tests with piles subjected to real waves were conducted in three different flumes with three different ranges of sand grain sizes (d_{50} =0.18, 0.36, 0.58 mm) and with cylindrical piles with six

different diameters. They evaluated the normalized maximum scour depth by the pile diameter (S_m/D) under live-bed condition by the following expression:

$$\frac{S_m}{D} = 1.3[1 - \exp[-0.03(KC - 6)]] \qquad KC \geq 6 \tag{2-78}$$

where KC is Keulegan-Carpenter number which is related to the wave-period in a wave flow. For steady flow or wave-flow with very large wave-period, KC tends to infinity. Eq. (2-78) is only valid for live-bed conditions. For the value of the KC less than 6, both vortex shedding and the HSV are non-existent, which means the scour depth is practically zero.

Sumer et al. (1993) is an extended study of the Sumer et al. (1992) for the piles with different cross-sections. The study aimed to understand the influence of the cross-section shape of the cylinders on scour around them in the marine environment. For this purpose, they chose piles with square cross-sections with two different orientation angles to the flow, namely square (90° orientation angle to the flow) and diamond (45° orientation angle to the flow) piles and investigated the equilibrium scour depth S_m and time scale of the scour process T. So, a series of experiments were conducted in three different flumes for piles with different size and shapes in live-bed conditions. Similar to the case of the equation for circular cylinder (Eq. (2-78)), they represented the results of their study with the following expressions for square piles:

$$\frac{S_m}{D} = 2[1 - \exp[-0.015(KC - 11)]] \qquad KC \geq 11 \tag{2-79}$$

and for diamond piles:

$$\frac{S_m}{D} = 2[1 - \exp[-0.019(KC - 3)]] \qquad KC \geq 3. \tag{2-80}$$

They noted that the time scale of scouring can be a function of KC and θ. They also compared the strength of the shed vortices downstream of the piles with different cross-sections to find the possible effect of it on the time scale of the scouring by the following equation:

$$\frac{\Gamma}{DU_\infty} = \frac{1}{4}\left(\frac{U_0}{U_\infty}\right)^2 \frac{1}{St} \tag{2-81}$$

where Γ is the strength of the shed vortices exposed to steady current flow and U_0 is the potential flow velocity at the top of the pile boundary layer at the point of separation (which is different case by case). As a result, they found stronger shed vortices in the case of a square pile compare to that of cylindrical and diamond piles and connected this finding to the faster scouring process around square piles tests in their works.

In one of the most recent and detailed experimental studies of scouring subjected to waves and current Sumer et al. (2012) investigated the backfilling of scour holes around the piles. The idea behind backfilling is that in correct conditions, a previously generated scour hole around a pile may be backfilled. The result of their work illustrated that the corresponding scour depth in equilibrium condition after backfilling is independent of the initial condition, and it is equal to scour depth in equilibrium condition for the same flow condition (waves, current or combined waves and current) as backfilling. They also found that the time scale of backfilling is a function of initial and backfilling flow characteristics.

In another study, Qi et al. (2019) conducted a series of experimental tests of local scour around twin piles under combined current and wave flow. The tests were conducted in a flume 52 m long, 1 m wide and 1.5 m high which was able to produce currents and wave simultaneously. The sandy bed in the flume was covered with sand d_{50}= 0.15 mm. Two pairs of piles with diameters D=12 cm and 8 cm at four different flow skew angles (α_s=0°,30°,60°, 90°) and different values of $0 \leq G/D \leq 3$, where G represents the distance between the piles, were considered as shown in Figure (2-15). It was found that with increase in G/D the pile group effect mitigates and gradually vanishes for $G/D \geq 3$. The maximum pile group effect on the scour depth occurs for side-by-side arrangements with G/D=0. An empirical equation was

established to estimate the maximum scour depth around twin piles based on G/D and α_s with maximum error lines in a range of 25%.

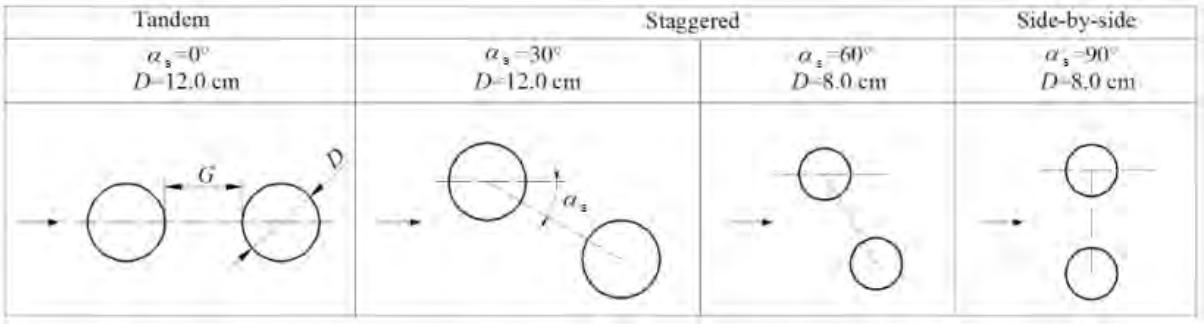


Figure (2-15) The layout of the piles in Qi et al. (2019).

2.5 NUMERICAL STUDIES

2.5.1 Numerical studies of flow behaviour around piles/piers on rigid bed

Similar to the experimental investigations discussed in section 2.4.1, a large number of numerical works such as Richardson and Panchang (1998), Tseng et al. (2000), Salaheldin et al. (2004), Kirkil et al. (2005), Kirkil et al. (2008), Kirkil et al. (2009), Chang et al. (2013) and Tao and Li (2015) have studied the flow behaviour around piles/piers on rigid beds. In this group, different hydrodynamic models were employed to better understand the formation of horseshoe and wake vortex structures and the bed shear stress distribution on both rigid flat and scoured beds around structures.

Salaheldin et al. (2004) numerically studied the flow behaviour and bed shear stress adjacent to a vertical circular cylinder mounted on a rigid flat bed using FLUENT. To solve the flow field, unsteady-RANS equations in combination with three different variants of the k-ε model (the standard, the renormalization group (RNG), and the realizable k-ε model) and the Reynolds stress model (RSM) was applied. The experimental data from Melville (1975), Dargahi (1987), and Ahmed and Rajaratnam (1998) was used for the comparison. It was found that the RSM

turbulence model gives the most satisfactory results, however its performance needs to be examined in scoured bed as well.

In one of the most recent works, Alemi et al. (2019) numerically simulated the flow behaviour around a complex structure on a scoured bed as shown in Figure (2-16). The deformed bed around the obstacle was obtained from the experiment which was conducted for the same condition by Beheshti and Ataie-Ashtiani (2016), where they mentioned the limitation of the performance of their measuring instruments below the pile cap. Hence, a custom LES model was employed to predict the flow field around the pile on the scoured bed. The continuous wall function (Cebeci and Chang, 1978) was incorporated to solve the boundary layer flow close to the walls. Initially, two test cases were applied to validate the model. 1) flow in a channel with periodic hill constriction, 2) flow around a single circular cylinder in a scoured bed. They pointed out that their model was capable of determining the most relevant flow features around the pile.

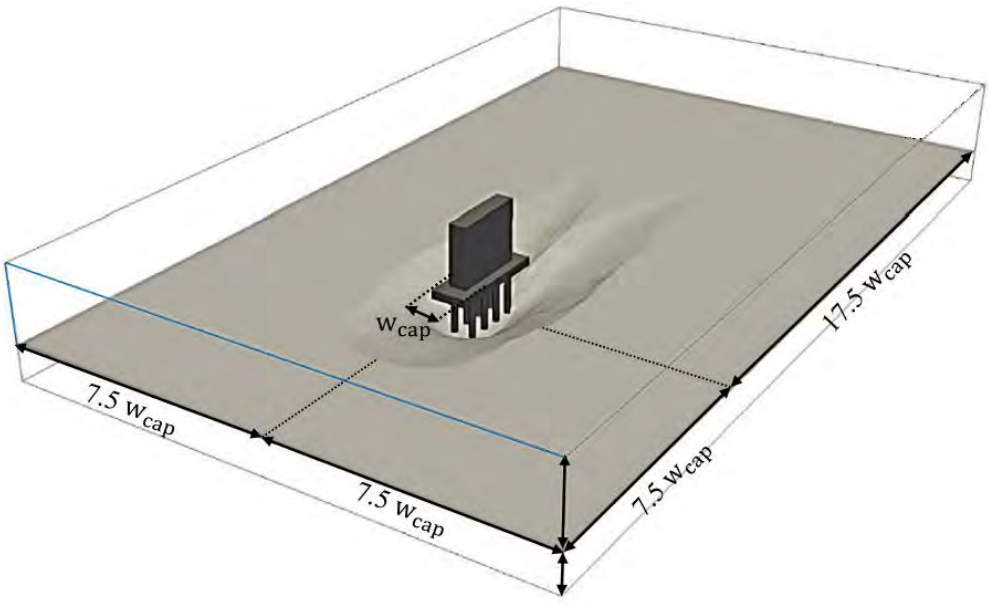


Figure (2-16) Computational domain and the complex bridge pier structure in Alemi et al. (2019).

2.5.2 Numerical studies of scour on sandy mobile bed

A pioneering example of the use of the classical approach for modelling of scour around piles/piers dates back at the 1990s when Olsen and Melaaen (1993) and Olsen and Kjellesvig (1998) developed a first 3D model for predicting local scour around a circular cylinder on a mobile bed under clear-water condition for non-cohesive sediment. The hydrodynamic part of their model solved the Reynolds Averaged Navier-Stokes (RANS) equation in combination with k-ε turbulence model. The sediment transport included the suspended load part which could not satisfy the continuity for cells close to the bed. Besides, their model lacked the transient term, and thus, was unable to predict the maximum scour depth correctly.

In a notable work, Roulund et al. (2005) investigated the flow and scour around a vertical pile numerically in live-bed condition. The bed was covered with non-cohesive sand. The simulation of the flow field was carried out with steady RANS model in combination with k-ω turbulence model. Therefore, it was incapable of predicting the formation of lee wake vortices behind the pile. The top boundary of the computational domain was modelled with slip boundary condition to support the air-water interface. The boundary layer flow was resolved using the Cebeci and Chang (1978) wall function. The velocity and turbulent properties were specified at the inlet for an undisturbed flow condition. The sediment transport only included a bedload model which was a 2D extension of the model of Fredsoe and Deigaard (1992). The model was validated against their experimental scour test. A good agreement between the numerical and experimental results was found. Most of the later works on classical modelling of scour have been inspired by Roulund's work.

Göthel and Zielke (2007) presented a model for predicting scour around a cylinder pile exposed to steady and wave currents. Their model only included bedload transport following Rijn (1993)

and sand sliding following Weilbeer (2001). Validation of their model was carried out by comparing the results of their numerical model with experimental data from Roulund et al. (2005), Sumer et al. (1992), and Sumer and Fredsøe (2001b). They also numerically modelled the hypothetical scour protection by increasing the bed roughness for the area which had been assumed to be covered by stones as a scour protector. Their work led to a better understanding of the possible increase in bed shear stress due to the presence of scour protectors and the identification of affected areas.

Liu and García (2008) introduced a model for local sediment scour around piles under wave impact which included both bedload and suspended load transport components. Their flow model employed the standard k-ε turbulence closure model. They used Engelund and Fredsøe (1976) to calculate the bedload transport. The sediment concentration at the reference level was employed by Rijn (1984) where the reference level was assumed to be located at 5% of water depth from the bed. They validated their model against experimental data from Chatterjee et al. (1994) and Sumer and Fredsøe (2001b).

Escauriaza and Sotiropoulos (2011) investigated the initial stages of erosion and the development of scour by HSV system in the vicinity of a mounted cylindrical pier. They applied detached-eddy simulation (DES) approach in combination with one-equation eddy viscosity model of Spalart and Allmaras to solve the hydrodynamic model to be able to accurately resolve most of the turbulent stresses produced by the HSVs. The employed bedload transport model in their work was inspired by works of Kovacs and Parker (1994) and Parker et al. (2003). They reported that their model was able to reproduce most of the characteristics observed by Dargahi (1990) during the initial scour around the cylindrical pile.

Khosronejad et al. (2012) numerical investigated formation of local scour around circular, square, and diamond bridge piers in clear-water conditions. They developed their model based on the fluid-structure interaction curvilinear immersed boundary (FSI-CURVIB) method by Khosronejad et al. (2011) to handle the moveable bed of the channel with embedded hydraulic structures. For the hydrodynamic part of the model, they applied unsteady-RANS model closed with k-ω turbulence model. The Cebeci and Bradshaw (1977) wall function reconstructed the boundary layer velocity near the wall in their work. The morphodynamic part of the model contained a bedload model as it was described in Khosronejad et al. (2011). They reported that the accuracy of their model depended on piers cross-section geometry which was addressed with a bluntness factor (BF). The bluntness factor is a character of describing the mounted structure nose geometry which is in connection with the strength of the mean HSV and severity of the bimodal HSV fluctuations (Fleming et al., 1991; Fleming et al., 1993). The BF for the case of wing/body junction can be defined as follows:

$$BF = \frac{1}{2}\frac{R}{X}\left(\frac{D_w}{S_D} + \frac{S_D}{X}\right) \tag{2-82}$$

where R is the radius of the leading-edge, X is the length of the chordwise position of the nose from the maximum width of the wing D_w, and S_D is the distance from the leading edge along the structure surface to the maximum width of the wing as shown in Figure (2-17). Based on the definition in Eq. (2-82), the bluntness factor for square and diamond shape piers is $BF \to \infty$ and 0, respectively. Therefore, in the case of square pier formation of strong HSV which wrapped around the pier with a remarkable impact on scouring, and in the case of the diamond pier a weak HSV with a very low contribution on scouring can be inferred (Khosronejad et al., 2012). Khosronejad et al. (2012) also mentioned that for the case of the diamond pier the local acceleration of the flow around the pier side edges is the main reason of increase in bed shear

stress and consequently scouring in the vicinity of the pier. Their model was not able to accurately capture the dynamics of the HSV system and predict the scouring around the square and circular pier.

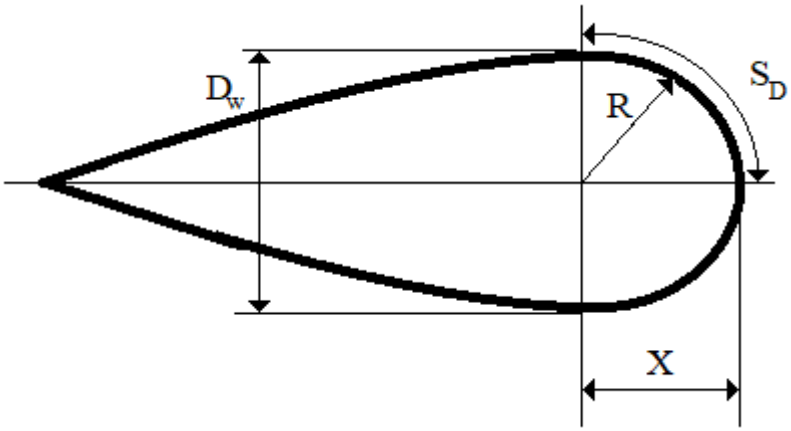


Figure (2-17) Schematic of a wing and corresponding variables in calculation of bluntness factor.

Kim et al. (2014) numerically investigated the progression of scour patterns around two adjacent circular cylinders in side-by-side and tandem arrangements with diverse spacing ratios between 0.25 to 4 in clear-water condition. For the first time in the literature, Large Eddy Simulation (LES) approach was employed to solve the Navier-Stokes equation which was followed by a Lagrangian approach similar to the work of De Ruiter (1983) for sediment transport. They validated their model by experimental data from Khosronejad et al. (2012). From their results, they found out that in the case of two side-by-side cylinders when $G/D \geq 1.5$, the local scour patterns are similar to those of a single cylinder. On the other hand, for tandem cylinder arrangement, they realized that local scouring at the nose of the upstream cylinder is similar to that of a single cylinder. Furthermore, the presence of the upstream cylinder considerably weakened the local scouring at the rare cylinder for $G/D \leq 2.75$.

Stahlmann and Schlurmann (2012) and Stahlmann (2013c) highlighted the lack of knowledge and understanding of scour progression around complex offshore foundation structures and introduced a model which was highly inspired by the work of Roulund et al. (2005). The model solves the combined waves and tidal current flow fields using the unsteady-RANS equations in combination with k-ω SST turbulence model. They used Cebeci and Chang (1978) as a near-wall treatment method. The sediment transport model considered both bedload and suspended load, however they did not pay enough attention to solve the suspended load model over the reference level height from the bed. The model was applied to simulate scour around a tripod foundation as presented in Figure (2-18). The results were compared with experimental measurements from small- and large-scale model tests.

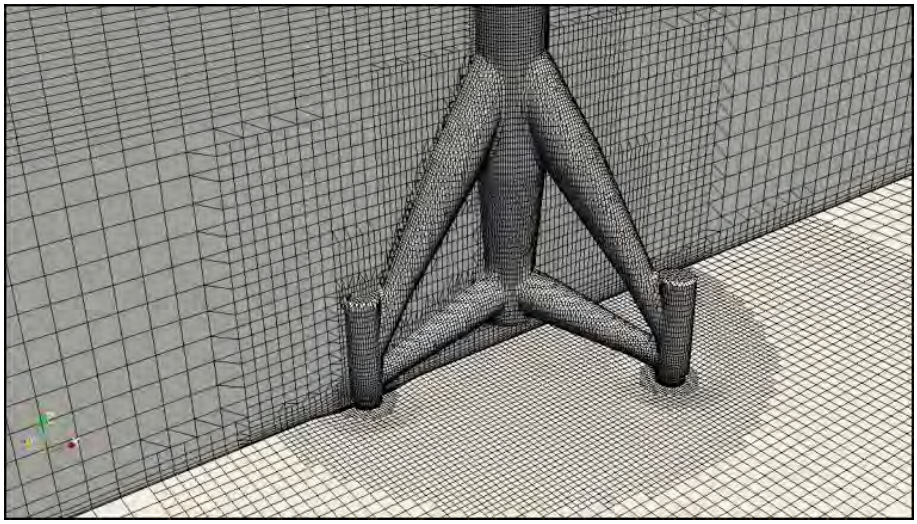


Figure (2-18) The tripod structures and generated computational grid for flow and scour simulations from Stahlmann (2013a)

The works of Sumer et al. (2014), Baykal et al. (2015) and Baykal et al. (2017) used a similar hydro-morphodynamic model for different applications. The flow field was modelled with unsteady-RANS equations and turbulent terms were modelled by k-ω turbulence model. The sediment transport contained both bedload and suspended load models. The model benefited

from a truncated computational domain to solve an advection-diffusion equation for the suspended load model. In this modification, the computational cells below the reference level were omitted from the original computational mesh. Therefore, the advection-diffusion was solved only for grids over the reference level. Baykal et al. (2015) applied the model to investigate the effects of lee-wake vortices, as well as suspended sediment transport with defining three different scenarios of scour around a vertical pile on steady currents. On the other hand, Sumer et al. (2014) and Baykal et al. (2017) used the model to investigate the backfilling of a scour hole around circular piles. They validated their results against the experimental outputs from Sumer et al. (2012). This approach was computationally expensive, as Baykal et al. (2017) reported that for a backfilling case, 8 months of computational time was needed to simulate 1 hour of real-time condition.

Hamidi and Siadatmousavi (2017) used SSIIM model to predict the flow behaviour and scour around different arrangement of two piers. In their work the turbulent terms in the flow governing equations were modelled by k-ε and k-ω turbulence models and sediment transport included both bedload and suspended load transport components. Their model used a wall function which is valid for log-law region to resolve the near-wall velocity profile. The experimental data from Ataie-Ashtiani and Aslani-Kordkandi (2012) for scour patterns adjacent to two side-by-side circular cylinders were used for validation of the model. Their results revealed that the model underestimated the sediment deposition at downstream of the piles.

Zhang et al. (2017) ran a set of numerical simulations to study local scour around a different arrangement of a group of up to three adjacent piles under steady current flow in clear-water conditions. Flow-3D was applied to investigate the local scour. The software used the volume of fluid (VOF) method to capture the water-air interface. RANS equations in combination with the RNG k-ε turbulence closure was applied to solve the hydrodynamic equations. Sediment

transport was modelled by both bedload and suspended load models. The model was validated against experimental data from Khosronejad et al. (2012) for the scour around a single circular pile. The simulations were conducted for circular piles with D=1.5 m and G/D= 2, 3 and 4. It was observed that with increase in the spacing ratio the pile group effect decreases, as for G/D= 4, there was almost no interaction between the piles effects.

In a more recent study, Omara et al. (2019) used FLOW-3D v. 11.2 to numerically estimate the flow behaviour and scour depth around vertical and inclined bridge piers with square and circular cross-section shapes. They applied RNG k-ε turbulence model in their model to solve turbulent stresses in unsteady-RANS equations and sediment transport was performed with both bedload and suspended load models. In their work, the model was validated against the experimental data from Ghiassi and Abbasnia (2013), Bozkus and Yildiz (2004) and Vaghefi et al. (2016) for scour depth around a vertical square pier, a inclined circular pier in the downstream direction and an inclined circular pier perpendicular to the flow, respectively. They pointed out that the prediction capability of the model was attached to the pier shape and inclined direction.

Other recent numerical studies of scour around piles/piers with using the classical model, the works of Zhang et al. (2015), Ahmad et al. (2020) and Pan et al. (2020) can be mentioned. In addition to the case of a junction flow and scour around piles/piers, the classical approach has also been used widely in 2D modelling of prediction of the evolution of scour underneath of the submarine horizontal pipelines e.g. Brørs (1999), Li and Cheng (1999), Li and Cheng (2001), Liang and Cheng (2005), Liang et al. (2005), Smith and Foster (2005), Fuhrman et al. (2014) and Lu et al. (2015), Li et al. (2020).

Apart from the classical approach, which solves the dynamic equations for only the fluid-phase, some researchers have employed two-phase flow models to predict scour development. In these approaches, sediment phase has been considered as a continuous phase (Eulerian approach) or discrete elements (Lagrangian approach).

Works of Lee et al. (2016), Cheng et al. (2017), Bakhtyar et al. (2009), Revil-Baudard and Chauchat (2013), Nagel et al. (2020) have followed the Eulerian approach. Nagel et al. (2020) for the first time used the Euler-Euler model in 3D simulation of scour around the cylinder. They validated their model against Roulund's experimental and numerical data for fluid flow and scour around the circular pile. The number of works that have followed the Lagrangian approach in scouring is very limited. In this group, the works of Chang and Scotti (2003), Bakhtyar et al. (2009) and Li et al. (2014) can be noted. In present study, the classical approach was chosen due to its mathematical simplicity and computational efficiency.

2.6 SUMMARY

In this chapter, the governing equations on fluid flow field and sediment transports modelling of classical approach is described and a review of previous experimental and numerical works on understanding the flow behaviour and scour around piles/piers is provided. Based on the conducted literature review:

- Attempts on numerical modelling of local scour around cylinders with different cross-section shapes has been carried out in works of Khosronejad et al. (2012) and Omara et al. (2019). It was found that the prediction capability of their models was dependent upon the pier shapes and its orientation angle to the flow and they were unsuccessful in prediction of local scour around piers with different cross-section shapes. This gap in

knowledge can be filled by developing a numerical model which can provide independent results for different piers configuration.

- Most of the studies in numerical modelling of scour has been conducted in clear-water condition (Khosronejad et al., 2012; Kim et al., 2014; Zhang et al., 2017; Omara et al., 2019), while very limited studies have been accomplished in live-bed conditions. This gap in knowledge provided an apportunity to numerically study the scour mechanism around piers with different cross-section shapes and also a group of two side-by-side piles under live-bed condition.

3 METHODOLOGY

3.1 INTRODUCTION

A novel numerical model is proposed, and a code is implemented in the OpenFOAM® framework. This is necessary for two main reasons. First, none of the previously developed numerical models in prediction of local scour are freely available. Second, the previously developed models were unsuccessful in prediction of local scour around piers with different cross-section shapes (Khosronejad et al., 2012; Omara et al., 2019).

The proposed model follows the classical approach in numerical investigation of local scour. The model solves the fluid flow field using the unsteady-RANS equations in combination with the *k-ω SST* turbulence closure, while the morphodynamic part of the model comprise of both bedload and suspended load models.

This chapter provides the details of the assumptions and considerations in the development of the proposed numerical model setup. The details of the employed hydrodynamic model and boundary conditions are provided in section 3.2. The calculation of bed shear stress in the present setup is presented in section 3.3. The implemented morphodynamic model which includes the sediment transport models and solving the mass-balance equation over the bed boundary of the computational domain is defined in section 3.4. Finally, OpenFOAM® CFD toolbox and its file structures are described in section 3.5.

3.2 HYDRODYNAMIC MODEL JUSTIFICATION

In many studies, as a few of them mentioned in section 2.5.2, the classical approach has been successfully applied in the investigation of scouring around vertical circular cylinders. Nevertheless, a review of previous numerical works on local scour around piers with different cross-section shapes revealed that the accuracy of these hydro-morphodynamic models in determining local scour varies with the piers cross-section shapes (e.g. works of Khosronejad et al. (2012) and Omara et al. (2019)). This limitation challenges the capability of the hydrodynamic part of these models in predicting flow behaviour and consequently the calculation of bed shear stress adjacent to the piers which is the primary input parameter to the sediment transport part of the models (Khosronejad et al., 2012).

The present work aims to bridge this gap in knowledge via providing a more robust tool. Hence, the unsteady-RANS model in combination with the *k-ω SST* turbulence closure model is employed to solve the flow field. The *k-ω SST* turbulence closure model has a proven capability in predicting adverse pressure gradients and separation flow (Menter, 1992a). On the other hand, as the physical modelling of local scour is a time-consuming process, the low computational cost and high accuracy of this combination in simulating the main turbulence structures around piles/piers are desirable. In the present work, the unsteady-RANS model in combination with the *k-ω SST* turbulence closure model, as provided in OpenFOAM® framework and described in section 2.2 is employed.

3.2.1 Hydrodynamic model boundary conditions

The computational domain in numerical modelling is limited and focused on the region where the physics of the problem is being studied (in the present work, scour around the piles). The boundaries of the finite computational domain need to be properly satisfied to represent the

equivalent physical behaviour from outside of the domain on the domain's boundaries. This is done by defining the boundary conditions on the boundaries of the computational domain. Boundary conditions model a wide range of behaviours from a fluid-structure interaction at walls to a continuous fluid body outside of the domain. In numerical modelling, boundary conditions are necessary constrains and the solution quantities need to be defined at the boundaries.

As shown in Figure (3-1), in the setup for numerical modelling of scouring around a pile/pier, the required boundaries are defined as inlet, outlet, rough sandy bed, smooth wall (pile/pier body), sides and top. To solve the hydrodynamic model over the computational domain, the flow and turbulence properties need to be quantified on all boundaries.

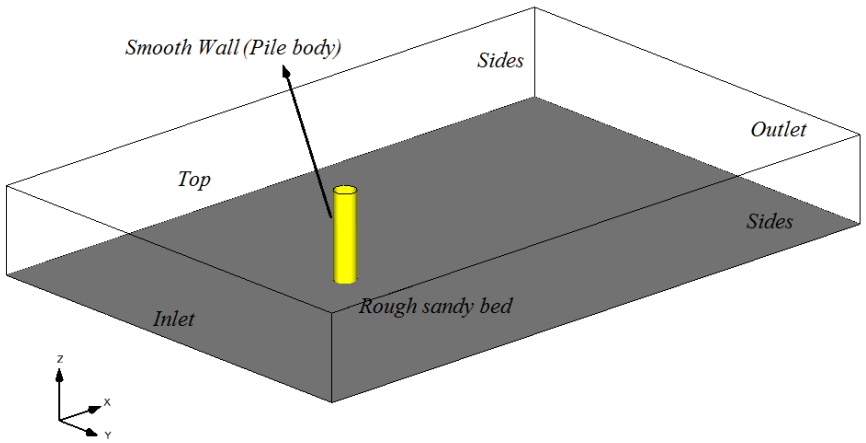


Figure (3-1) Computational domain and boundaries.

3.2.1.1 Top

In the case of a mounted pile/pier on a sandy bed, the structure is exposed to the flow of two phases of water and air. However, in the present work, for the purpose of simplicity and decreasing the computational burden, a single-phase (water-phase) model is chosen to solve the fluid flow. Therefore, the model does not have a free-surface facility and the model only solves

the water phase. The top boundary of the computational domain is limited to the water-air interface. In this case, the water-air surface is modelled with a plain surface with a slip boundary condition. The slip boundary condition behaves differently for different types of variables. For scalar quantities (e.g. pressure), it simply uses the Neumann condition (wall-normal zero gradient) at the boundary. However, in the case of vectorial variables (e.g. velocity), the tangential component to the boundary surface of the quantities is treated with Neumann condition (wall-normal zero gradient), while the normal component is handled with a Dirichlet boundary condition (zero value).

Using a single-phase model decreases the computational time by reducing the complexity of solving the governing equations of a two-phase flow model which includes interface-capturing technique such as volume of fluid (VOF) method (Ubbink and Issa, 1999). In the VOF method, the volume fraction of each of the two phases in each computational cell is represented by a scalar value defined in the range of 0 to 1. So, in comparison to the single-phase model, an extra term should be added to the governing flow equations. Moreover, the single-phase model decreases the computational time by truncation of the computational domain into only the water-phase, which leads to the decline in the number of computational cells. Conversely, considering a single-phase model to solve the fluid flow decreases the capability of the model in handling the sharp or substantial changes of the free-surface due to the presence of the pile/pier in the flow field (Figure (3-2)). Few studies have linked this aspect of the flow adjacent to the structures with the Froude number which indicates the ratio of inertial and gravitational forces. Roulund et al. (2005) mentioned the larger the value of the Froude number, the more significant is the variation in the free-surface elevation which is specified by ΔH in Figure (3-2). Froude number is defined by $Fr = U_\infty/\sqrt{gH}$. Roulund et al. (2005) illustrated that the single-

phase model assumption is a valid and acceptable assumption for the flow with $Fr < 0.2$, and in most practical cases the Froude number is undoubtedly smaller than 0.2.

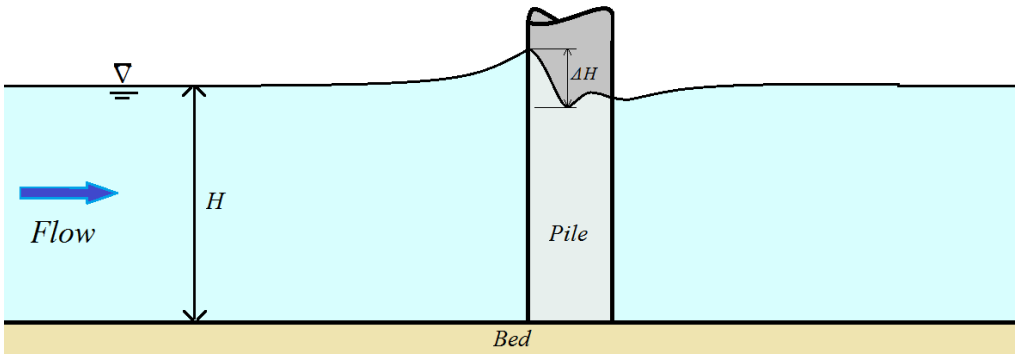


Figure (3-2) Schematic of the change on free-surface due to presence of the pile in high Froude number.

3.2.1.2 Inlet and outlet

The empirical investigation of the flow behaviour and scour around a mounted pile is usually conducted in long flumes to provide a fully developed approaching flow near the pile. In numerical modelling, on the other hand, it is not beneficial to model the entire flume due to its computational expenses, instead, the computational domain is mostly limited to the area of main interest around the pile. Hence, the approaching flow conditions are considered in the inlet condition. This can be followed by different methods. In one way, the approaching flow condition at the inlet can be achieved by employing the experimental measurement data of the approaching flow in case they are available as constant quantities (Dirichlet condition). Alternatively, if the data is not available, to provide the fully developed quantities at the inlet, a preliminary hydrodynamic simulation is conducted for the domain. In this case, a preliminary mesh with the same width and depth as the main mesh but without the presence of the pile is generated. The cyclic boundary condition is given at Inlet/Outlet of the preliminary mesh. The same flow rate as the preliminary mesh is supplied. As a result, the fully developed flow quantities for velocity and turbulent properties are achieved for the inlet condition of the main

mesh as a Dirichlet condition (constant values) while the pressure is satisfied with Neumann condition giving $\partial P/\partial \vec{N}$=0 (zero gradient condition).

In contrast, with sufficient distance downstream of the pile, the outlet boundary is set with zero normal gradients of all quantities except for pressure, which is equal to zero at the outlet boundary.

3.2.1.3 Rough sandy bed

For this boundary, hydrodynamic quantities including velocity, pressure and turbulence properties need to be specified. The velocity is determined with a no-slip condition ($\vec{u} = 0$), and pressure is set as zero gradient condition. The turbulent quantities (k, ω, ν_t) are obtained by applying a near-wall treatment method following Cebeci and Bradshaw (1977), as described in sections 2.2.5.1. This near-wall treatment model is only acceptable for the log-layer region. Therefore, in numerical modelling, it is valid when the centre of the first layer of the cells next to the wall is placed in the logarithmic region of the boundary layer. Using Cebeci and Bradshaw's (1977) wall-function, the dimensionless velocity and distance from the bed (wall) and the friction velocity is obtained. To calculate the turbulent flow properties in the *k-ω SST* model, the value of turbulent properties (kinematic energy, k, and turbulence frequency, ω) needs to be determined near the sandy bed. Investigations of Nezu (1977), Sumer et al. (2001), Sumer et al. (2003) and Fuhrman et al. (2010) proved that the turbulence kinematic energy, k, near the wall can be satisfied by Neumann condition ($\partial k/\partial \vec{N} = 0$) for both smooth and rough walls. In the present setup, the same approach is followed for treating turbulence kinematic energy near the wall. The other turbulent flow properties, turbulence frequency, ω, for the first layer of cells next to the wall is calculated following Ferziger and Peric (2008) which is valid for the logarithmic region of the boundary layer:

$$\omega = \frac{\sqrt{k}}{C_{\mu}^{0.25}\kappa y} \tag{3-1}$$

where C_{μ} has a value of 0.09. The kinematic turbulent viscosity, ν_t, is obtained by using the definition of dimensionless velocity near the wall and Eq. (2-18):

$$\tau_w = \rho u_f \frac{u}{u^+} = \frac{\rho u_f (u_{center} - u_{wall})}{\frac{1}{\kappa} ln(Ey^+/e^{\kappa \Delta B})} \tag{3-2}$$

where u_{center} is the velocity on the centre of the first layer of cells closest to the bed, and u_{wall} is velocity on the wall. Considering the definition of $\tau = \rho \nu \, \partial u/\partial y$, a new effective viscosity can be written as:

$$\nu_{new} = \frac{u_f y_c}{\frac{1}{\kappa} ln(Ey^+/e^{\kappa \Delta B})} = \frac{y^+ \nu}{\frac{1}{\kappa} ln(Ey^+/e^{\kappa \Delta B})} = \nu_t + \nu \tag{3-3}$$

where y_c is the orthogonal distance of the centre of the first layer of cells from the wall. Therefore, ν_t is defined by:

$$\nu_t = \nu \left(\frac{y^+ \kappa}{\ln (Ey^+/e^{\kappa \Delta B})} - 1 \right). \tag{3-4}$$

3.2.1.4 pile/pier bodies

The body of the pile/pier can be smooth or rough surface. For this surface, the same near-wall treatment, Cebeci and Bradshaw (1977), as applied for the sandy bed is chosen. This near-wall treatment can be adapted for both smooth and rough surfaces. Turbulent properties are also calculated following the same method as used for the sandy bed. The velocity and pressure quantities are also satisfied with no-slip and zero gradient condition, respectively.

3.2.1.5 Sides

In empirical tests, the sides of the flumes are limited with walls. In numerical modelling, wall condition can also be provided, however, in a reasonable condition a simplification can be considered. Where the effect of the side walls on the flow field around the pile is negligible, the symmetry boundary condition can be replaced with the wall condition. This effect can be evaluated simply by calculating the ratio of the pile width, w_p, to flume width, w_F (Roulund et al., 2005). The advantage of this simplification is that there is no need to use fine mesh grids adjacent to sides to satisfy the wall modelling provisions which can significantly decrease the number of computational grids.

3.3 BED SHEAR STRESS

The hydrodynamic and sediment transport models are connected through the bed shear stress since the calculated bed shear stress from the hydrodynamic model serves as the primary input parameter for sediment transport model. Hence, accurate calculation of bed shear stress is essential to obtain realistic sediment transport results. In the present setup, the bed shear stress in the vectorial form acting on the wall is calculated from the inner product of the stress tensor T and the unit normal vector of the face of the wall ($\vec{N}$):

$$\tau_w = T.\vec{N} \tag{3-5}$$

$$T = (\nu_t + \nu)(\nabla\vec{u} + \nabla\vec{u}^T) \tag{3-6}$$

3.4 MORPHODYNAMIC MODEL SETUP

In the classical approach, the morphodynamic part includes modelling sediment transport and solving a mass-balance equation over the bed. In the present setup, the sediment transport

includes bedload and suspended load components. For this purpose, the models presented in sections 2.3.5 and 2.3.7 are taken into account for modelling bedload and suspended load, respectively. The bedload model is solved on a 2D mesh, in accordance with the bed boundary of the computational domain. On the other hand, the suspended load model is solved on a 3D computational mesh over the reference concentration level. In the literature, different studies have employed different methods to solve the suspended load model (advection-diffusion model) over the reference level. More recently, Fuhrman et al. (2014), Sumer et al. (2014) and Baykal et al. (2017) dealt with this problem using a truncated version of the main computational mesh to solve the suspended load model. In their works, the computational grids below the reference level were removed and the suspended load model was solved on the truncated mesh.

In the present work, a different approach is followed to overcome this challenge. In the proposed numerical scheme, the centre of the first layer of cells closest to the bed of the computational mesh is adjusted in accordance with the reference level height from the bed. Rijn (1984) description is applied to calculate the reference concentration of suspended load, c_{Δ}, with the reference level height in the range of $3d_{50}$ to $4d_{50}$ based on works of Liang and Cheng (2005), Garcia and Parker (1991), Fang and Rodi (2000) and Davies et al. (1997). Therefore, the first layer of computational cells closest to the bed is adjusted to be located at the distance of $3d_{50}$ to $4d_{50}$ from the bed. This reference level height with good estimation is located in the log-law region of the boundary layer flow field. Hence, a simple near-wall treatment method, Cebeci and Bradshaw (1977), which is valid for the logarithmic boundary layer is applied to solve the near-wall flow field (Figure (3-3)). In Figure (3-3), d is the diameter of an ordinary sand particle, and d_{50} is the median sieve diameter of the sand particles. A similar approach was followed by Zhao and Cheng (2010) by employing Zyserman and Fredsøe (1994) model

to calculate c_Δ which offers Δ equal to $2d_{50}$. In comparison to the work of Zhao and Cheng (2010), the present work is well-adapted for the applied wall function by suggesting a larger Δ. This arrangement brings two advantages which leads to decrease in the computational burden while preserving accuracy. First, there is no need for the truncation of the computational mesh to solve the suspended load model, since the centre of the first layer of mesh close to the bed operates as a reference level, and second, there is no need for applying a continuous wall function (as it is used in Fuhrman et al. (2014), Sumer et al. (2014) and Baykal et al. (2017)) which uses an iterative process to calculate friction velocity.

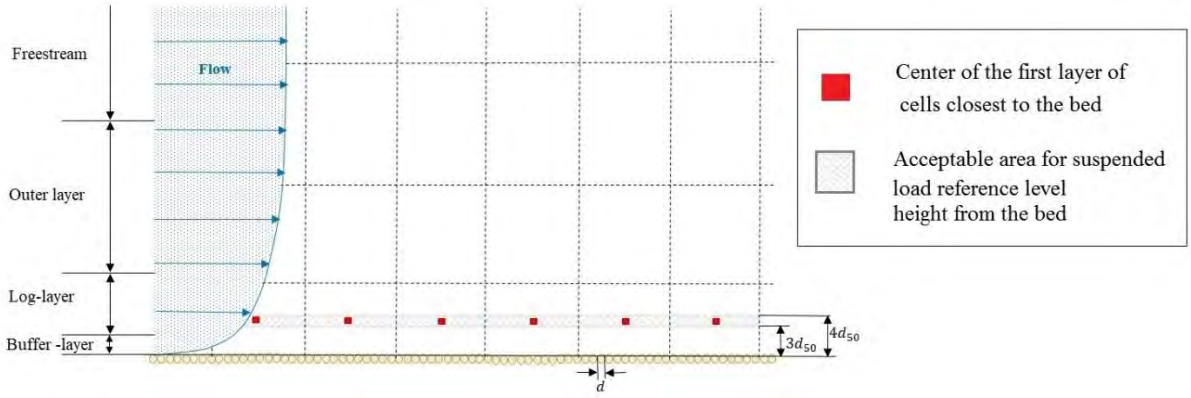


Figure (3-3) Schematic of the mesh grids, centre of first layer of cells close to bed and acceptable area for suspended load reference height from the bed.

3.4.1 Bedload model

The calculation of the bedload model does not need any boundary condition as the value of the bedload flux for each bed grid cells is computed explicitly and independently using empirical Eq. (2-59) for each bed face grid. For this purpose, the three components of the vector $\overrightarrow{u_B}$ in a sloping bed need to be calculated from the nonlinear system of coupled equations (Eq. (2-67)). In the present model, this is achieved employing a root-finding algorithm in the GNU Scientific Library (GSL).

3.4.2 Suspended load model

The advection-diffusion equation (Eq. (2-71)) is discretized and solved over the same 3D computational mesh as the one used to solve the hydrodynamic model. Hence, the value of fractional volumetric suspended sediment concentration, c, need to be set on the boundaries of the original computational mesh to solve the suspended load model. For the inlet boundary condition where the fully developed flow is provided for the hydrodynamic model properties, the same approach is also followed for concentration. Therefore, the concentration profile of suspended sediments in an undisturbed fully developed flow is set at the inlet as a Dirichlet condition. The outlet, top and walls (piles bodies and sandy bed) are treated with zero normal gradient, and the sides are satisfied with symmetry condition.

3.4.3 Entrainment and deposition

3.4.3.1 Entrainment

In the present setup, Rijn (1984) implementation method for the calculation of entrainment flux is used. In an investigation in Garcia and Parker (1991), a comparison between seven different entrainment models was done and Rijn (1984) method was found to give the most accurate result. Liu and García (2008), Zyserman and Fredsøe (1988), Stahlmann (2013c) and Zhou (2017) also used the same approach. In this approach, the entrainment rate, E_Δ, is calculated from:

$$E_\Delta = c_\Delta w_s \tag{3-7}$$

The applied entrainment model does not have an upper limit itself. To restrict the entrainment flux from unrealistic values, it should be bounded. Therefore, as a reasonable maximum concentration, Fredsoe and Deigaard (1992) considered a value of c_Δ=0.35 to bound the maximum possible entrainment flux.

3.4.3.2 Deposition

In the present work, deposition is calculated from the same approach as Liu and García (2008). Therefore, the deposition rate, D_Δ, is calculated by:

$$D_\Delta = w_s c_b \tag{3-8}$$

where c_b is sediment concentration very near the bed (the first layer of cells closest to the bed).

3.4.4 Fall velocity

As mentioned in section 2.3.6, a wrong estimation of the settling velocity may result in an error with a magnitude of factor three or more regarding the suspended load transport computation (Jiménez and Madsen, 2003). Therefore, choosing a reasonable value of the settling velocity is very important. In the present setup, a fall velocity of a single grain, w_{s0}, is obtained from the method proposed by Soulsby (1997):

$$w_{s0} = \frac{\nu}{d}[(10.36^2 + 1.049D_*^3)^{0.5} - 10.36]. \tag{3-9}$$

Thereby, to calculate the particle fall velocity, w_s, the output of Eq. (3-9) is substituted in Eq. (2-68) given by Richardson and Zaki (1997).

3.4.5 Mass-balance equation for sediment

In the present setup, The Exner equation (Eq. (2-76)) is calculated using the third order Adam-Bashforth explicit time integration scheme, similar to the approach followed by Jacobsen (2011). In this approach, the bed level change in time step $i+1$, Δh^{i+1}, is calculated by:

$$\Delta h^{i+1} = \frac{1}{12}\left[23F^i - 16F^{i-1} + 5F^{i-2}\right]\Delta t \tag{3-10}$$

where

$$F = \frac{-1}{1-n}[\nabla.\overrightarrow{q_b} - E_\Delta + D_\Delta]. \quad (3\text{-}11)$$

and Δt is the time step size. The mass-conservation equation is solved over a bed boundary mesh in 2D. To implement this in OpenFOAM® framework, the Finite Area Method (FAM) (Tuković, 2005) is used to generate a 2D mesh according to the bed boundary of the 3D computational domain. The corresponding data of bedload and deposition and entrainment from the 3D mesh needs to be mapped onto the 2D mesh. Then, the Exner equation is solved. Figure (3-4) shows the 3D computational domain and the corresponding 2D bed mesh. Finally, the resultant morphological changes Δh are mapped back as a displacement profile to the bed of the 3D mesh, however, the results need to be already checked for bed filtration and sand sliding.

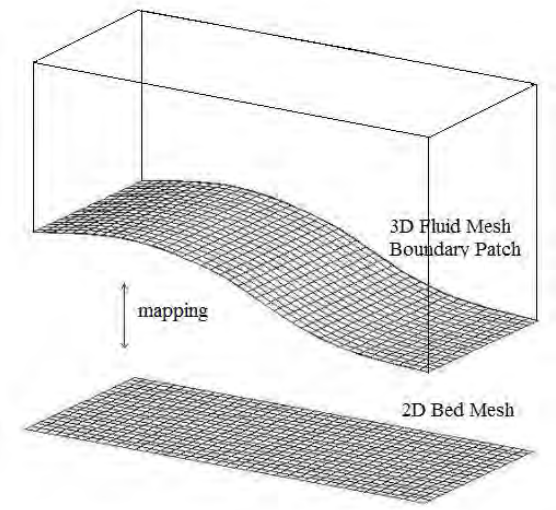


Figure (3-4) The 3D computational domain and corresponding 2D bed mesh to solve Exner equation.

3.4.6 Filtration of bed elevation

Due to the nature of the Exner equation, numerical instability may occur during the solution. Therefore, a filtering method is used to control spurious oscillations. To suppress this numerical instability, different filtration methods may be used in OpenFOAM® framework. In this study, two filtration methods, one which is used in the works of Jensen et al. (1999) and Stahlmann

(2013c), and the other employed in the works of Jacobsen (2011) and Zhou (2017) were investigated and compared. Codes for both methods were implemented in OpenFOAM® framework. Both of these filtration methods perform as a smoother on the bed elevation changes and use interpolation between each grid cell and its neighbours.

In the approach followed by Stahlmann (2013c), interpolation is applied between the centre of the neighbour bed boundary faces. In order to find bed elevation changes after filtration for the centre of face *i*, $\widehat{\Delta h}_i$, few steps have to be taken. First, a filtered value of the face *i*, $\tilde{h}_i$, is calculated as:

$$\tilde{h}_i = 0.65(h_i + \Delta h_i) + 0.35(h_{in} + \Delta h_{in}) \tag{3-12}$$

where h_i is the geodetic height of the face centre i, and Δh_i is the face elevation changes after solving Exner equation. The subscript "in" is used to specify the mean values for neighbour faces of the face *i*. Second, another filtered value, $\tilde{\tilde{h}}_\iota$, based on the first filtered values calculated as:

$$\tilde{\tilde{h}}_\iota = 1.35\tilde{h}_i - 0.35\tilde{h}_{in}. \tag{3-13}$$

Finally, the bed elevation changes, $\widehat{\Delta h}_\iota$, calculated from

$$\widehat{\Delta h}_i = \tilde{\tilde{h}}_\iota - h_i. \tag{3-14}$$

The smoother is applied on faces which satisfy:

$$|(h_{in} + \Delta h_{in}) - h_i| > \frac{1}{8} d_{xy} \tag{3-15}$$

where d_{xy} provides the average distance of the face *i*, from neighbour cells on the xy surface. The result of this filtration method is only valid for the case of equidistant (uniform) mesh. In the case of non-equidistant (non-uniform) mesh, it doesn't satisfy the mass conservation.

Jacobsen (2011) and Zhou (2017) followed a different approach. They use the available interpolation schemes in OpenFOAM® between face centres and points. In this method, the bed elevation changes after filtration for centre of face i, $\widehat{\Delta h}_i$, obtained from two interpolations between face centres and points. These interpolation schemes include correction factors which ensure that the applied scheme satisfies the mass-conservation. It is to be noted that this method is applied to the bed elevation change and not the geodetic height of the faces. Therefore, in the case of evolution of scour hole formation the effect of the smoother method approaches zero in time with approaching equilibrium conditions. Also, there is no constraint on this filtration method, and it is applied on whole bed boundary mesh in each time step. In the present setup, the later approach is followed for filtration.

3.4.7 Sand sliding model

Two different techniques for the purpose of modelling the sand sliding process, namely, Artificial Transport Rate Method (ATRM) and Geometry-Based Method (GBM) were investigated. These methods were compared in terms of reliability, computational time and numerical diffusion for different 3D test cases. The full description of the methods, the applied test cases and the results of the comparisons are available in Appendix I. Subsequently, codes for both methods were implemented in OpenFOAM® framework. In the proposed approach, ATRM was applied as a sand sliding model, as it offers a solution with a considerably lower numerical error in compare to that of the GBM.

3.4.8 Coupling procedure

The applied classical approach in the present setup entails a coupling between selected hydrodynamic and implemented morphodynamic models. In this approach, at each time step, first, the hydrodynamic model is solved on the 3D computational mesh. Second, bed shear

stress, as the primary parameter for solving sediment transport models, is calculated. Then, the bedload model on a 2D mesh, in accordance with the bed boundary, and the suspended load model on a 3D computational mesh over the reference concentration level, are passively solved. Finally, the results of the sediment transport model are reflected by solving the mass conservation equation over the 2D mesh and transferring the results as a deformation on the bed. The deformed mesh is used as a renewed computational mesh for the next time step of the solution. Figure (3-5) shows the general form of coupling procedure in a flowchart for the classical approach which has to be repeated in every time step of the simulation. In the presented flowchart the corresponding time step to solve the hydrodynamic model is the same as the one chosen for solving the morphodynamic model.

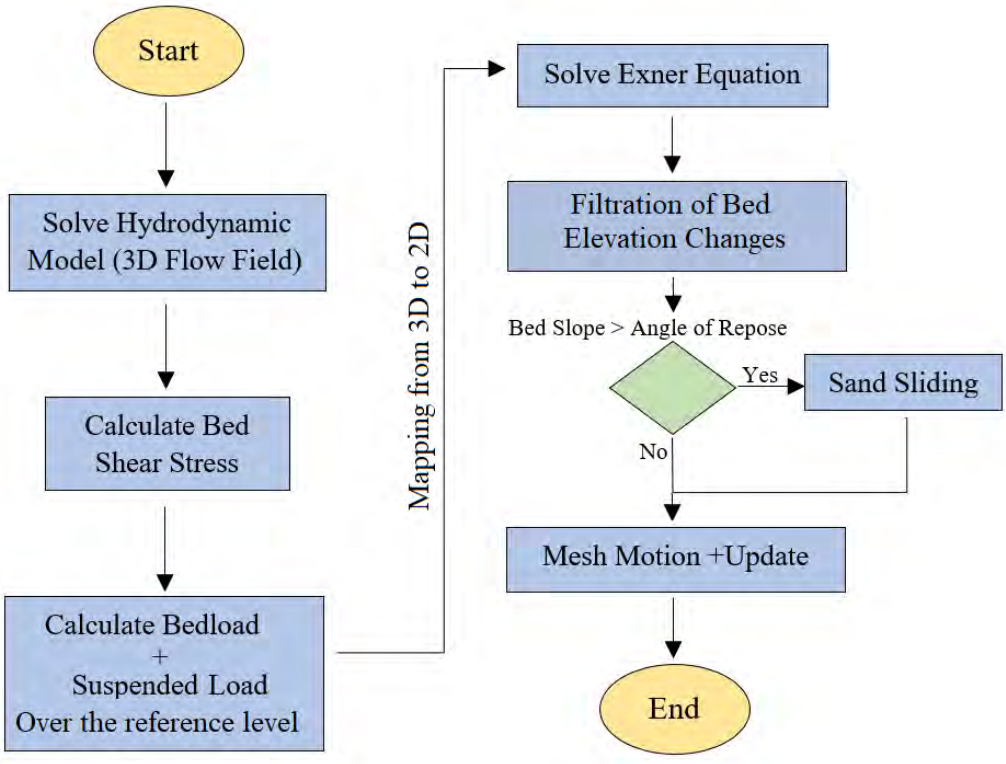


Figure (3-5) Flow chart of the hydrodynamic and sediment transport coupling procedure in each time step of the scouring modelling.

3.4.9 Mesh motion method

The resulted bed elevation changes from the consecutive processes of mass conservation equation, bed filtration and sand sliding need to be mapped back on the bed of the 3D computational mesh as a vertical displacement. This vertical displacement changes the morphology of the bed boundary of the computational domain as a mobile sandy bed. The process of deformation of the mesh boundary and adaptation of the internal mesh grids according to that is taken into account by means of moving mesh (dynamic mesh) approach. For this purpose, OpenFOAM® provides a mesh motion function based on the Laplacian operator smoother (Jasak and Tukovic, 2006). Two choices are available in OpenFOAM® framework for the dynamic mesh approach. One operates on face centres, while the other one performs on mesh points. In the proposed setup, the mesh motion is carried out in the vertical direction by solving a mesh motion function as:

$$\nabla.(\gamma_m \nabla V_z) = 0 \qquad (3\text{-}16)$$

The equation is solved over the internal grids of the computational domain, where γ_m is the diffusion coefficient, and V_z is the scalar quantities which gives the vertical motion for cells. Meanwhile, appropriate boundary conditions and numerical scheme need to be defined to solve Eq. (3-16) over the 3D computational domain.

3.5 OPENFOAM® CFD TOOLBOX

For the present setup, a code is implemented in foam-extend 4.0 toolbox. Foam-extend is an unofficial extended version of OpenFOAM® software. OpenFOAM® is a toolbox designed for numerical modelling of various range of applications (e.g. complex fluid flow, multi-phase flow, heat transfer and chemical reaction) which was originally developed by Henry Weller in Imperial College London in 2004. Since then, different version and variants of it have been

released. The software is freely available and can be installed in different operation systems Unix/Linux/Windows and can be used with or without Graphical User Interface (GUI). OpenFOAM® is written in C++ programming language and all source code and libraries are modifiable which makes it a flexible tool to be applied for different applications. It also provides a wide range of pre-defined solvers that can be used for different applications. Foam-extend version which has been applied here is chosen since the extended versions include several extra features and extension of the code which are not available in the official versions.

3.5.1 File structure of a test case in OpenFOAM®

Generally, to be able to run a test case using OpenFOAM® a structure of necessary files is required. A typical structure of the files for a simulation case in OpenFOAM® is shown in Figure (3-6). The number of required files to run a test case may be more or less than the illustrated file structure. In Figure (3-6), Folder *0* includes the initial and boundary condition values for all variables used in the simulation. In folder *constant* the constant values, the considered dynamic mesh and turbulence model properties and data of generated computational mesh are stored. The *system* folder includes 3 main files. The *controlDict* file includes the time step size controller, post-processing functions, applied solver, and read and write options. The *fvSchemes* contains the applied numerical schemes used to solve the discretized form of different terms of the governing equations in numerical modelling. The *fvSolutions* contains the applied algorithms and methods, defined tolerances and convergence criteria to solve the governing equations.

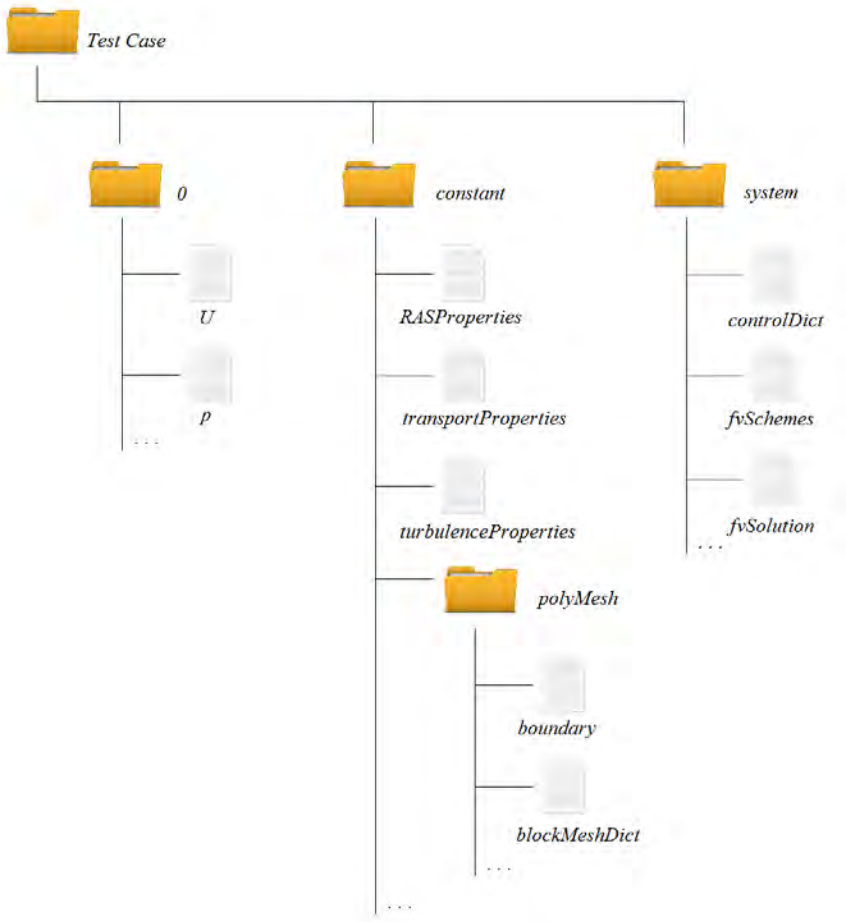


Figure (3-6) Typical structure of a test case in OpenFOAM®.

3.6 SUMMARY

In this chapter, the implemented model in the framework of OpenFOAM® was described. The model aims to bridge the gap in knowledge of local scour around pile/piers with different cross-section shapes by providing a more robust and reliable tool.

- The present setup benefits from unsteady-RANS equations in combination with *k-ω SST* turbulence closure model to solve the hydrodynamic part of the model, while the sediment transport part of the model comprise of both bedload and suspended load models.

- In the proposed scheme, the centre of the first layer of cells closest to the bed of the computational mesh is adjusted in accordance with the reference level height from the bed. Therefore, the first layer of computational cells closest to the bed is located at the distance of $3d_{50}$ to $4d_{50}$ from the bed. This reference level height with good estimation is located in the log-law region of the boundary layer flow field. Hence, a simple near-wall treatment method, Cebeci and Bradshaw (1977), which is valid for the logarithmic boundary layer is applied to solve the near-wall flow field (Figure (3-3)).

The combination of the selected hydrodynamic model and the applied morphodynamic model provides a robust tool in modelling of scour prediction. In the next section, the reliability of the proposed combination is examined by providing eight different test cases.

4 VALIDATION OF THE PROPOSED MODEL

4.1 INTRODUCTION

In this chapter, the results of validating the proposed model using test cases from the literature are presented. Eight different test cases are applied to step by step evaluate the performance of the model. The first four test cases are used to validate different parts of the model (hydrodynamic and suspended load models), while the latter four are used to validate the full-model, i.e. coupled hydrodynamic and morphdynamic model where the morphodynamic part entails both bedload and suspended load models. For each test case, a brief description is provided followed by details of results and comparisons with model simulations.

In the first test case, the performance of the employed wall function (Cebeci and Bradshaw, 1977) in the proposed model is compared against the experimental equations for flow velocity profiles over a homogeneous bed. In the second and third test cases, the performance of the hydrodynamic model which solves the unsteady-RANS equations in combination with the *k-ω SST* turbulence model is examined using experimental measurements from Roulund et al. (2005) for the fluid flow field around circular piles mounted on rigid smooth and rough beds. In the fourth test case, the net entrainment test, an advection-diffusion equation (Eq. (2-71)) is solved along with the hydrodynamic model to simulate the sediment concentration due to suspended-load sediment transport. The simulation results are compared to the experimental results of Rijn (1986).

In the next four test cases, the coupled hydro- and morphodynamic model is used to simulate the deformation of the bed due to sediment transport. In test case five, a 2D case of a submerged

horizontal jet is employed and the progression of the bed deformation due to scour is compared with experimental results from Chatterjee et al. (1994). In test case six, a simulation is conducted for the evolution of a 3D scour hole around a circular pile, and results are compared to Roulund et al. (2005) empirical test in live-bed condition. Finally, in the last two test cases, the development of the scour hole around square and diamond piers are simulated for test cases based on experimental tests of Khosronejad et al. (2012) in clear-water flow condition.

4.2 TEST CASE 1: HOMOGENOUS BED MODEL

To assess the performance of the adapted wall function Eq. (2-26) (Cebeci and Bradshaw, 1977), a series of simple tests were considered. In this test case, the velocity profile of flow over a homogenous bed from the simulation result was compared with the log-law profile from the experimental equation of Cebeci and Bradshaw (1977). In the provided tests, a 2D channel domain with 20 m long and 5 m depth was assumed as shown in Figure (4-1). The relevant mesh with around 10000 grids was generated using blockMesh utility in OpenFOAM®. The grids were uniform in the horizontal direction (x-direction) while they grew with an expansion ratio of 1.02 in the vertical direction (y-direction) with the smallest grid close to bed with a height of 0.02 m. It was assumed that the boundary layer thickness is equal to the flow depth. The tests were run for the bed boundary with four different equivalent roughness heights k_s = 0, 0.001, 0.005, 0.01 m. The steady-state solver, simpleFoam, in OpenFOAM® which employs the SIMPLE algorithm (Patankar and Spalding, 1983) was applied to solve the RANS model where the shear stress terms were modelled with the *k-ω SST* turbulence model. The simulations were stopped when the residual for flow field properties reached the predefined value of $1 \times e^{-7}$. The applied bed boundary condition was the same as the one described in section 3.2.1 for flow and turbulent properties. The inlet and outlet boundary of the domain were satisfied with cyclic boundary conditions with a mean velocity of 1 *m/s*, which ensure the

turbulence flow with boundary layer thickness Reynolds number $Re_\delta = U_\infty \delta/\nu$ =5 × 10^6. The pressure difference between the inlet and outlet was calculated based on energy loss in the domain. The slip boundary was used for the top boundary and sides of the domain were satisfied with empty boundary conditions for a 2D case. Table (4-1) shows the calculated values of u_f, y^+, k_s^+, and the experimental equation for each test case. u_f was calculated using Eq. (2-18). The presented y^+ is the calculated value for the centre of the first layer of grids from the bed.

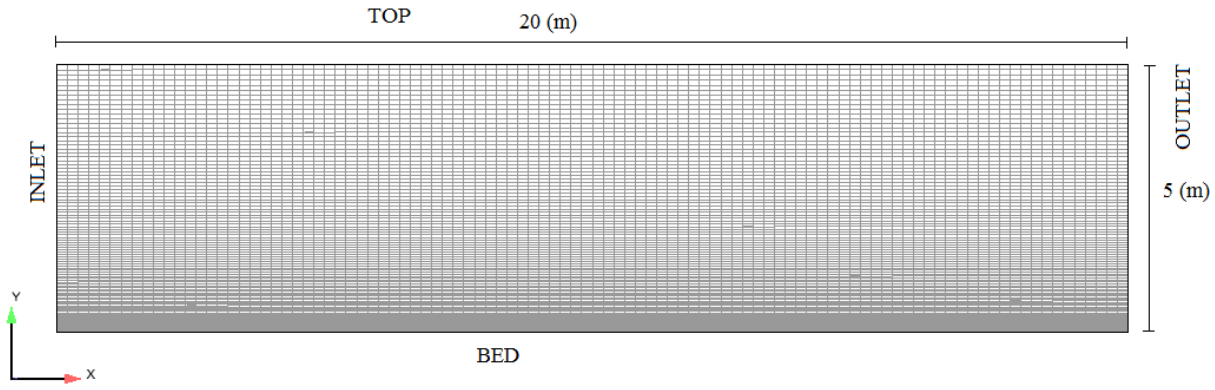


Figure (4-1) Generated mesh for the homogenous bed test.

Table (4-1) Homogenous bed model test series data.

$Case$	k_s (m)	u_f $(^m/_s)$	$k_s^+ = {}^{k_s u_f}/_{\nu}$	y^+	u^+ (Cebeci and Bradshaw, 1977)
1	0	0.0324	0	324	$\frac{1}{\kappa}\ln(y^+) + 5.2$
2	0.001	0.0404	40	404	$\frac{1}{\kappa}\ln(y^+) - 2.65$
3	0.005	0.0486	243	486	$\frac{1}{\kappa}\ln(y^+) - 6.96$
4	0.01	0.0527	527	527	$\frac{1}{\kappa}\ln(y^+) - 8.47$

In Figure (4-2), the simulation results for the velocity distribution profile in the *y*-direction are compared with results from Cebeci and Bradshaw (1977) for each test case. Root-Mean-Square Error (RMSE) was applied to calculate the quantitative deviation of the simulations against

Cebeci and Bradshaw (1977) wall function equations listed in Table (4-1). Results show a good agreement between the simulations and estimated values from the functions with RMSE values of less than 0.02 for all cases. Some deviations between the results can be observed for high values of y^+. This indicates that in the regions with high value of y^+ the velocity profile does not follow the logarithmic boundary layer conditions. This means that boundary layer was not developed across the entire water depth. Figure (4-3) shows changes in velocity profiles as a result of changes in k_s. The results show that increase in k_s leads to increase in the maximum velocity. The results of the test case 1 confirm that the applied near-wall treatment in the simulations has a promising capability in reproducing the boundary layer flow over a flat bed.

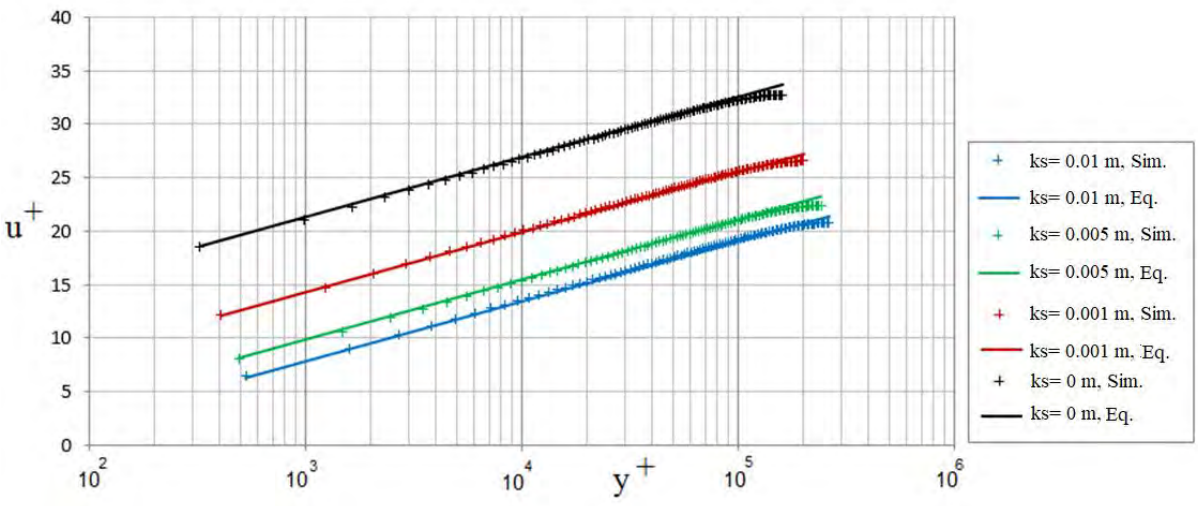


Figure (4-2) Comparison between simulation results and Cebeci and Bradshaw (1977) wall function equations.

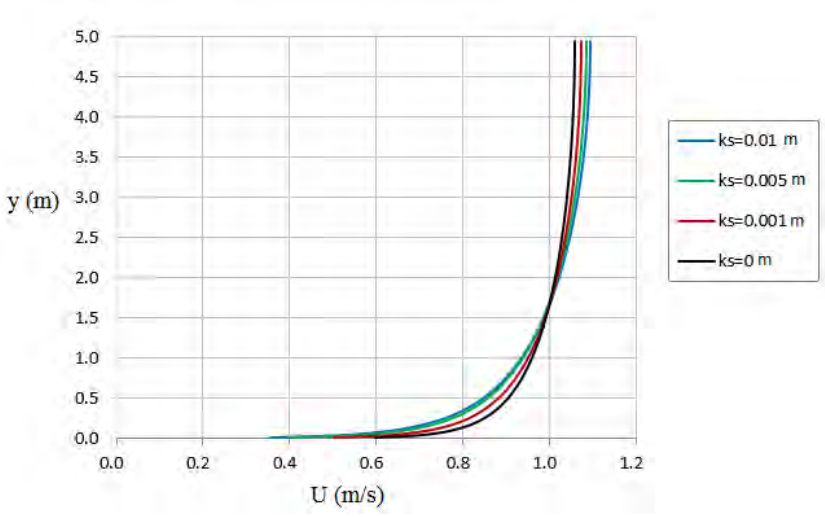


Figure (4-3) Velocity profiles for different applied k_s.

4.3 TEST CASE 2: FLOW AROUND A VERTICAL CIRCULAR PILE MOUNTED ON A SMOOTH RIGID BED

4.3.1 Experimental details

This test case was adopted from Roulund et al. (2005) where experiments were conducted in a 35 m long and 3 m wide flume with a smooth and rigid bed. A hydraulically smooth surface pile with a diameter of $D = 0.536\ m$ was fixed on the bed 20 m downstream of the inlet section. The flow was a steady current with water depth maintained at 0.54 m, having a depth average velocity of 0.326 m/s. Table (4-2) shows the experimental conditions. Flow field and bed shear stress measurements were carried out by a two-component laser-Doppler anemometer (LDA) and a one-component hot-film probe, respectively.

Table (4-2) Experimental conditions for smooth bed test case (Roulund et al., 2005).

Bed condition	Rigid smooth bed
Water depth H (m)	0.54
Boundary layer thickness (m)	0.54
Mean flow velocity (m/s)	0.326
Boundary layer thickness Reynolds number $Re_\delta = U_\infty \delta/\nu$	1.8×10^5
Pile Reynolds number $Re_D = U_\infty D/\nu$	1.7×10^5
Froude number $Fr = U_\infty/(gH)^{0.5}$	0.14
Undisturbed Friction velocity u_f (m/s)	
From Log. Fit	0.013
From Hot-film Meas.	0.015

4.3.2 Numerical details and results

For the purpose of numerical modelling, a 10 m long and 4 m wide computational domain was considered in which a 0.54 m diameter pile was placed 4 m downstream of the inlet. Figure (4-4a) shows the 3D computational domain and the applied boundary conditions. Symmetry boundary condition was considered for all quantities on the sides of the computational domain, which is reasonable due to the negligible effect of the flume width on flow velocity near the pile (Roulund et al., 2005). Fully developed flow conditions were used for velocity and turbulence properties at the inlet. The inlet flow condition was obtained from a preliminary hydrodynamic simulation which was conducted for a domain with the same velocity, width and depth as the original mesh and considering cyclic boundary conditions at inlet/outlet, but without the presence of the pile. The model only included the water-phase, therefore, the water-air interface was modelled by considering the slip boundary condition on the top boundary, which is an acceptable assumption in this test case since the Froude number is small (Roulund et al., 2005). The outlet was treated with zero gradients of all quantities except for pressure, which is equal to zero at the outlet boundary. The bed and the cylinder were treated with no-

slip conditions and the Cebeci and Bradshaw (1977) model was adopted as a near-wall treatment on surfaces.

Mesh dependency study was done using two meshes with different numbers of cells as shown in Table (4-3). The normal resolution of the first layer of cells near the wall was set equal to $0.0083D$ for all meshes which reassure $y^+ > 30$ for a smooth wall. Figure (4-4b) shows the top view of the fine mesh from Table (4-3) which is employed for the present numerical simulation.

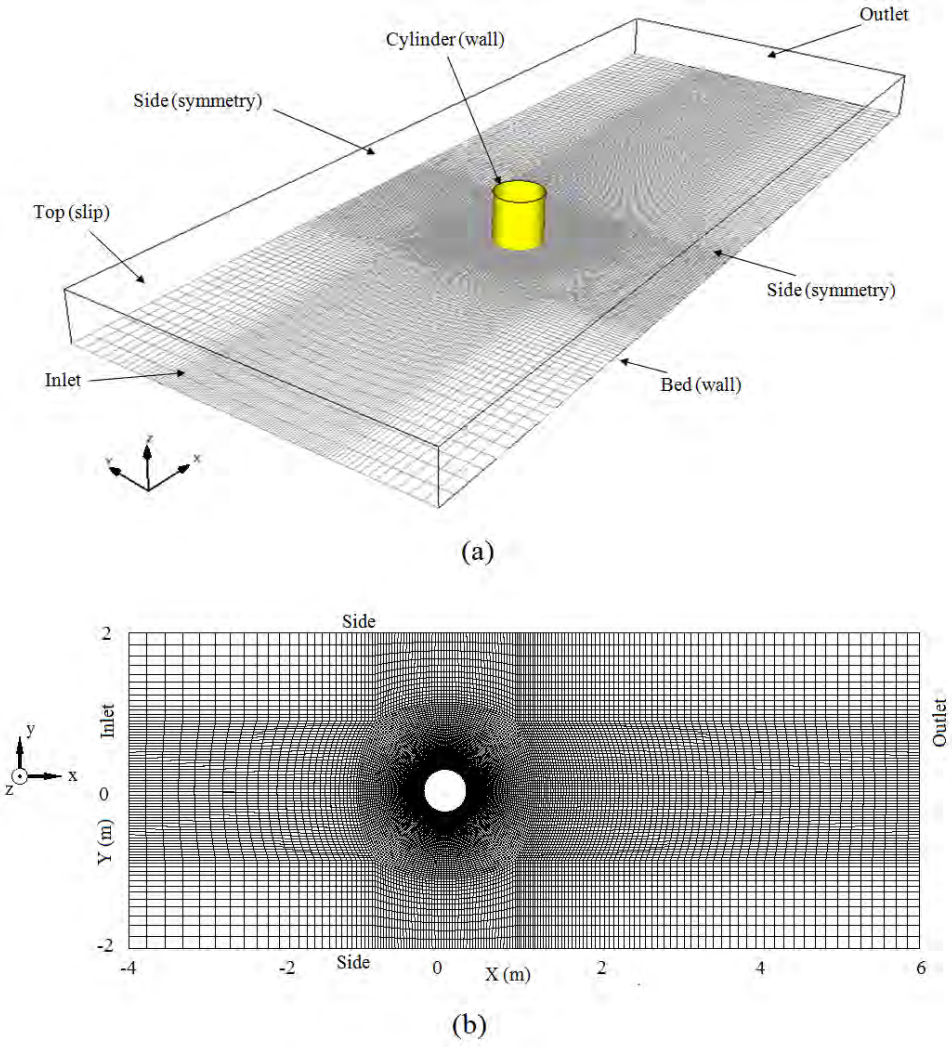


Figure (4-4) (a) 3D computational mesh and boundaries, (b) Generated mesh (Mesh1 in Table 4-1) for flow around a cylinder with a smooth bed test case (top view).

Table (4-3) Generated meshes for mesh dependency study.

Mesh	Fine	Coarse
Total number of cells	1.9 million	1.7million
Number of cells around the pile	280	260
Number of cells across the water depth	52	46
Minimum cell thickness next to the pile	0.0083D	0.0083D

To illustrate the formation of HSVs and lee-wake shed vortices upstream and downstream of the pile in unsteady-RANS simulations, the Q-criterion concept (Hunt et al., 1988) was applied. Q-criterion illustrates a vortex as a "connected fluid region with a positive second invariant of ∇u" (Kolář, 2007) which can be obtained by:

$$Q = \frac{1}{2}\left(\left|\Omega_{ij}\right|^2 - \left|s_{ij}\right|^2\right) > 0 \qquad (4\text{-}1)$$

where, Ω_{ij} and s_{ij} are vorticity and strain rate tensors, respectively, which can be defined by:

$$\Omega_{ij} = \frac{1}{2}\left(\frac{\partial u_i}{\partial x_j} - \frac{\partial u_j}{\partial x_i}\right), \qquad s_{ij} = \frac{1}{2}\left(\frac{\partial u_i}{\partial x_j} + \frac{\partial u_j}{\partial x_i}\right). \qquad (4\text{-}2)$$

Figure (4-5) shows the Q-criterion for iso-surfaces indicating vortex formations around piles at t=200 seconds of the unsteady-RANS simulation. It was found that the simulation results converged after 100 seconds of simulation.

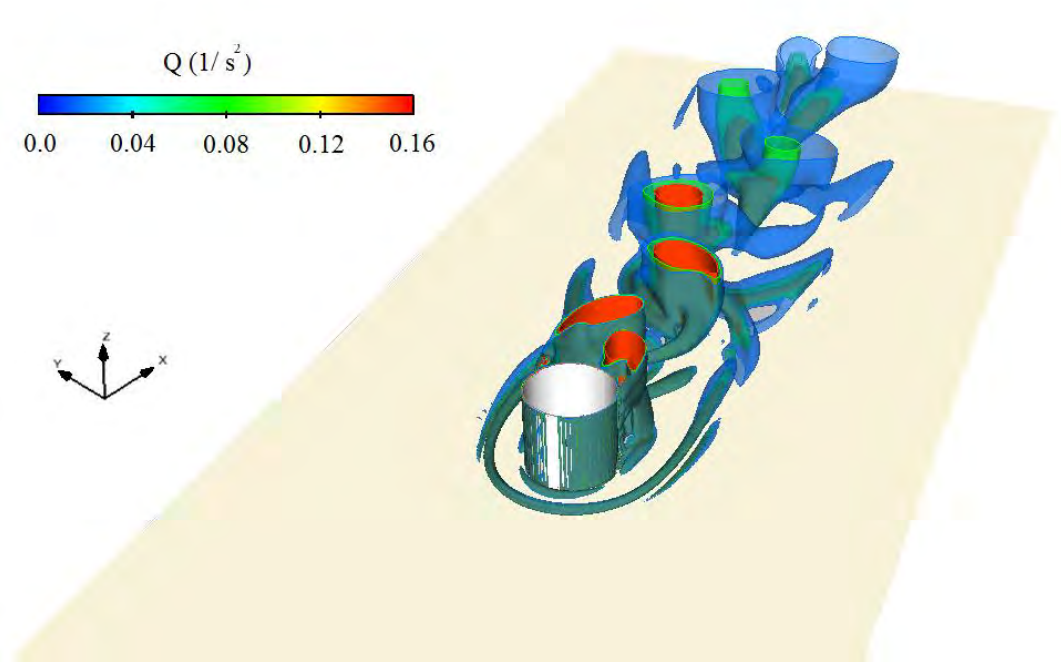


Figure (4-5) Formation of horseshoe and lee-wake vortices around the circular pile using the Q-criterion technique.

The pile Reynolds number is $Re_D = 1.7 \times 10^5$, and the flow around the cylinder is highly turbulent and includes reverse flow and vortex shedding structures. The velocity from both steady-RANS and unsteady-RANS models was compared with that from experimental and numerical results reported by Roulund et al. (2005). This was done to evaluate the impact of the formation of the lee-wake vortices downstream of the pile in simulations. Hence, the *k-ω SST* turbulence closure was used for both steady-RANS and unsteady-RANS simulations, using SIMPLE by Patankar and Spalding (1983) and PISO by Issa (1986) algorithms, respectively.

The comparison was performed for mean velocity components in the x- (Figure (4-6 a-c)) and z- (Figure (4-6 d-f)) directions, at different heights from the bed on the symmetry plane (y=0). The mean velocity components were calculated from the time-averaged values of the instantaneous velocities from t=200 to 300 seconds. Compared to steady-RANS, unsteady-RANS results gave a better agreement with experimental data in modelling turbulent flow

structures downstream of the pile. However, unsteady-RANS tends to over-estimate the area of formation of the horseshoe vortex in front of the pile. This discrepancy was explained by Levchenya et al. (2010) who illustrated that the intensity and position of HSV structures near the junction body (cylinder) can be related to the grid resolution around it. They argued that using rather fine computational grids near the junction body (cylinder) can produce qualitatively correct results in terms of intensity and position of vortex structures, however, in the present model, due to the limitation imposed by the applied near-wall treatment explained in section 3.2.1.3, using a finer grid size is not possible. Root-Mean-Square Error (RMSE) was applied to calculate the quantitative deviation of the simulation results from the experimental data for both mean velocity components in the x- and z- directions at z=0.5 (cm). As a result, values of 0.034, 0.033 and 0.045 were found for URANS (fine), URANS (coarse) and RANS model results, respectively. These results confirm that the URANS model predicts the flow field around the circular cylinder with better accuracy at upstream and downstream of the pier.

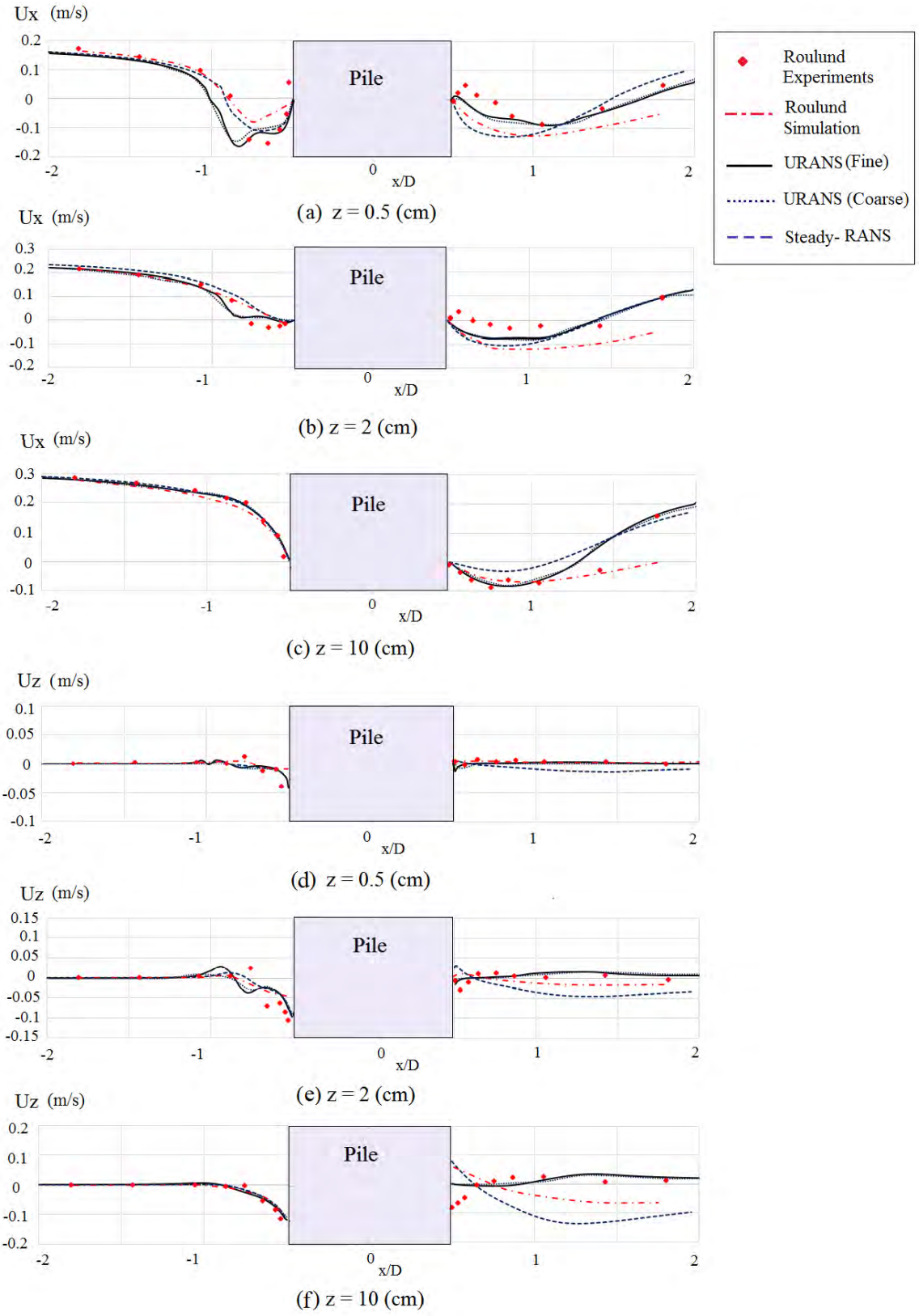


Figure (4-6) The velocity components in the x- and z- direction for flow around the cylinder with a smooth bed along the symmetry line on plane y=0 for different heights from the bed.

The calculated bed shear stress by the unsteady-RANS model was also compared with experimental and numerical data from Roulund et al. (2005) whom only reported the bed shear stress along a line on the symmetry plane upstream of the pile (Figure (4-7a)). In Figure (4-7a), bed shear stress amplification (BSSA) is defined as:

$$BSSA = \frac{\|\tau_w\|}{\tau_\infty}, \tag{4-3}$$

where τ_∞ is the magnitude of bed shear stress of the undisturbed flow field. The negative values for bed shear stress are related to the formation of HSV in front of the pile. Figure (4-7a) shows a good agreement between the experimental and numerical results in the region outside the HSV, however, the model under-predicts the value of bed shear stress in the horseshoe region and over-estimates the area of formation of the horseshoe in comparison to the results reported by Roulund et al. (2005). The main reason behind this observed difference is the inaccuracy of the model in predicting the HSV attributes including its intensity and position. Figure (4-7b) shows the distribution of the absolute value of $BSSA$ on the bed, which is calculated from the time-averaged instantaneous bed shear stress values. It is seen that the maximum time-averaged bed shear stress occurs on the sides of the cylindrical pile at a radial angle around 70° from the head of the pile.

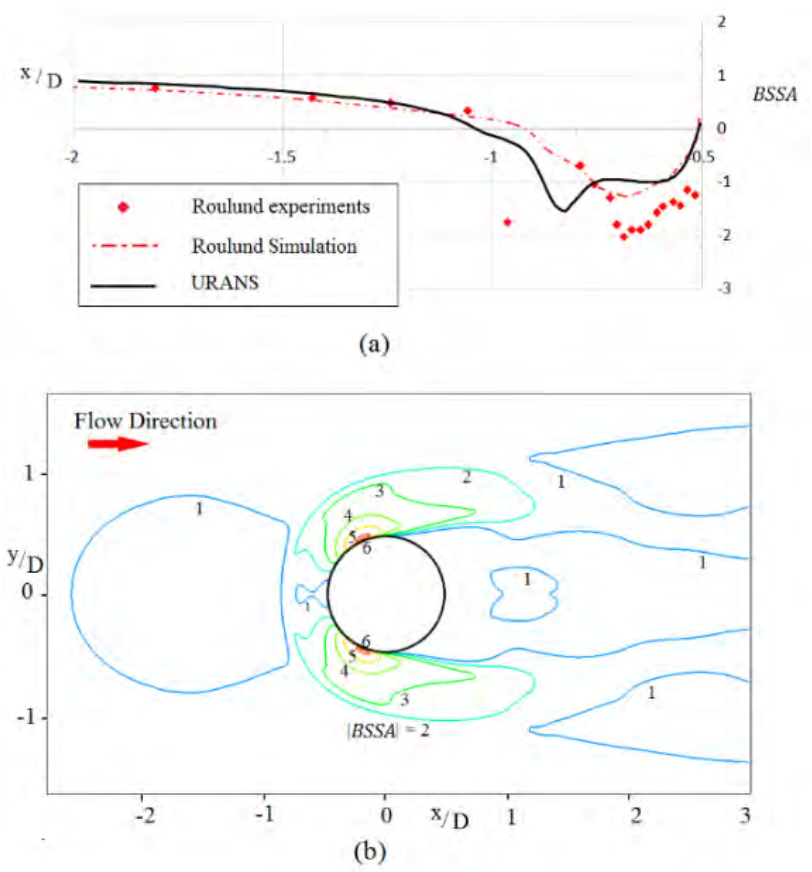


Figure (4-7)(a) Comparison of $BSSA$ between the unsteady-RANS model and numerical and experimental results reported by Roulund et al. (2005) (b) distribution of the absolute value of $BSSA$ on the bed around the cylinder pile.

4.4 TEST CASE 3: FLOW AROUND A CIRCULAR PILE MOUNTED ON A ROUGH RIGID BED

4.4.1 Experimental details

This experiment was adapted from the work of Roulund et al. (2005) in a flume 28 m long and 4 m wide. A circular pile with a hydraulically smooth surface and a diameter of $D = 0.536\ m$ was placed 20 m downstream of the inlet section. The test was carried out on a rigid bed with a steady current flow. The bed of the flume was rough with a Nikuradse equivalent sand roughness of $k_s = 0.01\ m$. The water depth in the experiment was maintained at 0.54 m giving

a depth average velocity of 0.326 m/s. Table (4-4) shows the conditions for the test. Flow field measurements were carried out by a two-component laser-Doppler anemometry (LDA).

Table (4-4) Test conditions for flow around a cylinder with the rough bed (Roulund et al., 2005).

Bed condition	Rigid rough bed
Water depth H (m)	0.54
Boundary layer thickness (m)	0.54
Mean flow velocity (m/s)	0.326
$Re_\delta = U_\infty \delta/\nu$	1.8×10^5
$Re_D = U_\infty D/\nu$	1.7×10^5
Froude number $Fr = U_\infty/(gH)^{0.5}$	0.14
Undisturbed Friction velocity u_f (m/s)	
From Log. Fit	0.023
From Hot-film Meas.	---
Bed Nikuradse equivalent sand roughness k_s (m)	0.01
$k_s^+ = k_s u_f/\nu$	230

4.4.2 Numerical details and results

The same mesh and similar boundary conditions as the one used for modelling flow behaviour around a cylinder with the smooth bed test (test case 2) were applied here. Both steady-RANS and unsteady-RANS simulations were conducted, and the results were compared with the experimental and numerical results reported by Roulund et al. (2005) (Figure (4-8a-f)). The simulation converged after the first 100 seconds of simulation and the mean velocity was calculated from the time-average of the instantaneous velocity of each time step from t=200 to 300 seconds. The simulation results show that the computed components of mean velocity in the x-direction from unsteady-RANS have a good agreement with experimental results, however, similar to the smooth bed test case, a difference between the results in the area of formation of the HSV is observed. The results for the component of mean velocity in the z-direction (Figure (4-8d-f)) show some deviation from experimental measurements downstream of the pile, which increases with distance from the bed. This difference can be a result of using

a RANS model with a rather large grid size near the walls, which results in an inaccurate prediction of the velocity field in the wake region. RMSE was applied to calculate the quantitative deviation of the simulation results from the experimental data for both mean velocity components in the x- and z- directions at z=0.5 (cm). As a result, values of 0.045 and 0.049 was found for URANS and RANS model results, respectively. The simulation results of test case 2 and 3 revealed that the unsteady-RANS equations in combination with the *k-ω SST* turbulence model have a high capability in reproducing the junction flow properties around circular piles.

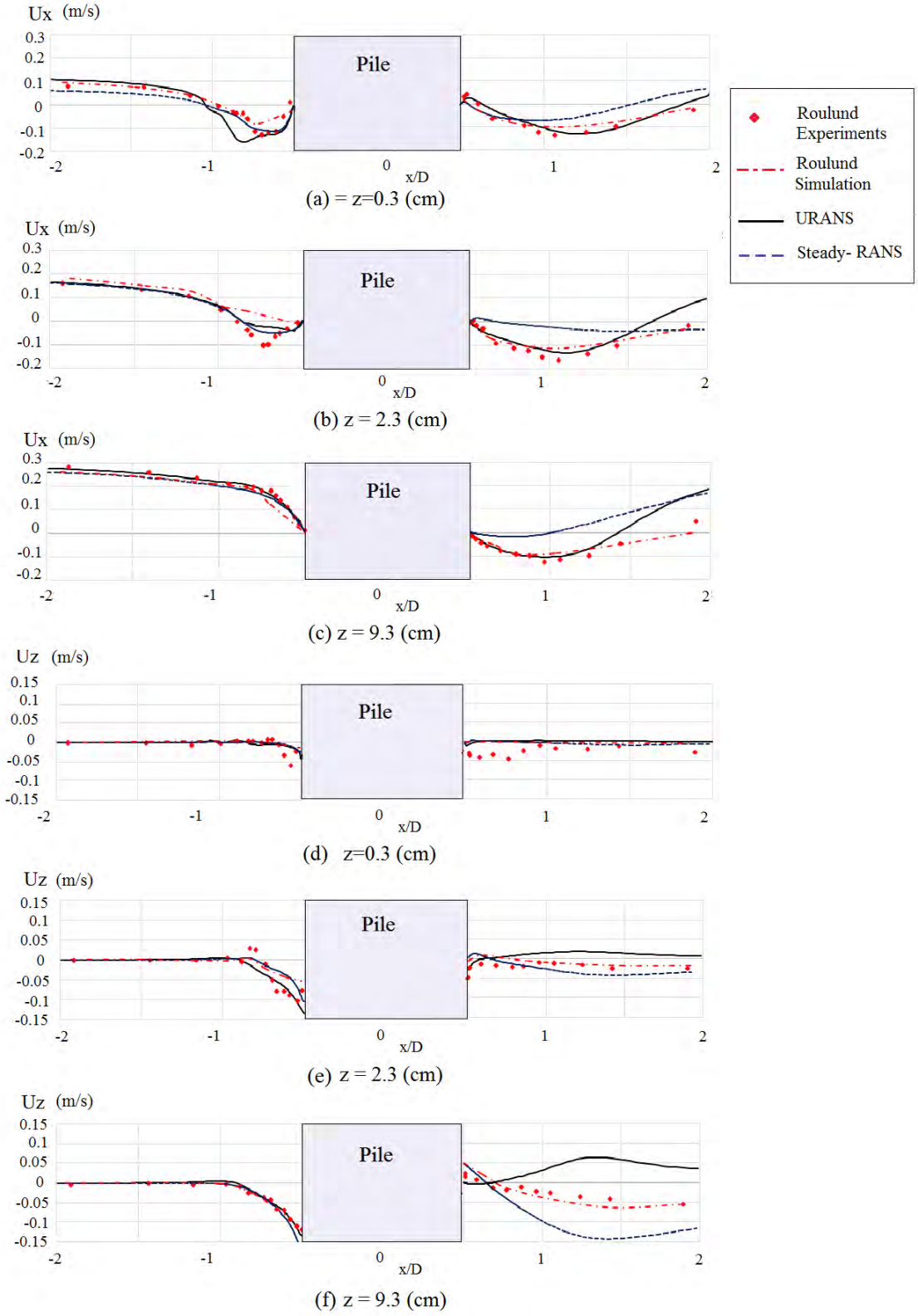


Figure (4-8) The velocity components in the x- and z-direction for flow around a cylinder with the rough bed along the symmetry line on plane y=0 for different heights from the bed.

4.5 TEST CASE 4: NET ENTRAINMENT

4.5.1 Experimental details

To validate the developed suspended load model (section 3.4.2), the net entrainment test of Rijn (1986) was simulated. A schematic drawing of this test is shown in Figure (4-9). The inlet flow was steady and free of sediments with a mean velocity of 0.67 *m/s* and water depth of $H = 0.25\ m$. The bed consisted of two parts, a rigid bed and a sandy bed. The rigid bed had a length of $20\ H$, and the sand covered bed had a length of $40H$. The median sediment particle diameter on the bed was $d_{50} = 0.23\ mm$ and the representative suspended particle size was $0.2\ mm$ with a settling velocity of 0.022 *m/s*. The Nikuradse equivalent sand roughness of the rigid bed was $k_s = 0.5\ mm$ and for the sandy bed which included the bed forms effect, $k_s = 0.01\ m$. The sediment concentration was measured at four different heights from the bed at $y/H = 0.06, 0.1, 0.2, 0.4$ and at four distances from the start of the sandy bed at $x/H = 4, 10, 20, 40$.

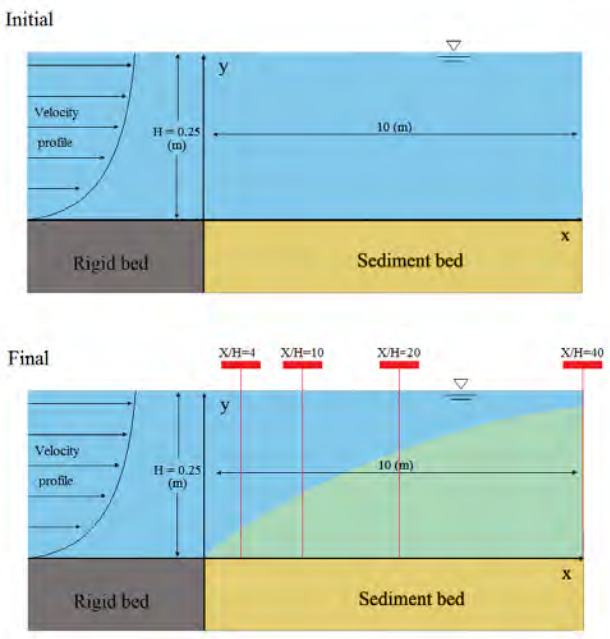


Figure (4-9) A schematic illustration of Rijn (1986) net entrainment test.

4.5.2 Numerical details and results

For this test case, the advection-diffusion equation (Eq. (2-71)) which simulates the suspended load part of the sediment transport was solved along with the hydrodynamic model. The generated 2D mesh used for modelling this test case had a length of 60 H (15 m), and a height equal to the depth of the water, $H = 0.25\ m$. The Δx of all cells was $0.02\ m$, and a minimum cell height of $\Delta y = 2\ mm$ was considered for the layer of cells closest to the bed. The cell height in the y-direction grew with an expansion ratio of 1.02. The flow field was solved with the unsteady-RANS model with the *k-ω SST* turbulence closure, and a fully developed flow was considered for the inlet boundary. The test case was solved with the transient solver for a total simulation time of $t = 200$ seconds to ensure steady flow conditions. For this case, the calculation of the skin-friction component of the bed shear stress was carried out using the proposed equation by Celik and Rodi (1991) as suggested by Liang et al. (2005):

$$\tau_w = \left[1 - \left(\frac{k_s}{H}\right)^{0.06}\right]\tau_{Tot}, \tag{4-4}$$

where τ_{Tot} is the total bed shear stress on the sandy bed which includes two parts. The skin friction component τ_w which comes from the contribution of individual sand grains and responsible for the initiation of motion of sediment on the bed, and the bed form-drag component τ_f due to the presence of ripples or large bed-forms.

$$\tau_{Tot} = \tau_w + \tau_f \tag{4-5}$$

Figure (4-10) demonstrates the distribution of sand concentration along the sandy bed for different sections together with the experimental data. The sediment concentration decreases sharply with the increase in the distance from the bed. Overall, an acceptable agreement is

achieved, which indicates that the numerical suspended load model is capable of reproducing the same sediment profile for this test case.

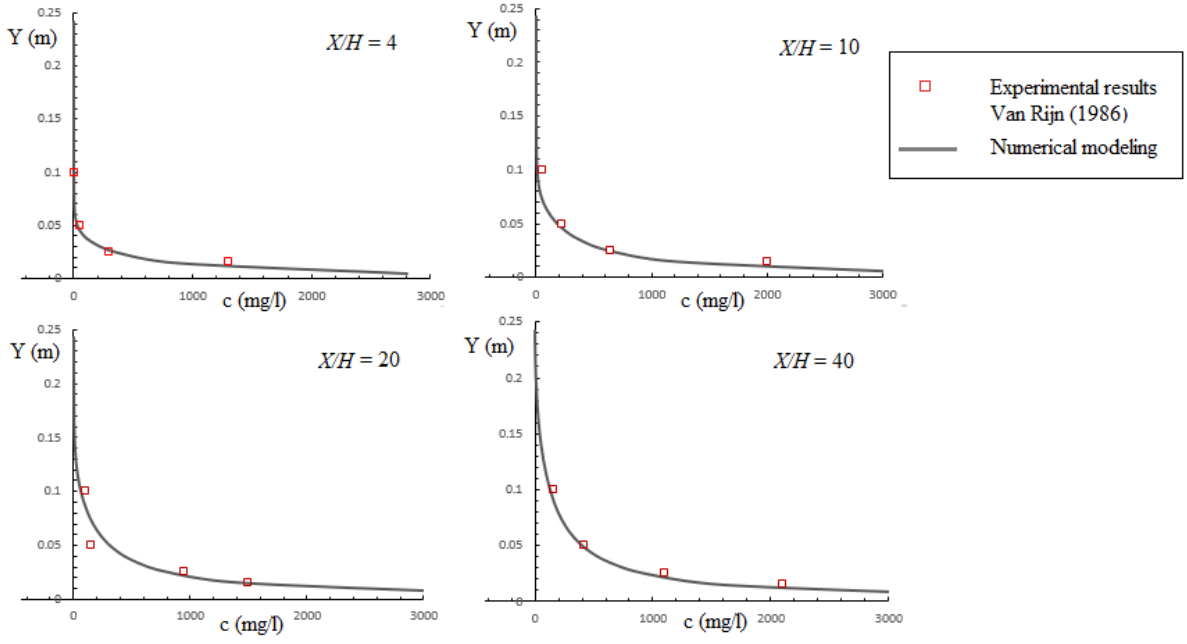


Figure (4-10) Concentration distribution along the sandy bed.

4.6 TEST CASE 5: SUBMERGED HORIZONTAL JET

4.6.1 Experimental details

A schematic drawing of this test case from Chatterjee et al. (1994) is shown in Figure (4-11). The experiment was conducted in a glass wall flume having a length of 3.66 m and a width of 0.6 m. The water entered the flume as a jet flow with a horizontal speed of 1.56 m/s from a sluice gate that had a height of 0.02 cm, resulting in a flow rate of 0.0204 m^2/s where the water depth was $H = 0.291\ m$. The first section of the flume was a rigid smooth bed with 0.66 m long. The rest of the bed was covered with sand with a particle diameter of $d_{50} = 0.76\ mm$, and a density of $s = 2.65$. The settling velocity for the sand was estimated to be $w_s =$

0.122 *m/s*, and the porosity of the sand was $n = 0.43$. The angle of repose for this test case was equal to 29°.

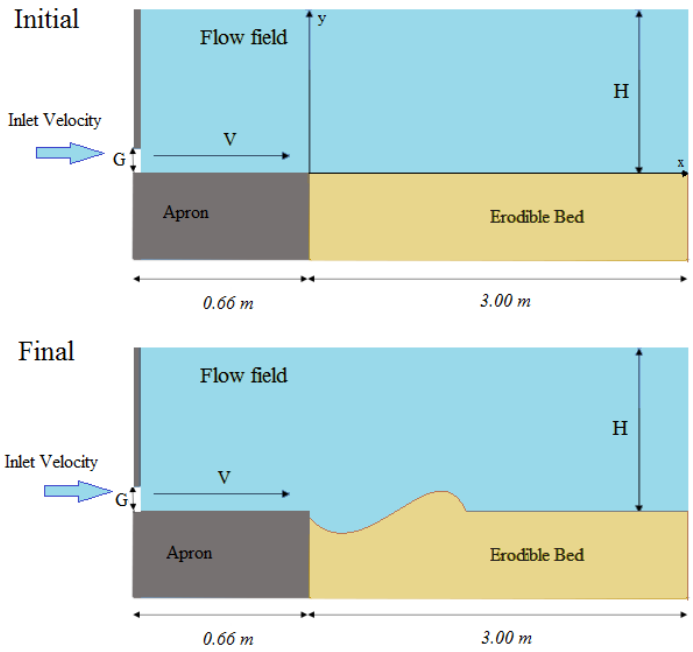


Figure (4-11) A schematic illustration of Chatterjee et al. (1994) submerged horizontal jet test.

4.6.2 Numerical details and results

For this test case, numerical modelling was performed in 2D. The mesh consisted of around 17000 cells most of which were concentrated around the bottom and the beginning of the moveable bed as shown in Figure (4-12). It is to be noted that Figure (4-12a) is focused only on the region of the conjunction of mobile and rigid bed sections, and the whole mesh is not shown. The thickness of the first layer of mesh close to the bed was 5 mm. The depth of the water in the numerical domain was considered to be 40 *cm* which means in comparison to the experiment the domain is extended for around 10 *cm*. This assumption was made to decrease the effects of the assumed plane surface on top of the domain on the formation of a dune downstream of the flume. Furthermore, as shown in Figure (4-12b), an initial pit and dune with a depth of 1.5 *cm* at the start of the mobile part of the bed was considered to overcome the mesh

motion limitation at the beginning of the movable bed with maintaining the mass conservation for the bed. This assumption helped the mesh to compress or expand in the y-direction at the beginning of the mobile bed. However, due to the limitation of the dynamic mesh method in smoothing the internal mesh, the internal mesh was not able to follow the bed boundary motion correctly. Hence, after 3 minutes of the simulation, this part of the mesh was kept fixed. The effect of the assumed pit and dune in the results of the model was negligible since in the first few seconds of the simulation the form of this part was completely changed.

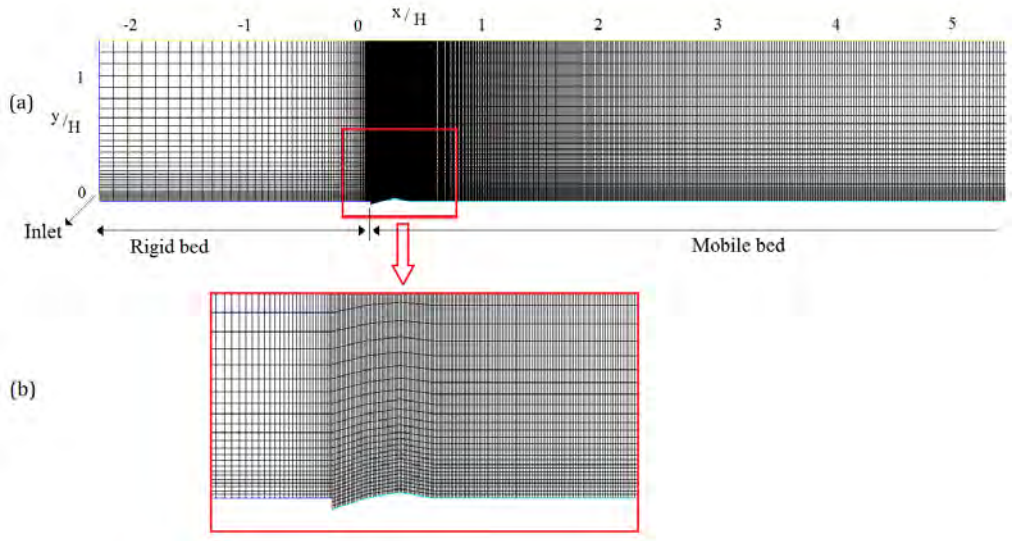


Figure (4-12) (a) Generated mesh for Chatterjee et al. (1994) test, (b) area of rigid and movable bed contact and assumed pit and dune.

The full morphodynamic model was applied for this test case which includes bedload and suspended load sediment transport models and solving the mass balance of sediment over the bed. From the experiment, it was found that it took around 60 mins for the evolution of scouring to stop. Therefore, $T = 60\ mins$ was considered as the required time to reach the equilibrium state. Figure (4-13) shows the velocity contours and the deformed bed at times $t = T/60, 2T/15,\ T/3$ and T. It is observed that a pit and dune was formed from the early stages of the simulation and expanded in time.

Figure (4-14) illustrates a comparison between the simulated and measured morphology of the bed at times $t = T/60, 2T/15,\ T/3$ and T. A good agreement can be seen for the pit and dune formation, however, due to the model's restriction, i.e. fixing the beginning part of the mobile bed, a difference between simulation and measurements is observed, which indicates some inaccuracy in solving the mass conservation equation. The model underestimated the height of the dune formed downstream of the flume in comparison with that of the experimental results.

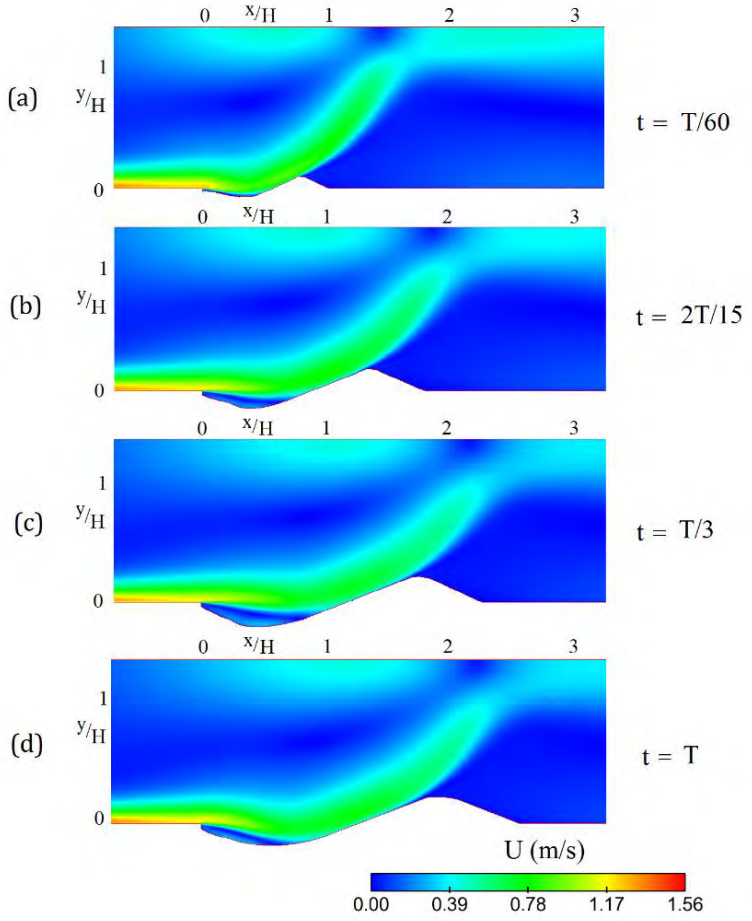


Figure (4-13) The velocity contour and deformed bed at 4 different times (a) $t = T/60,\ (b)t = 2T/15, (c)t = T/3\ and\ (d)t = T$

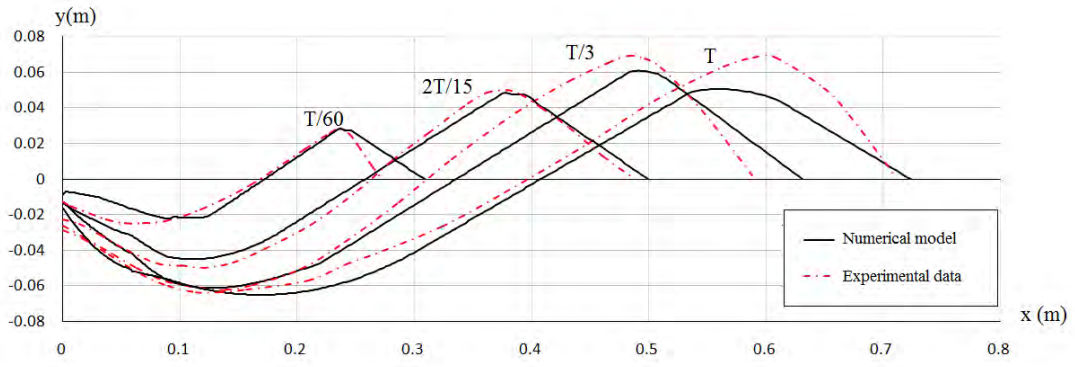


Figure (4-14) Comparison of the formation of pit and dune on the bed between the numerical results and experimental data for different times.

4.7 TEST CASE 6: SCOURING AROUND A CIRCULAR PILE IN LIVE-BED CONDITION

4.7.1 Experimental details

To study the local scour around a vertical circular pile, the experiments by Roulund et al. (2005) was adapted. This experiment was conducted in a flume, 10 m long and 4 m wide. A 0.1 m diameter pile was fixed at 6.6 m downstream of the inlet section. The bed was covered with loose sand with a particle diameter of $d_{50} = 0.26\,mm$ and a Nikuradse equivalent sand roughness of $k_s = 0.55\,mm$. The test was conducted on a mobile bed and under steady current flow. The water depth in the experiment was maintained at 0.4 m and the depth average velocity was $0.46\,m/s$. Figure (4-15) and Table (4-5) show the test details.

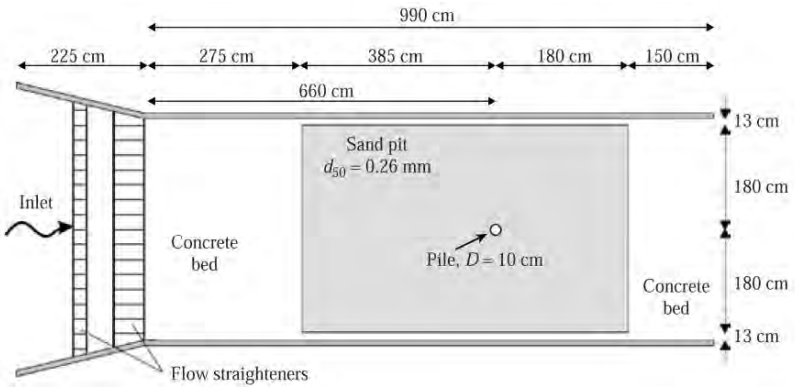


Figure (4-15) Test conditions of scour around a cylinder test (Roulund et al., 2005).

Table (4-5) Test conditions for scour around a cylinder test (Roulund et al., 2005).

Bed condition	Loose sand
Water depth H (m)	0.4
Boundary layer thickness (m)	0.2
Mean flow velocity (m/s)	0.46
$Re_\delta = U_\infty \delta/\nu$	9.2×10^4
$Re_D = U_\infty D/\nu$	4.6×10^4
Froude number $Fr = U_\infty/(gH)^{0.5}$	0.23
Undisturbed Friction velocity due to skin friction u_f (m/s)	0.028
Bed Nikuradse equivalent sand roughness k_s (m)	0.55×10^{-3}
$k_s^+ = k_s u_f /\nu$	17

4.7.2 Numerical details and results

The 3D mesh for this test case included around 400,000 cells. The top view of the mesh is shown in Figure (4-16). The thickness of the first layer of mesh close to the bed was $2\ mm$. The top boundary was simulated with slip boundary conditions. The symmetry boundary condition was considered at the sides of the computational domain for all quantities. This assumption with considering the ratio of the cylinder diameter to flume width in the experimental setup (D/w_F=0.026) is justifiable as its effects are negligible. The bed boundary was considered as a mobile bed with a roughness factor of $k_s = 0.55\ mm$ similar to the experiment. The inlet boundary was supplied with the velocity profile obtained from the curve fitting of the provided profile in Roulund et al. (2005) in Figure (4-17). The outlet was treated with zero values for the gradient of all quantities except for the pressure, which was equal to zero at the outlet boundary. unsteady-RANS model in combination with the full sediment transport model was used for this simulation.

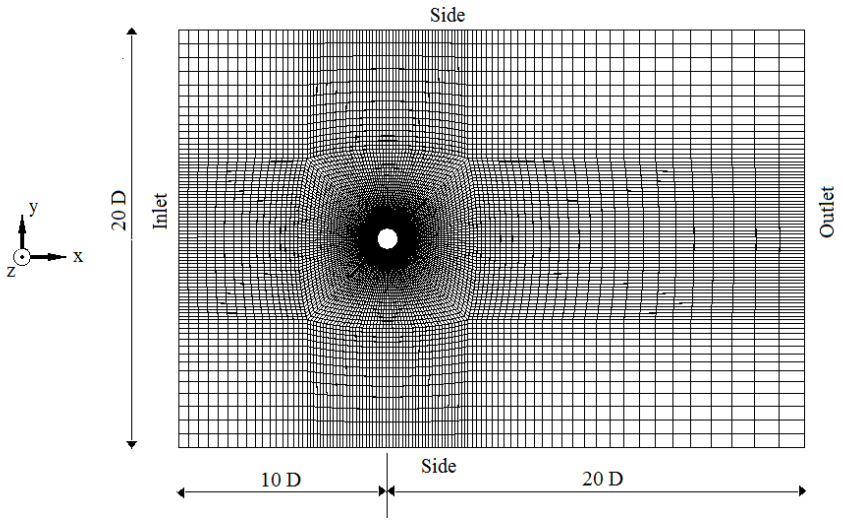


Figure (4-16) Top view of generated mesh for scour around a cylinder test case.

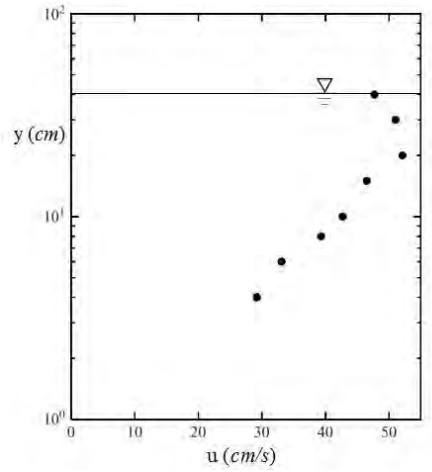


Figure (4-17) Undisturbed mean flow velocity profile (Roulund et al., 2005).

The experimental test reached the equilibrium scour stage after around 2 hours. However, changes in the results after the first hour of the simulation were small. Hence, to reduce the required simulation time, the model was only run for an hour of physical time when the scour depth is more than 95% of that in equilibrium condition (quasi-equilibrium condition) which required around 3 months of simulation time on a 2.3 GHz CPU with 8 GB RAM. Figure (4-18) shows a sequence of simulated bed deformation pictures at times t= T/60, T/12, T/4 and T from the start of the simulation where T=60 *mins*. It is observed that the deformation of the bed and

scouring adjacent to the pile starts from the early stages of the simulation and extends in terms of the maximum depth and the area affected by it. Dargahi (1990), from their observation in their scouring experiments, pointed out that there was an initial stage before the beginning of the scouring and formation of HSVs upstream of the pile which lasted about 20 seconds. This initial stage was the corresponding time for the expansion of the boundary layer over the bed. It is here assumed that the measured scouring experimental data from Roulund are based on the start of the formation of HSVs and the observation of sign of scouring upstream of the pile as it can be derived from Roulund's results. In Figure (4-19), the evolution of the scour hole in terms of the scour depth in front and back of the pile is compared with the experimental and simulation results of Roulund et al. (2005), Stahlmann (2013c) and Gothel (2008). The results of the present work have a very good agreement with the experimental results in terms of predicting the maximum scour hole during evolution. The maximum discrepancy in the prediction of maximum scour hole depth is less than 4.6% during the evolution process, however, the model over-estimates the scour depth at the back of the pile from an early stage of the simulation and the maximum difference happens after 5 minutes of simulation which is around 30%. The accuracy of the simulations was compared in calculating quantitative deviation of the simulation results from the experimental data using RMSE. As a result of the comparison, values of 0.032 and 0.074 was found for the proposed model and Roulund simulation results, respectively.

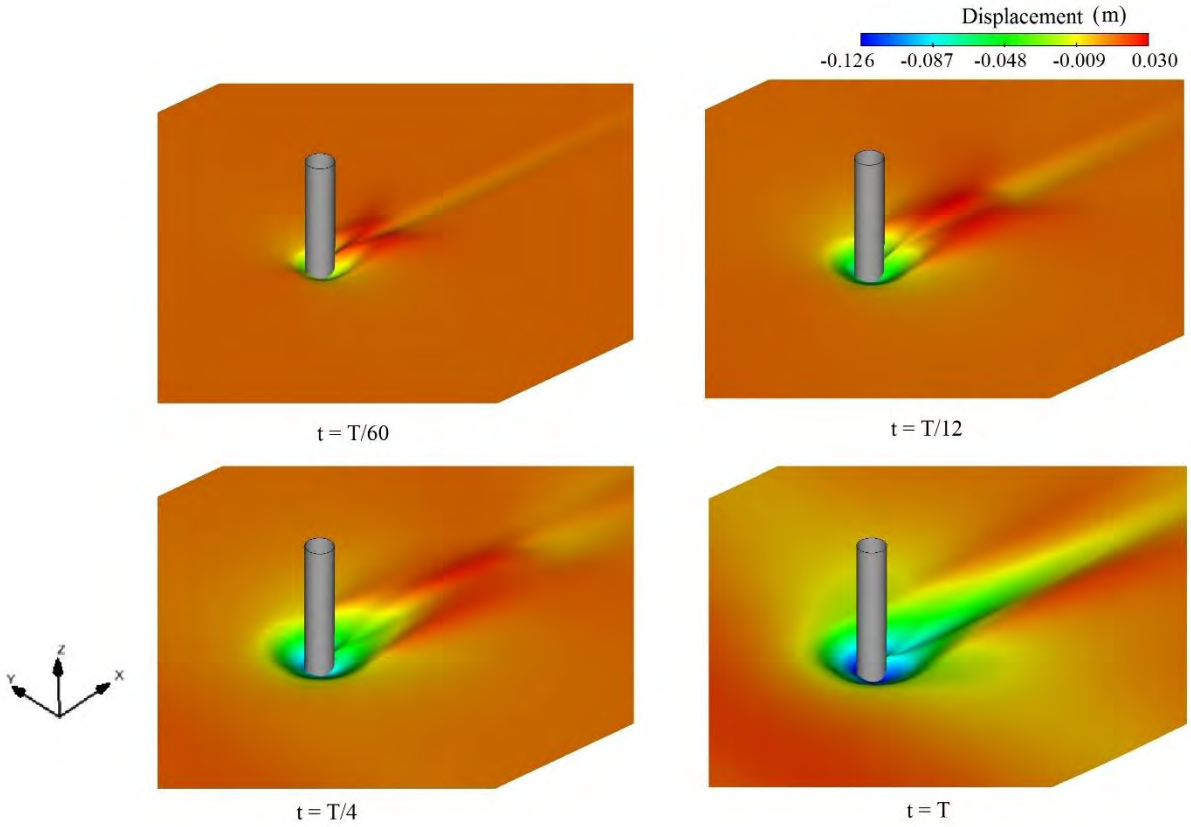


Figure (4-18) Simulated bed displacement at 4 different times of the simulation $t = T/60,\ T/12,\ T/4$ and T.

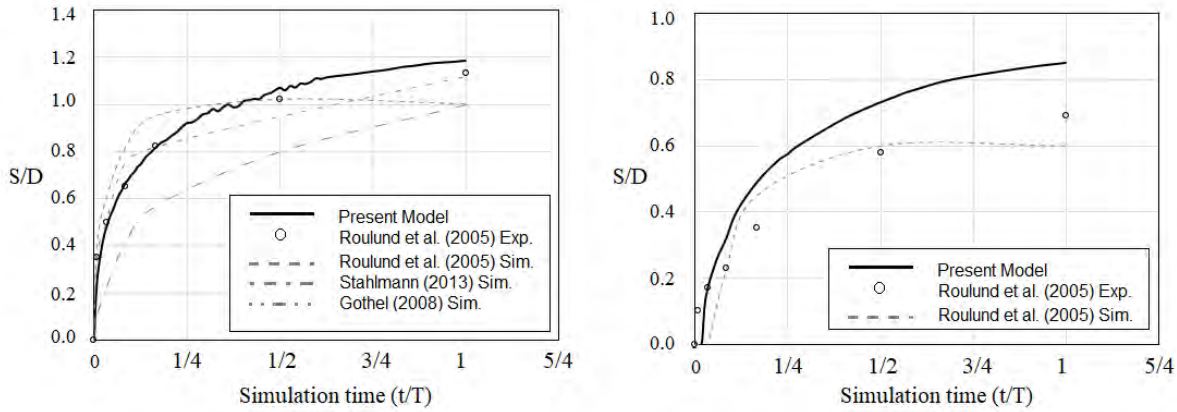


Figure (4-19) Changes in maximum scour depth with time (a) upstream and (b) downstream of the pile.

4.8 TEST CASE 7 & 8: SCOUR AROUND A SQUARE SHAPED PIER WITH DIFFERENT ORIENTATION ANGLE TO THE FLOW IN CLEAR-WATER CONDITION

4.8.1 Experimental details

The formation of HSV upstream of the mounted piles/piers is one of the main factors in the development of the local scour. Khosronejad et al. (2012) mentioned that the intensity of the main HSV is in connection with the bluntness factor (BF) (Eq.(2-82)). Piers with larger bluntness factor face stronger HSVs. To evaluate the robustness of the developed model on the evolution of scour hole around piers with different cross-section shapes, the model was verified against experimental cases from Khosronejad et al. (2012) for square and diamond piers with $BF \to \infty$ and 0, respectively.

The experimental test was conducted in a flume with 10 *m* long and 1.21 *m* wide. In both tests, the piers were mounted at 4 *m* downstream of the flume inlet. Tests were conducted for a pier with edge length of 16.51 *cm* but with different orientation angles (90° and 45°) to the flow. Hence in the case of the square pier, the pier width to the flow direction was 16.51 *cm* and for the diamond pier, 23.35 *cm*. Both tests were carried out under clear-water scour conditions and the bed was covered with sand particles with mean diameter of $d_{50} = 0.85\ mm$, while different flow condition was applied for the tests. For the square pier, the experiment was run for the undisturbed flow with mean average velocity of 0.22 *m/s* and uniform flow depth of 13.9 *cm* and for the case of the diamond pier, 0.21 *m/s* and 15.7 *cm*, respectively.

4.8.2 Numerical details and results

Numerical simulation for both cases was followed in a computational domain with 3 *m* long and 2 *m* wide where the piers were located in 1 *m* downstream of the inlet. The height of the domain was equal to the water depth in each case. A mesh dependence study was also done for

these cases and 3D meshes with around 350,000 cells were chosen. The inlet flow was supplied from a preliminary hydrodynamic simulation which was conducted for a domain with the same condition as the original mesh and with 3 m length. The length was considered 3 m to provide the undisturbed flow with the same condition as the experiment for the numerical model. The other boundaries were treated with similar conditions as the circular pier test case. Bed Nikuradse equivalent sand roughness for this case was equal to $3d_{50}$ as suggested by Khosronejad et al. (2012), and the piers body was considered as hydraulically smooth surface. The critical Shields parameter value for horizontal bed in this test was calculated from equation proposed by Soulsby (1997)(Eq. (2-49)). Both experimental tests were run for one hour.

Figure (4-20) shows the time evolution of scour depth for the first 1 hour of physical modelling for both diamond and square piers. S/w_p is dimensionless scour depth where w_p is the pier width perpendicular to the flow direction. The results from experimental measurements are compared with simulation results from Khosronejad et al. (2012) and the present model. In the case of square pier, the result from the present model outperforms the numerical model of Khosronejad et al. (2012), while both simulation results underestimated the scour progression. The numerical results for diamond pier are roughly similar. In the equilibrium condition for the present model, the differences of 6.7% and 13.1% from the experimental measurements are observed for the square and diamond pier cases, respectively.

Figure (4-21) shows a comparison between the topography of the scoured bed from the simulation and the laboratory measurements from Khosronejad et al. (2012) for the diamond and square piers. The experimental results is only provided for one side of the symmetry plane y=0 in Khosronejad et al. (2012). On the other hand, the present simulation results are almost symmetric with respect to the plane y=0. Hence, for the sake of comparison, in each case, the experimental results are provided in one side and numerical results on the other side of the

symmetry plane. In the square pier case, Khosronejad et al. (2012) as a result of laboratory measurements mentioned that the maximum scour depth happened in the front corners of the pier, while the area with significant depth was observed around the nose of the pier. The present numerical model, as presented in Figure (4-21a), also found the maximum scour depth in the front corners of the pier, however it failed to accurately predict the depth of the scoured area around the front side of the pier. In contrast, the maximum deposition height position given by the numerical model is in accordance with experimental measurements. For the diamond pier, as shown in Figure (4-21b), a good agreement in the position of the maximum scour depth and deposition height is observed between the numerical simulation results and experimental data. The result of simulations was compared in calculating quantitative deviation against the experimental data using RMSE. The calculated RMSE for the proposed model and simulation results of Khosronejad against the experimental data shows the values of 0.022 and 0.084 for square pier and 0.046 and 0.032 for diamond pier, respectively. The obtained results from the simulations indicated that the present model has a good capability in prediction of main characteristics of scour around square-shaped piers.

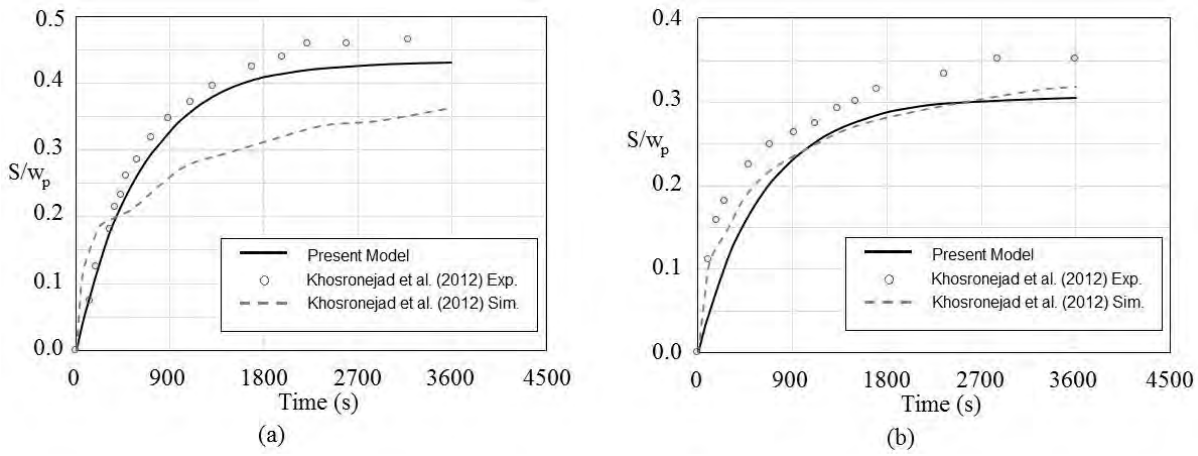


Figure (4-20) Changes in scour depth with time in case of (a) square and (b) diamond pier.

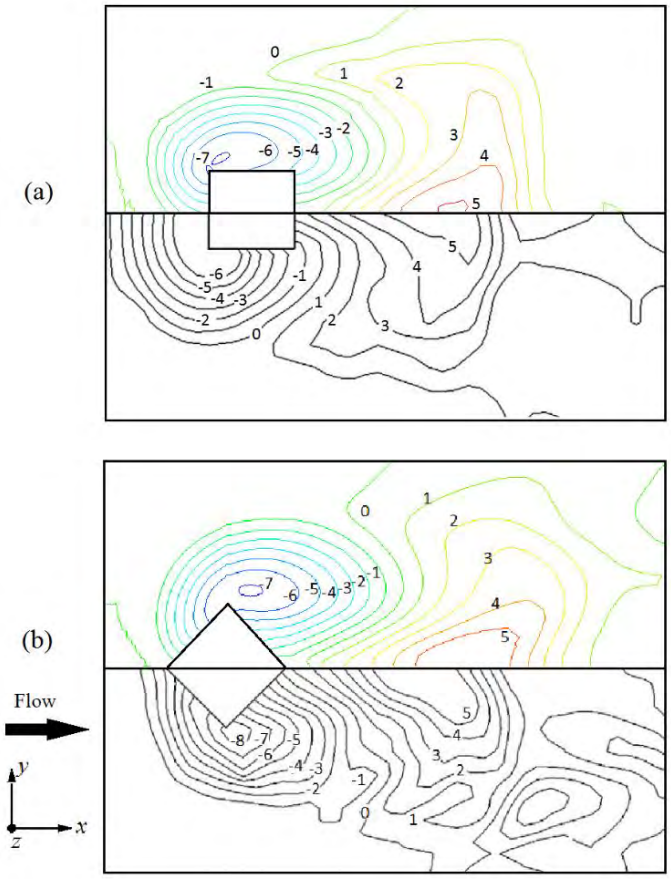


Figure (4-21) Comparison of measured (bottom) and computed (top) bed topography at equilibrium condition for (a) square pier, (b) diamond pier (the measurement unit is centimetre).

4.9 SUMMARY

In this Chapter, eight different 2D and 3D test cases were employed to validate the credibility of the developed hydro- and morphodynamic model. In the first test case, the performance of the employed wall function (Cebeci and Bradshaw, 1977) in the proposed model is compared against the experimental equations for flow velocity profiles over a homogeneous bed. In the second and third test cases, the performance of the hydrodynamic model which solves the unsteady-RANS equations in combination with the *k-ω SST* turbulence model is examined using experimental measurements from Roulund et al. (2005) for the fluid flow field around circular piles mounted on rigid smooth and rough beds. In the fourth test case, the net

entrainment test, an advection-diffusion equation (Eq. (2-71)) is solved along with the hydrodynamic model to simulate the sediment concentration due to suspended-load sediment transport. The simulation results are compared to the experimental results of Rijn (1986).

In the next four test cases, the coupled hydro- and morphodynamic model is used to simulate the deformation of the bed due to sediment transport. In test case five, a 2D case of a submerged horizontal jet is employed and the progression of the bed deformation due to scour is compared with experimental results from Chatterjee et al. (1994). In test case six, a simulation is conducted for the evolution of a 3D scour hole around a circular pile, and results are compared to Roulund et al. (2005) empirical test in live-bed condition. Finally, in the last two test cases, the development of the scour hole around square and diamond piers are simulated for test cases based on experimental tests of Khosronejad et al. (2012) in clear-water flow condition.

The accuracy of the simulations was investigated using RMSE to calculate quantitative deviation of the simulation results from the experimental data in all simulation cases. In all cases good agreement between the experimental data and simulation results were found. The measurement of scour depth in equilibrium condition around vertical piers for the simulations revealed the differences of 4.6%, 6.7% and 13.1% from the experimental measurements for the circular, square, and diamond pier cases, respectively. These results confirmed that the prediction capability of the present model is almost independent of the pier cross-section shapes. Therefore, the model can confidently be applied for prediction of the flow behaviour and scour patterns around piles/piers with different cross-sections or different arrangements of a group of piles in live-bed conditions.

5 FLOW BEHAVIOUR AND SCOUR AROUND SINGLE PIERS WITH DIFFERENT CROSS-SECTION SHAPES

5.1 INTRODUCTION

Cylinders with square and hexagon cross-sections are common pier shapes, however study of scour around them has been rarely done. In this chapter, the flow field and temporal scour development around single piers with square and hexagon cross-section shapes with different orientation angles to the flow in live-bed condition are examined. In each case, the orientation angles are chosen corresponding to minimum and maximum value of BF. Two sets of numerical simulations, on a rigid and mobile bed, were carried out for each case under steady current. The developed numerical model, which had been validated against different test cases, as provided in chapter 4, was applied to simulate scour. The simulations were conducted for the flow and bed conditions similar to that of the Roulund's experimental scour test around a circular pier provided in Table (4-5). First, in section 5.2, the results of numerical investigation around a square-shaped pier with 90° and 45° orientation angles to the flow are presented. Then, in section 5.3, the simulation results of study around a hexagon-shaped pier with 60° and 30° orientation angles to the flow are provided. Finally, in section 5.4, the formation of scour around the single piers with different cross-section shapes are compared in term of maximum scour hole depth and scour progression in time.

5.2 SQUARE-SHAPED PIERS

5.2.1 Generated meshes and boundary conditions

The 3D computational domain and boundaries for the case of a square pier are pictured in Figure (5-1). The domain size and the location of the pier in both square and diamond pier cases were similar to the setup for the modelling of scour around the circular pier presented in Section 4.7. Therefore, computational domains with 2 m width, 3 m length and 0.4 m height where the piers set at 1m downstream of the inlet boundary were considered. A square-shaped pier with a side length of 10 cm with two different orientation angles to the flow 90° (square pier) and 45° (diamond pier) was considered for the simulations. This led to the pier width to the flow direction of 10.0, and 14.1 cm for the square and diamond pier cases, respectively. The boundaries were satisfied with conditions similar to that used in the numerical simulation of scour around the circular pile in Section 4.7. Therefore, the top boundary was simulated with slip boundary conditions. The symmetry boundary condition was considered at the sides of the computational domain for all quantities. The bed boundary was considered as a sandy bed with a roughness factor of $k_s = 0.55\ mm$. The inlet boundary was supplied with the velocity profile obtained from the curve fitting of the provided profile in Figure (4-17). The outlet was treated with zero values for the gradient of all quantities except for the pressure, which was equal to zero at the outlet boundary.

Meshes with around 400,000 grids were chosen for both square and diamond piers. Besides, in both cases, the normal resolution of the first layer of cells nearest to the bed was determined equal to 2 mm. This value was chosen to assure that the centre of the first layer of meshes closest to the bed was placed in the log-layer region of the boundary layer, while concurrently it satisfied the requirements of the reference level height from the bed. The top view of a part of

the generated meshes in *XY* plane for the square and diamond piers are displayed in Figure (5-2). The meshes were generated in ANSYS ICEM CFD. It is to be noted that the similar computational domains were used for both sets of tests on rigid and mobile beds.

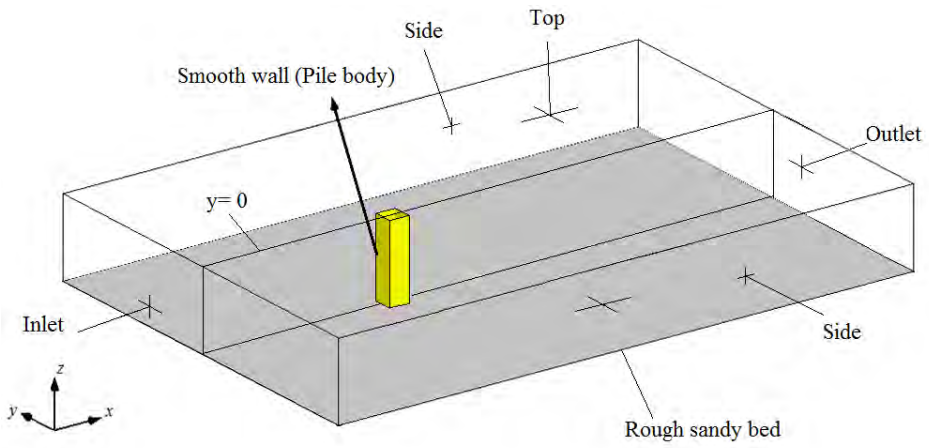


Figure (5-1) 3D view of the computational domain and boundaries for the square pier.

5.2.2 Numerical modelling on a rigid bed

To study the flow behaviour in the vicinity of the piers, the hydrodynamic model was solved for both square and diamond piers mounted on a rigid flat sandy bed. In each case, models were run for 70 s, while they reached fully developed flow after around first 40 s of the simulation. Figure (5-3) illustrates the top view of the formation of HSV and lee-wake shed vortices upstream and downstream of the piers in unsteady-RANS simulations using the iso-surfaces technique for the Q-criterion concept (Hunt et al., 1988) for $Q = 1(1/s^2)$ at T=70 s. It is noticed that the separated flow starts to form on the front and side corners of the square and diamond piers, respectively, which results in the production of the reverse-vortex flows and quasi-periodic vortex shedding downstream of the piers. It is also observed that the behaviour of the HSVs upstream of the piers is almost independent of the quasi-periodic motion of the

shed vortices, while the elongated part of the HSVs downstream of the piers can be affected by the shed vortices.

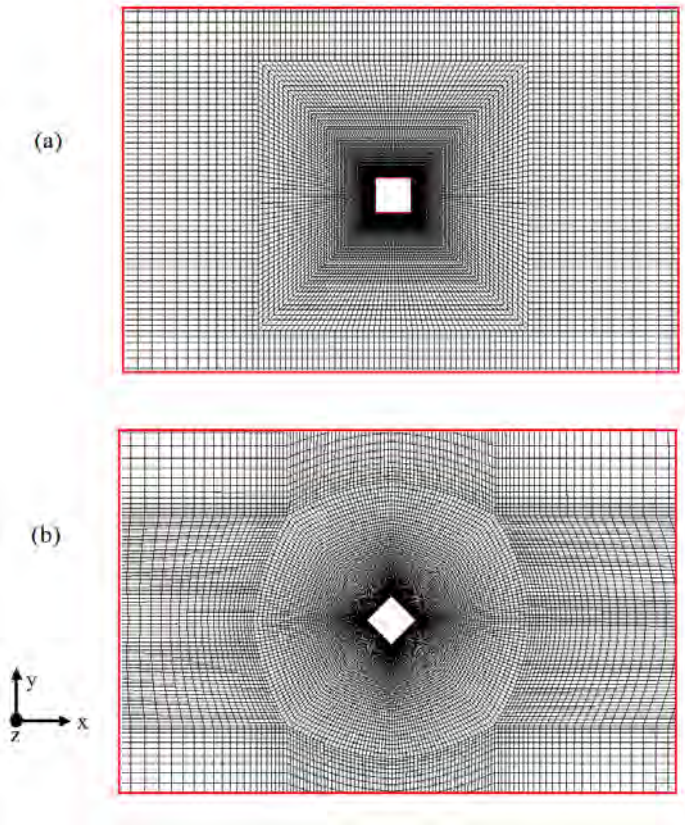


Figure (5-2) Top view of the generated meshes for (a) square and (b) diamond piers.

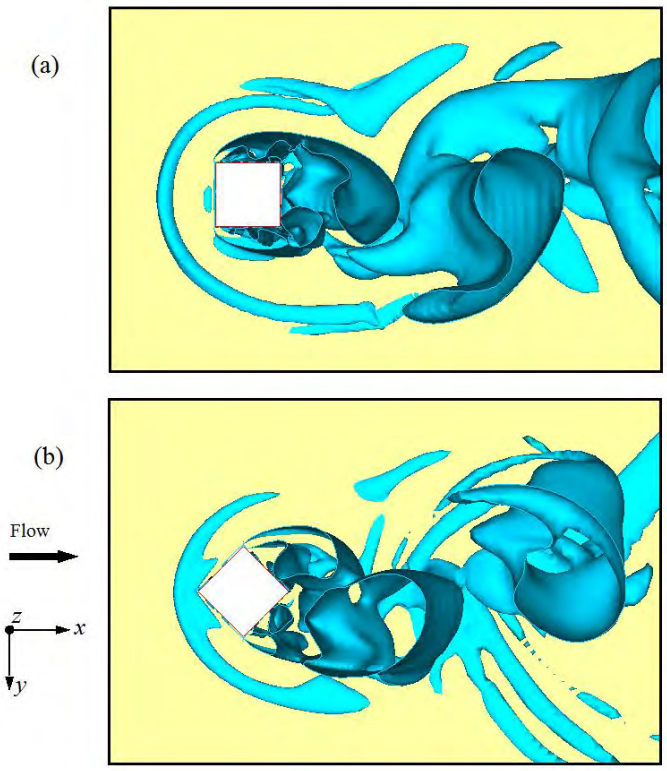


Figure (5-3) Turbulence structures around (a) square and (b) diamond piers using the Q-criterion concept at time T=70 s.

Figure (5-4) shows the contours of mean flow velocity and its components in x and y directions for both square and diamond piers at plane z= 0.2 m. The mean flow velocity fields were calculated from the time-averaged values of the velocities from t=50 to 70 s. It is seen that changes in the cross-section shape and the orientation angle of the piers lead to the change in the adjacent flow field. The mean velocity is symmetric with respect to plane y=0 in all cases. The results indicate that in both cases, the flow velocity increases in the sides of the piers as a result of local flow acceleration. The low-velocity areas are observed at upstream and downstream sides of the piers which are due to the formation of high- and low-pressure areas, respectively.

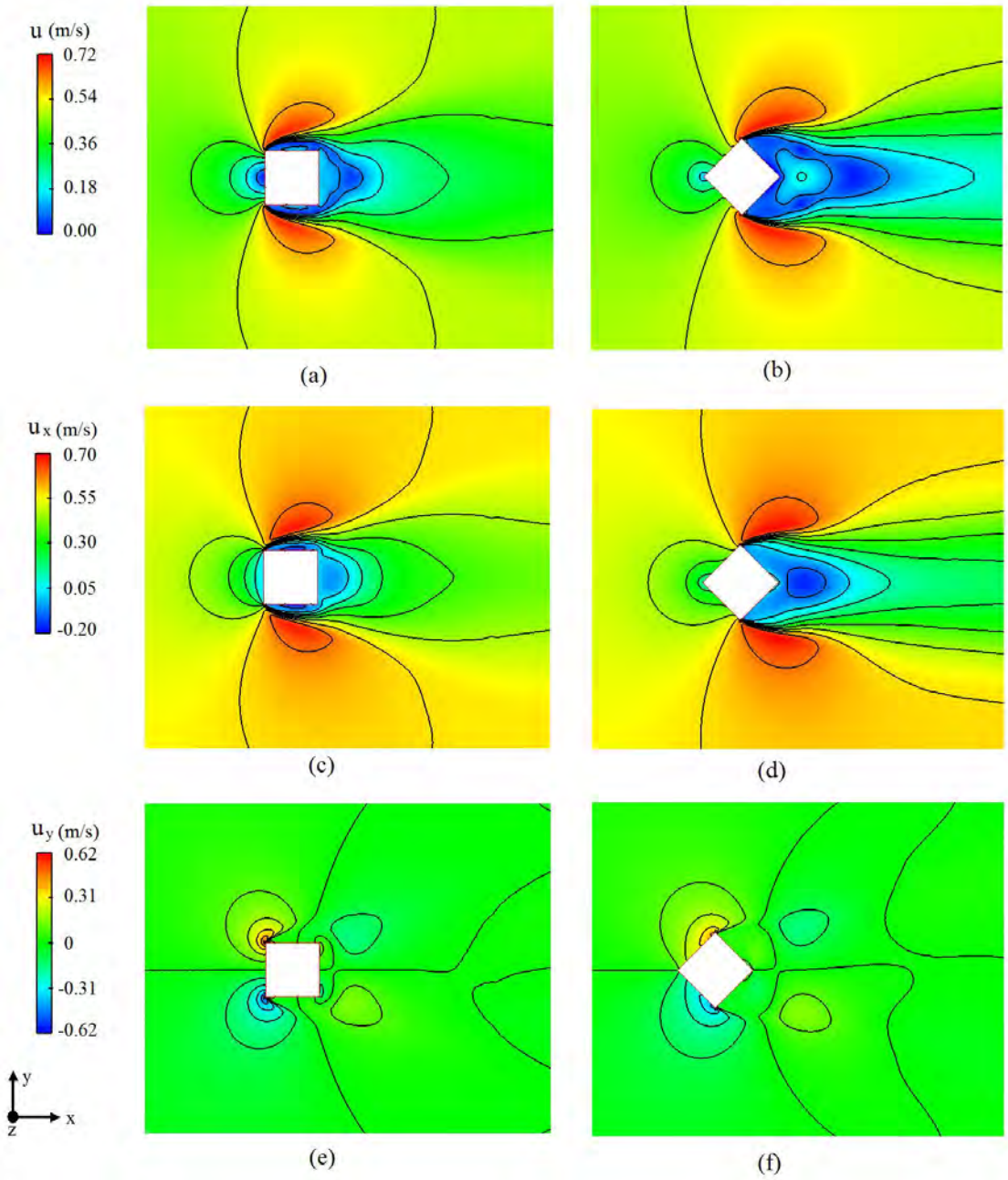


Figure (5-4) (a, b) Mean flow velocity and its component in (c, d) x-direction and (e, f) y-direction at plane z= 0.2 m around the square and diamond piers.

Presence of the pier generates Kármán vortex street at downstream which impacts local scour progression adjacent to pier. Therefore, study the strength of these turbulent structures is beneficial in better understanding of the scour hole formation. As mentioned in section 2.4.2,

Sumer et al. (1993) proposed that the strength of the nascent shed vortices downstream of the piers exposed to steady current flow can be approximated by the following equation:

$$\frac{\Gamma}{w_p U_\infty} = \frac{1}{4}\left(\frac{U_0}{U_\infty}\right)^2 \frac{1}{St} \tag{5-1}$$

which is similar to Eq. (2-81) where Γ is the strength of the shed vortices and $\Gamma/w_p U_\infty$ is the normalized vortex strength where U_∞ is the undisturbed flow velocity and U_0 is the potential flow velocity. For the diamond pier, the potential flow velocity is measured at the top of the pier boundary layer and at the point of separation, while for the case of the square pier, it is calculated at the top of the shear layer spreading from the separation point (Sumer et al., 1993; Inamuro et al., 1993). Here, the same approach is applied to calculate the potential flow velocity in the case of square and diamond piers. St in Eq. (5-1) is the Strouhal number which is defined by:

$$St = \frac{f w_p}{U_\infty} \tag{5-2}$$

The frequency of vortex shedding is calculated using the frequency of the dimensionless lift force coefficient which is obtained by:

$$C_L = \frac{F_L}{\frac{1}{2}\rho U^2 A_{Ref}} \tag{5-3}$$

where F_L is the lift force acting on the pier body, and A_{Ref} is the area of the pier corresponding to the width of the pier. Figure (5-5) depicts the calculated C_L for both square and diamond piers in time. Due to the stochastic nature of the turbulent flow in the near-wake region, some amplitude and frequency modulations might be anticipated for the calculation of C_L (Konstantinidis and Liang, 2011). Accordingly, the Fast Fourier Transform (FFT) technique is

performed over C_L sampled data and a frequency of vortex shedding f of 0.58 and 0.61 $1/s$ is calculated for square and diamond piers, respectively.

The ratio of U_0/U_∞ is found to be 1.436 and 1.376 for the square and diamond piers. In result, the value of Γ/DU_∞ is calculated 4.09 and 2.53 using Eq. (5-1), respectively. The results show that shed vortices are stronger in the square pier than that of the diamond pier, which is in agreement with experimental measurements from Sumer et al. (1993) which found values of 3.6 and 2.15 for investigated square and diamond piers, respectively.

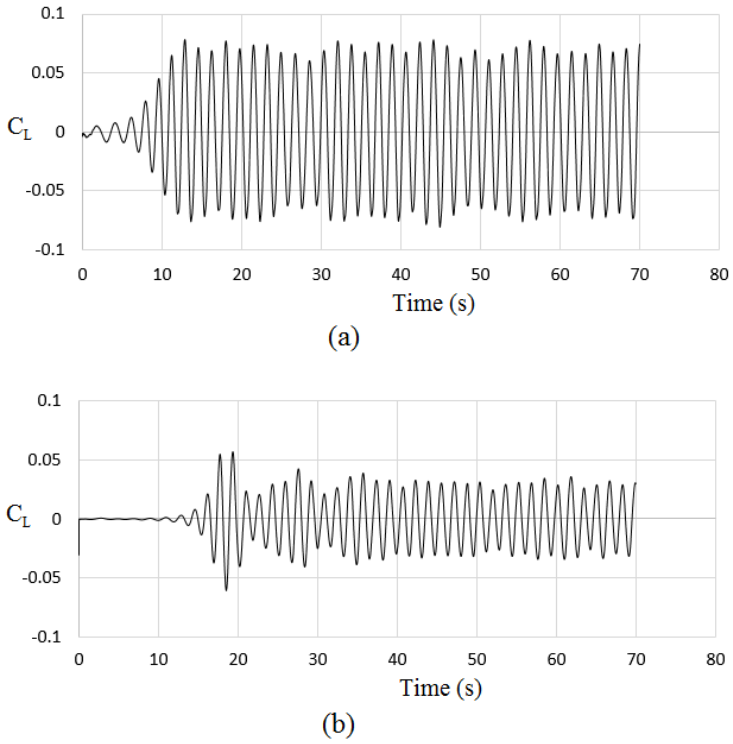


Figure (5-5) Variations of the lift force coefficient for (a) square and (b) diamond piers.

Figure (5-6) illustrates the traced streamlines over the mean flow fields at plane y=0 upstream of the piers. Due to the impact of the square pier nose, a strong down-flow is formed upstream of the pier. The down-flow impinges the bed and produces a HSV system. As shown in Figure (5-6a), formation of two HSVs is predicted upstream of the square pier which includes one

main vortex rotating in the clockwise direction and one smaller vortex rotating in the counter-clockwise direction and very close to the pier body. In the case of the diamond pier, very weak down-flow is observed upstream of the pier nose. In summary, the predicted HSV system comprises of only one small vortex upstream of the pier which is in contrast to the square pier.

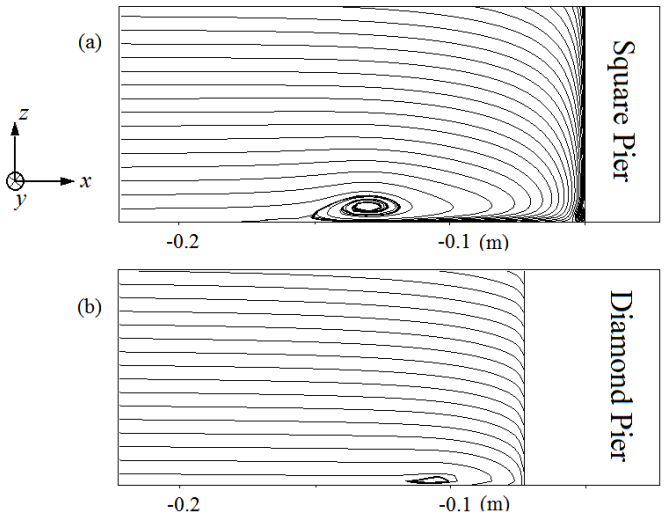


Figure (5-6) Formation of HSVs upstream of (a) square pier and (b) diamond pier.

The obtained bed shear stress from the flow field results serves as the primary input to the sediment transport models. Hence, a precise calculation of the bed shear stress is essential to achieving realistic sediment transport simulations. The results of the distribution of the absolute value of bed shear stress amplification (BSSA) as defined in Eq. (4-3) for the case of square and diamond piers is depicted in Figure (5-7). It is noticed that the presence of the square pier leads to a considerably stronger BSSA field upstream and around the pier, in comparison to the diamond pier, which reveals the formation of strong adverse pressure gradient and HSV in case of the square pier. These may result in stronger and faster scour development around the square pier.

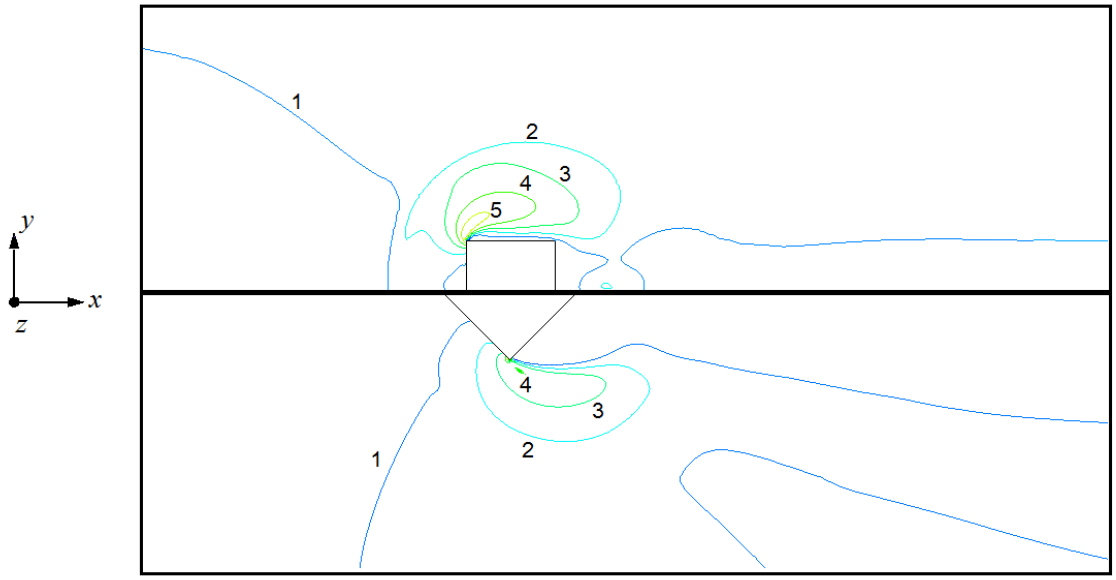


Figure (5-7) Distribution of the absolute value of $BSSA$ on the bed around the square (top) and diamond (bottom) pier.

5.2.3 Numerical modelling on a mobile bed

The coupled hydro- and morphodynamic model was employed to study local scour. In these set of simulations, the bottom boundary of the domains was set as a mobile bed. The models were run for T= 1 hr of physical time of the scouring process similar to that for the circular pile test case and it was assumed that the quasi-equilibrium condition is obtained for all cases within this time. Figure (5-8) shows the topography of the scoured bed at times $t = 30, 120, 900, 3600$ s from the start of the simulations for both square and diamond piers. In both cases, it was observed that scouring started from the early stages of the simulation and extended in terms of the maximum depth and the affected area. In both cases, the maximum scour depth happened on the sides of the piers. As expected, stronger scouring occurred around the square pier, corresponding to the remarkably stronger HSV and lee-wake vortices, while for the diamond pier, scouring was more likely due to the local acceleration of flow velocity and lee-wake vortices. Observing the morphology of the bed over time shows that some asymmetry may arise

downstream of the piers. This dissimilarity which is in accordance with the nature of scouring can be explained with the stochastic nature of quasi-periodic lee-wake vortices along with the nature of sand sliding.

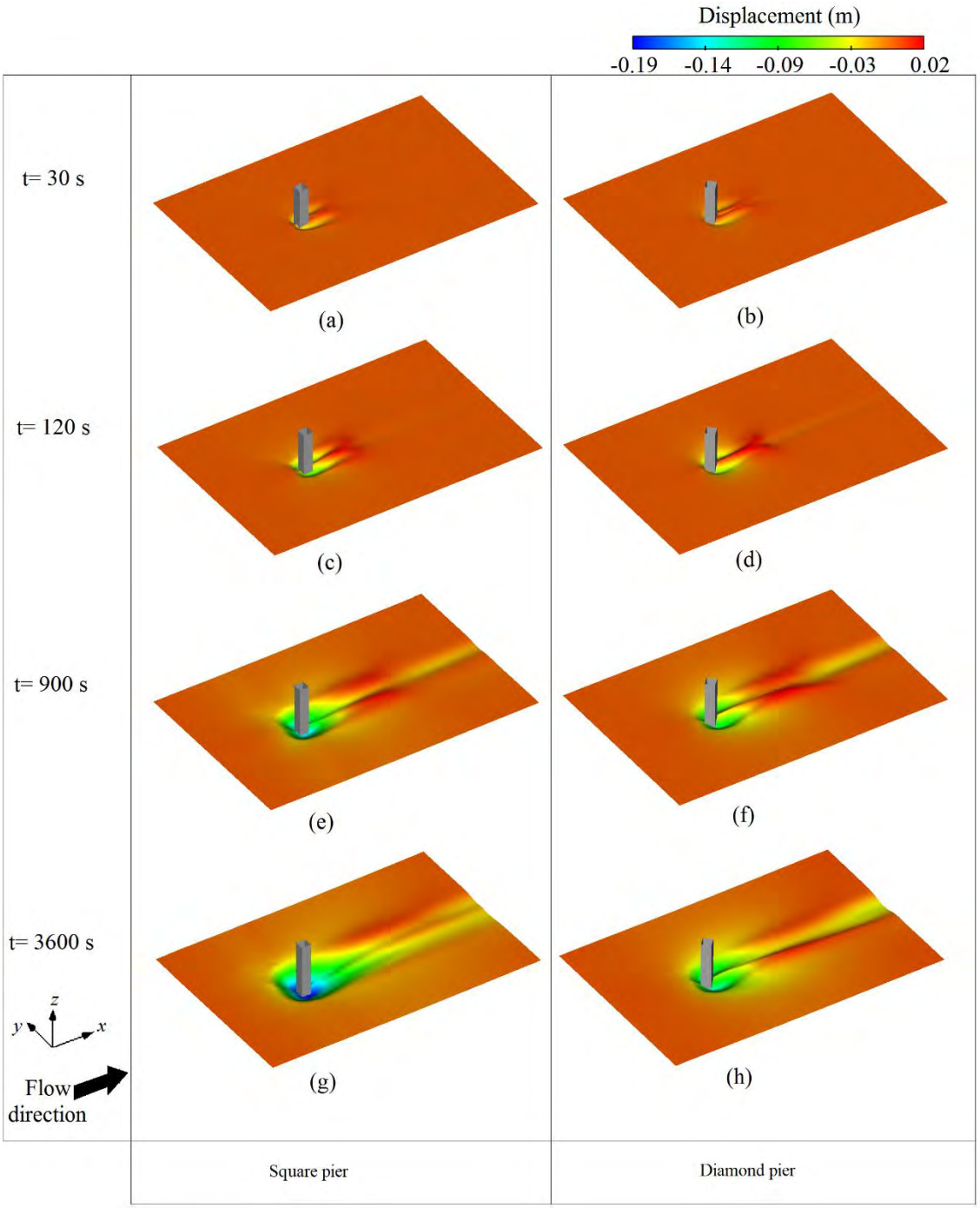


Figure (5-8) Bed deformation at 4 different times of the simulation t =30, 120, 900, 3600 s for the square and diamond piers.

Figure (5-9) illustrates the flow field at plane y=0 upstream and downstream of the piers in the quasi-equilibrium scour depth condition. The instantaneous flow velocity vector field is used to visualize the development of the HSV upstream of the piers. The presence of the square pier produced a strong adverse pressure gradient upstream of the pier and led to the formation of HSV which was spread over the entire scour hole upstream of the pier. On the other hand, in case of the diamond pier, the formed HSV was small and feeble with low impact on the progression of scouring.

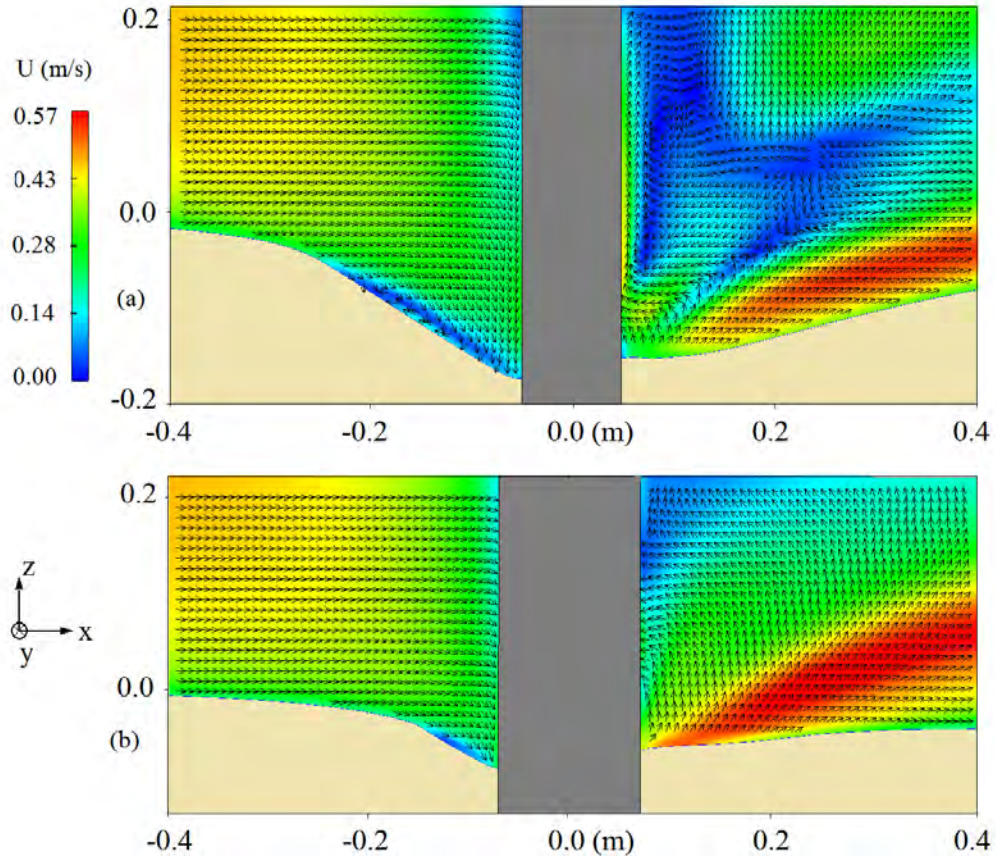


Figure (5-9) Instantaneous flow velocity vector field in symmetry plane (y=0) for (a) the square and (b) diamond piers.

To have a better understanding of the morphology of the deformed bed in quasi-equilibrium condition, the corresponding contour of bed displacement around the circular, square and diamond pier is displayed in Figure (5-10). It is observed that for the square pier, the area with

maximum scour depth is wrapped around the entire front side of the pier, while in case of the diamond pier this area is attached to the side corners, and in case of the circular pier, it occurred in a radial angle around 70° from the head. Furthermore, it is also noticed that in case of the square pier the affected area by scouring is larger than the two others as a result of a deeper scour hole.

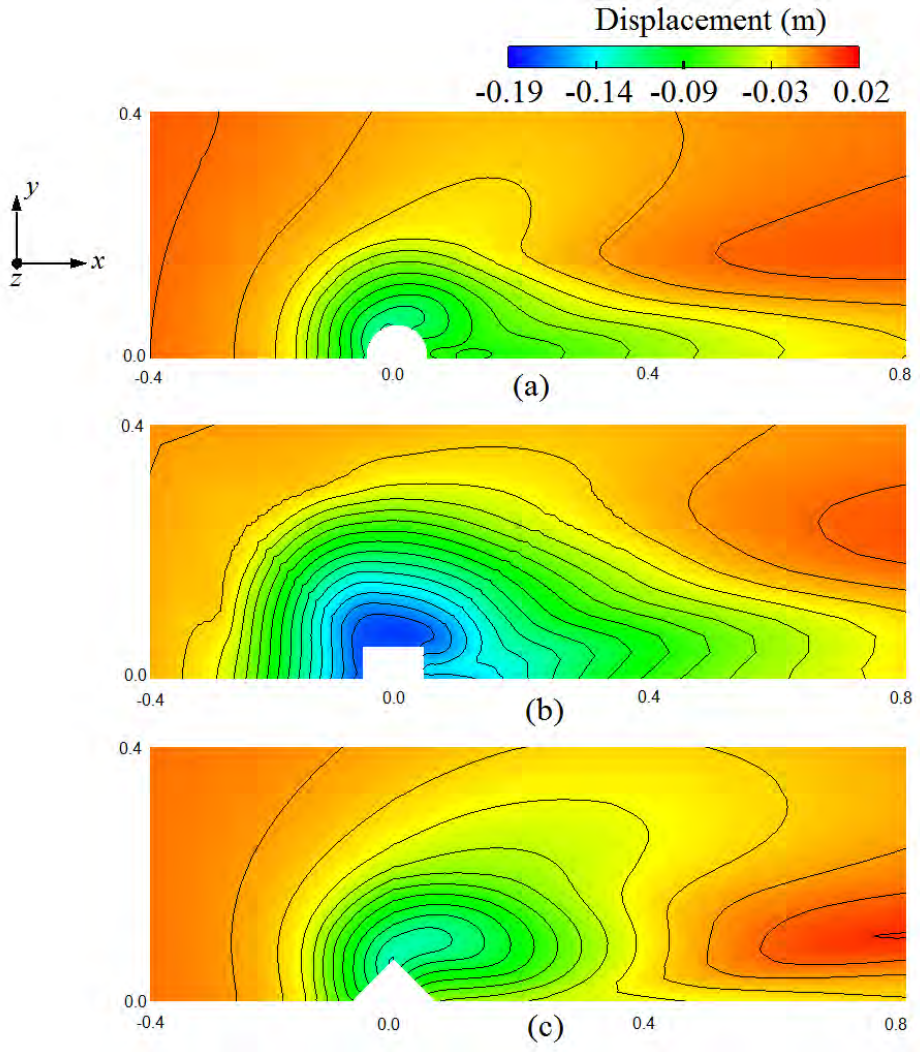


Figure (5-10) bed displacement contour around the (a) circular, (b) square and (c) diamond pier.

5.3 HEXAGON-SHAPED PIERS

In this section, a study of scour around hexagon-shaped piers, similar to the study for the square-shaped piers in section 5.2, is conducted. A regular hexagon-shaped pier with a side length of 5.77 cm and two different orientation angles to the flow of 30° and 60° was considered for the investigation of flow field and scour simulations. Accordingly, the pier's width to the flow direction was 10, and 11.54 cm for the piers with 30° and 60° orientation angles, respectively.

5.3.1 Generated meshes and boundary conditions

The size of the domains and the location of the piers were similar to the setup for the modelling of scour around the circular pier in Section 4.7. Therefore, computational domains with 2 *m* width, 3 *m* length and 0.4 *m* height where the piers sat at 1*m* downstream of the inlet boundary were considered. The boundaries were treated with conditions similar to the ones used for the study of scouring around the circular pier. Meshes with around 400,000 grids were chosen. Similar computational domains were considered for both sets of tests on rigid and mobile beds. The top view of part of the generated meshes in the *XY* plane for regular hexagon piers is displayed in Figure (5-11). The meshes were generated in ANSYS ICEM CFD.

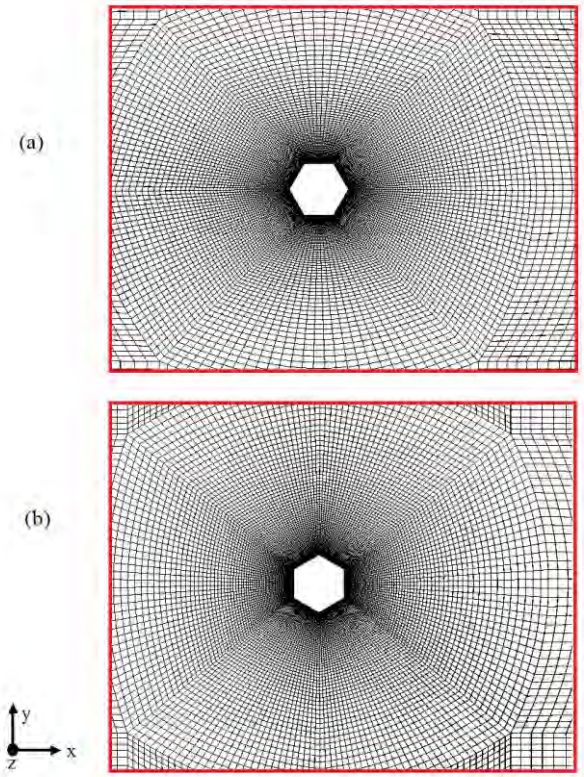


Figure (5-11) Top view of the generated meshes for regular hexagon pier with (a) 30° and (b) 60° orientation angles to the flow.

5.3.2 Numerical modelling on a rigid bed

To study the flow field in the vicinity of the piers, the hydrodynamic simulations were carried out for mounted hexagon piers on a rigid flat sandy bed. In each case, the simulation was run for 70 s, while the simulation reached fully developed flow after around first 30 s of the simulation. Figure (5-12) illustrates the top view of the formation of HSV and lee-wake shed vortices upstream and downstream of the piers in unsteady-RANS simulations using the iso-surfaces technique for the Q-criterion concept for $Q = 1(1/s^2)$ at T=70 s. It is observed that the separated flow started to form on the side corners of the piers, which produced the reverse-vortex flows and Kármán vortex street downstream of the piers. It is also noted that the attributes of HSVs wrapped upstream of the piers are almost independent of the quasi-periodic

motion of the shed vortices, while the elongated part of the HSVs downstream of the piers can be affected by the shed vortices.

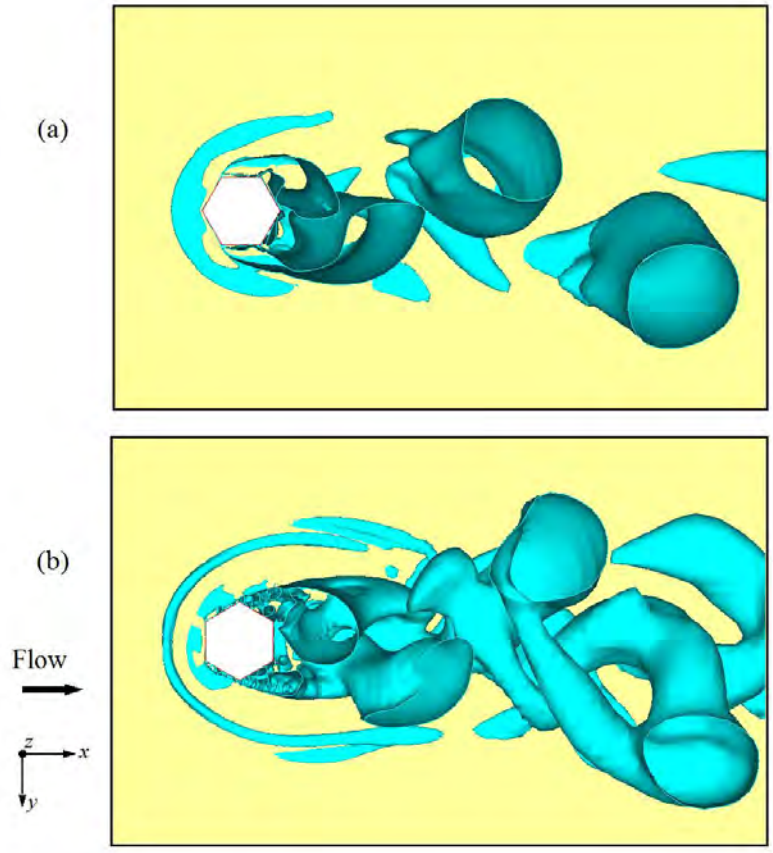


Figure (5-12) Turbulence structures around a hexagon pier with (a) 30° and (b) 60° orientation angles to the flow using the Q-criterion concept at time T=70 s.

Figure (5-13) shows the contours of mean flow velocity and its components in x and y directions for the hexagon piers with different orientation angles to the flow in plane z= 0.2 m. The mean flow velocity fields were calculated from the time-averaged values of the velocities from t=50 to 70 s. The mean flow velocity is symmetric with respect to plane y=0 in all cases. The results indicate that in both cases, the flow velocity increases in the sides of the piers as a result of local flow acceleration. The low-velocity areas are observed at upstream and downstream sides of the piers which are due to the formation of high- and low-pressure areas,

respectively. It is also found that changes in the cross-section shape and the orientation angle of the piers lead to the change in flow field adjacent to them.

Figure (5-14) illustrates the results of the distribution of the absolute value of the bed shear stress amplification (BSSA). The presence of the hexagon pier with 60° orientation angle to the flow leads to a considerably stronger BSSA field upstream and around the pier in comparison to the hexagon pier with 30° orientation angle to the flow, which may result in stronger and faster scour development around it. The formation of the robust BSSA field upstream of the pier with 60° orientation angle reveals the formation of stronger adverse pressure gradient and HSV in comparison to the pier with 30° orientation angle.

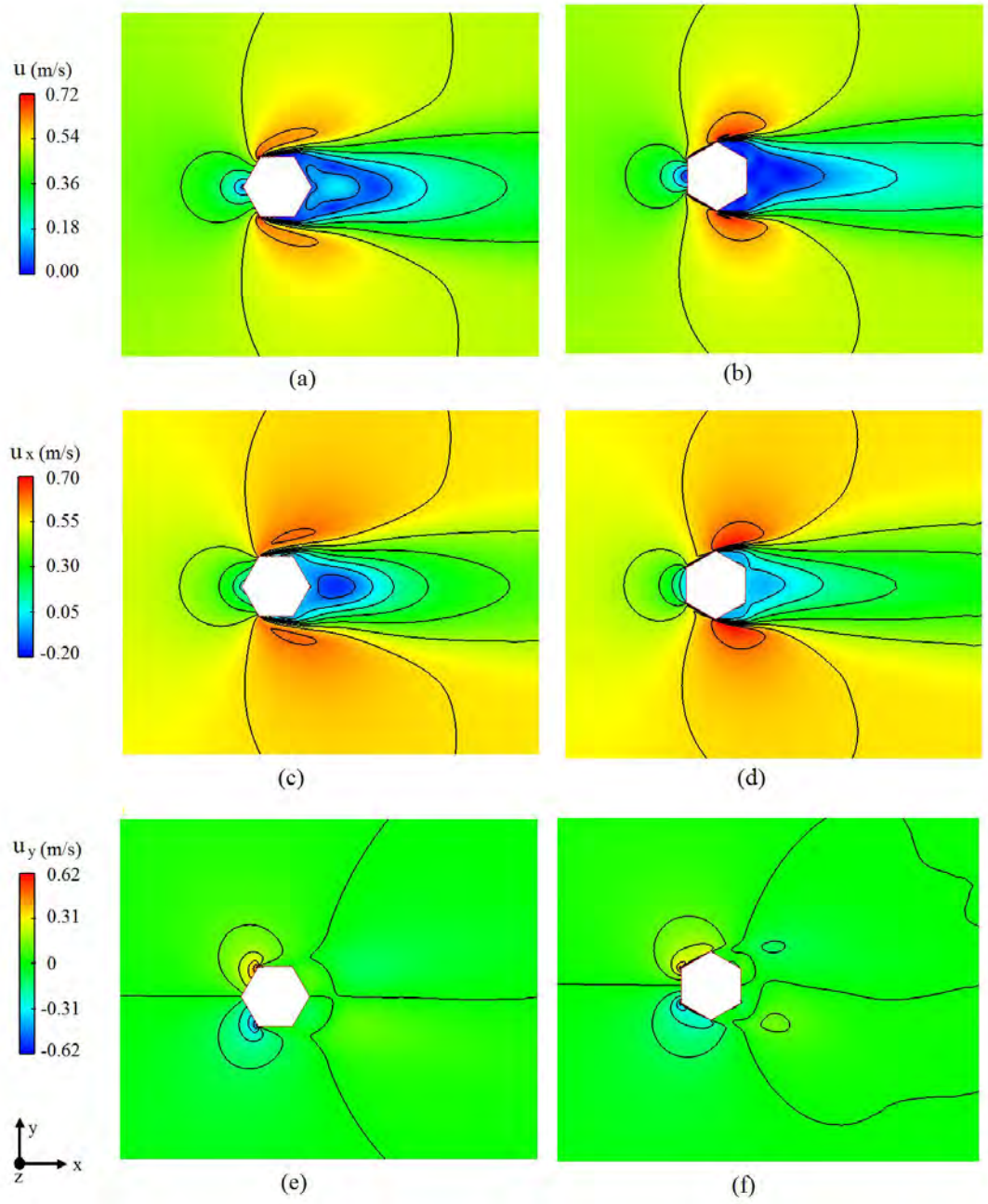


Figure (5-13) (a, b) Mean flow velocity and its component in (c, d) x-direction and (e, f) y-direction at plane z= 0.2 m around the hexagon pier with different orientation angles.

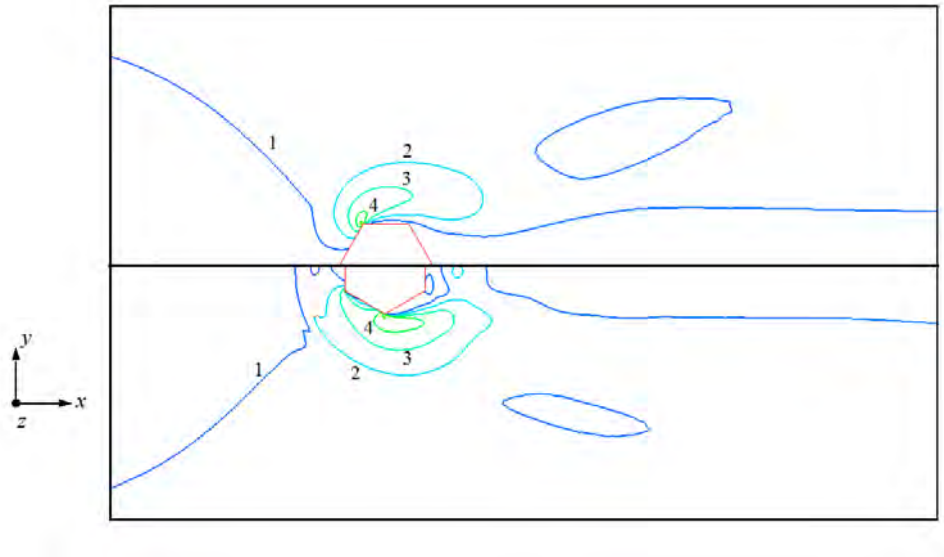


Figure (5-14) Distribution of the absolute value of $BSSA$ on the bed around the hexagon pier with (Top) 30° and (Bottom) 60° orientation angles to the flow.

5.3.3 Numerical modelling on a mobile bed

In this section, the local scour progression around the hexagon pier with different orientation angles on the mobile bed is investigated by using the coupled hydro- and morphodynamic model. Similar to the previous cases for square-shaped piers described in section 5.2.3, the models were run for T= 1 hr of physical time of the scouring process. Figure (5-15) shows the bed morphology changes at times $t = 30, 120, 900, 3600$ s from the start of the simulations for the piers. In both cases, the maximum scour depth happened on the sides of the piers. The simulations reveal a formation of deeper scour hole around the hexagon pier with 60° orientation angle to the flow in compare with that of the hexagon pier with 30° orientation angle after 1 hr of physical time. Some asymmetries can be observed around the piers which is in accordance with the nature of scouring due to the stochastic nature of quasi-periodic lee-wake vortices along with the nature of sand sliding.

Figure (5-16) illustrates the instantaneous flow field at plane y=0 upstream and downstream of the hexagon pier with different orientation angles to the flow in the quasi-equilibrium scour depth condition. The instantaneous flow velocity vector field is used to visualize the development of the HSV upstream of the piers. The presence of the hexagon pier with 60° orientation angle to the flow produced a strong adverse pressure gradient upstream of the pier and led to the formation of HSV. On the other hand, in the case of the hexagon pier with 30° orientation angle to the flow, the formed HSV was weak with low impact on the scour development.

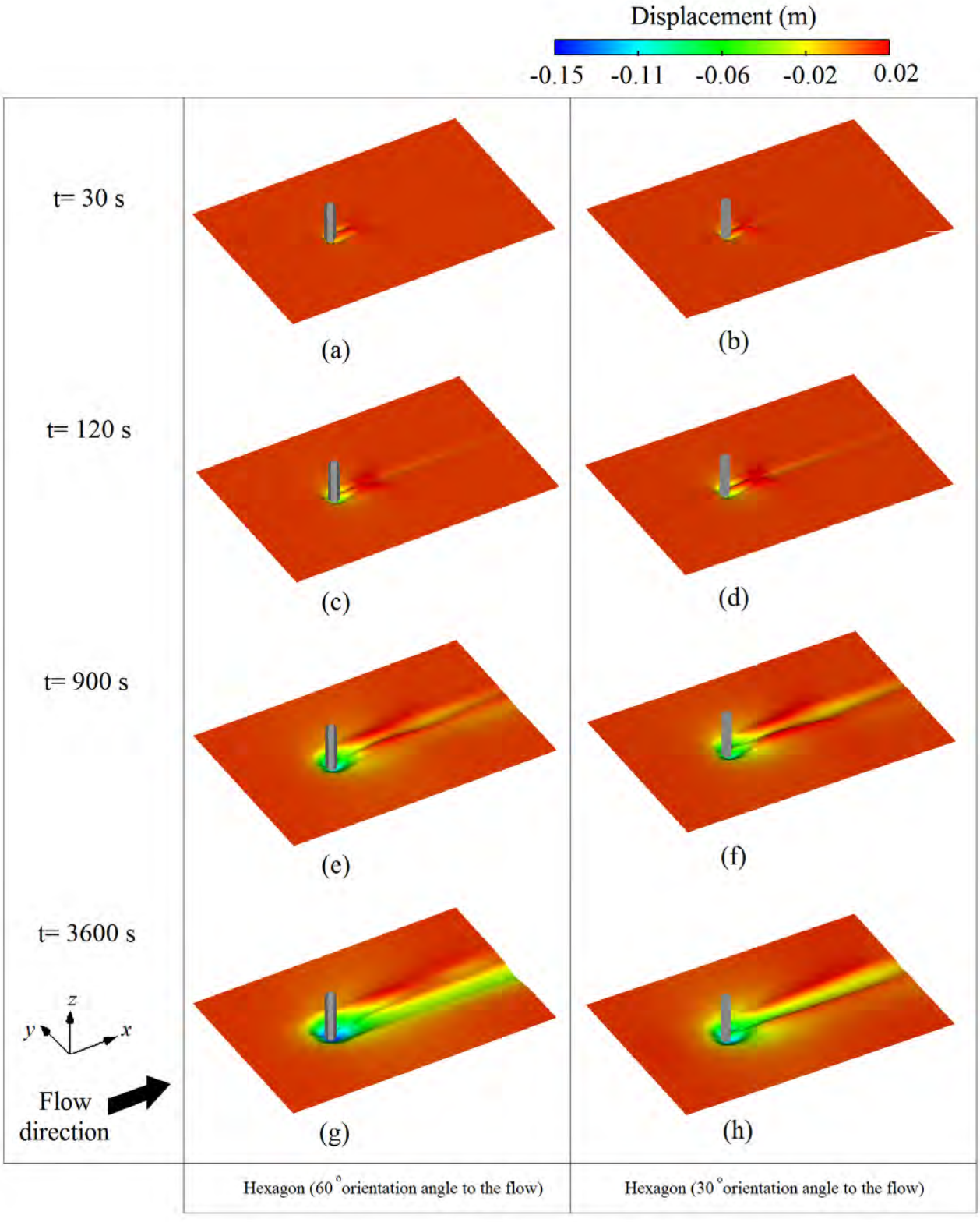


Figure (5-15) Bed deformation at 4 different times of the simulation t =30, 120, 900, 3600 s for the hexagon pier with different orientation angles.

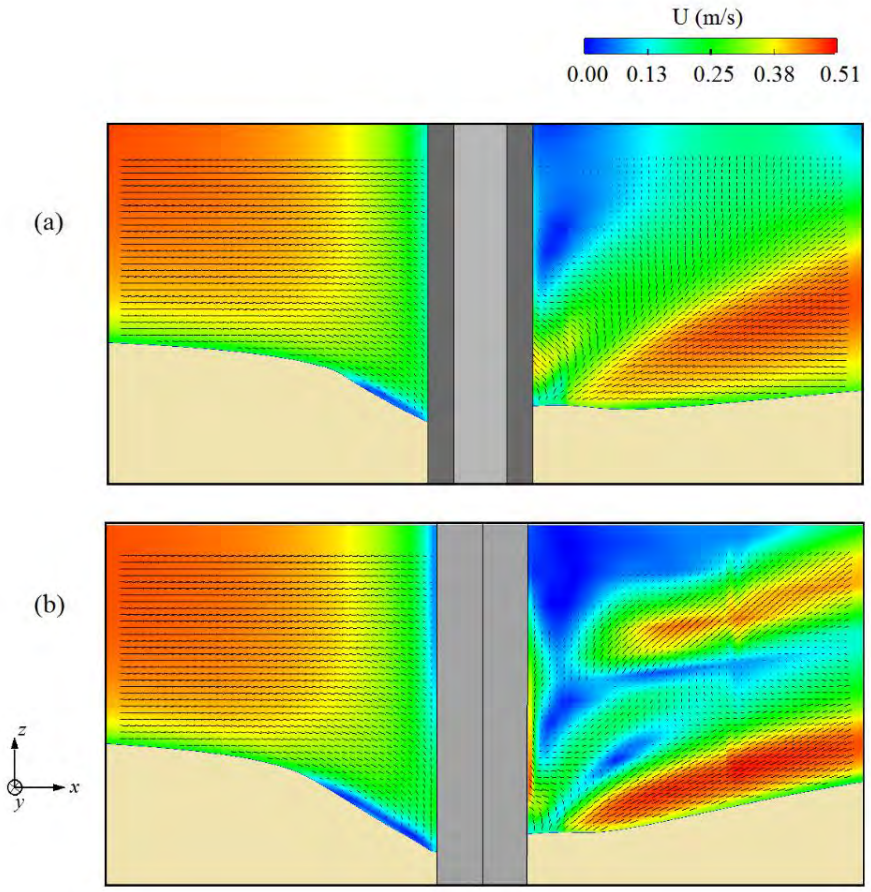


Figure (5-16) Flow velocity vector field in symmetry plane (y=0) for the hexagon pier with (a) 30° and (b) 60° orientation angles to the flow.

Figure (5-17) displays the bed displacements in the quasi-equilibrium condition for hexagon-shaped piers. In both cases, the maximum scour depth occurred on the sides of the piers. A deeper scour hole is observed for the hexagon pier with 60° orientation angle to the flow. The simulation results of the bed displacements in case of the hexagon pier with 30° orientation angle to the flow shows almost symmetry results with respect to plane y=0, however, some dissimilarity can be noticed in the pier with 60° orientation angle to the flow. This asymmetry can be addressed by referring to the nature of the applied sand sliding procedure.

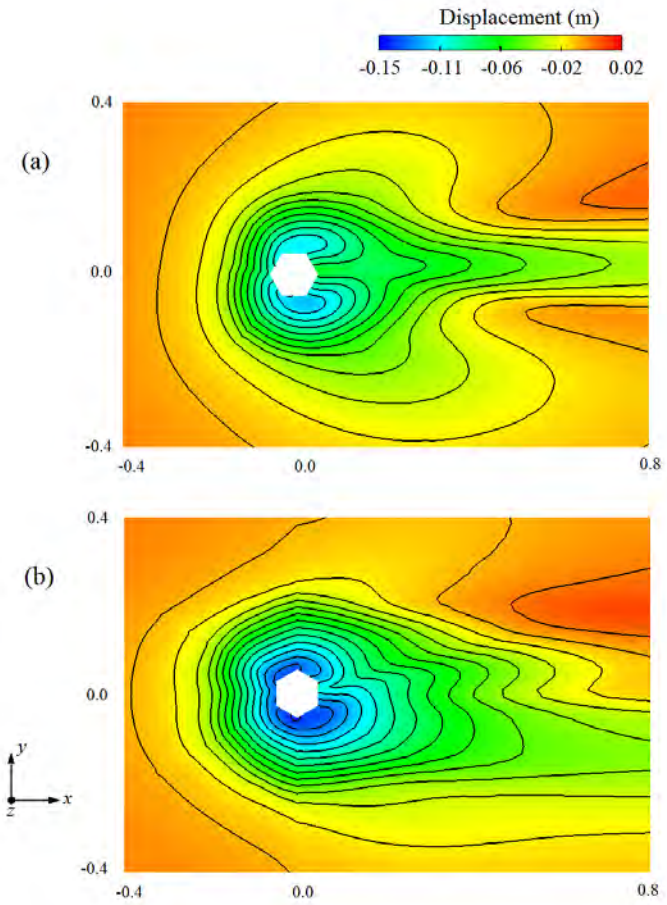


Figure (5-17) Bed displacement contour in quasi-equilibrium condition for hexagon pier with (a) 30° and (b) 60° orientation angles to the flow.

5.4 TEMPORAL DEVELOPMENT OF SCOUR AROUND SINGLE PIERS

In this section, the development of scour from simulation results for the square-shaped, hexagon-shaped and circular piers are compared in terms of a normalized local scour depth S/w_p in time. This improves understanding of the impact of change in the piers' cross-section shape on scour depth in time. The simulations were carried out for the first one hour of scouring for all cases. Figure (5-18) displays the changes in scour hole depth in time for piers with different cross-section shapes with different orientation angles. It is observed that in all cases the evolution process is progressed with rather similar speed. The rate of increase in scour depth

reduces in time for all cases. It is discovered that the rate of increase in the scour depth around the square pier is faster than all other piers which led to a deeper scour hole after one hour of scouring with S/w_p=1.94, while the rate of increase in scour depth around the diamond pier was lowest with S/w_p=1 in quasi-equilibrium condition. It is also found that for the hexagon-shaped piers the development of normalized scour depths were S/w_p=1.29 and 1.18 in quasi-equilibrium condition for 60° and 30° orientation angles to the flow, respectively.

The results reveal the impacts of the piers orientation angle to the flow on normalized equilibrium scour depth. The normalized scour depth in quasi-equilibrium condition for the square pier is almost twice (1.94) of that for the diamond pier. This effect diminishes with an increase in the number of sides of the piers cross-section, since this ratio in case of the hexagon-shaped pier for 60° and 30° orientation angles to the flow is 1.09. On the other hand, from the results, it can be inferred that with an increase in the number of sides of the pier's cross-section, the resultant normalized scour depth in equilibrium condition tends to get closer to that of the circular pier. The different piers specifications and equilibrium scour depths as a result of simulations are provided in Table (5-1).

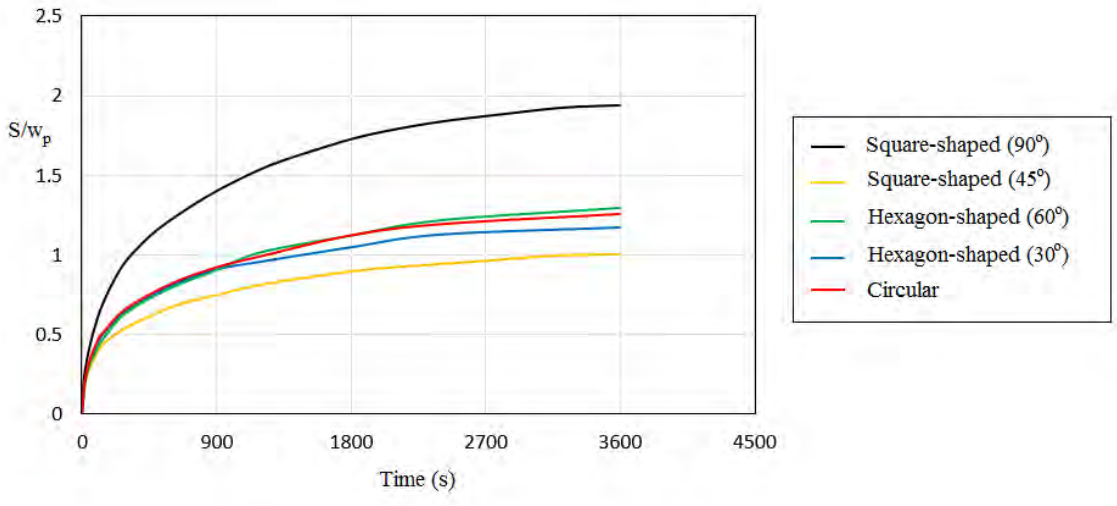


Figure (5-18) Changes in scour depth in time for square-shaped, hexagon-shaped and circular piers.

Table (5-1) Piers specifications and equilibrium scour depth.

Pier	pier width to the flow direction w_p (cm)	Maximum scour depth S (cm)	Normalized scour depth S/w_p (dimensionless)
Square (90°)	10	19.4	1.94
Square (45°)	14.2	14.2	1.00
Hexagon (30°)	10	11.8	1.18
Hexagon (60°)	11.54	14.9	1.29
Circular	10	12.5	1.25

5.5 SUMMARY

Flow behaviour and scour development around single piers with different cross-section shapes were investigated. A square-shaped pier with 90° and 45° orientation angles to the flow and a hexagon-shaped pier with 60° and 30° orientation angles to the flow were studied. Similar flow and bed material condition was assumed for all simulations. It was found that the maximum and minimum normalized quasi-equilibrium scour depth occur for the square-shaped piers with 90° and 45° orientation angles to the flow. It was also realized that with increase in the number of sides of the pier's cross-section the impact of change in orientation angle to the flow on normalized scour depth decreases.

6 FLOW BEHAVIOUR AND SCOUR AROUND A GROUP OF TWO IDENTICAL SIDE-BY-SIDE CIRCULAR PILES

6.1 INTRODUCTION

Substituting a porous structure containing an array of piles for a single pile can offer advantages in terms of scour reduction. For this purpose, as mentioned in sections 2.4 and section 2.5, investigation of scouring around a group of piles with different arrangements, pile numbers and spacing ratios have been carried out in different studies (e.g. Ataie-Ashtiani and Beheshti, 2006; Kim et al., 2014; ; Zhang et al., 2017; Qi et al., 2019). In this chapter, two sets of numerical simulations on a rigid and mobile beds are conducted for a group of two side-by-side circular piles with different spacing ratios G/D= 1, 2 and 3 under steady current and live-bed condition, where G represents the distance between the piles. These spacing ratios are chosen based on the literature, as for larger spacing ratios the pile group effects are assumed to be negligible (in the present study, it is assumed that the pile group effects are completely negligible for $G/D \geq 5$). To the author's best knowledge, this is the first numerical study of pile groups in live-bed condition. Similar to chapter 5, the tests are conducted with the flow and bed condition resembling to that of Roulund's empirical scour test. In section 6.2, the generated meshes and dimensions of the computational domains are discussed. In section 6.3, the first set of tests are run for the group of piles mounted on a rough rigid bed to examine the flow behaviour and bed shear stress around the side-by-side piles arrangements with different spacing ratios. In section 6.4, the tests are carried on for a sandy mobile bed to investigate the evolution of scour around pile groups. The evolution of scour in time and scour patterns for different arrangements of the piles are discussed.

6.2 GENERATED MESHES AND BOUNDARY CONDITIONS

The 3D computational domains and boundaries for the case of two side-by-side piles used for both rigid and mobile bed simulations are presented in Figure (6-1a). Figure (6-1b) shows the dimensions of the computational domain in XY plane, where the height of the domain is equal to the water depth in the z- direction. As shown, the computational domain width varies with the changes in the spacing ratio to diminish the effects of side boundaries on the simulations. Therefore, the distance of the piles from the side boundaries were kept constant and equal to 9.5D. The boundary conditions were quantified with the values defined for the numerical simulation of Roulund's scour test. The generated meshes included around 600,000 grids where the thickness of the first layer of mesh closest to the bed is 2 *mm*.

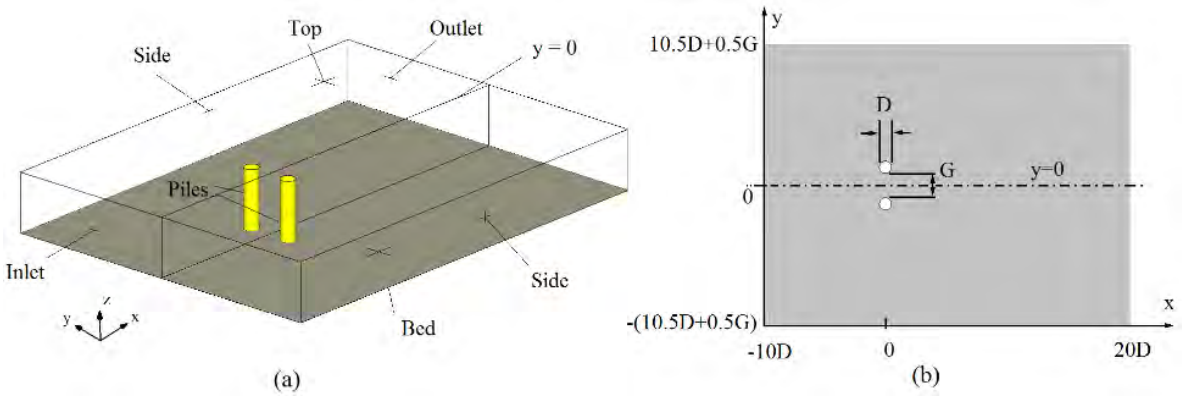


Figure (6-1) (a) 3D view of the computational domain and boundaries and (b) top view for a group of two side-by-side piles.

The generated meshes for the bed around the mounted piles for different spacing ratios are displayed in Figure (6-2). The meshes were generated in ANSYS ICEM CFD. In the present modelling, unsteady-RANS equations were applied which are capable of simulation of the periodic motion of lee-wake vortices downstream of the piles. The lee-wake vortices frequency downstream of the piles may occur with phase difference for each of the piles in the group of

two side-by-side piles. Therefore, in this case, simulations are conducted with presence of the two side-by-side piles.

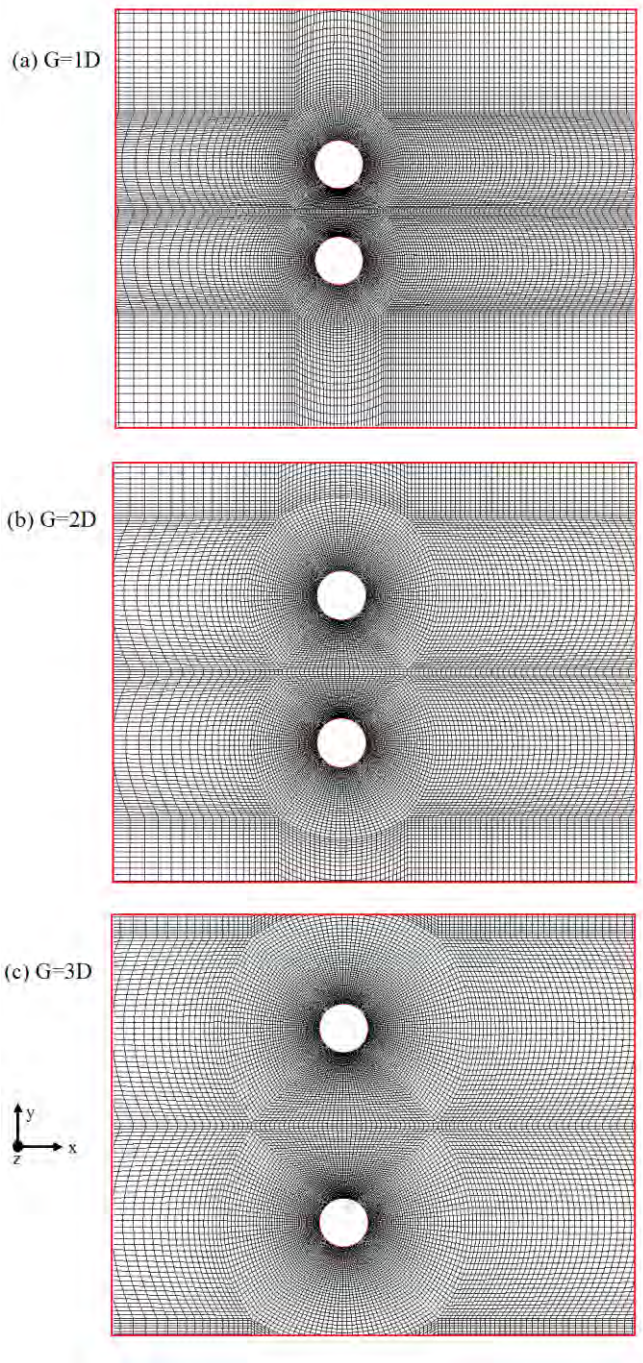


Figure (6-2) The generated meshes for the bed boundary of the computational domains for (a) G=1D, (b) G=2D, (c) G=3D.

6.3 NUMERICAL MODELLING ON A RIGID BED

The modelling on a rigid bed was considered for three different spacing ratios between the piles G/D= 1, 2 and 3. The simulations were conducted for 100 seconds and the fully developed flow was obtained after the first t= 50 s of the simulations. To compare the local flow field, the contours of mean flow velocity at x= 0 plane is provided for the pile groups with different spacing ratios in Figure (6-3a-c) and a single pile in Figure (6-3d). The mean flow velocity fields were calculated from the time-averaged values of the velocities from t=70 to 100 s. It is illustrated that the flow velocity adjacent to the piles in both inner and outer areas depend on the G/D ratio. A decrease in spacing ratio increases the flow velocity around the piles while contracting the streamlines. On the other hand, with an increase in the spacing ratio, the effect of pile group mitigates, as for G/D= 3 the effect of the pile group in the flow field is small.

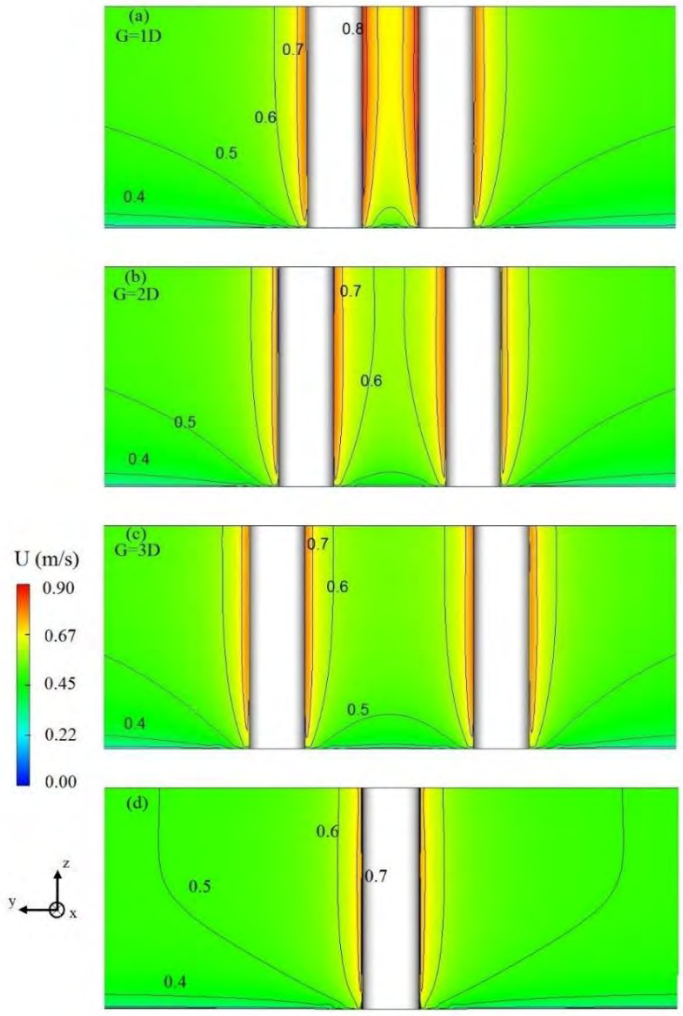


Figure (6-3) Mean flow field adjacent to two side-by-side piles with (a) G=1D, (b) G=2D, (c) G=3D and (d) a single pile in plane x=0.

The behaviour of the flow between the two piles is similar to a jet flow. This behaviour is intensified by a decrease in the spacing between the piles. The contours of mean flow velocity on the plane y=0 and z=20 cm for different spacing ratios between the piles are shown in Figure (6-4) and Figure (6-5). In Figure (6-4), the dash-dotted lines show the approximate location of the piles on both sides of the plane y=0. It is observed that in the case of $G= 1D$, the highest velocity of the jet-like flow occurs in the area between the piles while it is leaning downstream. An area of stagnation can also be found downstream of the piles and very close to the bed.

Moving downstream from the piles both of these effects quickly disappear. An increase in the spacing ratio between the piles e.g. G= $2D$ and $3D$, decreases these effects on the flow. Figure (6-5) shows that the mean flow velocity is almost symmetric with respect to plane y=0 between the piles. The differences are negligible and can be due to the inaccuracy of the simulations. The top view of the jet flow and its changes with G/D ratio can be seen.

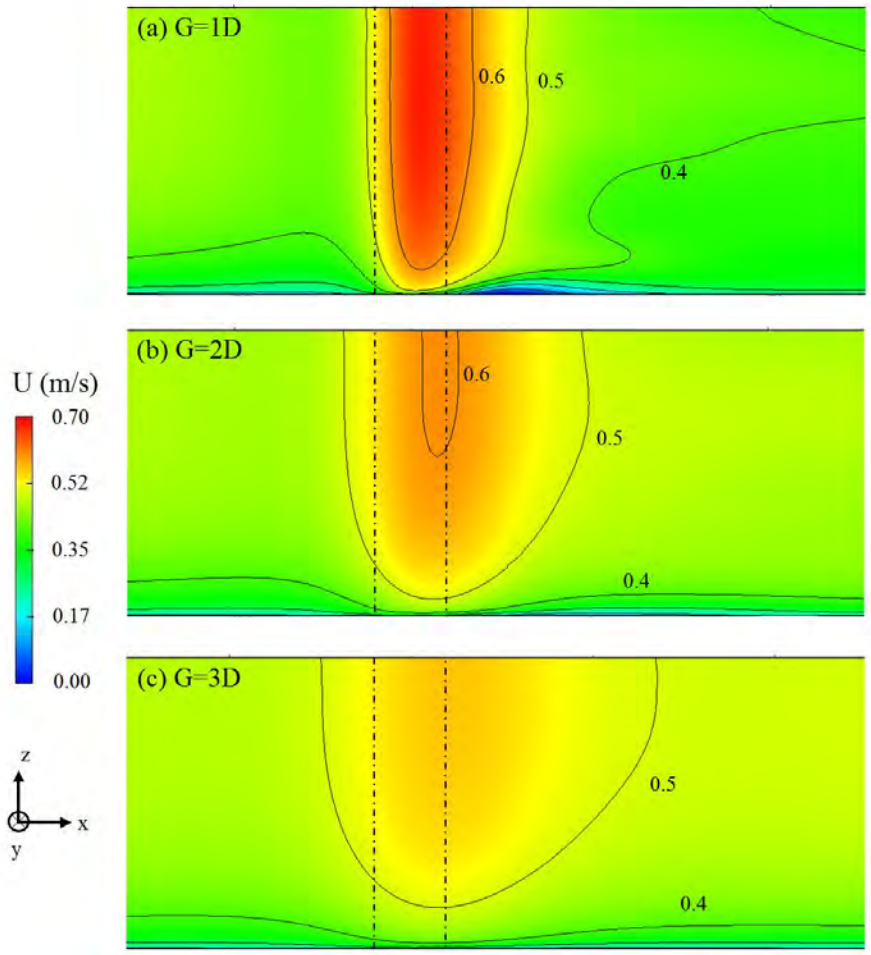


Figure (6-4) Mean flow velocity in plane y=0 for different spacing ratios between the piles with (a) G=1D, (b) G=2D, and (c) G=3D.

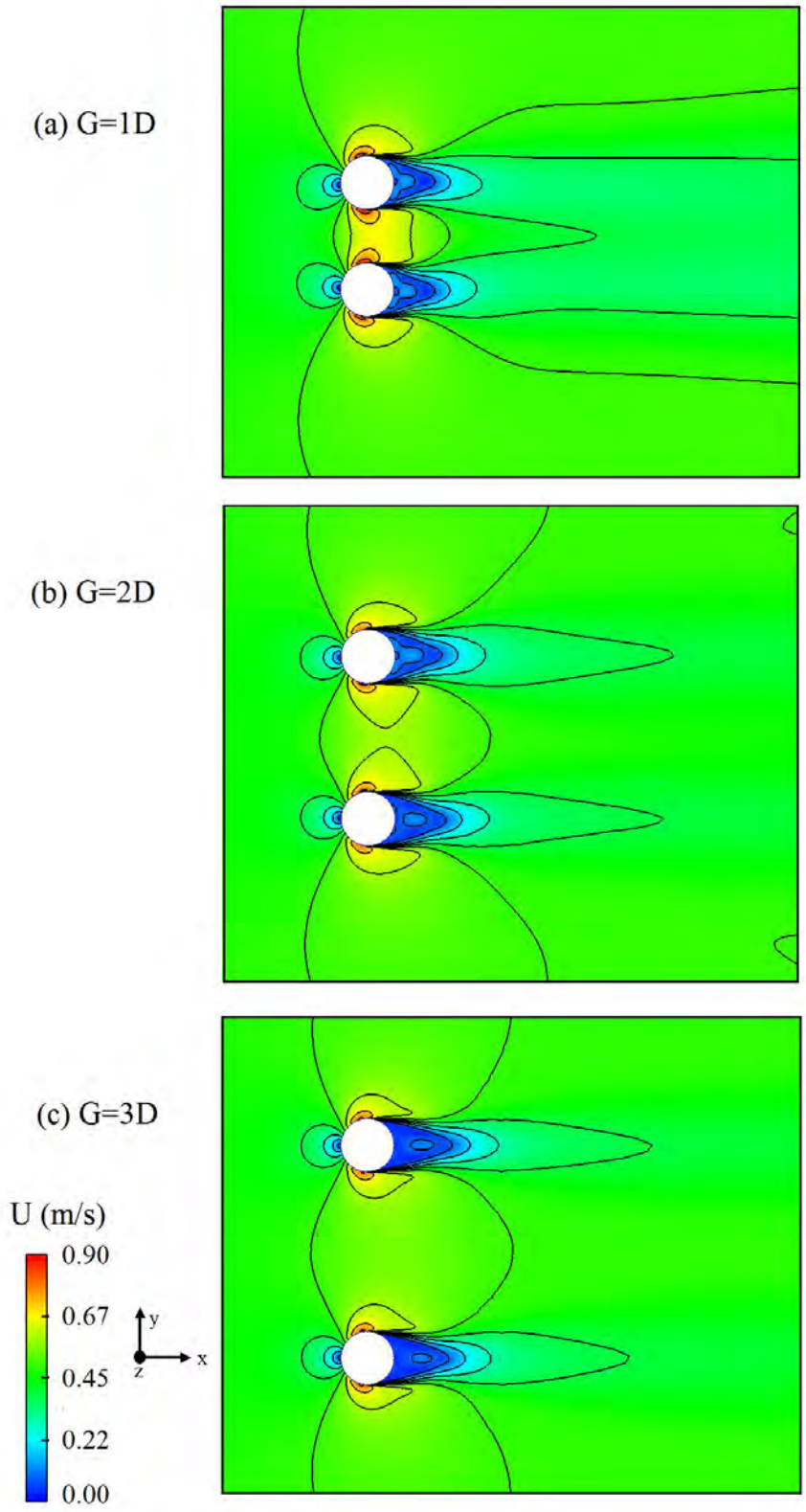


Figure (6-5) Mean flow velocity in plane z= 20 cm for different spacing ratios between the piles with (a) G=1D, (b) G=2D, and (c) G=3D.

Figure (6-6) shows the traced streamlines from lines at z=0.5 cm and z=10 cm above the bed upstream of the piles. For streamlines traced from z=0.5 cm, the formation of the HSVs can be seen from the whirling streamlines upstream of the piles in all pile group arrangements. For the case of the pile group with G= 1D, the contraction of streamlines is combined with the whirling motions due to the HSVs in the inner area between the piles. This effect vanishes with an increase in spacing between the piles. It is also observed that the streamlines traced at z=0.5 cm cannot reach the area adjacent to the piles. This behaviour occurs due to the downflow upstream of the piles. The traced streamlines from z=10 cm have almost no interaction with the formation of HSVs. however, in this case, the contraction of the streamlines is more distinctive in the case of G= 1D in comparison to that of the larger spacing ratios e.g. G= 2D and 3D.

The Formation of turbulent structures e.g. horseshoe and lee-wake vortices are demonstrated by applying the Q-criterion concept around the pile groups as defined in Eq. (4-1). Figure (6-7) presents the top view of the Q iso-surfaces for Q= 0.1 $1/s^2$ at t =100 s indicating the formation of the turbulent structures upstream and downstream of the piles. As shown, in the case of the pile group with G= 1D, turbulent structures from both piles are mixed and formed a highly turbulent area in between and downstream of the piles. For the case of G= 1D, the formation of lee-wake vortices downstream of the piles shows a roughly symmetric pattern for both piles with respect to plane y=0. On the other hand, with an increase in the spacing between the piles, as presented for the case of pile group with G= 3D, the HSVs upstream and lee-wake vortices downstream of the piles separately formed for each pile. The phase difference on the frequencies of the lee-wake vortices downstream of the piles can be observed by variation in the spacing ratios.

The results of the distribution of the absolute value of $BSSA$, defined in Eq. (4-3), for different arrangements of two side-by-side piles are displayed in Figure (6-8). The results reveal that a

decrease in the value of G/D significantly raises the magnitude of the bed shear stress in the inner area between the piles which may lead to a deeper scour hole there in the case of sandy mobile bed. The maximum $BSSA$ for all cases occurs in the inner area between the piles with the values of 6.13, 5.47 and 5.37 for the spacing ratios of G/D=1, 2 and 3, respectively. It is also seen that for the case of G/D=1, the maximum time-averaged bed shear stress for the inner and outer sides of each pile occurs at different radial angles. Observation shows that this angle for the inner and outer areas are around 70° and 80° from the head of the piles, respectively. With an increase in the spacing ratio, the maximum $BSSA$ tends to occur in a symmetric manner in the sides of each piles. Observation of the stagnation area upstream of the piles reveals that with the smaller spacing ratio the area is tilted into the inner region between the piles, while this effect gradually vanishes with an increase in the spacing ratio.

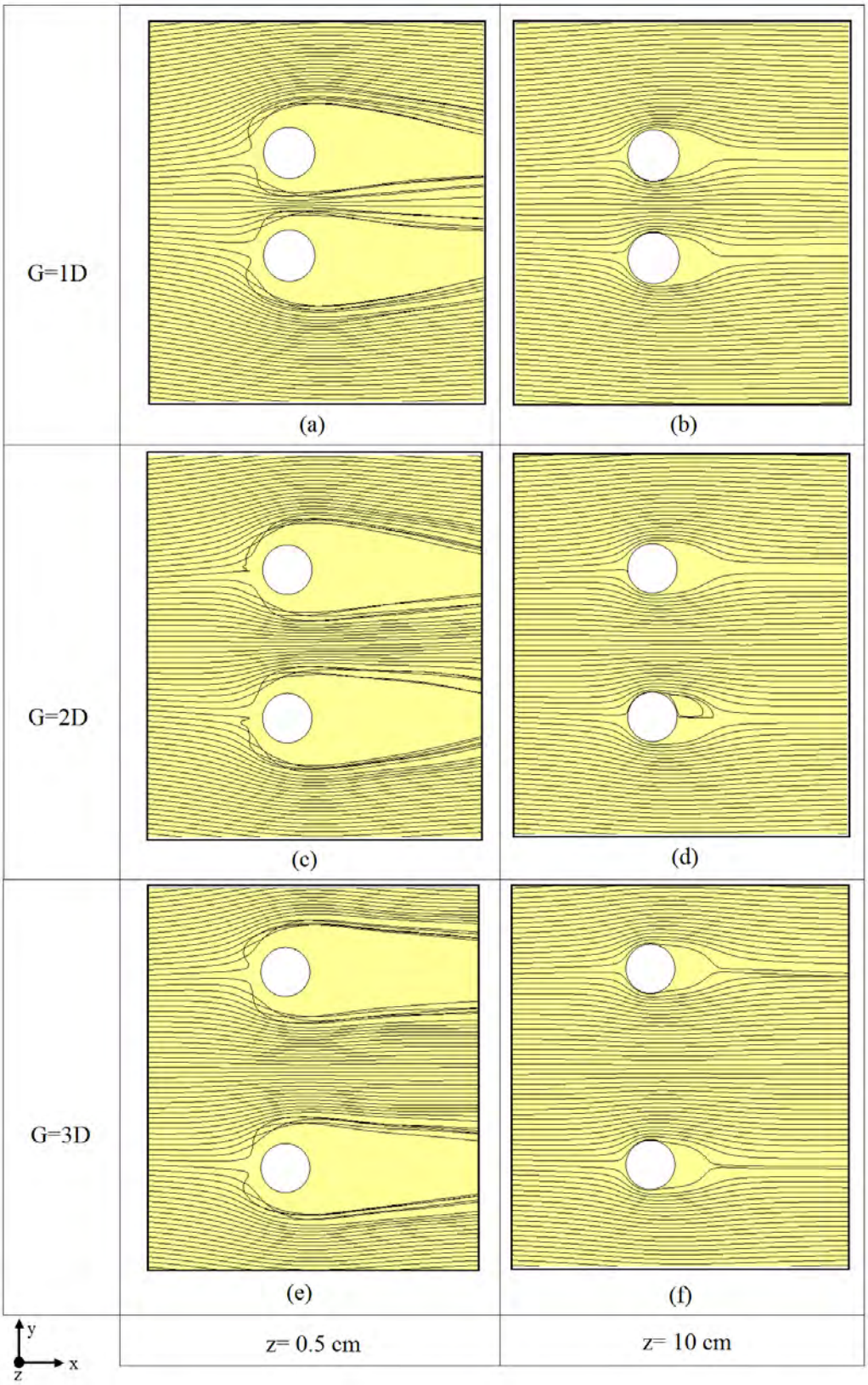


Figure (6-6) The traced streamlines from lines at z=0.5 cm and z=10 cm upstream of the pile groups with different arrangements.

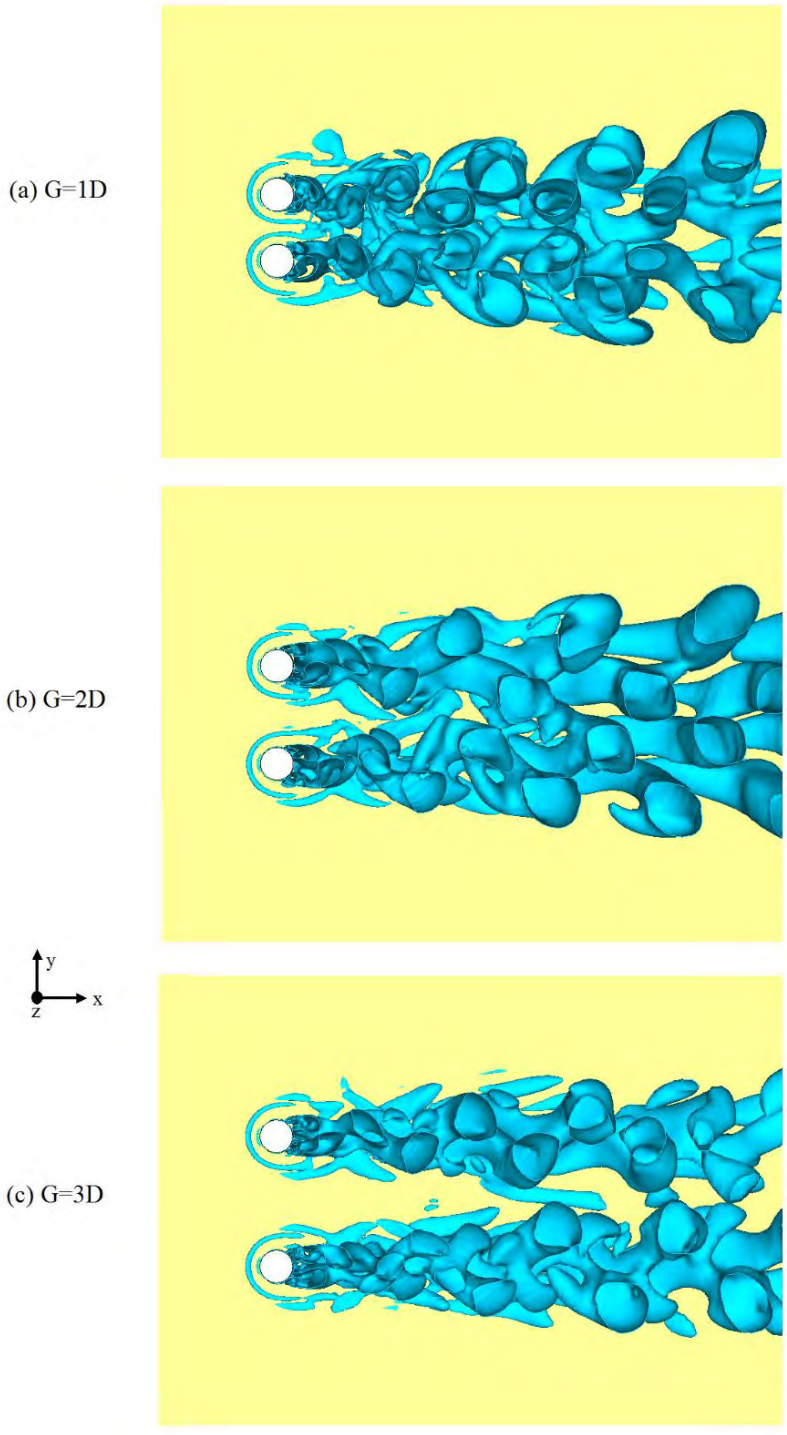


Figure (6-7) Formation of turbulent structures with applying iso-surfaces for Q= 0.1 $1/s^2$ at t =100 s for the pile groups with (a) G=1D, (b) G=2D, and (c) G=3D.

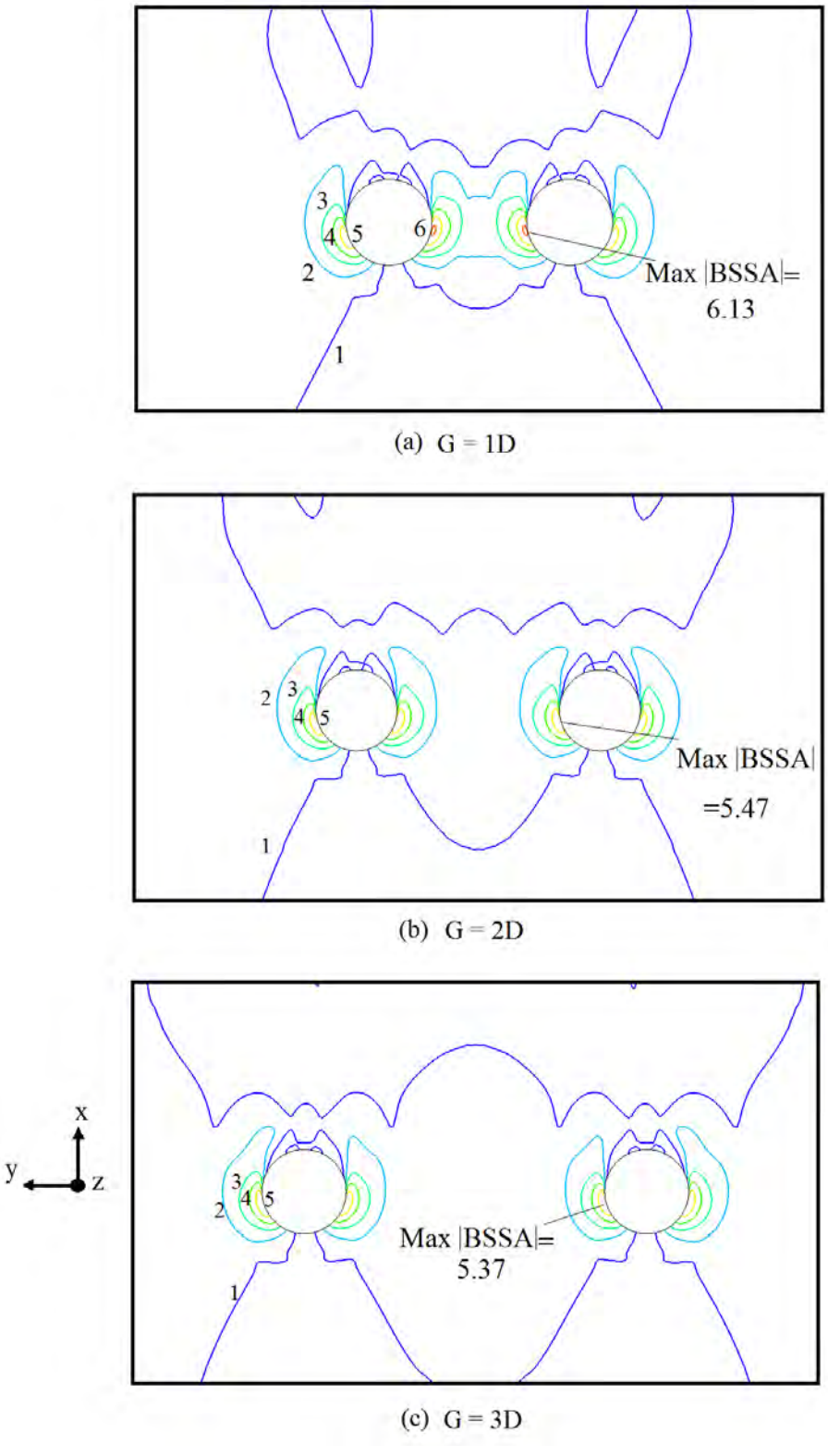


Figure (6-8) Distribution of the absolute value of BSSA on the bed around the pile groups with (a) G=1D, (b) G=2D, and (c) G=3D.

6.4 NUMERICAL MODELLING ON A MOBILE BED

The simulations on the mobile bed were carried out on the same geometries, flow and bed condition as the one described for the pile group tests on the rigid bed. It is assumed that in all cases the equilibrium condition (quasi-equilibrium) was achieved after the first 1 hour of the simulation. Therefore, all the simulations were carried on for an hour of physical time which took around 6 months of simulation time on a 2.3 GHz CPU with 8 GB RAM. Figure (6-9), Figure (6-10), and Figure (6-11) show a sequence of simulated bed deformations at times t=30, 60, 900 and 3600 s from the start of the simulations. It is observed that the deformation of the bed and scouring adjacent to the piles starts from the early stages of the simulation and extends in terms of the maximum depth and the area affected by it. The scouring adjacent to a single pile is mostly due to the formation of HSVs upstream and lee-wake vortices downstream as well as the local acceleration of the flow in the sides of the pile. In pile group arrangements, the pile group effect can be also added to the affecting factors. A decrease in the spacing ratio increases the pile group effect which consequently leads to increase in local sediment transport capacity and deeper equilibrium scour. In a condition with sufficient spacing between the piles the pile group effect will be small enough that scour patterns around each pile in a group of piles will be similar to that of a single pile.

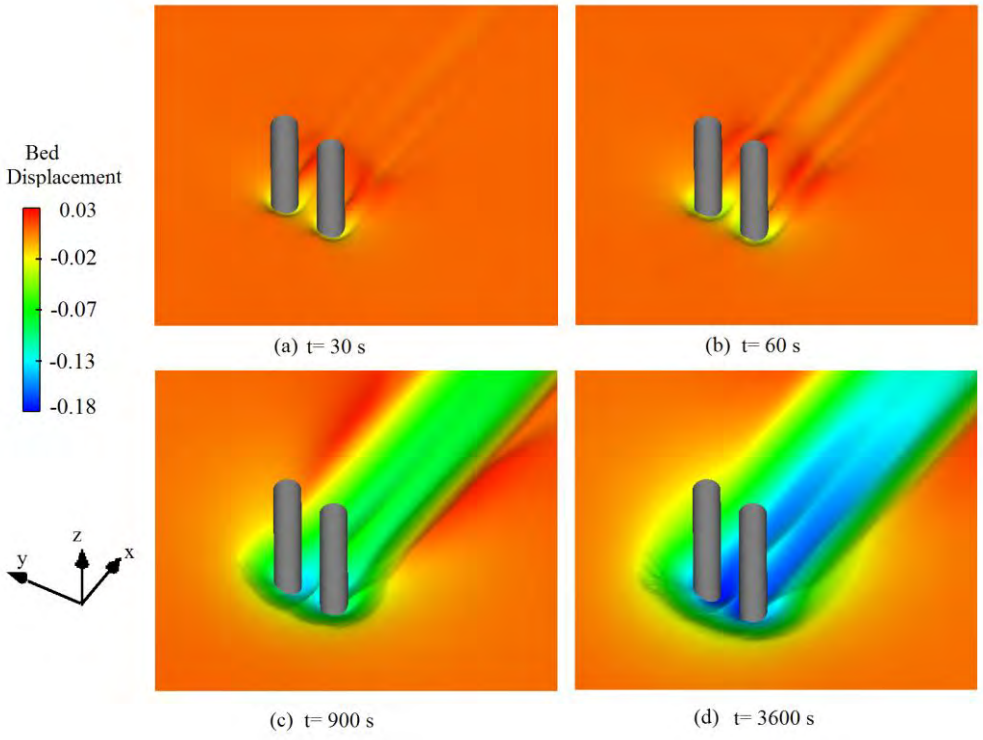


Figure (6-9) Scoured bed at 4 different times of the simulation (a) t =30 s, (b) t=60 s, (c) t=900 s, and (d) t=3600s for two side-by-side piles with G = 1D.

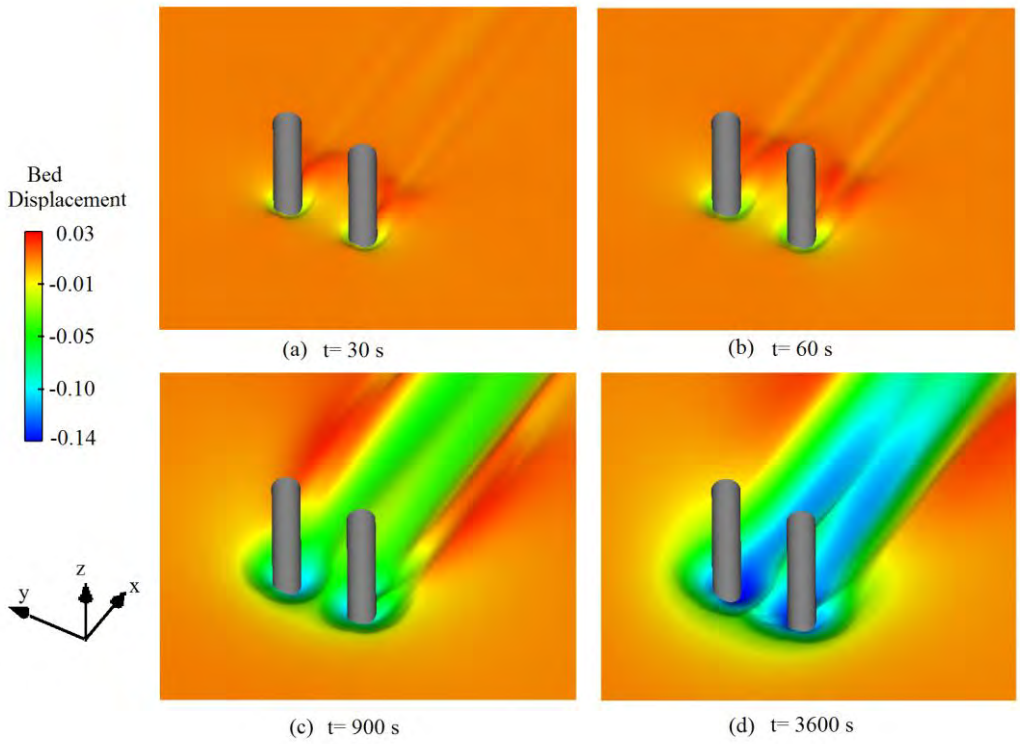


Figure (6-10) Scoured bed at 4 different times of the simulation (a) t =30 s, (b) t=60 s, (c) t=900 s, and (d) t=3600s for two side-by-side piles with G = 2D.

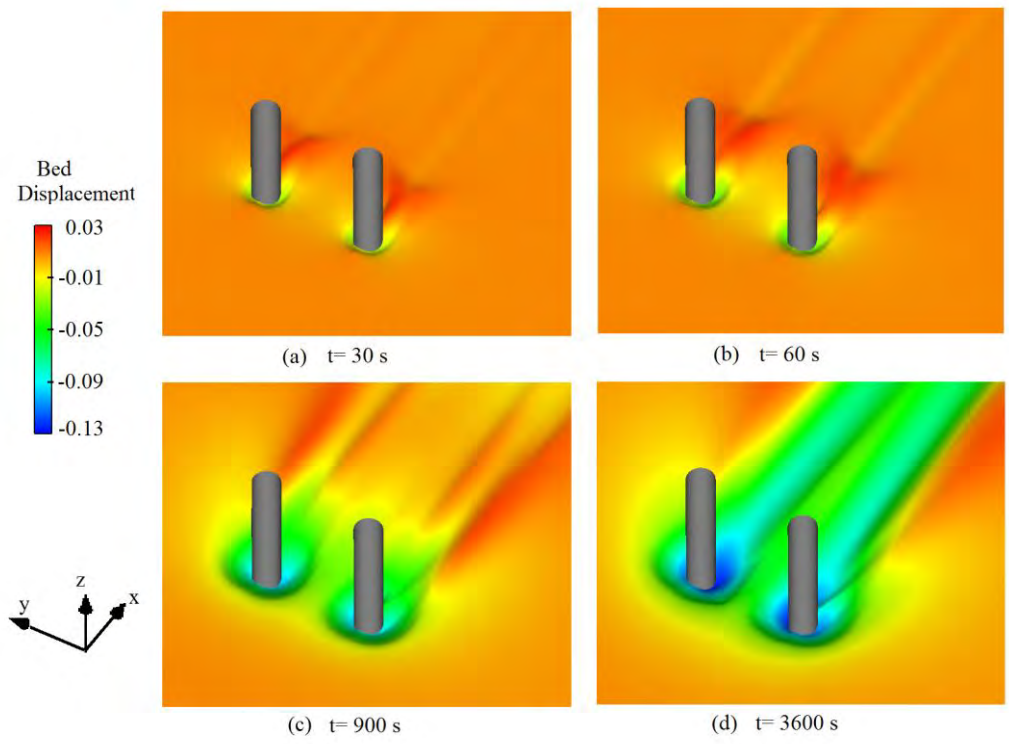


Figure (6-11) Scoured bed at 4 different times of the simulation (a) t =30 s, (b) t=60 s, (c) t=900 s, and (d) t=3600s for two side-by-side piles with G = 3D.

Figure (6-12) displays the bed morphology and the contours of instantaneous flow velocity at plane x= 0 and t =3600 s for pile groups with different spacing ratios. Generally, a deeper scour hole is observed in the area between the piles in all cases. However, due to stronger turbulent structures and higher contraction of streamlines in the case of G/D=1, a deeper hole is observed adjacent to the piles in comparison to that of the two other cases. The effect mitigates with an increase in spacing between the piles.

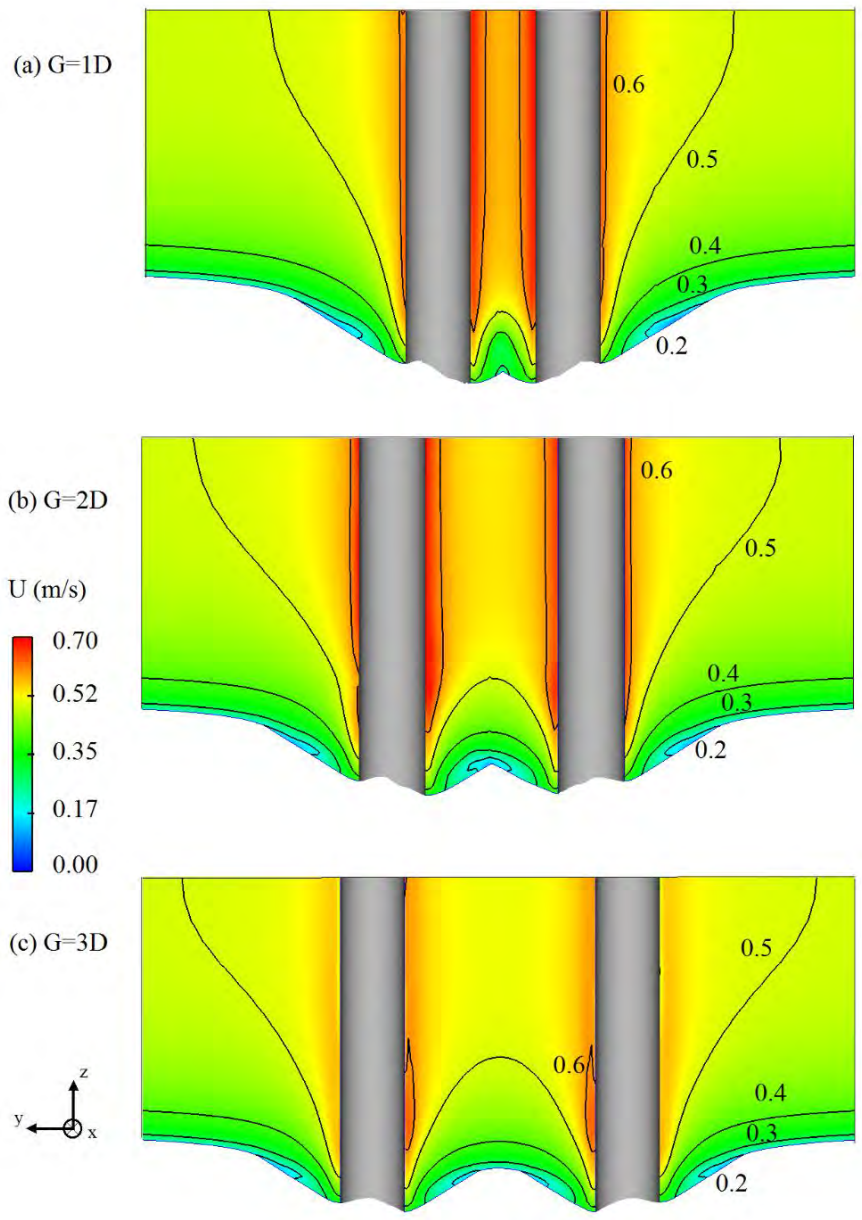


Figure (6-12) Instantaneous flow field adjacent to two side-by-side piles mounted in equilibrium scoured bed with (a) G=1D, (b) G=2D, (c) G=3D at plane x=0 and t =3600 s.

Figure (6-13) displays the topography of the two side-by-side piles in quasi-equilibrium condition for different spacing ratios. The maximum scour depth occurs in between the piles where the maximum scour depth is S_m = 17.4, 13.8 and 12.9 cm for the pile groups with G/D=1, 2 and 3, respectively. The scour patterns are almost symmetric around the piles with

respect to plane y=0. The area of the accumulated sand downstream of the piles are tilted toward the outer sides of the pile groups in all cases with angles 50˚, 30˚ and 20˚ from the back of the piles, in case of G/D=1, 2 and 3, respectively. This area is expected to form in the back of the pile (i.e. angle= 0˚) in the case of a single pile scouring.

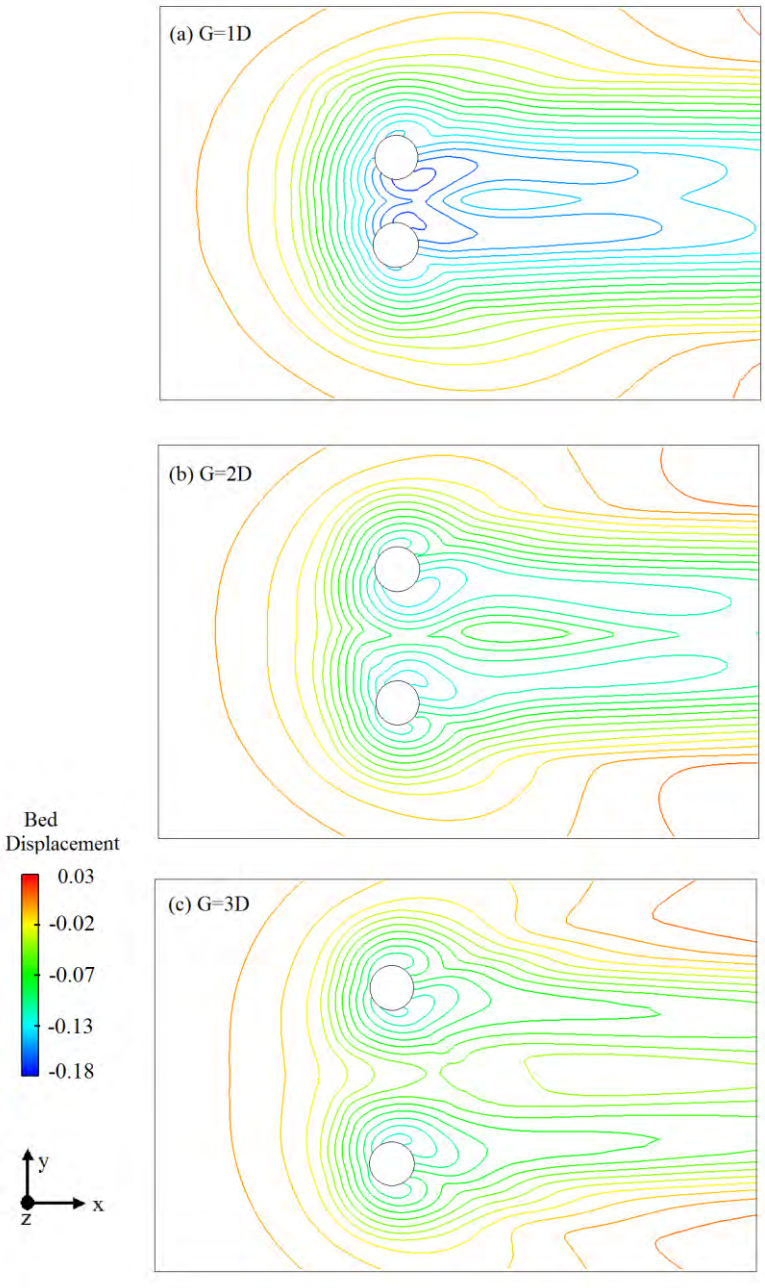


Figure (6-13) Comparison of the computed bed topography at quasi-equilibrium condition around the pile groups with (a) G=1D, (b) G=2D, and (c) G=3D.

It is assumed that the scour development reaches the equilibrium condition (quasi-equilibrium) after the first one hour of physical time for all cases similar to that of the single pile. Hence, Figure (6-14) presents the evolution of dimensionless scour hole depth S/D in time for different spacing ratios of two pile groups and the single pile until the equilibrium condition. It is observed that the evolution process of the scour hole for all cases follow a rather similar trend. A deeper scour hole appears in the case of two side-by-side piles with G/D=1 from the early stages of the evolution in comparison to that of the other cases. It is also observed that with increase in the spacing ratio of the two side-by-side piles, the evolution process converges to that of the single pile.

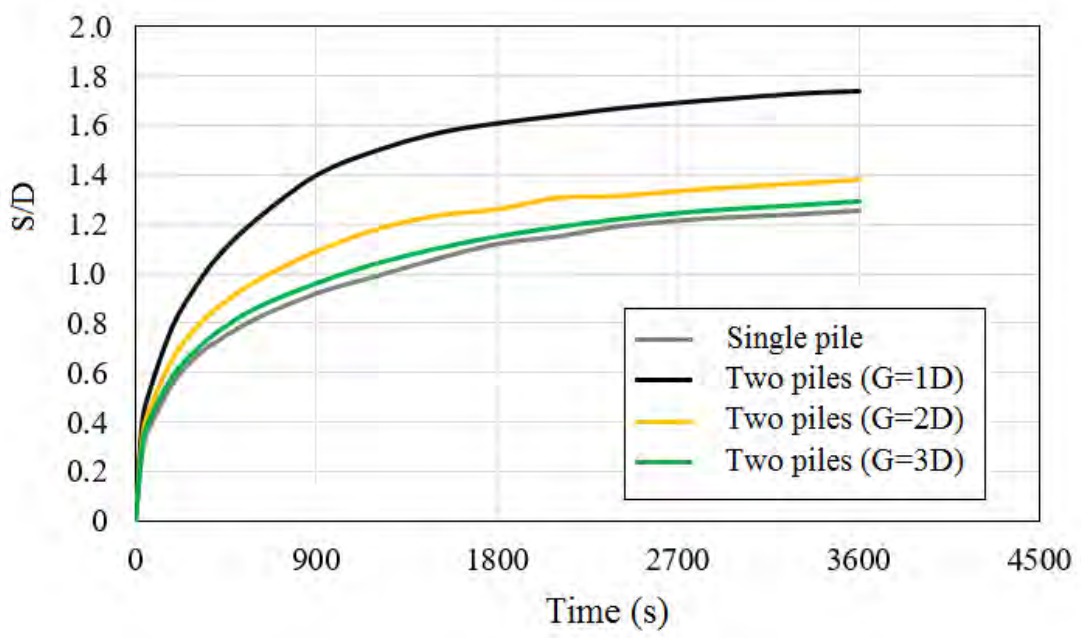


Figure (6-14) Evolution of scour depth for two side-by-side piles with G=1D, 2D and 3D and a single pile.

Figure (6-15) displays values of the dimensionless equilibrium scour hole depth S_m/D for different arrangements of two side-by-side piles with G/D=1, 2 and 3. It is also assumed that the pile group effects are completely negligible in the case of G/D=5. Hence, S_m/D equal to that of a single pile is considered for two side-by-side piles with G/D=5. Sumer et al. (1993)

inferred that for the case of a single pier, the equilibrium scour depth under steady-current flow and live-bed condition is only proportional to the cross-section shape of the pier and pier width to the flow direction, w_p. With considering this, for the available data from the simulations, a curve is fitted and a formula is yielded as following:

$$\frac{S_m}{D} = 1.25 + 1.81\ exp\left(-1.31\left(\frac{G}{D}\right)\right), \quad \frac{G}{D} \geq 1. \tag{6-1}$$

In this equation, only the impact of the side-by-side piles arrangements with different spacing ratios, G/D, is considered. The proposed equation reveals an inverse correlation between the spacing ratio and the dimensionless equilibrium scour hole depth adjacent to piles which indicates a good fit to the data with Root-Mean-Square Error (RMSE) less than 0.01. The equation is only valid for $G/D \geq 1$, as the physics of the problem may change for lower spacing ratios. Eq.(6-1) can be generalized in case of live-bed condition for two identical circular side-by-side piles, however more investigation is needed to understand the impacts of other factors.

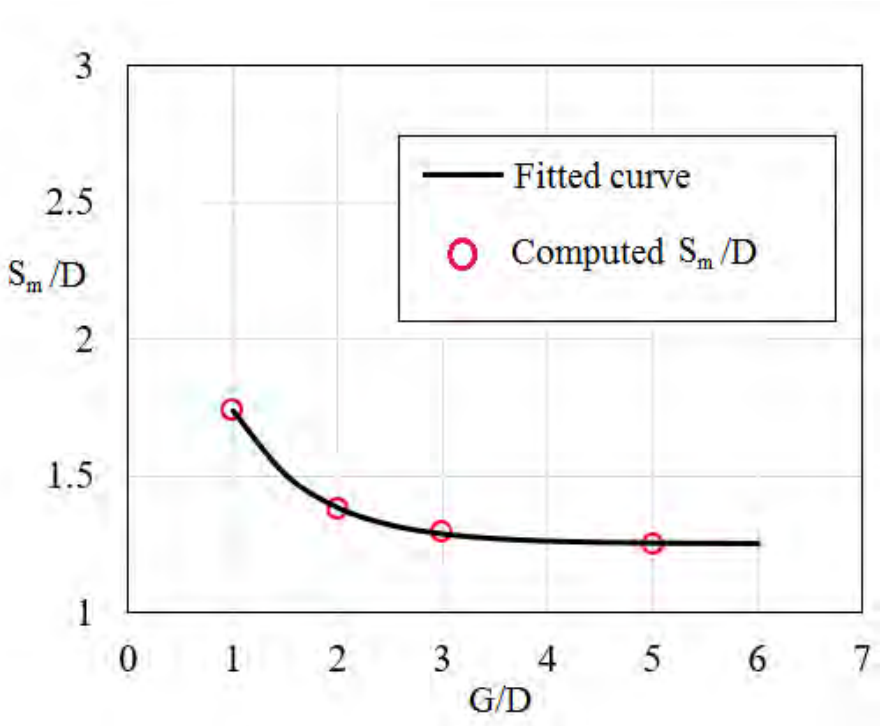


Figure (6-15) Equilibrium scour depth for two side-by-side piles with different spacing ratios.

6.5 SUMMARY

In this section, the prediction of flow behaviour and scour pattern around pile groups was carried out. The results for the flow field, bed shear stress and scour pattern for two identical side-by-side piles for different G/D values were provided. The results revealed that for $G/D \geq 3$ the pile group effect gradually vanishes. An equation was fitted for the computed equilibrium scour depths for different spacing ratios which can be used for prediction of the maximum scour depth adjacent to two side-by-side piles under current steady flow and live-bed condition for a specific range ($G/D \geq 1$).

7 SUMMARY AND CONCLUSIONS

The main aim of this investigation was to gain a deeper knowledge of flow behaviour and scour formation adjacent to bridge piers and offshore wind turbine foundations in shallow waters. In this context, investigations of the evolution of local scour were conducted by developing (Chapter 3) and implementing a numerical model using a coupling approach between a hydrodynamic and a morphodynamic model. First, the model was validated using eight test cases from the literature (Chapter 4). Then, it was applied to square- and hexagon-shaped piers (Chapter 5) as well as a group of two identical side-by-side piles (Chapter 6) all in steady current flow and live-bed condition.

7.1 NUMERICAL MODEL DEVELOPMENT

To develop the numerical model, a coupled approach between a hydrodynamic and a morphodynamic model was implemented in the framework of OpenFOAM®. In this approach, the bottom boundary of the computational domain was determined as a mobile sandy bed. The flow field was governed by incompressible unsteady RANS equations. The Reynolds stress tensors were modelled with *k-ω SST* turbulence closure which has a proven capability in the prediction of adverse pressure gradient and separation. The morphodynamic part of the model consisted of sediment transport models and mass-balance equation over the bed. Sediment transport processes which leading to local scour were modelled by the means of a bedload and a suspended-load model for non-cohesive sand. The bedload rate was computed by solving a semi-empirical equation and employing a root-finding algorithm in the GNU Scientific Library (GSL), while an advection-diffusion equation was solved to fulfil the suspension transport in

case of a non-uniform and transient flow. In the proposed scheme, the centre of the first layer of cells closest to the bed of the computational mesh was adjusted in accordance with the reference level height from the bed. Therefore, the first layer of computational cells closest to the bed was located at the distance of $3d_{50}$ to $4d_{50}$ from the bed. This reference level height with good estimation was located in the log-law region of the boundary layer flow field. Hence, a simple near-wall treatment method, Cebeci and Bradshaw (1977), which is valid for the logarithmic boundary layer was applied to solve the near-wall flow field (Figure (3-3)). The morphological evolution of the seabed due to the sediment transport fluxes was expressed by a means of a mass-balance equation on a 2D mesh corresponding to the bed boundary of the 3D domain. The result of the mass-balance equation was followed by a smoother and a sand sliding technique to suppress the spurious oscillations. Finally, a dynamic mesh technique was used to map the result as a deformation on the bed of the 3D computational mesh.

The model was validated against eight different test cases for flow and sediment transport modelling (Chapter 4). In the first test case, the performance of the applied wall function (Cebeci and Bradshaw, 1977) in CFD model was compared against the experimental equations for the velocity profile of the flow over a homogeneous bed. In second and third test cases, the performance of the hydrodynamic model which solved the unsteady-RANS equations in combination with *k-ω SST* turbulence model was examined with the experimental measurements from Roulund et al. (2005) for the fluid flow field around the circular piles mounted on rigid smooth and rough bed, respectively. In the fourth test case, the net entrainment test, an advection-diffusion equation was solved along with the hydrodynamic model to simulate the sediment concentration due to suspended-load sediment transport. The simulation results were compared to the experimental results of Rijn (1986). In the later four test cases, the coupled hydro- and morphodynamic model was employed to simulate the deformation of the

bed due to sediment transport. In test case five, a 2D case of a submerged horizontal jet was employed and the progression of the bed deformation due to scour was compared with the experimental results from Chatterjee et al. (1994). In test case six, the simulation was conducted for the evolution of a 3D scour hole around a circular pile similar to Roulund et al. (2005) empirical test in live-bed condition. Finally, in the last two test cases, the development of the scour hole around the square and diamond piers similar to experimental tests of Khosronejad et al. (2012) were numerically carried out in clear-water flow condition.

The results showed quite good agreement in terms of the fluid flow field, bed shear stress distribution and local scouring evolution between the simulation and experimental data in different test cases. For instance, the discrepancy in the prediction of maximum scour hole depth in case of circular, square and diamond piers between the simulation and experimental measurements were less than 4.6%, 6.7% and 13.1%, respectively. The accuracy of the simulations was investigated using RMSE to calculate quantitative deviation of the simulation results from the experimental data in scour simulation cases. The small deviation between simulation results and experimental measurements in scour around piers with different cross-section shape in comparison to other studies simulation results, as mentioned above, confirmed the independency of the present model results from the changes in piers geometry.

7.2 FLOW AND SCOUR AROUND SINGLE PILES WITH DIFFERENT CROSS-SECTIONS AND A GROUP OF TWO SIDE-BY-SIDE CIRCULAR PILES

The model was applied to predict the flow field, bed shear stress and the development of local scour around a square-shaped pier with 45˚ and 90˚ orientation angle to the flow, a hexagon-shaped pier with 30˚ and 60˚ orientation angle to the flow and a group of two identical side-by-

side circular cylinders with different spacing ratios G/D= 1, 2 and 3 under current flow and live-bed condition. The flow and bed material characteristics similar to one applied for scour evolution test around the circular pile in Roulund et al. (2005) were considered in all simulations. Scour simulations were carried out for one hour of physical time when a quasi-equilibrium condition was assumed to be obtained. The followings were concluded from the results:

- In case of single pier modelling, it was found that the maximum and minimum normalized quasi-equilibrium local scour depth occur for the square-shaped piers with 90° and 45° orientation angles to the flow. The normalized scour depth in quasi-equilibrium condition for the square pier was almost twice (1.94) of that for the diamond pier. This ratio in case of the hexagon-shaped pier for 60° and 30° orientation angles to the flow mitigated to a value of 1.09. From these results, it was realized that an increase in the number of sides of the piers cross-section decrease the impact of the change in orientation angle to the flow in terms of normalized scour depth. It was also inferred that with an increase in the number of sides of the piers cross-section the resultant normalized scour depth in equilibrium condition tend to get closer to that of the circular pier regardless of pier orientation angle to the flow.

- In the case of the local scour simulation around a group of two identical side-by-side piles, it was noticed that a deeper scour hole is observed in the area between the piles in all cases. However, due to the stronger turbulent structures and higher contraction of streamlines in the case of G/D=1, a deeper hole was observed adjacent to the piles in comparison to that of two other cases. The effect mitigated with an increase in spacing between the piles. The scour depth in quasi-equilibrium condition of 17.4, 13.8 and 12.9 cm for the pile groups with G/D=1, 2 and 3 were observed, respectively. The

results depicted that for $G/D \geq 3$ the pile group effect gradually vanishes, while it was assumed that the pile group effects are completely negligible for $G/D \geq 5$. An equation was fitted for the computed equilibrium scour depths for different spacing ratios which can be used for prediction of the maximum scour depth adjacent to two side-by-side piles under steady current flow and live-bed condition for a specific range ($G/D \geq 1$).

7.3 PERSPECTIVES AND FUTURE WORK

Even though the general capability of the present model in prediction of scour investigation is illustrated, there are few limitations that the model suffers from. Overcoming these limitations will improve the accuracy and speed of the simulations.

- **Parallel computing:** Numerical modelling of scour evolution is computationally very expensive as the simulations need to be ran for a long period of physical process of scouring. While in the developed model, several reasonable assumptions are applied to accelerate the simulation process with maintaining the accuracy, such as modelling of air-water interface with the slip boundary condition or modelling of side walls with the symmetry boundary condition, it is still computationally very costly, and requires simulation time of up to 6 months regarding the simulation of scour process around the group of two side-by-side piles on a single CPU core. Applying parallel computing into the implemented code can play a significant rule in accelerating the simulations and can open up possibilities for applying more complex simulation cases.
- **Air-water interaction at free-surface:** One of the limitations in the developed model is the modelling of the water-air interface with the slip boundary condition at the top boundary of the computational domain. Roulund et al. (2005) indicated that this is an acceptable assumption while $Fr < 0.2$ which is a valid assumption for most practical

cases. Nevertheless, the effect of this assumption needs to be clarified in different cases. As in the 2D test case of a submerged horizontal jet (Chatterjee et al., 1994), section 4.6, an extra 10 cm was added to water depth to minimize the impact of the slip boundary condition on the formation of the ripple and dune.

- **Two-phase flow modelling:** Apart from the classical approach in modelling of scour, recently, great success is achieved in the two-phase flow modelling approach of scour by work of Nagel et al. (2020). In their work, for the first time, the Euler-Euler approach was applied for 3D simulation of scour evolution process around a circular cylinder. In this approach, the conservation and momentum equations are solved for both the fluid phase (water) and the particle phase (sediment). This approach has more computational cost than the classical approach, nevertheless, it can be considered as a reliable and new approach for future scour simulations.

APPENDIX I

Numerical Investigation of Different Sand Sliding Methods for Morphodynamic Modelling of scour around offshore structures

Amir Bordbar*, Soroosh Sharifi, Hassan Hemida

School of Engineering, University of Birmingham, Edgbaston, Birmingham B15 2TT, UK.

Abstract

In numerical modelling of sea (river) bed by applying a morphodynamic model, a discrete sand sliding procedure needs to be followed to avoid unrealistic bed profiles to occur. In this work, two commonly employed sand sliding techniques, namely, the Artificial Transport Rate Method (ATRM) and Geometry-Based Method (GBM) are coded and implemented in OpenFOAM® framework. Three 3D test cases of sand heap avalanche with different bed boundary grid structures are considered to compare the methods' performance in terms of simulation time and mass continuity. The first two test cases are an extension of a 2D sand heap with uniform and non-uniform orthogonal quadrilateral grids on the bed, respectively, and the third test case is a quarter of a 3D sand heap with non-equidistant and non-orthogonal quadrilateral grids on the bed. The results of the analysis show that in all test cases ATRM requires higher computational time to complete simulations while its results are significantly independent of the bed mesh structures with mass continuity errors less than 0.2%. On the other hand, GBM results depend on bed mesh structure and geometry of the problem and can yield quite unacceptable results.

Keywords: *Scour, Sediment Transport, Sand Sliding, Repose Angle, Offshore Foundation.*

1. Introduction

The natural behaviour of granular materials indicates that when the slope angle of the granular covered bed exceeds a critical angle relative to a horizontal plane, the gravity force overcomes the frictional forces at the location. As a result, a volume of materials shifts downwards due to the shear failure until the slope is lower than the critical angle. This critical angle and this phenomenon are known as the angle of repose (φ_r) and granular sliding process, respectively (Roulund et al., 2005). The angle of repose has different definitions, methods of measurement, and applications. A good review of the methods for

measurement of the angle of repose for different applications can be found in Al-Hashemi and Al-Amoudi (2018). In case of sediment particles, studies of Yizheng and Baoling (1996), Shi et al. (2007), Yang et al. (2012), Yang et al. (2009), Kwoll et al. (2017) can be mentioned for the investigation of the angle of repose for sand, silt and clay. In the sea (river) bed covered with sands, granular (sand) sliding may occur due to scouring around offshore structures. Formation of strong turbulent flow around offshore structures embedded or lying on sea (river) bed washes bed materials around them and leads to the progression of the scour hole. During the evolution of the scour hole, there are areas where local bed slope may exceed the angle of repose, and as a result, sand sliding occurs (Roulund et al., 2005).

Numerical modelling of scour is carried out with different approaches which can generally be divided into two groups of single- or two-phase categories. In two-phase approaches, bed materials are considered as a separate phase which is solved simultaneously with the fluid phase, while in the single-phase approach only the fluid phase is modelled. Nevertheless, the sand sliding is essential in both approaches. In the two-phase flow models, the physical description of the sand sliding process is defined within the model by setting up granular rheology parameters and solving a momentum balance equation (Andreotti et al., 2013). The two-phase modelling of scour is investigated in works of Amoudry et al. (2008), Cheng et al. (2017), Mathieu et al. (2019), Nagel et al. (2020). On the other hand, in the single-phase models, which is known as the classical approach, there is no physical description of the angle of repose in the model. This group, which has been widely used in the literature for prediction of the evolution of scour (Liang et al., 2005; Gothel, 2008; Dixen et al., 2013; Fuhrman et al., 2014; Baykal et al., 2017 and etc.), applies empirical sediment transport formulas and illustrates the morphology of sandy bed as a deformation of the bed boundary of the computational domain. In this approach, a sand sliding procedure is needed to be separately employed by applying the definition of the angle of repose as a threshold for the sliding mechanism.

The focus of this study is on employing different sand sliding methods for the classical approach. To reveal the importance of the sand sliding method in the classical approach, an example from Liang et al. (2005) is illustrated in Fig. (1). The figure displays results of a 2D numerical modelling of scour below a horizontal pipeline with and without sand sliding procedure, where x/D and y/D are the dimensionless horizontal and vertical axis, respectively, and D is the diameter of the pipe. The results show that in the case without sand sliding procedure during the development of the bed morphology, the bed slope angle may surpass the angle of repose to an invalid slope, as shown for the area in the red circle in Fig (1b).

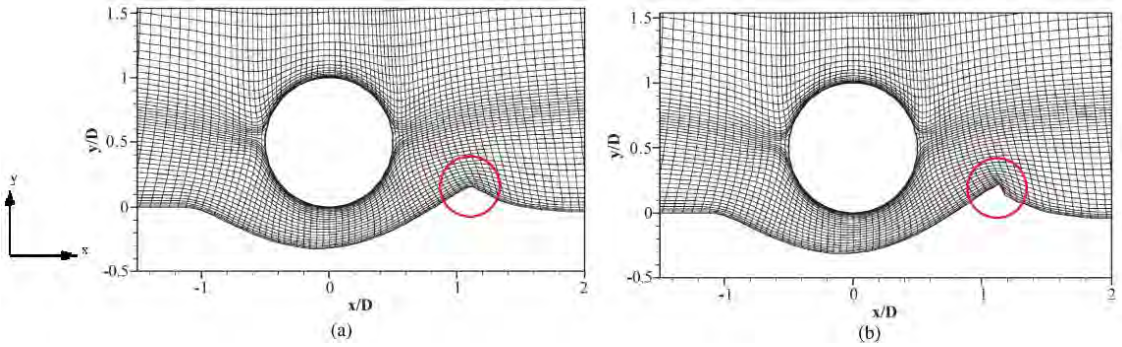


Fig.1 Numerical results of scouring around a 2D pipeline (a) with and (b) without sand sliding method from Liang et al. (2005).

In the literature, two methods are commonly adopted for 3D numerical modelling of sand sliding procedure: Artificial Transport Rate Method (ATRM) and Geometry-Based Method (GBM). Roulund et al. (2005) developed ATRM and applied it in 3D numerical modelling of scour around a circular pile. Since then, ATRM has been used by various researches (Stahlmann, 2013c; Baykal et al., 2015; and Baykal et al., 2017) for the study of scour around offshore structures. The other method, GBM, has been widely applied for two-dimensional scour cases (Niemann, 2004; Liang et al., 2005; Marieu et al., 2008; Niemann et al., 2011; Jacobsen et al., 2014; Jacobsen and Fredsoe, 2014; and Li et al., 2020). Jacobsen (2015) extended the method for 3D unstructured meshes and some later studies (e.g. Zhou, 2017 and Damarnegara, 2019) used it in the study of 3D scouring. Apart from the abovementioned studies that used sand sliding procedure to limit the bed slope, few other works (e.g. Burkow and Griebel, 2016) applied a slope limiting algorithm to keep the bed slope below the critical slope. The slope limiting algorithm works as a smoother and does not follow the nature of the sand sliding procedure. Hence, it is not considered as a sand sliding method in this study.

Although ATRM and GBM are applied in different studies, there is no information on how these methods compare in terms of mass continuity and computational time. This work describes and compares these two commonly used techniques by investigating them on three test cases. In the next section, the mathematical models and the implementation of both approaches, as well as a method to measure numerical error based on mass conservation is provided. In the result section, different test cases of the 3D avalanche of a sand heap are presented and tested using both methods. In first and second test cases, sand sliding for a 3D expansion of a 2D sand heap with uniform and non-uniform orthogonal mesh grids on the bed is explored, while in the third test case, sand sliding for a quarter of a 3D sand heap with non-equidistant and non-orthogonal mesh grids on the bed is investigated. Finally, in the conclusion section, based on the obtained results and comparisons, the reliability of the models is discussed.

2. Mathematical model

This section provides a detailed description of ATRM and GBM sand sliding procedures. Both methods follow an iterative procedure in pseudo time step to simulate the instantaneous action of sand sliding. Besides, to compare the accuracy and reliability of the models a method for the assessment of numerical error is also provided.

2.1. Artificial Transport Rate Method (ATRM)

Observation of Roulund et al. (2005) on upstream face of scour hole around a circular pile showed that local sand sliding began at an angle slightly higher than the determined angle of repose for the sand ($\varphi_r + 2^\circ$) and finally stopped at an angle slightly below the angle of repose ($\varphi_r - 2^\circ$). Hence, they implemented the same procedure in their numerical model. Therefore, the procedural steps of ATRM on all grid faces of the mobile sand-covered bed boundary in each iteration is as follows: (a) A vertical component of the unit normal vector of all bed faces ($\boldsymbol{n}.\boldsymbol{e_z}$) is calculated, where $\boldsymbol{n}$ is the unit normal vector of the bed boundary face and $\boldsymbol{e_z}$ is a unit normal vector along the positive vertical direction of the reference coordinate system. (b) The bed boundary faces with slope angle higher than the critical value ($\varphi_r + 2^\circ$), where $\cos(\varphi_r + 2^\circ) > \boldsymbol{n}.\boldsymbol{e_z}$ is true, are identified and flagged. (c) For all flagged faces, a slope direction of the face, $\boldsymbol{s}$, is calculated using,

$$\boldsymbol{s} = (\boldsymbol{n}.\boldsymbol{e_z})\boldsymbol{n} - \boldsymbol{e_z}. \tag{1}$$

(d) An artificial scalar transport rate q_A as a bedload flux is then dedicated to the flagged faces in the face slope direction to obtain a transport flux vector, $\boldsymbol{q_V}$,

$$\boldsymbol{q_V} = \frac{\boldsymbol{s}}{|\boldsymbol{s}|} q_A. \tag{2}$$

The q_A needs to be estimated for each test to have an efficient solution. A small chosen value for q_A can substantially increase the number of iterations and simulation time and a large chosen value may lead to unstable results. In this work, a simple estimation of optimum value of q_A per unit of time is carried out by calculating,

$$q_A = \frac{r^2}{2}\left(\tan(\varphi_r + 2^\circ) - \tan(\varphi_r - 2^\circ)\right) \tag{3}$$

where r is size of the smallest side of the smallest grid face on the bed. The value of q_A from Eq. (3) ensures that the changes for all bed faces follow the Roulund et al. (2005) observation from the experiments. (e) To incorporate the $\boldsymbol{q_V}$ of bed faces for modifying the bed deformation, a mass conservation equation is solved over the entire bed domain:

$$\frac{\partial h}{\partial t} = -\nabla . \boldsymbol{q_V} \tag{4}$$

where h is the grid face centre displacement in the vertical direction and t is a pseudo time. (f) The Flags are taken from flagged face if the face satisfies $\cos(\varphi_r - 2^\circ) < \boldsymbol{n}.\boldsymbol{e_z}$ and calculated changes are considered for the next iteration. Finally, the procedure will continue until no bed face is flagged.

2.2. Geometry-Based Method (GBM)

The first steps of GBM is similar to ATRM: (a) The candidate faces for sand sliding are identified by evaluating the inequality $\cos(\varphi_r) > \boldsymbol{n}.\boldsymbol{e_z}$ according to Jacobsen (2015). (b) The slope of the candidate faces is then decreased to a new realistic slope $\bar{\varphi}_r$, where, $\bar{\varphi}_r$ is the bed slope after sand sliding. The unit normal vector for a candidate face after sand sliding, $\overline{\boldsymbol{n}}$, can be calculated from,

$$\overline{\boldsymbol{n}} = \sqrt{\frac{1 - cos^2\bar{\varphi}_r}{1 - (\boldsymbol{n}.\boldsymbol{e_z})^2}}\boldsymbol{n_h} + cos\bar{\varphi}_r\boldsymbol{e_z} \tag{5}$$

where $\boldsymbol{n_h}$ is the projection of $\boldsymbol{n}$ on the horizontal plane. In Eq. (5) the face is rotated around the centre of the face (p_0) from $\boldsymbol{n}$ to $\overline{\boldsymbol{n}}$, in a way that the horizontal projection of the steepest slope of the face stays in the same direction. (c) The vertical displacement of face vertex p_i, Δh_{p_i}, due to sand sliding is calculated as,

$$\Delta h_{p_i} = \frac{(\boldsymbol{p_i} - \boldsymbol{p_0}).\boldsymbol{n_h}}{\boldsymbol{n}.\boldsymbol{e_z}} - \frac{(\boldsymbol{p_i} - \boldsymbol{p_0}).\overline{\boldsymbol{n}}_{\boldsymbol{h}}}{\overline{\boldsymbol{n}}.\boldsymbol{e_z}} \tag{6}$$

where $\overline{\boldsymbol{n}}_{\boldsymbol{h}}$ is the projection of $\overline{\boldsymbol{n}}$ on the horizontal plane. Eq. (6) ensures the desired slope for the face. However, in case of non-equidistantly meshes, this equation does not satisfy the mass conservation. (d) Hence, a modification of vertical displacement of the face vertex p_i, $\Delta h^*_{p_i}$, is required,

$$\Delta h^*_{p_i} = \Delta h_{p_i} - \frac{\sum_{i \epsilon S_{Cf}} A_i \Delta h_{p_i}}{\sum_{i \epsilon S_{Cf}} A_i} \tag{7}$$

where S_{Cf} is the set of all vertices belonging to the corrected face f, and A_i is the affected area by vertical displacement of vertex p_i which is calculated from,

$$A_i = \sum_{f \epsilon S_i} A_{q,\{f,i\}} \tag{8}$$

where S_i is the set of faces possess p_i, and $A_{q,\{f,i\}}$ is the projection of the area of a quadrilateral formed with vertices p_i, its neighbours on face f and face centre in horizontal plane as shown in Fig. (2). (e) The new position of the vertex p_i, $\boldsymbol{p_i^*}$, is calculated from,

$$\boldsymbol{p_i^*} = \boldsymbol{p_i} + \Delta h^*_{p_i}\boldsymbol{e_z}. \tag{9}$$

(f) Calculated changes for all candidate faces are considered for the next iteration. The procedure will continue until no face needs the modification. In this work to be able to compare the rheology of the resultant sandy bed from both methods, it is assumed that for GBM, an approach similar to Roulund et al. (2005) observation from the experimental results is also carried out. Therefore, sliding starts on faces with a slope angle greater than $\varphi_r + 2^\circ$, and GBM modifies them to a new realistic slope of $\bar{\varphi}_r = \varphi_r - 2^\circ$.

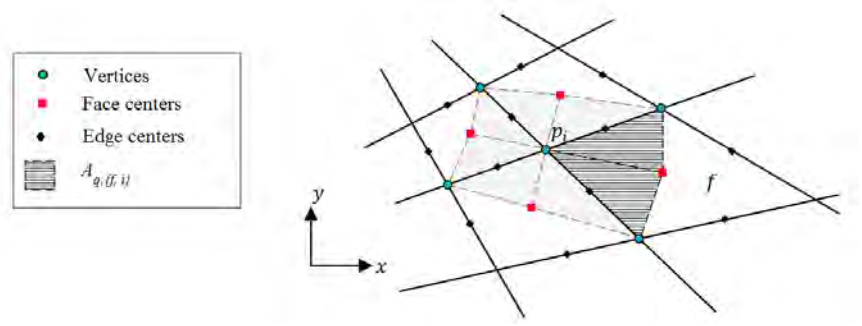


Fig.2 Affected area by vertical displacement of vertex p_i.

In the present study, both models are implemented in OpenFOAM® framework and applied for the provided test cases in the result section. There is no experimental data available to validate the models. Therefore, the verification criteria for the methods are defined based on the following the natural behaviour of the sand to avoid the slope angles higher than $\varphi_r + 2^\circ$.

2.3. Numerical mass conservation assessment

To evaluate the accuracy of the implemented sand sliding models an assessment based on mass conservation law is carried out. In all test cases, it is assumed that the computational domain is isolated and the transfer of sand from the domain boundaries is set to zero. Therefore, theoretically, the initial and final mass of sand in the domain is equal. However, in numerical modelling some discrepancies may occur due to the limitation of the models which is known as mass conservation (continuity) error. Hence, in all tests, initial and final mass of the sand heap for each model is computed by:

$$M = \rho(1-\varepsilon) \sum_{f \epsilon S_{bed}} \sum_{t \epsilon S_f} A_{t,f} h_{t,f} \qquad (10)$$

where M is the total mass of sand heap, ρ and ε are the specific density and porosity of sand, respectively, and S_{bed} includes all bed boundary faces. The effect of non-planar faces is considered in the calculation of the total mass. Therefore, as shown in Fig. (3), for the case of a quadrilateral face f of the bed, the face is divided into four triangles with the triangle base on the quadrilateral side and opposite vertex on the quadrilateral centre. Hence, in Eq. (10), S_f includes triangles in face f, $A_{t,f}$ is the projected area of

triangle i of face f on the horizontal plane and $h_{t,f}$ is the height of the centroid of the triangle i of face f from the reference bed level. The assessment is done by calculating the error in mass conservation from:

$$Error\% = \frac{|M_{Final} - M_{Initial}|}{M_{Initial}} \times 100 \quad (11)$$

where $M_{Initial}$ and M_{Final} are initial and final mass of the sand heap, respectively.

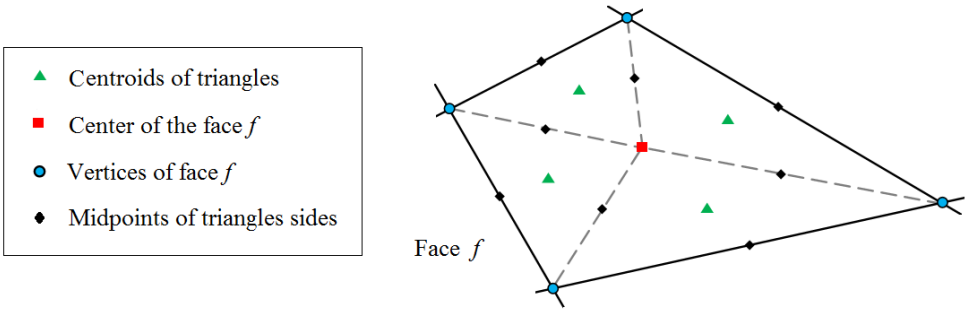


Fig.3 Four triangles formed inside a quadrilateral face f.

3. Results and discussion

This section presents the results of simulating sand sliding over three different 3D test cases of an avalanche of a sand heap using the two sand sliding models. For all investigated test cases, the computational mesh is generated in ANSYS ICEM CFD. It is assumed that the domain is filled with water and the mobile bed boundary of the domain is covered with sands with mean grain size $d_{50} = 0.26\,mm$, angle of repose $\varphi_r = 32^{\circ}$, porosity $\varepsilon = 0.4$, and specific density of 2650 kg/m^3, while, different bed materials can be adapted for test cases. In all test cases, a sand heap with an initial pre-determined angle higher than the angle of repose is considered on the bed. No flow field is involved in the tests and sliding is the only cause of sand motion. The sand sliding procedure operates in pseudo time steps and only the final results are comparable.

Different bed grid structures are used to evaluate the performance of the methods in the test cases. In the first two tests, the geometry of the domain is a 3D extension of the 2D sand heap configuration from Zhou (2017). The difference between test cases 1 & 2 is that they are generated with uniform and non-uniform orthogonal bed boundary grids, respectively. In the third test case, on the other hand, a more complex geometry of a quarter of a 3D sand heap with non-orthogonal bed boundary grids is considered. The performance of the methods for these test cases in terms of mass continuity and computational time is compared.

3.1. Test cases 1 & 2: 3D expansion of 2D sand heap with uniform and non-uniform meshes

The setup for test cases 1 & 2 are provided in Fig. (4). The sand heap is placed in the middle of the computational domain with side angles larger than the angle of repose. For both test cases, the bed boundary faces of the generated meshes are orthogonal quadrilaterals. For each test case, two sets of fine and coarse meshes are generated. In test case 1, uniform meshes are considered for the bed while in test case 2 non-uniform meshes with an expansion ratio of 1.1 in the x- and y-directions are applied on the bed. Therefore, for test case 1, the fine mesh entails 3496 faces and coarse mesh 2679 faces in the bed boundary, and for test case 2, the fine and coarse meshes contain 1416 and 952 faces in the bed, respectively. The sides of the domain in contact with the sand heap are considered as symmetry while the other sides and top are wall boundary conditions.

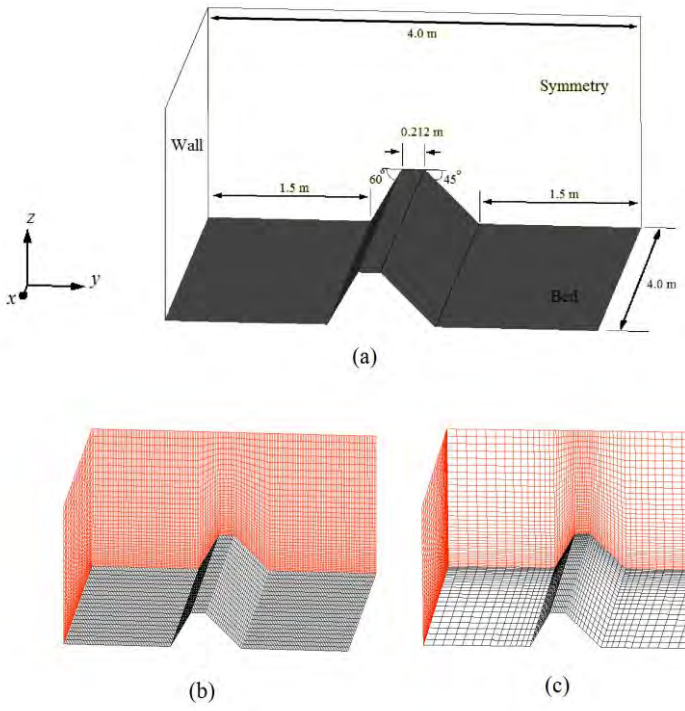


Fig.4 (a) Schematics of the test case 1 & 2 (b) the generated fine meshes for the test case 1 and (c) test case 2.

The vertical displacement contours of the bed boundary points of the final results for fine meshes of test cases 1 & 2 are presented in Fig. (5). The final results obtain when there are no faces with the slope angle higher than $\varphi_r + 2^\circ$ in the bed. The overall shape of the results for all four meshes (two for each test case) is very similar together for simulations with ATRM. On the other hand, GBM outcomes show some discrepancy for different test cases, while there is not much difference in results of fine and coarse

meshes of each test case. Generally, the final sand heap shape in ATRM results is wider with a lower height than that of GBM. The final sand heap results from ATRM, for both test case 1 and 2 has the approximate height of 0.39 m and width of 1.56 m. However, for GBM, the approximate height and width, for test case 1 are 0.44 m and 1.51 m, and for test case 2 are 0.45 m and 1.54 m, respectively. The difference between the GBM results indicates that the method is sensitive to the bed mesh structures. Moreover, the edges of the final sand heap from GBM simulations are sharper than that of ATRM as shown in Fig. (5). The reason for these differences can be partly explained with an interpolation procedure employed in ATRM which acts as a smoother. ATRM needs an interpolation scheme to transfer the data from the bed face centres (where the data are stored) into the points, however, there is no need for interpolation in GBM since the data directly exerts on the points. The applied interpolation scheme is the original interpolation routine in OpenFOAM® which is a distant weighted interpolation scheme and may produce mass conservation error.

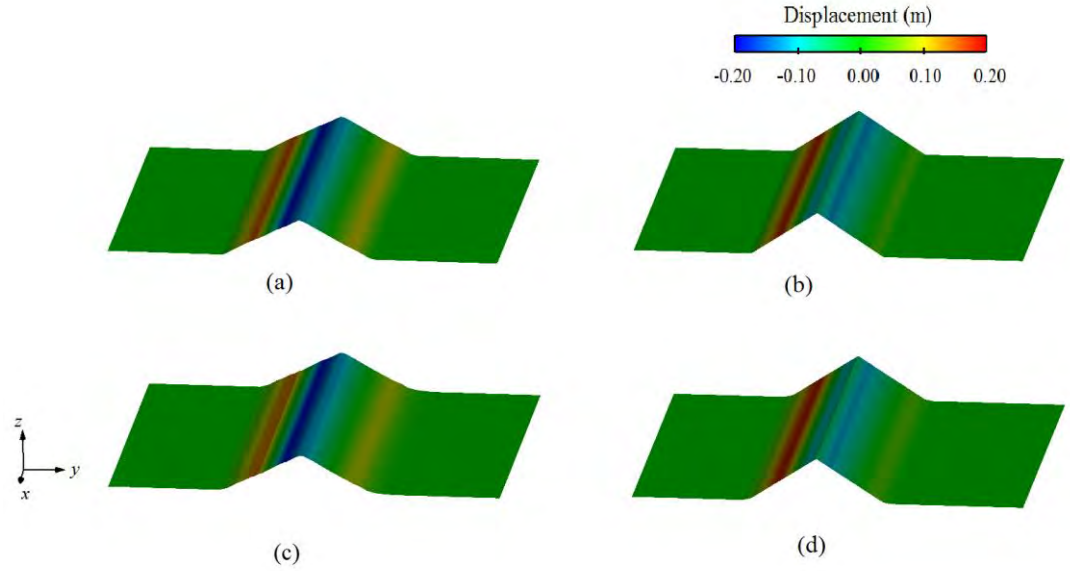


Fig.5 Vertical displacement contour of final results for the fine mesh of test case 1 using (a) ATRM and (b) GBM, and test case 2 using (c) ATRM and (d) GBM.

3.2. Test case 3: A quarter of a 3D sand heap

The setup for test case 3 is shown in Fig. (6). The geometry is a quarter of a 3D sand heap with a maximum initial angle equal to 59°. The sides in contact with the sand heap are considered as symmetry while the other sides and top are satisfied with wall conditions. The bed boundary grid of the generated mesh includes non-equidistant and non-orthogonal quadrilaterals. For this test case also two sets of fine and coarse meshes are employed with 2951 and 1735 bed boundary faces, respectively. The vertical

displacement contours of the bed boundary points for the coarse mesh are displayed in Fig. (7). As shown, the results obtained by ATRM are smoother than GBM which can be a result of the interpolation scheme implemented in ATRM.

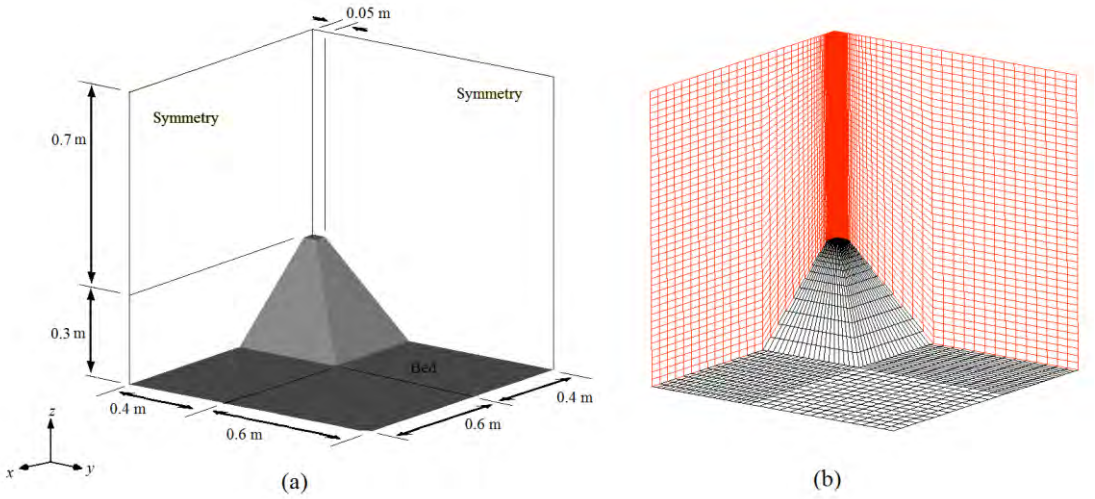


Fig.6 (a) schematics and (b) the generated coarse mesh for test case 3.

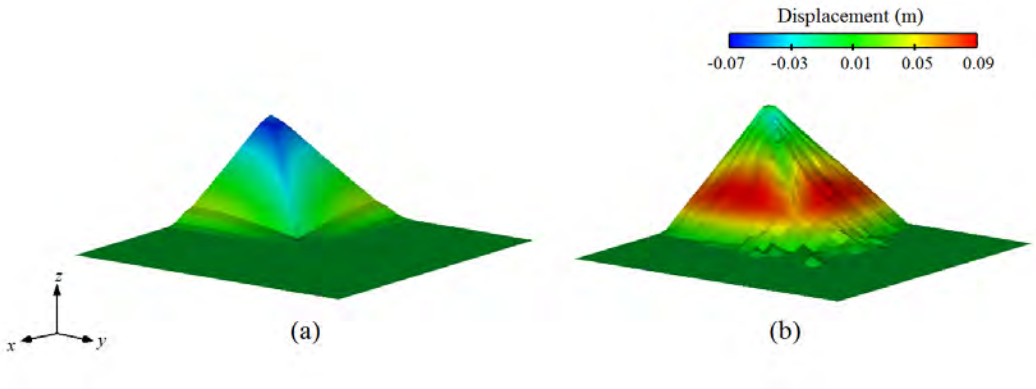


Fig.7 Vertical displacement contours of final results for the coarse mesh of the test case 3 using (a) ATRM (b) GBM.

In this work, all the simulations are run on a 2.3 GHz CPU with 8 GB RAM. The number of iterations and required computational time to converge to final results for both methods and all test cases are provided in Fig. (8). From the results in Fig (8), it is found that GBM is faster than ATRM with lower number of needed iterations. The sudden performance of GBM on each boundary grid face to reach the new realistic slope leads to a lower number of required iterations and faster solution.

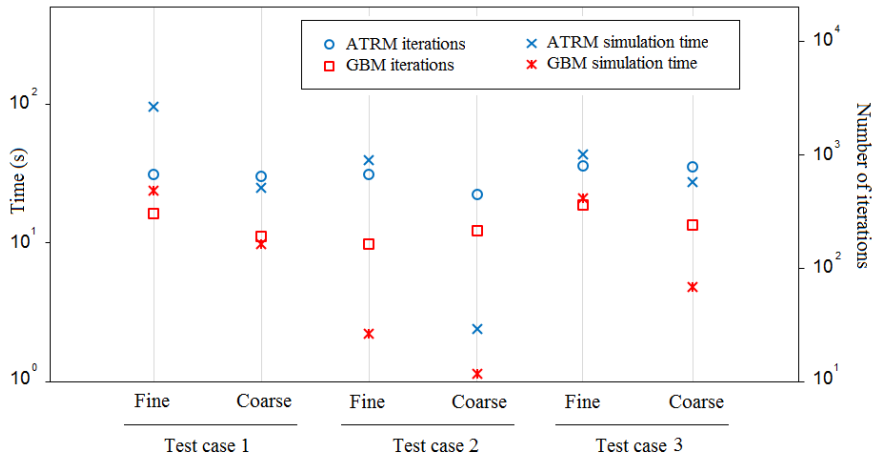


Fig.8 Simulation time and number of iterations for all simulations.

Table.1 Percentage of mass continuity error for ATRM and GBM for all simulations.

	Test case 1		Test case 2		Test case 3	
Mesh	Fine	Coarse	Fine	Coarse	Fine	Coarse
ATRM (%)	0.01	0.02	0.01	0.16	0.18	0.11
GBM (%)	0.09	0.03	5.43	5.03	44.76	87.06

Table (1) illustrates the results of mass conservation assessment for all test cases. Two conclusions can be drawn from this table. (a) the results illustrate that using a finer grid bed mesh does not necessarily lead to more accurate results in sand sliding methods. (b) the results reveal that the mass continuity error of ATRM is considerably low in the range of less than 0.2% for all test cases, while for GBM, it can vary for different geometry or bed mesh structures and can lead to invalid results.

GBM has good consistency for 2D cases where no non-planar faces can arise. The first test case is very similar to a 2D case as a uniform size meshes are applied. Consequently, the mass continuity error is negligible. However, adding an expansion ratio in the generated mesh for the same geometry in test case 2 remarkably enlarges the error. Going one step further where the domain entails a 3D geometry with non-equidistant and non-orthogonal grids on the bed in test case 3 shows that the result is completely dominated by numerical error. Jacobsen (2015) pointed out the effect of non-planar faces on the accuracy of calculated face normal vectors on GBM. Although this is a source of error in both methods, it has more impact on GBM due to the nature of the method. In fact, the performance of GBM on face points intensifies the error. In GBM in order to correct the slope angle of a face, face vertices move vertically. Movement of these points with no correction in neighbour face vertices creates non-planar face in all neighbour faces which tends to generate more error. Therefore, GBM, as described in

Jacobsen et al. (2015), is very sensitive to the generated mesh and geometry of the problem and may failed in the mass conservation assessment, as shown in Table (1) for test case 3.

4- Conclusion

One of the main challenges in numerical modelling of scour around offshore structures is to avoid unrealistic scour profiles using sand sliding methods. This work numerically investigated the performance of two different sand sliding procedures on three different test cases. A comparison in terms of the number of iterations, computational time, and mass conservation error of the models was conducted. It was found that for all cases, GBM performs faster that ATRM with lower number of iterations. On the other hand, the results of the mass conservation assessment illustrated that ATRM performance is independent of the structure of the bed boundary with almost no mass conservation error (less than 0.2%) while it is not true for GBM. Simulation with GBM may lead to a completely unacceptable result as it is shown in test case 3 for a quarter of a 3D sand heap with non-equidistant and non-orthogonal grids on the bed mesh. Therefore, the results of the analysis showed that although ATRM requires higher computational time to complete simulations, it offers a solution with a considerably lower numerical error while GBM can yield quite unacceptable results.

References

AL-HASHEMI, H. M. B. & AL-AMOUDI, O. S. B. J. P. T. 2018. A review on the angle of repose of granular materials. 330**,** 397-417.

AMOUDRY, L., HSU, T. J. & LIU, P. F. J. J. O. G. R. O. 2008. Two-phase model for sand transport in sheet flow regime. 113.

ANDREOTTI, B., FORTERRE, Y. & POULIQUEN, O. 2013. *Granular media: between fluid and solid*, Cambridge University Press.

BAYKAL, C., SUMER, B. M., FUHRMAN, D. R., JACOBSEN, N. G. & FREDSØE, J. 2015. Numerical investigation of flow and scour around a vertical circular cylinder. *Philosophical Transactions of the Royal Society A: Mathematical, Physical and Engineering Sciences,* 373**,** 20140104.

BAYKAL, C., SUMER, B. M., FUHRMAN, D. R., JACOBSEN, N. G. & FREDSØE, J. 2017. Numerical simulation of scour and backfilling processes around a circular pile in waves. *Coastal Engineering,* 122**,** 87-107.

BURKOW, M. & GRIEBEL, M. 2016. A full three dimensional numerical simulation of the sediment transport and the scouring at a rectangular obstacle. 125**,** 1-10.

CHENG, Z., HSU, T.-J. & CALANTONI, J. J. C. E. 2017. SedFoam: A multi-dimensional Eulerian two-phase model for sediment transport and its application to momentary bed failure. 119**,** 32-50.

DAMARNEGARA, A. 2019. Scour at the foot of seawalls (Doctoral dissertation, Lyon).

DIXEN, M., SUMER, B. M. & FREDSØE, J. 2013. Numerical and experimental investigation of flow and scour around a half-buried sphere. *Coastal Engineering,* 73**,** 84-105.

FUHRMAN, D. R., BAYKAL, C., SUMER, B. M., JACOBSEN, N. G. & FREDSØE, J. 2014. Numerical simulation of wave-induced scour and backfilling processes beneath submarine pipelines. *Coastal Engineering,* 94**,** 10-22.

GOTHEL, O. 2008. Numerical modeling of flow and wave-induced scour around vertical structures.

JACOBSEN, N. G. & FREDSOE, J. 2014. Formation and development of a breaker bar under regular waves. Part 2: Sediment transport and morphology. *Coastal Engineering,* 88**,** 55-68.
JACOBSEN, N. G., FREDSOE, J. & JENSEN, J. H. J. C. E. 2014. Formation and development of a breaker bar under regular waves. Part 1: Model description and hydrodynamics. 88**,** 182-193.
JACOBSEN, N. G. J. I. J. F. N. M. I. F. 2015. Mass conservation in computational morphodynamics: uniform sediment and infinite availability. 78**,** 233-256.
KWOLL, E., VENDITTI, J., BRADLEY, R. & WINTER, C. J. J. O. G. R. E. S. 2017. Observations of coherent flow structures over subaqueous high-and low-angle dunes. 122**,** 2244-2268.
LI, Y., ONG, M. C., FUHRMAN, D. R. & LARSEN, B. E. J. C. E. 2020. Numerical investigation of wave-plus-current induced scour beneath two submarine pipelines in tandem. 156**,** 103619.
LIANG, D., CHENG, L. & LI, F. 2005. Numerical modeling of flow and scour below a pipeline in currents: Part II. Scour simulation. *Coastal engineering,* 52**,** 43-62.
MARIEU, V., BONNETON, P., FOSTER, D. & ARDHUIN, F. J. J. O. G. R. O. 2008. Modeling of vortex ripple morphodynamics. 113.
MATHIEU, A., CHAUCHAT, J., BONAMY, C. & NAGEL, T. J. W. 2019. Two-phase flow simulation of tunnel and lee-wake erosion of scour below a submarine pipeline. 11**,** 1727.
NAGEL, T., CHAUCHAT, J., BONAMY, C., LIU, X., CHENG, Z. & HSU, T.-J. J. A. I. W. R. 2020. Three-dimensional scour simulations with a two-phase flow model. 103544.
NIEMANN, S., FREDSØE, J. & JACOBSEN, N. G. J. J. O. H. E. 2011. Sand dunes in steady flow at low Froude numbers: Dune height evolution and flow resistance. 137**,** 5-14.
NIEMANN, S. L. 2004. Modelling of sand dunes in steady and tidal flow.
ROULUND, A., SUMER, B. M., FREDSØE, J. & MICHELSEN, J. 2005. Numerical and experimental investigation of flow and scour around a circular pile. *Journal of Fluid Mechanics,* 534**,** 351-401.
SHI, Y.-L., LU, J., ZHAN, Y.-Z., HUANG, C. & YU, J. 2007. Calculation of angle of repose and dry density of sediment [J]. 40**,** 14-17.
STAHLMANN, A. Numerical and experimental modeling of scour at foundation structures for offshore wind turbines. 2013 2013. International Society of Offshore and Polar Engineers.
YANG, F.-G., LIU, X.-N., YANG, K.-J. & CAO, S.-Y. J. J. O. H., SER. B 2009. Study on the angle of repose of nonuniform sediment. 21**,** 685-691.
YANG, L., SHI, B., GUO, Y. J. J. O. P. E. & TECHNOLOGY, P. 2012. Study on dynamic angle of repose for submarine pipeline with spoiler on sandy seabed. 2**,** 229-236.
YIZHENG, Z. & BAOLING, X. J. I. J. H. E. 1996. Under water angle of rest for non-cohesive sediment [J]. 1.
ZHOU, L. 2017. *Numerical modelling of scour in steady flows (Doctoral dissertation).*

APPENDIX II

Prediction of Scour Around Single Vertical Piers with Different Cross-Section Shapes

Amir Bordbar*[1], Soroosh Sharifi[1], Hassan Hemida[1]

[1]School of Engineering, University of Birmingham, Birmingham, UK

Abstract. In the present work, a 3D numerical model is proposed to study local scouring around single vertical piers with different cross-section shapes under steady-current flow. The model solves the flow field and sediment transport processes using a coupled approach. The flow field is obtained by solving the Unsteady Reynolds Averaged Navier-Stokes (URANS) equations in combination with the *k-ω SST* turbulence closure model and the sediment transport is considered using both bedload and suspended load models. The proposed model is validated against the empirical measurements of local scour around single vertical piers with circular, square, and diamond cross-section shapes obtained from the literature. The measurement of scour depth in equilibrium condition for the simulations reveal the differences of 4.6%, 6.7% and 13.1% from the experimental measurements for the circular, square, and diamond pier cases, respectively. The model displayed a remarkable performance in the prediction of scour around circular and square piers where horseshoe vortices (HSVs) have a leading impact on scour progression. On the other hand, the maximum deviation was found in the case of the diamond pier where HSVs are weak and have minimum impact on the formation of local scour. Overall, the results confirm that the prediction capability of the present model is almost independent of the strength of the formed HSVs and pier cross-section shapes.

Keywords: Scour, Steady Current Flow, Sediment Transport, Bridge Piers, Offshore Wind Turbine.

1 Introduction

The existence of a marine structure under a flow field substantially changes the behavior of the flow, creating a complex 3D flow behavior with separation, swirling, and recirculation motions. For marine structures mounted on an erodible seabed or riverbed (i.e. sandy bed) these changes can be strong enough to wash out part of the sediments adjacent to the structure, a process known as scouring, which is of importance in connection with the stability of the structure (Sumer et al., 1993). In the case of bridge piers, scouring around piers is the most frequent cause of bridge failure which causes significant maintenance and repair costs (Topczewski et al., 2016). Similarly, in the offshore wind industry, scouring around the piles of shallow water wind turbines have a significant effect on the stability of this structure. Observations show that the maximum possible scour around a pile in an unprotected bed can be up to twice the size of the pile diameter (Sumer and Fredsøe, 2001a). This means that typical piles foundation length have to be overdesigned for an extra 8-10 m, which imposes a huge extra cost (Hansen et al., 2007). Hence, protecting piles/piers from scour damage in an economically efficient way is a considerable engineering challenge, which can be achieved by safe design of the pile's foundation against scour damage or applying scour protection systems such as installing a scour protection mattress or rock armor.

* Corresponding author: Amir Bordbar, Ph.D. Candidate, School of Engineering, University of Birmingham, Birmingham, UK,

To better understand scouring and the factors affecting it, extensive experimental investigations have been carried out over the past few decades. A large number of these studies focus on turbulence structures on rigid flat beds and investigate the formation of horseshoe vortices (HSVs), due to adverse pressure gradient, and lee-wake vortices as primitive mechanisms of scouring upstream and downstream of pile/piers, respectively. Works of Baker (1980), Dargahi (1989), Seal and Smith (1999) and Agui and Andreopoulos (1992) are noticeable studies in this group. Additionally, various experimental investigations of scouring on mobile beds have been conducted in both river and marine environments. For instance, Dargahi (1990) and Melville and Chiew (1999) experimentally investigated the formation of scouring around a circular cylinder in steady current, and attempted to explain the evolution of scouring from the early to final stages. Sumer et al. (1992) and Sumer et al. (1993) did a series of experiments for investigating scouring around circular, square and diamond cross-section columns for both steady and wave-current flows. Dey et al. (1995) and Graf and Istiarto (2002) carried out a wide range of tests for measuring flow patterns around circular cylinders mounted in a scour hole.

Numerical modelling has also been widely used by several researchers to understand flow and scour mechanisms. Tseng et al. (2000), Salaheldin et al. (2004), Kirkil et al. (2005), Kirkil et al. (2008) and Kirkil et al. (2009), and loads of others studied the flow behavior around pile/piers on rigid bed. In these works, different hydrodynamic models were employed to better understand the formation of horseshoe and wake vortex structures and the bed shear stress distribution on both rigid flat and scoured beds around piles. On the other hand, a massive number of studies attempted to model local scouring process around piles/piers. A group of them carried out the modelling by coupling a hydrodynamic model with a morphodynamic model to simulate the time development of scour evolution, which is specified as a classical approach here. In classical approach, a boundary (e.g. bottom or bed) of the numerical domain is presented as a sandy bed-water interface, and deformation of this boundary due to scour is provided by solving a mass conservation equation on the boundary as a result of sediment transport. An early example of this approach for modelling of scour around the piles/piers dates back to the nineties when Olsen and Melaaen (1993) and Olsen and Kjellesvig (1998) developed the first 3D model for predicting local scour on a mobile bed for clear water regime and cohesionless sediment conditions. However, their model lacked the transient term, and thus, was unable to predict the maximum scour depth correctly. In a notable work, Roulund et al. (2005) investigated the flow and scour around a vertical pile both numerically and experimentally in a live-bed with non-cohesive sand. They also developed a 2D numerical description model for the bedload which was an extension of the bedload model in Engelund and Fredsøe (1976). However, their scour simulation model did not incorporate suspended sediment transport, and the flow model used a steady solution. Therefore, it was incapable of predicting the formation of lee-wake vortices behind the pile. Göthel and Zielke (2007) presented a model for predicting scour around a cylinder pile exposed to steady and wave currents. However, similar to Roulund et al. (2005) approach, their model only included bedload transport and ignored the suspended load. They numerically modelled the hypothetical scour protection by increasing the bed roughness for the area which had been assumed to be covered by stones as a scour protector. Their work led to a better understanding of the possible increase in bed shear stress due to presence of scour protectors and the identification of affected areas. Liu and García (2008) introduced a model for local sediment scour around piles under wave impact which included both bedload and suspended load transport components. Their flow model employed the standard k-ε turbulence closure model. They validated their model against experimental data from Sumer and Fredsøe (2001b). Khosronejad et al. (2012) carried out experimental and numerical investigation of scour around bridge piers with cylindrical, square, and diamond cross-section shapes. They used the fluid–structure interaction curvilinear immersed boundary (FSI-CURVIB) method by Khosronejad et al. (2011) to handle the moveable bed of the channel with embedded hydraulic structures. They applied the Unsteady Reynolds Averaged Navier-Stokes (URANS) in combination with the k-ω turbulence closure model to solve the flow field and found that the accuracy of their model could vary depending on the pier's cross-section shape.

Escauriaza and Sotiropoulos (2011) applied detached-eddy simulation (DES) approach to solve the hydrodynamic model to be able to accurately resolve most of the turbulent stresses produced by the HSVs and used a bedload transport model which was inspired by works of Kovacs and Parker (1994) and Parker et al. (2003). They reported that their model was able to reproduce most of the characteristics

observed by Dargahi (1990) during initial scour around the cylindrical pile. Kim et al. (2014), for the first time, employed Large Eddy Simulation (LES) approach to solve the Navier-Stokes equations and followed an approach similar to work of De Ruiter (1983) for sediment transport. They validated their model by experimental data from Khosronejad et al. (2012). Stahlmann and Schlurmann (2012) and Stahlmann (2013) highlighted the lack of knowledge and understanding of scour progression around complex offshore foundation structures, and introduced a model which was highly inspired by the work of Roulund et al. (2005). The model solves the combined waves and tidal current flow fields and its sediment transport model considers both bedload and suspended-load, and was applied to simulate scour around wind turbines with tripod foundations. As most recent works, the works of Sumer et al. (2014), Baykal et al. (2015) and Baykal et al. (2017) can be mentioned which used a similar hydro-morphodynamic model. However, their model followed the classical approach, it benefited from a truncated computational domain to solve an advection-diffusion equation for the suspended load model. Baykal et al. (2015) applied the model to investigate the effects of lee-wake vortices, as well as suspended sediment transport on scouring around a vertical pile on steady current. On the other hand, Sumer et al. (2014) and Baykal et al. (2017) used the model to investigate backfilling of a scour hole around circular piles. They validated their results against the experimental outputs from Sumer et al. (2012). In another work, Omara et al. (2019) applied FLOW-3D to numerically estimate the flow behavior and scour depth around vertical and inclined bridge piers. The URANS equations in combination with the RNG k-ε turbulence model was used to solve flow field while their sediment transport models included both bedload and suspended load. The model was validated against the experimental data from Ghiassi and Abbasnia (2013) for scour depth around a square pier. They pointed out that the prediction capability of the model was attached to the pier shape and its inclined direction.

Many studies, including the ones mentioned above, have successfully applied the classical approach in the investigation of scouring around vertical circular cylinders. Nevertheless, a review of previous numerical works on local scour around piers with different cross-section shapes revealed that the accuracy of these hydro-morphodynamic models in determining local scour varies with the piers cross-section shapes (e.g. works of Khosronejad et al. (2012) and Omara et al. (2019)). This limitation challenges the capability of the hydrodynamic part of the classical models in predicting the strength of formed HSVs upstream of mounted piers with different cross-section shapes (Khosronejad et al., 2012). In the present work, URANS equations in combination with the k-ω *SST* turbulence closure model is adopted to solve the hydrodynamic part of the model. The k-ω *SST* turbulence model has a proven capability in predicting adverse pressure gradients and separation flow (Menter, 1992). As the physical modelling of local scour is a time-consuming process, the low computational cost and high accuracy of this combination in simulating the main turbulence structures around piles/piers are desirable. In addition, proper attention is given to adjust the height of the centre of the first layer of the computational cells closest to the bed from the bed to ensure the requirements of the hydrodynamic and morphodynamic part of the model are satisfied. These considerations lead to propose a reliable tool for prediction of scour around piers with different cross-section shapes.

In the next section, a description of the mathematical model, including details of the proposed hydro- and morphodynamic models are briefly described. In section 3, the capability of the model in terms of prediction of the temporal development of local scour and the deformed bed in equilibrium condition is examined around circular, square and diamond piers. These cases are chosen as the strength of the HSVs is different around them. Observations by Khosronejad et al. (2012) determined the formation of strong HSVs upstream of the circular and square piers, while very week HSVs was found for the case of diamond piers. Finally, in the conclusion section, the main contribution of this work is presented.

2 Description of the mathematical model

For the purpose of the present study, a model is implemented in the OpenFOAM® framework using the classic modeling approach. In this manner, at each time step, first, the hydrodynamic model is solved on the 3D computational mesh. Second, the flow field results are used to calculate the bed shear stress,

as the primary parameter for solving sediment transport models. Then, the bedload model on a 2D mesh, in accordance with the bed boundary, and the suspended load model on a 3D computational mesh are passively solved. Finally, the results of the sediment transport model are reflected by solving the mass conservation equation over the 2D mesh and transferring the results as a deformation on the bed. The deformed mesh is used as a renewed computational mesh for the next time step of the solution.

2.1 Hydrodynamic model

The model only solves the water-phase in the computational domain. Hence, the domain is limited by a water-air interface at the top. This is a valid assumption for almost all practical cases as long as the ratio of the inertial force to the gravitational force, Froude number (Fr), is small (e.g. $Fr < 0.2$) in the flow (Roulund et al., 2005). The URANS equations are employed to solve a single-phase incompressible flow which in the Cartesian coordinate system with the convention of Einstein's summation are as follows:

$$\frac{\partial u_i}{\partial x_i} = 0 \tag{1}$$

$$\frac{\partial u_i}{\partial t} + u_j \frac{\partial u_i}{\partial x_j} = f_i - \frac{1}{\rho}\frac{\partial P}{\partial x_i} + \nu \frac{\partial^2 u_i}{\partial x_i \partial x_j} + \frac{1}{\rho}\frac{\partial \tau_{ij}}{\partial x_j} \tag{2}$$

where u_i and f_i are the ensemble average velocity and the body force in the x_i direction respectively, t is the time, ρ is the fluid density, P is the mean pressure, ν is the molecular kinematic viscosity of fluid and τ_{ij} is the Reynolds stress component which is modeled using the *k-ω SST* turbulence closure model. The PISO algorithm by Issa (1986) is chosen for solving the hydrodynamic model with a courant number of $Co < 0.5$ to satisfy the numerical stability of solution.

2.1.1 Boundary conditions

The boundaries of the computational domain for all simulations include top, sides, outlet, inlet, cylinder body surface, and bed, as shown in Fig.1. The top boundary which simulates the water-air interface is adapted with a slip boundary condition. The slip boundary condition behaves differently for different types of variables. For the scalar quantities (e.g. pressure), it simply uses Neumann condition (wall-normal zero gradients) at the boundary. However, in the case of vectorial variables (e.g. velocity), the tangential component to the boundary surface of the quantities is treated with Neumann condition (wall-normal zero gradients), while the normal component is handled with Dirichlet boundary condition (zero value). The symmetry boundary condition is considered at the sides of the computational domain for all quantities, which considering the ratio of the pier width to flume width in the experimental setups is justifiable as its effects are negligible. The outlet is treated with zero values for the gradient of all quantities except for the pressure, which is equal to zero at the outlet boundary. The approaching flow condition at the inlet is achieved using different methods which are described separately for each simulation in the result and discussion section. In order to have an accurate estimation of flow velocity near the wall, which is essential for the calculation of shear velocity and bed shear stress, near-wall treatment is applied. The walls which included mobile bed boundary and pier's body are treated by Cebeci and Bradshaw (1977) near-wall treatment model which is originally suggested for the log-layer region of the boundary layer. Therefore, the center of the first layer of the cells next to the wall should be placed in the logarithmic region of the boundary layer. Based on Cebeci and Bradshaw (1977), where the roughness of the surface is known, the near-wall treatment for the logarithmic region of the boundary layer can be defined by:

$$u^+ = \frac{1}{\kappa}\ln(Ey^+) - \Delta B \tag{3}$$

$$u^+ = \frac{u}{u_f}, \qquad y^+ = \frac{u_f y}{\nu} \tag{4}$$

where $u^+$and $y^+$are non-dimensional velocity and distance for the log-law region in the equilibrium turbulent boundary layer, respectively, u_f is friction velocity, y is the distance of the center of the first layer of the mesh from the wall, and $E = 9.8$ is the roughness-dependent constant. Substituting $u^+$and y^+ from equation (4) into equation (3), the only unknown variable in equation (3) is the friction velocity which is calculated following the Newton-Raphson method. ΔB depends on the wall roughness and is calculated using equations provided by Cebeci and Bradshaw (1977). This approach provides three regimes based on the value of the dimensionless (normalized) roughness height (k_s^+) defined by:

$$k_s^+ = \frac{k_s u_f}{\nu}. \tag{5}$$

ΔB in the three regimes is obtained as:

Hydrodynamically smooth surface ($k_s^+ < 2.25$):
$$\Delta B = 0 \tag{6}$$

Transitional surface ($2.25 \leq k_s^+ \leq 90$):
$$\Delta B = \frac{1}{\kappa}\ln\left[\frac{k_s^+ - 2.25}{87.75} + C_s k_s^+\right]\sin\left[0.4258\,(\ln k_s^+ - 0.811)\right] \tag{7}$$

Fully-rough surface ($k_s^+ > 90$):
$$\Delta B = \frac{1}{\kappa}\ln\left[1 + C_s k_s^+\right] \tag{8}$$

where k_s is the equivalent roughness height and C_s is the roughness constant. The value of turbulent properties (kinematic energy, k, and turbulence frequency, ω) needs to be determined near the walls. In the present setup, the turbulence kinematic energy, k, near the wall is satisfied by Neumann condition for both smooth and rough walls (Nezu, 1977, Sumer et al., 2001, Sumer et al., 2003, and Fuhrman et al., 2010). The turbulence frequency, ω, for the first layer of cells next to the wall is calculated following Ferziger et al. (2008) which is valid for the logarithmic region of the boundary layer:

$$\omega = \frac{\sqrt{k}}{C_\mu^{0.25}\kappa y} \tag{9}$$

where C_μ has a value of 0.09.

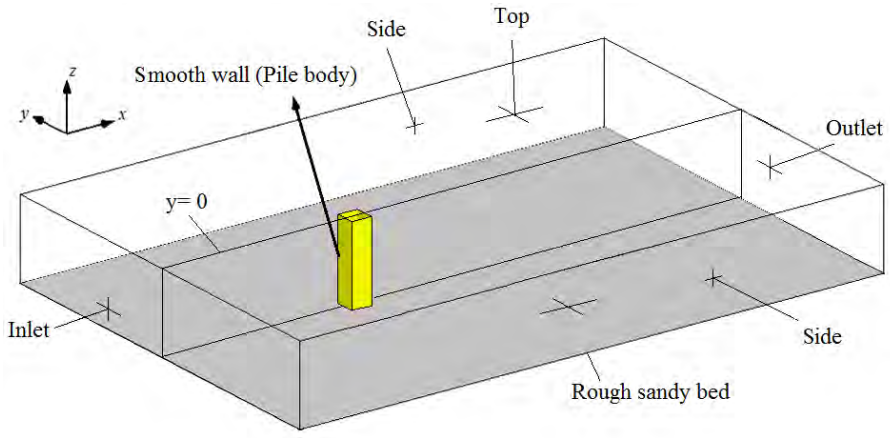


Fig 1. Boundaries of the computational domain for test case of scouring around a square pier.

2.2 Bed shear stress

The hydrodynamic and sediment transport models are connected through the bed shear stress since the calculated bed shear stress from the hydrodynamic model serves as the primary input parameter to the morphodynamic model. Therefore, an accurate calculation of bed shear stress is essential for obtaining realistic sediment transport results. Here, the vector of the bed shear stress acting on the wall is calculated from the inner product of the stress tensor, $\boldsymbol{T}$, and the unit normal vector of the face of the wall ($\vec{n}$):

$$\boldsymbol{T} = (v_t + v)(\nabla U + \nabla U^T) \tag{10}$$

$$\vec{\tau} = \boldsymbol{T}.\vec{n} \tag{11}$$

where v_t is the turbulence viscosity defined by:

$$v_t = v\left(\frac{y^+\kappa}{\ln\left(Ey^+/e^{\kappa\Delta B}\right)} - 1\right) \tag{12}$$

where $\kappa = 0.4$ is the von Karman constant.

2.3 Sediment transport model

The adopted sediment transport model includes bedload and suspended load components. The bedload model computes the flux of the sediments that roll, slide or jump along the bed in a thin layer very close to the bed. For sediments transported above the bedload layer, the suspended load model calculates the sediment flux. These two sediment transport modes are separated by a hypothetical layer called the reference level. The bedload rate, q_B, is calculated based on the model given by Roulund et al. (2005), which is an extension of Engelund and Fredsøe (1976) model for a 2D bed. To solve the suspended load part of the model, the advection-diffusion equation is chosen to fulfill the case of non-uniform and transient flow around structures:

$$\frac{\partial c}{\partial t} + \nabla.\left[(\vec{u} + \vec{w}_s)c\right] = \nabla.\left[\left(\nu + \frac{\nu_t}{\sigma_c}\right)\nabla c\right] + S_c \tag{13}$$

where c is the volumetric (dimensionless) suspended sediment concentration, $\vec{u}$ and $\vec{w}_s$ are the fluid velocity and sediment fall velocity vectors, respectively. $\nu + \nu_t/\sigma_c$ is the sediment diffusivity coefficient, where ν is the kinematic viscosity of the fluid, ν_t is the turbulence viscosity and σ_c is the concentration-dependent turbulent Schmidt number which is chosen as 0.8 similar to Liang and Cheng (2005). S_c is the source/sink term for the entrainment, E_Δ, and deposition rate, D_Δ, $S_c = E_\Delta - D_\Delta$. The entrainment rate, E_Δ, is obtained from:

$$E_\Delta = c_e w_s \tag{14}$$

where w_s can be calculated by the method proposed by Soulsby (1997) and c_e is the equilibrium (reference) concentration of suspended load at a reference level height from the bed, Δ. c_e as described by Rijn (1984) given by:

$$c_e = 0.015\frac{d_{50}T^{1.5}}{\Delta d_*^{0.3}} \tag{15}$$

where Δ is adopted based on the average particle diameter, d_{50}, and in the range of $3d_{50}$ to $4d_{50}$. In equation (15), T is the dimensionless transport stage parameter:

$$T = \frac{\theta - \theta_c}{\theta_c} \tag{16}$$

where θ is Shields parameter, and θ_c is the critical Shields parameter corresponding to the initiation of sand particle motion on a horizontal bed, and d_* is non-dimensional grain size,

$$d_* = \left[\frac{g(s-1)}{\nu^2}\right]^{1/3} d_{50} \tag{17}$$

where, g is the acceleration of gravity, and s is relative density of the sand. The deposition rate, D_Δ, is obtained from the approach applied by Liu and García (2008):

$$D_\Delta = c_b w_s \tag{18}$$

where c_b is the sediment concentration at the reference level.
In the present study, the first layer of computational cells closest to the bed is adjusted to be located at the distance of $3d_{50}$ to $4d_{50}$ from the bed in accordance with the adopted reference level height from the bed. Hence, the sediment concentration at the first layer of mesh closest to the bed is equal to the sediment concentration at the reference level, c_b. This condition is initially checked for all applied test cases, however, due to the expansion and contraction of the meshes due to the bed deformation in simulation process, some minor deviations may occur.
In the present model, both hydrodynamic and morphodynamic models are solved in each simulation time step and calculated changes as a result of solving mass conservation equation by Exner (1925) are implemented as a bed deformation in the computational domain. A sand sliding method, similar to the one used in Roulund et al. (2005), is also employed to avoid unreal bed slopes. To smooth the internal domain base on the deformed bed in the vertical direction, the Laplacian operator smoothing approach is considered to control mesh motion.

3 Results and discussions

To ensure that the applied coupled model is capable of predicting the local scour progression around vertical piers with different cross-section shapes, it is validated against three experimental test results reported by Roulund et al. (2005) and Khosronejad et al. (2012). In the first test case, the experimental measurements from Roulund et al. (2005) in the temporal development of local scour around a circular pier under live-bed condition is provided. In the second and third test cases, the experimental data from Khosronejad et al. (2012) in the formation of scour holes around square and diamond piers under clear-water condition is presented.

3.1 Scouring around a circular pier

3.1.1 Experimental data

This experiment was conducted in a flume, 10 m long and 4 m wide. A 0.1 m diameter pile with the hydraulically smooth body was fixed at 6.6 m downstream of the inlet section. The bed was covered with sand with a particle diameter of $d_{50} = 0.26\ mm$. The test was conducted under live-bed and steady current flow. The water depth in the experiment was maintained at 0.4 m and the depth average velocity was U= 0.46 m/s. Fig. 2 shows the details of the test flume.

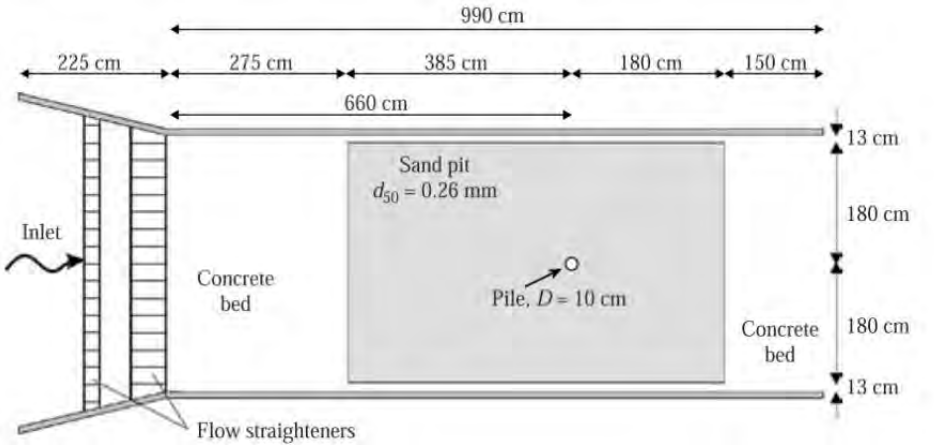


Fig 2. Test conditions for scouring around a circular pier (Roulund et al., 2005).

3.1.2 Numerical simulation

An initial mesh dependency study was done and a 3D mesh with around 400,000 cells was chosen as the top view of it is shown in Fig. 3. In this test case, the height of the center of the first layer of mesh closest to the bed was considered 1 mm (around $4d_{50}$) to satisfy the morphodynamic requirement of the model. With a good estimation, these points (centers) are located in the logarithmic region of the hydrodynamic boundary layer. The bed boundary was considered as a mobile bed with a roughness factor of $k_s = 2.5\, d_{50}$ and the critical Shields parameter for the horizontal bed of θ_{c0}=0.05 as proposed by Roulund et al. (2005). The inlet boundary was supplied with the velocity profile obtained from the curve fitting of the provided profile in Roulund et al. (2005) as shown in fig. 4. The experimental test reached equilibrium scour stage after around 2 hours. However, the changes in the results after the first hour were small. Hence, to reduce the required simulation time, the model was only run for $T = 1$ hour of physical time which required around 3 months of simulation time on a 2.3 GHz CPU with 8 GB RAM. Fig. 5 shows a sequence of simulated bed deformation pictures at times $t = T/60, T/12, T/4, T$ from the start of the simulation. It is observed that the deformation of the bed and scouring adjacent to the pier starts from early stages of the simulation and extends in terms of the hole depth and the area affected by it. In fig. 6, the evolution of the scour hole in terms of the scour depth, S, in front and back of the pile, in the form of dimensionless scour depth, S/D, is compared with the experimental and simulation results of Roulund et al. (2005), Stahlmann (2013) and Gothel (2008). Dargahi (1990) pointed out that there is an initial stage before the beginning of scouring and formation of HSVs upstream of the piers. This initial stage is the corresponding time for the expansion of the boundary layer over the bed. It is here assumed that the measured scouring experimental data from Roulund et al. (2005) were based on the start of the formation of HSVs and the observation of sign of scouring upstream of the pile as it can be derived from Roulund's results. The results of the present work (Solid line in fig. 6) has a very good agreement with the experimental results in terms of predicting the maximum scour hole during evolution. The maximum discrepancy in the prediction of maximum scour hole depth is less than 4.6% during the evolution process, however, the model overestimates the scour depth at the back of the pier from an early stage of the simulation and the maximum difference happens after 5 minutes of simulation which is around 30%.

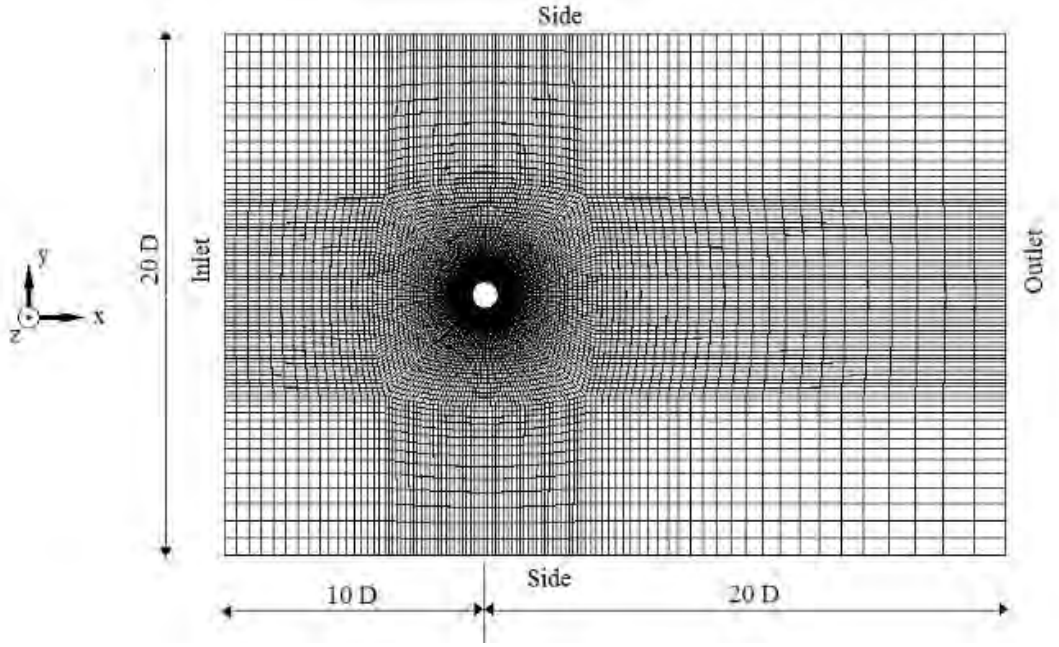


Fig 3. Top view of generated mesh for test case of scouring around a circular pier.

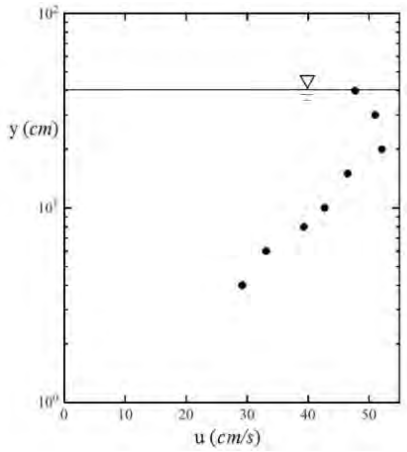


Fig 4. Undisturbed mean flow velocity profile (Roulund et al., 2005).

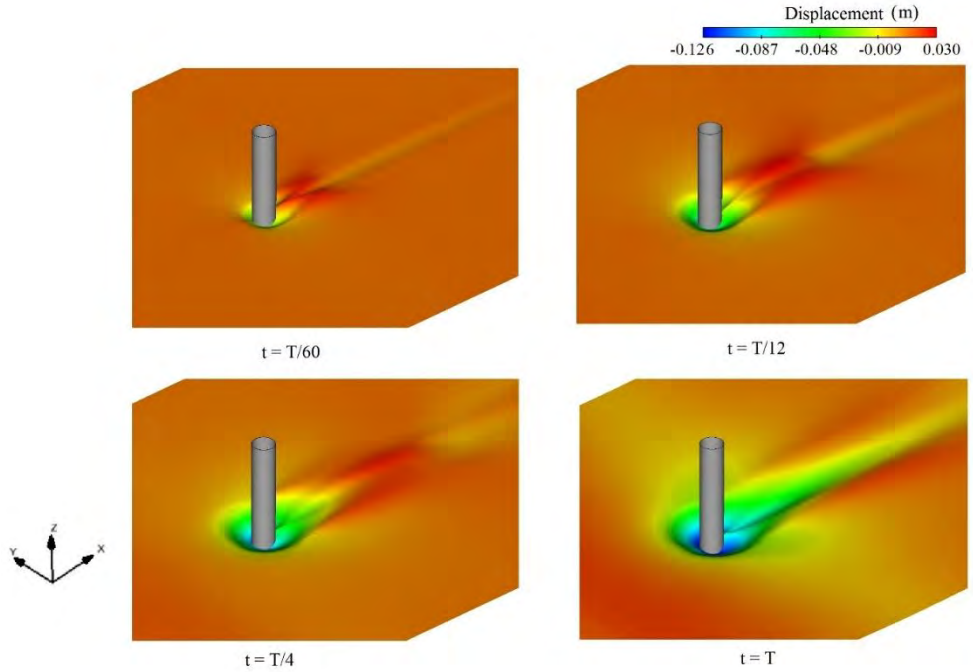
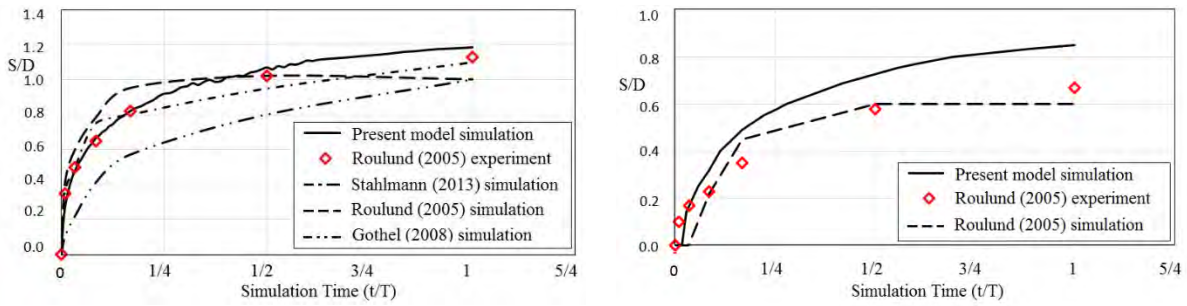


Fig 5. Simulated bed displacement at 4 different times of the simulation $t = T/60, T/12, T/4, T$.



(a) upstream of the circular pier (b) downstream of the circular pier

Fig 6. Changes in maximum scour depth with time.

3.2 Scouring around a diamond and square pier

3.2.1 Experimental data

The formation of HSV upstream of the mounted piers is one of the main factors in the development of the local scour. Khosronejad et al. (2012) mentioned that the intensity of the main HSV is in connection with the bluntness factor (BF). The bluntness factor is a character of describing the mounted pier nose geometry (Fleming et al., 1991; Fleming et al., 1993):

$$BF = \frac{1}{2}\frac{R}{X}\left(\frac{D_w}{S_D} + \frac{S_D}{X}\right) \tag{19}$$

where R is the radius of the leading-edge, X is the length of the chordwise position of the nose from the maximum width of the pier D_w, and S_D is the distance from the leading edge along the structure surface to the maximum width of the pier. Piers with larger bluntness factor face stronger HSVs. To evaluate the robustness of the developed model on the evolution of scour hole around piers with different cross-

section shapes, the model was verified against experimental cases from Khosronejad et al. (2012) for square and diamond piers with $BF \rightarrow \infty$ and 0, respectively.

The tests were conducted in a flume with 10 m long and 1.21 m wide. In both tests, the piers were mounted at 4 m downstream of the flume inlet. Tests were conducted for a square-shaped cylinder with an edge length of 16.51 cm but with 90° and 45° orientation angles to the flow corresponding to the square and diamond piers. Hence in the case of the square pier, the pier width to the flow direction, w_p, was 16.51 cm and for the diamond pier, 23.35 cm. The piers' body was considered as a hydraulically smooth surface. Both tests were carried out under clear-water conditions and the bed was covered with sand particles with the mean diameter of $d_{50} = 0.85\ mm$, while different flow condition was applied for the tests. For the square pier test, the experiment was run for the undisturbed flow with a mean average velocity of U = 0.22 m/s and uniform flow depth of 13.9 cm, while the mean averaged velocity and flow depth of 0.21 m/s and 15.7 cm were considered for the case of the diamond pier test.

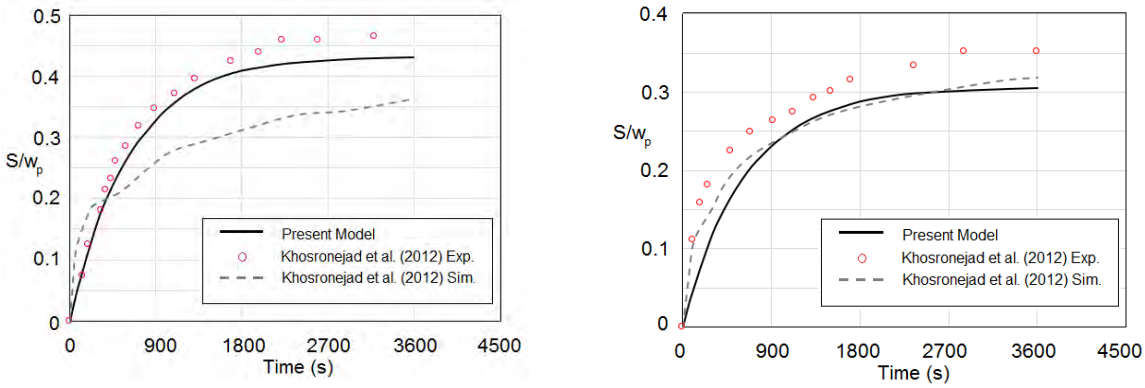
3.2.2 Numerical simulation

Numerical simulation for both cases was followed in computational domains 3 m long and 2 m wide where the piers were located 1 m downstream of the inlet. The height of the domain was set equal to the water depth in each case. In these test cases, the height of the center of the first layer of mesh closest to the bed was considered 2.5 mm to satisfy the hydrodynamic and morphodynamic requirements of the model. A mesh dependency test was also done for these cases and 3D meshes with around 350,000 cells were chosen. The approaching flow attributes at the inlet was supplied by a preliminary hydrodynamic simulation which was conducted for a domain with the same condition as the original mesh and with 3 m length but without the presence of the pier. The length of the preliminary simulation was kept 3 m to provide the approaching flow with the same condition as the experiments. The bed Nikuradse equivalent sand roughness for this case was considered equal to $3d_{50}$ as suggested by Khosronejad et al. (2012) and the critical Shields parameter value for horizontal bed was calculated from the equation proposed by Soulsby and Whitehouse (1997):

$$\theta_{c0} = \frac{0.3}{1 + 1.2d_*} + 0.055(1 - e^{-0.02d_*}). \tag{20}$$

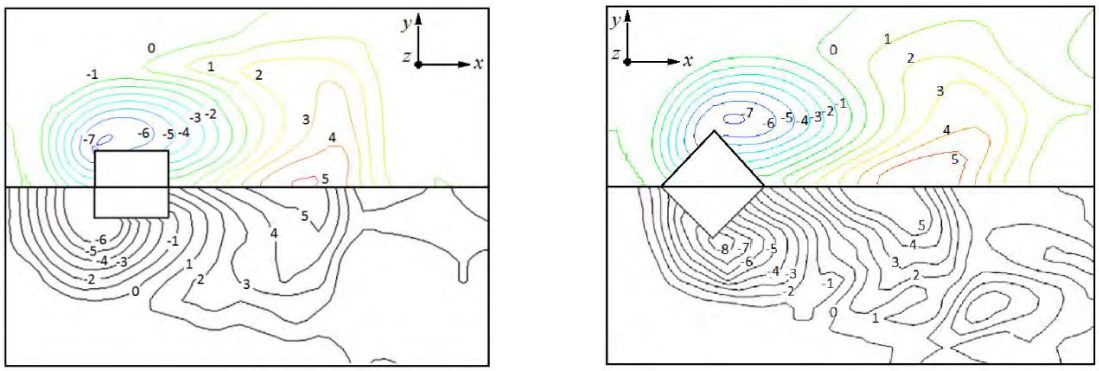
Fig. 7 displays the temporal evolution of scour depth for both diamond and square piers. The results from present simulations are compared with simulation and experimental results from Khosronejad et al. (2012). In the case of the square pier, the result from the present model outperforms the numerical model of Khosronejad et al. (2012), while both simulation results underestimated the scour progression. The numerical results for diamond pier are roughly similar. The measurement of scour depth in equilibrium condition for the present simulations shows the differences of 6.7% and 13.1% from the experiment data for the square and diamond pier cases, respectively.

A comparison between the bed topography in equilibrium condition for the results of the present simulations and the laboratory measurements from Khosronejad et al. (2012) for the diamond and square piers is shown in Fig. 8. The experimental data is only presented for one side of the symmetry plane y=0 in Khosronejad et al. (2012). Hence, for the sake of comparison, in each case, the experimental results are provided on the bottom side and the present model numerical results on the top side. In the square pier case, Khosronejad et al. (2012) as a result of laboratory measurements pointed out that the maximum scour depth occurred in the front corners of the pier, while the area with significant depth was seen around the nose of the pier. The present numerical model also found the maximum scour depth in the front corners of the pier, however, it failed to accurately predict the depth of the scoured area around the front side of the pier. In contrast, the maximum deposition height position given by the numerical model is in accordance with experimental measurements. For the diamond pier, a good agreement in the position of the maximum scour depth and deposition height is observed between the numerical simulation results and experimental data. The obtained results from the simulations indicated that the present model has a good capability in predicting the main characteristics of scour around the square and diamond piers.



(a) Square pier (b) Diamond pier

Fig 7. Changes in scour depth with time in case of (a) square and (b) diamond pier.



(a) Square pier (b) Diamond pier

Fig 8. Comparison of the present model simulation (top) and measured (bottom) bed topography at equilibrium condition (The measurement unit is cm).

4 Conclusion

In the present study, a 3D numerical model for the prediction of scour evolution around vertical cylinders was developed and implemented in OpenFOAM® framework. A coupled approach was applied for combining the hydrodynamic and morphodynamic parts. The proposed model is validated against the empirical measurements of local scour development around single vertical piers with circular, square, and diamond cross-section shapes obtained from the literature. The measurement of scour depth in equilibrium condition for the simulations revealed the differences of 4.6%, 6.7% and 13.1% from the experimental measurements for the circular, square, and diamond pier cases, respectively. The model displayed a remarkable performance in the prediction of scour around circular and square piers where HSVs have a leading impact on scour progression. On the other hand, the maximum deviation was found in the case of the diamond pier where HSVs are weak and have minimum impact on the formation of local scour. Overall, the results confirm that the prediction capability of the present model is almost independent of the strength of the formed HSVs and pier cross-section shapes.

References

AGUI, J. H. & ANDREOPOULOS, J. (1992), "Experimental investigation of a three-dimensional boundary layer flow in the vicinity of an upright wall mounted cylinder (data bank contribution)".

BAKER, C. J. (1980), "The turbulent horseshoe vortex", *Journal of Wind Engineering and Industrial Aerodynamics,* **6,** 9-23.

BAYKAL, C., SUMER, B. M., FUHRMAN, D. R., JACOBSEN, N. G. & FREDSØE, J. (2015), "Numerical investigation of flow and scour around a vertical circular cylinder", *Philosophical Transactions of the Royal Society A: Mathematical, Physical and Engineering Sciences,* **373,** 20140104.

BAYKAL, C., SUMER, B. M., FUHRMAN, D. R., JACOBSEN, N. G. & FREDSØE, J. (2017), "Numerical simulation of scour and backfilling processes around a circular pile in waves", *Coastal Engineering,* **122,** 87-107.

CEBECI, T. & BRADSHAW, P. (1977), "Momentum transfer in boundary layers", *Washington, DC, Hemisphere Publishing Corp.; New York, McGraw-Hill Book Co., 1977. 407 p.*

DARGAHI, B. (1989), "The turbulent flow field around a circular cylinder", *Experiments in Fluids,* **8,** 1-12.

DARGAHI, B. (1990), "Controlling mechanism of local scouring", *Journal of Hydraulic Engineering,* **116,** 1197-1214.

DE RUITER, J. C. C. (1983), "Incipient motion and pick-up of sediment as function of local variables", *unpublished notes, Delft Hydraulics, Delft*.

DEY, S., BOSE, S. K. & SASTRY, G. L. N. (1995), "Clear water scour at circular piers: a model", *Journal of Hydraulic Engineering,* **121,** 869-876.

ENGELUND, F. & FREDSØE, J. (1976), "A sediment transport model for straight alluvial channels", *Hydrology Research,* **7,** 293-306.

ESCAURIAZA, C. & SOTIROPOULOS, F. (2011), "Initial stages of erosion and bed form development in a turbulent flow around a cylindrical pier", *Journal of Geophysical Research: Earth Surface,* **116**.

EXNER, F. M. (1925), "Uber die wechselwirkung zwischen wasser und geschiebe in flussen", *Akad. Wiss. Wien Math. Naturwiss. Klasse,* **134,** 165-204.

FERZIGER, J. H., PERIĆ, M. & STREET, R. L. (2008) *Numerische Strömungsmechanik,* Springer.

FLEMING, J. L., SIMPSON, R. L., COWLING, J. E. & DEVENPORT, W. J. (1993), "An experimental study of a turbulent wing-body junction and wake flow", *Experiments in fluids,* **14,** 366-378.

FLEMING, J. L., SIMPSON, R. L. & DEVENPORT, W. J. (1991), "An experimental study of a turbulent wing-body junction and wake flow(Technical Report, 1 Jun. 1989- 31 Aug. 1991)".

FUHRMAN, D. R., DIXEN, M. & JACOBSEN, N. G. (2010), "Physically-consistent wall boundary conditions for the k-ω turbulence model", *Journal of Hydraulic Research,* **48,** 793-800.

GHIASSI, R. & ABBASNIA, A. H. (2013), "Investigation of vorticity effects on local scouring", *Arabian Journal for Science and Engineering***,** 537-548.

GOTHEL, O. (2008), "Numerical modeling of flow and wave-induced scour around vertical structures".

GÖTHEL, O. & ZIELKE, W. (2007) Numerical Modelling of Scour at Offshore Wind Turbines. *Coastal Engineering 2006: (In 5 Volumes).* World Scientific.

GRAF, W. H. & ISTIARTO, I. (2002), "Flow pattern in the scour hole around a cylinder", *Journal of Hydraulic Research,* **40,** 13-20.

HANSEN, E. A., SIMONSEN, H. J., NIELSEN, A. W., PEDERSEN, J. & HØGEDAL, M. (2007) "Scour protection around offshore wind turbine foundations, full-scale measurements". *132-138*.

ISSA, R. I. (1986), "Solution of the implicitly discretised fluid flow equations by operator-splitting", *Journal of computational physics,* **62,** 40-65.

KHOSRONEJAD, A., KANG, S., BORAZJANI, I. & SOTIROPOULOS, F. (2011), "Curvilinear immersed boundary method for simulating coupled flow and bed morphodynamic interactions due to sediment transport phenomena", *Advances in water resources,* **34,** 829-843.

KHOSRONEJAD, A., KANG, S. & SOTIROPOULOS, F. (2012), "Experimental and computational investigation of local scour around bridge piers", *Advances in Water Resources,* **37,** 73-85.

KIM, H. S., NABI, M., KIMURA, I. & SHIMIZU, Y. (2014), "Numerical investigation of local scour at two adjacent cylinders", *Advances in water resources,* **70,** 131-147.

KIRKIL, G., CONSTANTINESCU, G. & ETTEMA, R. (2005) The horseshoe vortex system around a circular bridge pier on equilibrium scoured bed. *Impacts of Global Climate Change.*

KIRKIL, G., CONSTANTINESCU, G. & ETTEMA, R. (2009), "Detached eddy simulation investigation of turbulence at a circular pier with scour hole", *Journal of Hydraulic Engineering,* **135,** 888-901.

KIRKIL, G., CONSTANTINESCU, S. G. & ETTEMA, R. (2008), "Coherent structures in the flow field around a circular cylinder with scour hole", *Journal of Hydraulic Engineering,* **134,** 572-587.

KOVACS, A. & PARKER, G. (1994), "A new vectorial bedload formulation and its application to the time evolution of straight river channels", *Journal of fluid Mechanics,* **267,** 153-183.

LIANG, D. & CHENG, L. (2005), "Numerical model for wave-induced scour below a submarine pipeline", *Journal of waterway, port, coastal, and ocean engineering,* **131,** 193-202.

LIU, X. & GARCÍA, M. H. (2008), "Three-dimensional numerical model with free water surface and mesh deformation for local sediment scour", *Journal of waterway, port, coastal, and ocean engineering,* **134,** 203-217.

MELVILLE, B. W. & CHIEW, Y.-M. (1999), "Time scale for local scour at bridge piers", *Journal of Hydraulic Engineering,* **125,** 59-65.

MENTER, F. R. (1992), "Improved two-equation k–ω turbulence models for aerodynamic flows. NASA STI". Recon Technical Report 93, 22809.

NEZU, I. (1977), "Turbulent structure in open-channel flows", *English translation of the Japanese dissertation of Iehisa Nezu.* .

OLSEN, N. R. B. & KJELLESVIG, H. M. (1998), "Three-dimensional numerical flow modeling for estimation of maximum local scour depth", *Journal of Hydraulic Research,* **36,** 579-590.

OLSEN, N. R. B. & MELAAEN, M. C. (1993), "Three-dimensional calculation of scour around cylinders", *Journal of Hydraulic Engineering,* **119,** 1048-1054.

OMARA, H., ELSAYED, S. M., ABDEELAAL, G. M., ABD-ELHAMID, H. F. & TAWFIK, A. (2019), "Hydromorphological numerical model of the local scour process around bridge piers", *Arabian Journal for Science and Engineering,* **44,** 4183-4199.

PARKER, G., SEMINARA, G. & SOLARI, L. (2003), "Bed load at low Shields stress on arbitrarily sloping beds: Alternative entrainment formulation", *Water resources research,* **39**.

RIJN, L. C. V. (1984), "Sediment transport, part II: suspended load transport", *Journal of hydraulic engineering,* **110,** 1613-1641.

ROULUND, A., SUMER, B. M., FREDSØE, J. & MICHELSEN, J. (2005), "Numerical and experimental investigation of flow and scour around a circular pile", *Journal of Fluid Mechanics,* **534,** 351-401.

SALAHELDIN, T. M., IMRAN, J. & CHAUDHRY, M. H. (2004), "Numerical modeling of three-dimensional flow field around circular piers", *Journal of Hydraulic Engineering,* **130,** 91-100.

SEAL, C. V. & SMITH, C. R. (1999), "Visualization of a mechanism for three-dimensional interaction and near-wall eruption", *Journal of Fluid Mechanics,* **394,** 193-203.

SOULSBY, R. (1997) *Dynamics of marine sands: a manual for practical applications,* Thomas Telford.

SOULSBY, R. & WHITEHOUSE, R. (1997) "Threshold of sediment motion in coastal environments.". Pacific Coasts and Ports' 97: Proceedings of the 13th Australasian Coastal and Ocean Engineering Conference and the 6th Australasian Port and Harbour Conference; Volume 1*: Centre for Advanced Engineering, University of Canterbury, 145*.

STAHLMANN, A. (2013) "Numerical and experimental modeling of scour at foundation structures for offshore wind turbines". *International Society of Offshore and Polar Engineers*.

STAHLMANN, A. & SCHLURMANN, T. (2012) "Numerical and Experimental Modeling of Scour at Tripod Foundations for Offshore Wind Turbines". *Proc of the 6th International Conference on Scour and Erosion, ,* Paris, France.

SUMER, B. M., BAYKAL, C., FUHRMAN, D. R., JACOBSEN, N. G. & FREDSØE, J. (2014) "Numerical calculation of backfilling of scour holes".

SUMER, B. M., CHRISTIANSEN, N. & FREDSØE, J. (1993), "Influence of cross section on wave scour around piles", *Journal of waterway, port, coastal, and ocean engineering,* **119,** 477-495.

SUMER, B. M., CHUA, L. H. C., CHENG, N. S. & FREDSØE, J. (2003), "Influence of turbulence on bed load sediment transport", *Journal of Hydraulic Engineering,* **129,** 585-596.

SUMER, B. M., COKGOR, S. & FREDSØE, J. (2001), "Suction removal of sediment from between armor blocks", *Journal of hydraulic engineering,* **127,** 293-306.

SUMER, B. M. & FREDSØE, J. (2001a), "Scour around pile in combined waves and current", *Journal of Hydraulic Engineering,* **127,** 403-411.

SUMER, B. M. & FREDSØE, J. (2001b), "Wave scour around a large vertical circular cylinder", *Journal of waterway, port, coastal, and ocean engineering,* **127,** 125-134.

SUMER, B. M., FREDSØE, J. & CHRISTIANSEN, N. (1992), "Scour around vertical pile in waves", *Journal of waterway, port, coastal, and ocean engineering,* **118,** 15-31.

SUMER, B. M., PETERSEN, T. U., LOCATELLI, L., FREDSØE, J., MUSUMECI, R. E. & FOTI, E. (2012), "Backfilling of a scour hole around a pile in waves and current", *Journal of Waterway, Port, Coastal, and Ocean Engineering,* **139,** 9-23.

TOPCZEWSKI, Ł., CIEŚLA, J., MIKOŁAJEWSKI, P., ADAMSKI, P. & MARKOWSKI, Z. (2016), "Monitoring of scour around bridge piers and abutments", *Transportation Research Procedia,* **14,** 3963-3971.

TSENG, M. H., YEN, C. L. & SONG, C. C. S. (2000), "Computation of three-dimensional flow around square and circular piers", *International journal for numerical methods in fluids,* **34,** 207-227.

APPENDIX III

Investigation of Scour around Two Side-by-Side Piles with Different Spacing Ratios in Live-bed

Amir Bordbar[1(✉)], Soroosh Sharifi[1] and Hassan Hemida[1]

[1] University of Birmingham, Birmingham B15 2TT, UK

Abstract. In this study, a developed model is employed for numerically investigating scour around a group of two identical side-by-side piles. The model benefits from a coupled approach between a hydrodynamic and a morphodynamic model which is successfully validated for predicting scour around a single circular pile. The hydrodynamic model solves unsteady Reynolds-Averaged Navier-Stokes (RANS) equations in combination with the k-ω-SST turbulence closure model. The morphodynamic model entails bedload and suspended load sediment transport models for non-cohesive sand. The morphological evolution of the bed due to the sediment transport fluxes is expressed by a means of a mass-balance equation. The model is run for two side-by-side piles with three different spacing ratios *G/D*=1, 2, and 3, where *G* represents the distance between the piles and *D* is the pile diameter, under steady-current flow and live-bed conditions. The results of the investigation reveal an inverse correlation between the spacing ratio and the scour hole depth adjacent to piles. The results are generalized and an equation is obtained for equilibrium scour hole depth as a function of the spacing ratio.

Keywords: Scour, Side-by-side piles, CFD, Sediment transport.

1 Introduction

The flow around riverine structures is characterized by strong 3D turbulent motions. In the case of bridge piers, these turbulent motions may wash off part of the sediments around the piers and cause local scour which may lead to bridge failures. A study over 30 years in the United States [1] concluded that 60% of total bridge failure cases were due to local scour. Hence, protecting bridge piers from scour damage can lead to significant savings in maintenance and repair costs which requires a thorough knowledge of scouring characteristics.

There are variety of elements that may affect the local scouring around piers. These factors generally include foundation geometry, fluid and flow parameters, and bed material parameters. In this study, the effect of foundation geometry in a group of two identical side-by-side circular piles with different spacing ratios on flow behavior and local scour is studied. In the literature, few experimental and numerical studies have investigated the impact of a group of side-by-side piles on scouring. Among them, Ataie-Ashtiani and Beheshti [2] experimentally investigated local scour around pile groups including two to eight circular piles with different arrangements and spacing ratios in clear-water steady current conditions. In total, 112 tests were carried out. It was found that scour around a pile group can be different from that of a single pile depending on pile spacing. In their study, for the case of two side-by-side piles, the maximum scour depth happened for the $G/D \approx 0.25$, where G represents the distance between the piles and D is the pile diameter. In this case, the maximum scour depth was 50% more than that for a single pile. In another work, Kim et al. [3] numerically investigated the progression of the scour patterns around two adjacent circular cylinders in side-by-side and tandem arrangements with diverse spacing ratios between 0.25 to 4 in clear-water condition. Large Eddy Simulation (LES) approach was employed to solve the Navier-Stokes equations which was followed by a Lagrangian approach for sediment transport. They validated their model against the experimental

data from Khosronejad et al. [4] for scour around a single circular pile. From their results, they found out that in the case of two side-by-side cylinders when $G/D \geq 1.5$, the local scour patterns are similar to those of a single cylinder. Zhang et al. [5] ran a set of numerical simulations to study local scour around a different arrangement of a group of up to three adjacent piles under steady current flow in clear-water conditions. Flow-3D was applied to investigate the local scour. The software used the volume of fluid (VOF) method to capture the water-air interface. Reynolds Averaged Navier-Stokes (RANS) equations in combination with the RNG k-ε turbulence closure was applied to solve the hydrodynamic equations. Sediment transport was modeled by both bedload and suspended load models. The model was validated against experimental data from Khosronejad et al. [4] for the scour around a single circular pile. The simulations were conducted for circular piles with D=1.5 m and G/D= 1, 2 and 3. It was observed that with increase in the spacing ratio the pile group effect decreases, as for G/D= 3, there was almost no interaction between the piles effects. Vaghefi et al. [6] experimentally studied the scour pattern around three side-by-side and tandem arrangements of circular cylinders in a 180° bend under clear-water and steady current flow conditions. Circular cylinders with constant G/D= 2 were placed at the positions of 60°, 90° and 120° of the bend. In their study, the maximum scouring depth occurred in the side-by-side arrangement at the position of 90° of the bend and around the pier closer to the outer bank. Qi et al. [7] made a series of experimental tests of local scour at twin piles under combined current and wave. Two pairs of piles with diameters D=12 cm and 8 cm at four different flow skew angles (α_s=0°,30°,60°, 90°) with different $0 \leq G/D \leq 3$ were considered. It is found that with increase in G/D the pile group effects gradually diminished. In their work, the maximum pile group effect on the scour depth was found to occur for G/D=0 in side-by-side arrangement. An empirical equation was established to estimate the maximum scour depth around twin piles based on G/D and α_s.

In the pertinent literature, most of the studies were done in clear-water condition and to the author's best knowledge, no numerical investigation on local scour around a pile groups has been carried out in live-bed condition. Therefore, this study aims to bridge this gap with studying the flow behavior and progression of local scour pattern around two identical side-by-side circular piles with different G/D= 1, 2 and 3 in steady current and live-bed conditions.

For this purpose, a coupled hydrodynamic and morphodynamic model is implemented in the framework of OpenFOAM®. The model only solves the water-phase around the piles. Hence, the computational domain is limited to the water-air interface on top. The model is validated against the experimental data of Roulund et al. [8] for scouring around a circular pile under steady current flow in live-bed condition. In this study, the similar flow and bed material condition as Roulund's scour test is used in all simulations.

2 Numerical method

2.1 Governing equations of the flow

In this study, the flow field is governed by incompressible unsteady RANS equations. The Reynolds stress terms in equations are modeled by the k-ω SST turbulence closure. The k-ω SST is chosen as it has a good capability in predicting adverse pressure gradients and separating flow. The computational domain and boundaries for a case of two side-by-side piles are presented in Fig. 1a. Fig. 1b shows the dimensions of the computational domain in the xy plane, while the height of the domain is equal to the water depth. The flow and turbulence properties need to be quantified in the boundaries of the computational domain. At the walls, which contain a smooth pile surface and the rough sandy bed, no-

slip boundary condition is considered while the near-wall treatment of Cebeci and Bradshaw [9] is imposed on the center of the first layer of mesh cells closest to the wall. This near-wall treatment is valid in the logarithmic region of the boundary layer and can be adapted for both smooth and rough walls to calculate friction velocity u_f. The top boundary of the domain is satisfied with the frictionless slip wall as the model does not consider the water-air interface. The sides are treated with symmetry boundary condition whereas the effects of the side walls on the approaching flow are ignored. In all simulations, the inlet flow is supplied with the approaching flow velocity profile from Roulund et al. [8] and pressure is treated with the Neumann (wall-normal zero gradient) condition. At the outlet, pressure is treated with Dirichlet condition and equal to zero while the all other flow properties are set as zero normal gradient.

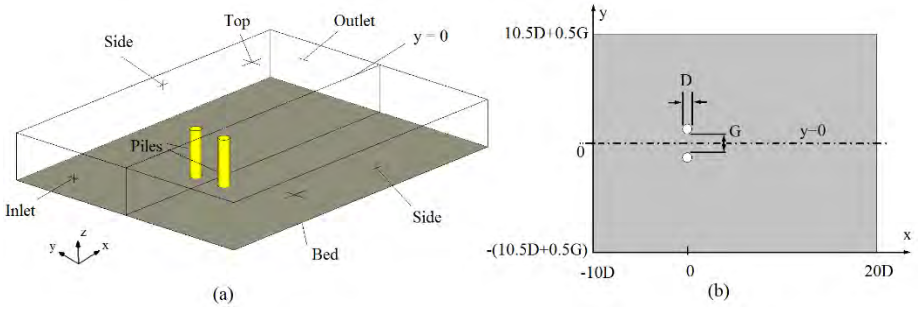


Fig. 1. (a) 3D view of the computational domain and boundaries and (b) top view for a group of two side-by-side piles.

2.2 Sediment transport and morphodynamic models

The sediment transport contains bedload and suspended load. Bedload includes a transfer of sediments that roll, slide or jump along the bed in a thin layer very close to the bed. In contrast, Suspended load includes sediment particles which transfer in the flow over the bedload without continuous contact with the bed and is dominated by fluid turbulence. These two sediment transport modes are separated by a hypothetical layer called the reference level with the height of Δ from the bed. In this study, the bedload rate for each computational grid, q_B, is calculated using a similar approach used by Roulund et al. [8] for a 2D bed. The suspended load is modeled solving an advection-diffusion equation to fulfill the case of a non-uniform and transient flow around structures:

$$\frac{\partial c}{\partial t} + \nabla.[(\vec{u} + \vec{w}_s)c] = \nabla.[D_s \nabla c] + S_\Delta \qquad (2)$$

where c is the value of fractional volumetric suspended sediment concentration, $\vec{u}$ and $\vec{w}_s$ are the fluid velocity and sediment fall velocity vectors, respectively, D_s is the sediment diffusivity coefficient and $S_\Delta = E_\Delta - D_\Delta$ is the source/sink term for the entrainment E_Δ and deposition rate D_Δ. In the present work, sediment fall velocity is calculated using the method proposed by Soulsby [10]. The entrainment rate, E_Δ, is obtained from:

$$E_\Delta = c_\Delta w_s \qquad (3)$$

where c_Δ is the reference level concentration of suspended load which is calculated as suggested by Rijn [11], where Δ is adopted based on the mean particle diameter d_{50} and equal to $4d_{50}$. The deposition rate D_Δ is obtained from the approach applied by Liu and García [12]:

$$D_\Delta = c_b w_s \qquad (4)$$

where c_b is the sediment concentration at Δ, which here, is equal to the sediment concentration in the center of the first layer of cells closest to the bed. The results of the sediment transport models are reflected as a deformation on the bed boundary of the computational domain. This is achieved by solving a mass-balance equation on a 2D mesh according to the bed boundary of the 3D domain.

3 Model validation

The model is validated against data collected from a physical scour test around a circular pile under steady current flow provided in Roulund et al. [8]. The experiment was carried out in a 10 m length and 4 m width flume. A circular pile with 0.1 m diameter was mounted in a sandy bed at 6.6. m downstream of the inlet section. The depth average of the flow for a test condition was 0.46 m/s with the water depth of 0.4 m. The sandy bed was covered with sand with a mean particle diameter d_{50}= 0.26 mm.

For the numerical modeling, a computational domain with 30D length and 20D width with a circular pile placed in the symmetry plane and at 10D downstream of the inlet was considered. The domain height was equal to water depth and equal to 4D. As a result of mesh dependency test, a generated mesh with around 400,000 cells was chosen. The thickness of the first layer of the grids closest to the bed was 2 mm to satisfy the requirements of the near-wall treatment method and the reference level height from the bed. Fig. 2 depicts the progression of the scour hole in terms of scour depth in front and back of the pile which is compared with the experimental and simulation results of Roulund et al. [8]. It is found that the maximum discrepancy in the prediction of maximum scour hole from the present simulation results and Roulund's experimental data was less than 5% during the evolution process.

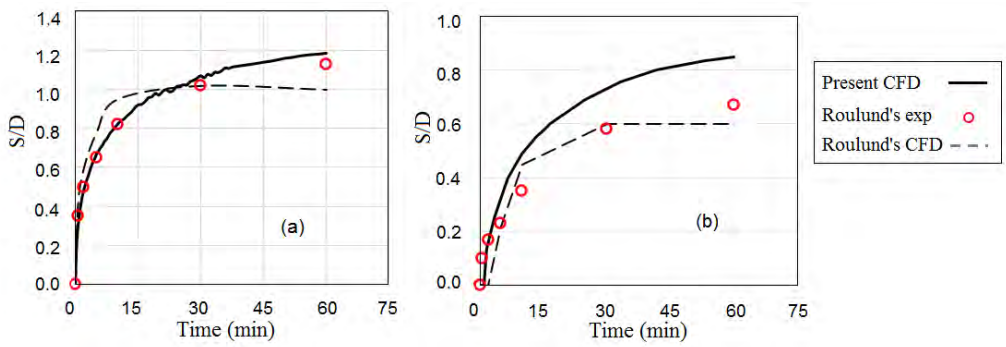


Fig. 2. The evolution of scour hole in terms of scour depth (a) in front and (b) in back of the circular pile.

4 Results

Two sets of simulations were conducted to investigate the flow behavior and formation of scour hole around a group of two circular side-by-side piles under steady current flow. One was on a rigid bed and the other one was on a mobile bed. A similar geometry (as shown in Fig. 1) and generated mesh was used for each case in both series of tests. The generated meshes included around 600,000 grids.

The first series of simulations were run to evaluate the influence of the changes in the spacing ratio in the local flow field and bed shear stress on the rigid rough bed. Fig. 3 shows the contours of flow field in x=0 plane. It is seen that the flow velocity between the piles highly depending on the G/D, while for $G/D \geq 3$ the effect of the pile group in the flow field is small.

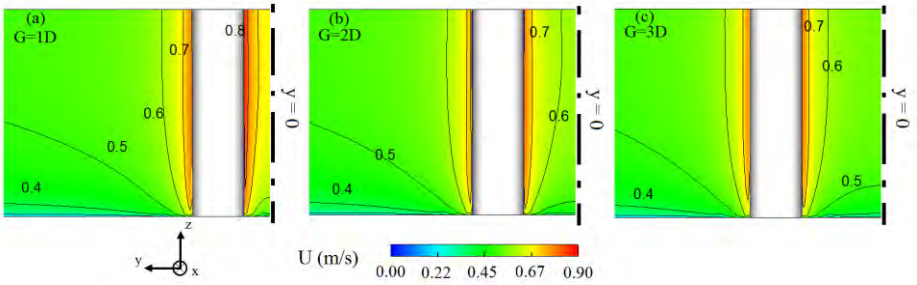


Fig. 3. Flow field adjacent to the two side-by-side piles in plane x=0 with (a) G=1D, (b) G=2D, and (c) G=3D.

The results of the bed shear stress distribution in a dimensionless form for different arrangements of two side-by-side piles are shown in Fig. 4. The dimensionless bed shear stress (BSS) is τ/τ_∞ where τ and τ_∞ are values of local and undisturbed bed shear stress, respectively. The results reveal that a

decrease in the value of G/D significantly raising the BSS between the piles which may result in deeper scour hole in the area.

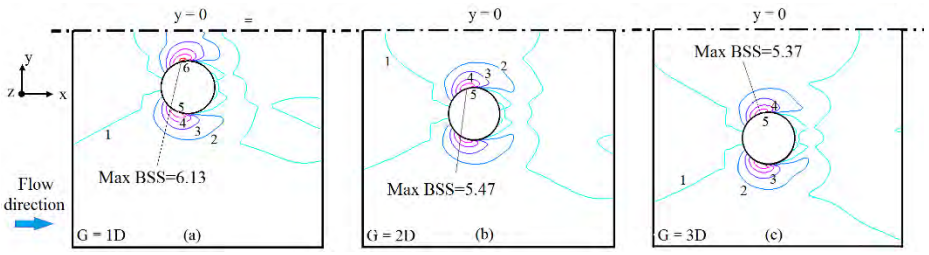


Fig. 4. Bed shear stress distribution around the two side-by-side piles for (a) G=1D, (b) G=2D, and (c) G=3D.

The second series of simulations were conducted on the mobile sandy bed to assess the progression of scour hole pattern adjacent to two side-by-side piles under current flow. Fig. 5 demonstrates the results of the scour hole pattern around piles at t=30 mins of physical time which took around 3 months of simulation time on a 2.3 GHz CPU with 8 MB RAM. The results indicate notable impacts of changes in G/D on scour pattern and maximum scour depth around the piles. The effects mitigate with increase in G/D, as for the case G= $3D$ the depth in inner and outer sides of the pile group is roughly similar to that of a single pile.

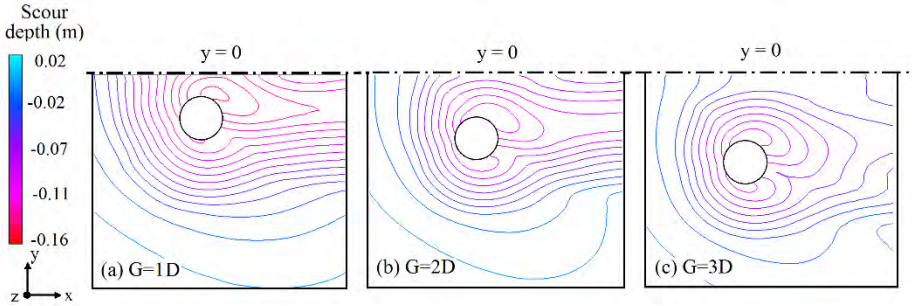


Fig. 5. Scour patterns around two side-by-side piles at t=30 mins for (a) G=1D, (b) G=2D, and (c) G=3D.

It was assumed that the scour development reaches the equilibrium condition after a first one hour of physical time for all cases similar to that of the single pile. Hence, Fig. 6a presents the evolution of dimensionless scour hole depth S/D in time for different spacing ratios of two pile groups and single pile until the equilibrium condition. The equilibrium depth for pile groups was obtained by elongation of the scour depth curves for the first 30 mins with maintaining the ratio with that of a single pile. Fig. 6b displays values of dimensionless equilibrium scour hole depth S_m/D for different arrangements of two pile groups. It was assumed that the pile group effects are completely negligible in G/D=5. Hence, S_m/D equal to that of a single pile was considered for two side-by-side piles with G/D=5. A curve was fitted for the set of data with a formula as following:

$$\frac{S_m}{D} = 1.23 + 1.73\ exp\left(-1.08\left(\frac{G}{D}\right)\right), \qquad \frac{G}{D} \geq 1. \tag{5}$$

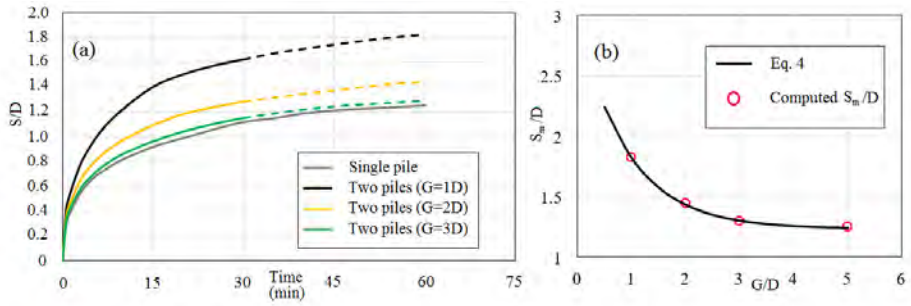


Fig. 6. (a) evolution of scour depth for two side-by-side piles and a single pile and (b) equilibrium scour depth for two side-by-side piles with different spacing ratios.

Sumer et al. [13] inferred that the equilibrium scour depth around a single pile under current flow and live-bed condition was only proportional to pile diameter D. With considering this, Eq. 4 can be generalized in case of live-bed condition for two identical circular side-by-side piles, however more investigation is needed to understand the impacts of the other factors.

5 Conclusion

In the present study, a numerical model for the prediction of flow behavior and scour pattern around pile groups is implemented. The results for the flow field, bed shear stress and scour pattern for two identical side-by-side piles for different G/D values are provided. The results depict that for $G/D \geq 3$ the pile group effect gradually vanishes. An equation is fitted for the computed equilibrium scour depths for different spacing ratios which can be used for prediction of maximum scour depth adjacent to two side-by-side piles under current steady flow and live-bed condition. The equation is valid for $G/D \geq 1$, as the physics of the problem may change for lower spacing ratios.

References

1. Briaud J.-L., Ting F. C. K., Chen H. C., Gudavalli R., Perugu S., Wei G.: SRICOS: Prediction of scour rate in cohesive soils at bridge piers. Journal of Geotechnical and Geoenvironmental Engineering 125(4):237-46 (1999).

2. Ataie-Ashtiani B., Beheshti A. A.: Experimental investigation of clear-water local scour at pile groups. J Journal of Hydraulic Engineering 132(10):1100-4 (2006).

3. Kim H., Nabi M., Kimura I., Shimizu Y.: Numerical investigation of local scour at two adjacent cylinders. Advances in water resources 70:131-47 (2014).

4. Khosronejad A., Kang S., Sotiropoulos F.: Experimental and computational investigation of local scour around bridge piers. Advances in Water Resources 37:73-85 (2012).

5. Zhang Q., Zhou X. L., Wang J. H.: Numerical investigation of local scour around three adjacent piles with different arrangements under current. J Ocean Engineering 142:625-38 (2017).

6. Vaghefi M., Motlagh M. J. T. N., Hashemi S. S., Moradi S.: Experimental study of bed topography variations due to placement of a triad series of vertical piers at different positions in a 180 bend. J Arabian Journal of Geosciences 11(5):102 (2018).

7. Qi W. G., Li Y. X., Xu K., Gao F. P.: Physical modelling of local scour at twin piles under combined waves and current. J Coastal Engineering 143:63-75 (2019).

8. Roulund A., Sumer B. M., Fredsøe J., Michelsen J.: Numerical and experimental investigation of flow and scour around a circular pile. Journal of Fluid Mechanics 534:351-401 (2005).

9. Cebeci T., Bradshaw P.: Momentum transfer in boundary layers. Washington, DC, Hemisphere Publishing Corp; New York, McGraw-Hill Book Co, 1977 407 p (1977).

10. Soulsby R.: Dynamics of marine sands: a manual for practical applications: Thomas Telford; 1997.

11. Rijn L. C. V.: Sediment transport, part II: suspended load transport. Journal of hydraulic engineering 110(11):1613-41 (1984).

12. Liu X., García M. H.: Three-dimensional numerical model with free water surface and mesh deformation for local sediment scour. Journal of waterway, port, coastal, and ocean engineering 134(4):203-17 (2008).

13. Sumer B. M., Christiansen N., Fredsøe J.: Influence of cross section on wave scour around piles. Journal of waterway, port, coastal, and ocean engineering 119(5):477-95 (1993).

REFERENCES

AGUI, J. H. & ANDREOPOULOS, J. (1992), "Experimental investigation of a three-dimensional boundary layer flow in the vicinity of an upright wall mounted cylinder (data bank contribution)".

AHMAD, N., KAMATH, A. & BIHS, H. (2020), "3D numerical modelling of scour around a jacket structure with dynamic free surface capturing", *J Ocean Engineering,* 200**,** 107104.

AHMED, F. & RAJARATNAM, N. (1998), "Flow around bridge piers", *Journal of Hydraulic Engineering,* 124**,** 288-300.

AL-HASHEMI, H. M. B. & AL-AMOUDI, O. S. B. J. P. T. (2018), "A review on the angle of repose of granular materials", 330**,** 397-417.

AL-SHUKUR, A.-H. K., OBEID, Z. H. J. I. J. O. C. E. & TECHNOLOGY (2016), "Experimental study of bridge pier shape to minimize local scour", 7**,** 162-171.

ALEMI, M., PÊGO, J. P. & MAIA, R. (2019), "Numerical simulation of the turbulent flow around a complex bridge pier on the scoured bed", *J European Journal of Mechanics-B/Fluids,* 76**,** 316-331.

AMOUDRY, L., HSU, T. J. & LIU, P. F. J. J. O. G. R. O. (2008), "Two-phase model for sand transport in sheet flow regime", 113.

ANDREOTTI, B., FORTERRE, Y. & POULIQUEN, O. (2013) *Granular media: between fluid and solid,* Cambridge University Press.

ATAIE-ASHTIANI, B. & ASLANI-KORDKANDI, A. (2012), "Flow field around side-by-side piers with and without a scour hole", *J European Journal of Mechanics-B/Fluids,* 36**,** 152-166.

ATAIE-ASHTIANI, B., BARATIAN-GHORGHI, Z. & BEHESHTI, A. J. J. O. H. E. (2010), "Experimental investigation of clear-water local scour of compound piers", 136**,** 343-351.

ATAIE-ASHTIANI, B. & BEHESHTI, A. A. (2006), "Experimental investigation of clear-water local scour at pile groups", *J Journal of Hydraulic Engineering,* 132**,** 1100-1104.

BAGHERIMIYAB, F. & LEMMIN, U. (2013), "Shear velocity estimates in rough-bed open-channel flow", *Earth surface processes and landforms,* 38**,** 1714-1724.

BAGNOLD, R. A. (1954), "Experiments on a gravity-free dispersion of large solid spheres in a Newtonian fluid under shear", *Proceedings of the Royal Society of London. Series A. Mathematical and Physical Sciences,* 225**,** 49-63.

BAKER, C. J. (1980), "The turbulent horseshoe vortex", *Journal of Wind Engineering and Industrial Aerodynamics,* 6**,** 9-23.

BAKHTYAR, R., YEGANEH-BAKHTIARY, A., BARRY, D. A. & GHAHERI, A. (2009), "Two-phase hydrodynamic and sediment transport modeling of wave-generated sheet flow", *Advances in Water Resources,* 32**,** 1267-1283.

BAKKER, A. J. C. F. D., ENGS (2006), "Applied computational fluid dynamics", 150.

BAYKAL, C., SUMER, B. M., FUHRMAN, D. R., JACOBSEN, N. G. & FREDSØE, J. (2015), "Numerical investigation of flow and scour around a vertical circular cylinder", *Philosophical Transactions of the Royal Society A: Mathematical, Physical and Engineering Sciences,* 373**,** 20140104.

BAYKAL, C., SUMER, B. M., FUHRMAN, D. R., JACOBSEN, N. G. & FREDSØE, J. (2017), "Numerical simulation of scour and backfilling processes around a circular pile in waves.", *Coastal Engineering,* 122**,** 87-107.

BEHESHTI, A. & ATAIE-ASHTIANI, B. (2016), "Scour hole influence on turbulent flow field around complex bridge piers", *Flow, Turbulence and Combustion,* 97**,** 451-474.

BOJANOWSKI, C. & KULAK, R. F. (2010) "Comparison of lagrangian, SPH and MM-ALE approaches for modeling large deformations in soil". 11th International LS-DYNA® Users Conference, Dearborn, MI, pp11-45 to*, 11-55*.

BOUSSINESQ, J. (1877) *Essai sur la théorie des eaux courantes,* Impr. nationale.

BOZKUS, Z. & YILDIZ, O. J. J. O. H. E. (2004), "Effects of inclination of bridge piers on scouring depth", 130**,** 827-832.

BRIAUD, J.-L., TING, F. C. K., CHEN, H. C., GUDAVALLI, R., PERUGU, S. & WEI, G. (1999), "SRICOS: Prediction of scour rate in cohesive soils at bridge piers", *Journal of Geotechnical and Geoenvironmental Engineering,* 125**,** 237-246.

BRØRS, B. (1999), "Numerical modeling of flow and scour at pipelines", *Journal of hydraulic Engineering,* 125**,** 511-523.

BURKOW, M. & GRIEBEL, M. (2016), "A full three dimensional numerical simulation of the sediment transport and the scouring at a rectangular obstacle", 125**,** 1-10.

CALLAGHAN, D. P., SAINT-CAST, F., NIELSEN, P. & BALDOCK, T. E. (2006), "Numerical solutions of the sediment conservation law; a review and improved formulation for coastal morphological modelling", *Coastal Engineering,* 53**,** 557-571.

CAMENEN, B. (2007), "Simple and general formula for the settling velocity of particles", *Journal of Hydraulic Engineering,* 133**,** 229-233.

CEBECI, T. & BRADSHAW, P. (1977), "Momentum transfer in boundary layers.", *Washington, DC, Hemisphere Publishing Corp.; New York, McGraw-Hill Book Co.*

CEBECI, T. & CHANG, K. C. (1978), "Calculation of incompressible rough-wall boundary-layer flows", *AIAA Journal,* 16**,** 730-735.

CELIK, I. & RODI, W. J. J. O. H. E. (1991), "Suspended sediment-transport capacity for open channel flow", 117**,** 191-204.

CHANG, W.-Y., CONSTANTINESCU, G., LIEN, H.-C., TSAI, W.-F., LAI, J.-S. & LOH, C.-H. J. J. O. H. E. (2013), "Flow structure around bridge piers of varying geometrical complexity", 139**,** 812-826.

CHANG, Y. S. & SCOTTI, A. J. J. O. T. (2003), "Entrainment and suspension of sediments into a turbulent flow over ripples", 4**,** 1-22.

CHATTERJEE, S. S., GHOSH, S. N. & CHATTERJEE, M. (1994), "Local scour due to submerged horizontal jet", *Journal of Hydraulic Engineering,* 120**,** 973-992.

CHEN, B. & LI, S.-W. J. J. O. C. R. (2019), "Temporal variation of live-bed pier scour under combined wave-current flow in a large-scale flume", 35**,** 348-356.

CHEN, B. & LI, S. J. J. O. H. E. (2018), "Experimental Study of Local Scour around a vertical cylinder under wave-only and combined wave-current conditions in a large-scale flume", 144**,** 04018058.

CHENG, Z., HSU, T.-J. & CALANTONI, J. (2017), "SedFoam: A multi-dimensional Eulerian two-phase model for sediment transport and its application to momentary bed failure", *Coastal Engineering,* 119**,** 32-50.

CONTECHES (2020), "Available at: https://conteches.com/erosion-control/hard-armor/a-jacks (Accessed: 20/12/2020).".

CRASWELL, T. & AKIB, S. J. E. (2020), "Reducing Bridge Pier Scour Using Gabion Mattresses Filled with Recycled and Alternative Materials", 1**,** 188-210.

DAMARNEGARA, A. (2019), "Scour at the foot of seawalls (Doctoral dissertation, Lyon).".

DARGAHI, B. (1989), "The turbulent flow field around a circular cylinder", *Experiments in Fluids,* 8**,** 1-12.

DARGAHI, B. (1990), "Controlling mechanism of local scouring", *Journal of Hydraulic Engineering,* 116**,** 1197-1214.

DARGAHI, B. J. B. N. T.-V. (1987), "Flow field and local scouring around a pier", 137.

DAS, M. M. (1970), "A literature review on bed-load transport due to wave action and localized scour in non-cohesive sediments, Final Report HEL 21-6", *University of California, Berkeley, Calif*.

DAVIDSON, L. (2006), "Evaluation of the SST-SAS model: channel flow, asymmetric diffuser and axi-symmetric hill".

DAVIES, A. G., RIBBERINK, J. S., TEMPERVILLE, A. & ZYSERMAN, J. A. (1997), "Comparisons between sediment transport models and observations made in wave and current flows above plane beds", *Coastal Engineering,* 31**,** 163-198.

DE RUITER, J. C. C. (1983), "Incipient motion and pick-up of sediment as function of local variables", *unpublished notes, Delft Hydraulics, Delft*.

DEY, S. (2003), "Threshold of sediment motion on combined transverse and longitudinal sloping beds", *Journal of Hydraulic Research,* 41**,** 405-415.

DEY, S., BOSE, S. K. & SASTRY, G. L. N. (1995), "Clear water scour at circular piers: a model", *Journal of Hydraulic Engineering,* 121**,** 869-876.

DIAB, R., LINK, O. & ZANKE, U. (2010), "Geometry of developing and equilibrium scour holes at bridge piers in gravel", *Canadian Journal of Civil Engineering,* 37**,** 544-552.

DIXEN, M., SUMER, B. M. & FREDSØE, J. (2013), "Numerical and experimental investigation of flow and scour around a half-buried sphere", *Coastal Engineering,* 73**,** 84-105.

DRIEST, E. R. V. (1956), "On turbulent flow near a wall.", *Journal of the aeronautical sciences,* 23**,** 1007-1011.

EADIE, R. W. & HERBICH, J. B. (1987) Scour about a single, cylindrical pile due to combined random waves and a current. *Coastal Engineering 1986.*

EINSTEIN, H. A. (1950), "The bed-load function for sediment transportation in open channel flows".

ENGELUND, F. & FREDSØE, J. (1976), "A sediment transport model for straight alluvial channels.", *Hydrology Research,* 7**,** 293-306.

ESCAURIAZA, C. & SOTIROPOULOS, F. (2011), "Initial stages of erosion and bed form development in a turbulent flow around a cylindrical pier.", *Journal of Geophysical Research: Earth Surface,* 116.

ETTEMA, R., MELVILLE, B. W. & BARKDOLL, B. J. J. O. H. E. (1998), "Scale effect in pier-scour experiments", 124**,** 639-642.

EXNER, F. M. (1925), "Uber die wechselwirkung zwischen wasser und geschiebe in flussen.", *Akad. Wiss. Wien Math. Naturwiss. Klasse,* 134**,** 165-204.

FANG, H. W. & RODI, W. G. (2000), "3-D numerical simulation for total sediment transport and its application", *J. Basic Sci. Eng,* 8**,** 154-164.

FERZIGER, J. H. & PERIC, M. (2008) *Numerische Strömungsmechanik,* Springer-Verlag.

FLEMING, J. L., SIMPSON, R. L., COWLING, J. E. & DEVENPORT, W. J. (1993), "An experimental study of a turbulent wing-body junction and wake flow", *Experiments in fluids,* 14**,** 366-378.

FLEMING, J. L., SIMPSON, R. L. & DEVENPORT, W. J. (1991), "An experimental study of a turbulent wing-body junction and wake flow(Technical Report, 1 Jun. 1989- 31 Aug. 1991)".

FREDSOE, J. & DEIGAARD, R. (1992) *Mechanics of coastal sediment transport,* World scientific publishing company.

FUHRMAN, D. R., BAYKAL, C., SUMER, B. M., JACOBSEN, N. G. & FREDSØE, J. (2014), "Numerical simulation of wave-induced scour and backfilling processes beneath submarine pipelines", *Coastal Engineering,* 94**,** 10-22.

FUHRMAN, D. R., DIXEN, M. & JACOBSEN, N. G. (2010), "Physically-consistent wall boundary conditions for the k-ω turbulence model", *Journal of Hydraulic Research,* 48**,** 793-800.

GARCIA, M. & PARKER, G. (1991), "Entrainment of bed sediment into suspension", *Journal of Hydraulic Engineering,* 117**,** 414-435.

GHIASSI, R. & ABBASNIA, A. H. (2013), "Investigation of vorticity effects on local scouring.", *Arabian Journal for Science and Engineering*

38**,** 537-548.

GOTHEL, O. (2008), "Numerical modeling of flow and wave-induced scour around vertical structures.", *PhD thesis, Leibniz University of Hanover, Faculty of Civil Engineering*

GÖTHEL, O. & ZIELKE, W. (2007) Numerical Modelling of Scour at Offshore Wind Turbines. *Coastal Engineering 2006: (In 5 Volumes).* World Scientific.

GRAF, W. H. & ISTIARTO, I. (2002), "Flow pattern in the scour hole around a cylinder", *Journal of Hydraulic Research,* 40**,** 13-20.

GRASS, A. J. M. T., REPORT NO. FL29 (1981), "Sediment transport by waves and currents. SERC London Cent".

GUY, H. P., SIMONS, D. B. & RICHARDSON, E. V. (1966) *Summary of alluvial channel data from flume experiments, 1956-61,* US Government Printing Office.

HAMIDI, A. & SIADATMOUSAVI, S. M. (2017), "Numerical simulation of scour and flow field for different arrangements of two piers using SSIIM model", *Ain Shams Engineering Journal*.

HANSEN, E. A., SIMONSEN, H. J., NIELSEN, A. W., PEDERSEN, J. & HØGEDAL, M. (2007) "Scour protection around offshore wind turbine foundations, full-scale measurements". *132-138*.

HELMY, A., ALI, M. & AHMED, H. (2017), "An Experimental Study Of Local Scour Around Piers In The Curved Channels".

HOLNBECK, S. R. & PARRETT, C. (1997) *Method for rapid estimation of scour at highway bridges based on limited site data,* US Department of the Interior, US Geological Survey.

HONG, J. H., CHIEW, Y. M., LU, J. Y., LAI, J. S. & LIN, Y. B. (2012), "Houfeng bridge failure in Taiwan", *Journal of Hydraulic Engineering,* 138**,** 186-198.

HUANG, W., YANG, Q., XIAO, H. J. C. & FLUIDS (2009), "CFD modeling of scale effects on turbulence flow and scour around bridge piers", 38**,** 1050-1058.

HUNT, J. C. R., WRAY, A. A. & MOIN, P. (1988), "Eddies, streams, and convergence zones in turbulent flows.".

INAMURO, T., ADACHI, T. & SAKATA, H. (1993) Simulation of aerodynamic instability of bluff body. *Computational Wind Engineering 1.* Elsevier.

ISSA, R. I. (1986), "Solution of the implicitly discretised fluid flow equations by operator-splitting", *Journal of computational physics,* 62**,** 40-65.

JACOBSEN, N. G. (2011), "A full hydro-and morphodynamic description of breaker bar development", *Technical University of Denmark*.

JACOBSEN, N. G. & FREDSOE, J. (2014), "Formation and development of a breaker bar under regular waves. Part 2: Sediment transport and morphology", *Coastal Engineering,* 88**,** 55-68.

JACOBSEN, N. G., FREDSOE, J. & JENSEN, J. H. J. C. E. (2014), "Formation and development of a breaker bar under regular waves. Part 1: Model description and hydrodynamics", 88**,** 182-193.

JACOBSEN, N. G. J. I. J. F. N. M. I. F. (2015), "Mass conservation in computational morphodynamics: uniform sediment and infinite availability", 78**,** 233-256.

JAMAN, H., DAS, S., KUILA, A., MAZUMDAR, A. J. A. J. F. S. & ENGINEERING (2017), "Hydrodynamic flow patterns around three inline eccentrically arranged circular piers", 42**,** 3973-3990.

JASAK, H. & TUKOVIC, Z. (2006), "Automatic mesh motion for the unstructured finite volume method", *Transactions of FAMENA,* 30**,** 1-20.

JENSEN, J. H., MADSEN, E. S. & FREDSØE, J. (1999), "Oblique flow over dredged channels. II: Sediment transport and morphology", *Journal of Hydraulic Engineering,* 125**,** 1190-1198.

JIMÉNEZ, J. A. & MADSEN, O. S. (2003), "A simple formula to estimate settling velocity of natural sediments", *Journal of waterway, port, coastal, and ocean engineering,* 129**,** 70-78.

JOHNSON, H. K. & ZYSERMAN, J. A. (2002), "Controlling spatial oscillations in bed level update schemes", *Coastal Engineering,* 46**,** 109-126.

KAWATA, Y. & TSUCHIYA, Y. (1989) Local scour around cylindrical piles due to waves and currents combined. *Coastal Engineering 1988.*

KHOSRONEJAD, A., KANG, S., BORAZJANI, I. & SOTIROPOULOS, F. (2011), "Curvilinear immersed boundary method for simulating coupled flow and bed morphodynamic interactions due to sediment transport phenomena.", *Advances in water resources,* 34**,** 829-843.

KHOSRONEJAD, A., KANG, S. & SOTIROPOULOS, F. (2012), "Experimental and computational investigation of local scour around bridge piers.", *Advances in Water Resources,* 37**,** 73-85.
KIM, H. S., NABI, M., KIMURA, I. & SHIMIZU, Y. (2014), "Numerical investigation of local scour at two adjacent cylinders", *Advances in water resources,* 70**,** 131-147.
KIM, H. S., ROH, M. & NABI, M. (2017), "Computational modeling of flow and scour around two cylinders in staggered array.", *J Water,* 9**,** 654.
KIM, S. C., FRIEDRICHS, C. T., MAA, J.-Y. & WRIGHT, L. D. (2000), "Estimating bottom stress in tidal boundary layer from acoustic Doppler velocimeter data", *Journal of Hydraulic Engineering,* 126**,** 399-406.
KIRKIL, G., CONSTANTINESCU, G. & ETTEMA, R. (2005) The horseshoe vortex system around a circular bridge pier on equilibrium scoured bed. *Impacts of Global Climate Change.*
KIRKIL, G., CONSTANTINESCU, G. & ETTEMA, R. (2009), "Detached eddy simulation investigation of turbulence at a circular pier with scour hole", *Journal of Hydraulic Engineering,* 135**,** 888-901.
KIRKIL, G., CONSTANTINESCU, S. G. & ETTEMA, R. (2008), "Coherent structures in the flow field around a circular cylinder with scour hole", *Journal of Hydraulic Engineering,* 134**,** 572-587.
KOBAYASHI, T., AIBARA, T. & HARADA, H. (1997) "Vorticity distribution of horseshoe vortex on scoured bed". *ASCE, 178-178*.
KOLÁŘ, V. (2007), "Vortex identification: New requirements and limitations.", *International journal of heat and fluid flow,* 28**,** 638-652.
KONSTANTINIDIS, E. & LIANG, C. (2011), "Dynamic response of a turbulent cylinder wake to sinusoidal inflow perturbations across the vortex lock-on range", *Physics of Fluids,* 23**,** 075102.
KOVACS, A. & PARKER, G. (1994), "A new vectorial bedload formulation and its application to the time evolution of straight river channels", *Journal of fluid Mechanics,* 267**,** 153-183.
KRAUS, N. C. (1988), "The effects of seawalls on the beach: an extended literature review", *Journal of coastal Research***,** 1-28.
KWOLL, E., VENDITTI, J., BRADLEY, R. & WINTER, C. J. J. O. G. R. E. S. (2017), "Observations of coherent flow structures over subaqueous high-and low-angle dunes", 122**,** 2244-2268.
LAUNDER, B. E. & SPALDING, D. B. (1972) *Mathematical models of turbulence,* Academic press.
LEE, C.-H., LOW, Y. M. & CHIEW, Y.-M. (2016), "Multi-dimensional rheology-based two-phase model for sediment transport and applications to sheet flow and pipeline scour", *Physics of Fluids,* 28**,** 053305.
LEE, S. O. & STURM, T. W. (2008) "Scaling issues for laboratory modeling of bridge pier scour". Proceedings 4th International Conference on Scour and Erosion (ICSE-4). November 5-7, 2008, Tokyo, Japan*, 111-115*.
LESSER, G. R., ROELVINK, J. A. V., VAN KESTER, J. & STELLING, G. S. (2004), "Development and validation of a three-dimensional morphological model", *Coastal engineering,* 51**,** 883-915.
LEVCHENYA, A. M., SMIRNOV, E. M. & GORYACHEV, V. D. (2010), "RANS-based numerical simulation and visualization of the horseshoe vortex system in the leading edge endwall region of a symmetric body", *International Journal of Heat and Fluid Flow,* 31**,** 1107-1112.
LI, F. & CHENG, L. (1999), "Numerical model for local scour under offshore pipelines", *Journal of Hydraulic Engineering,* 125**,** 400-406.
LI, F. & CHENG, L. (2001), "Prediction of lee-wake scouring of pipelines in currents", *Journal of waterway, port, coastal, and ocean engineering,* 127**,** 106-112.
LI, Y., KELLY, D. M., LI, M. & HARRIS, J. M. J. C. E. P. (2014), "Development of a new 3D Euler-Lagrange model for the prediction of scour around offshore structures", 1**,** 31.
LI, Y., ONG, M. C., FUHRMAN, D. R. & LARSEN, B. E. J. C. E. (2020), "Numerical investigation of wave-plus-current induced scour beneath two submarine pipelines in tandem", 156**,** 103619.
LIANG, D. & CHENG, L. (2005), "Numerical model for wave-induced scour below a submarine pipeline.", *Journal of waterway, port, coastal, and ocean engineering,* 131**,** 193-202.

LIANG, D., CHENG, L. & LI, F. (2005), "Numerical modeling of flow and scour below a pipeline in currents: Part II. Scour simulation", *Coastal engineering,* 52**,** 43-62.
LIN, C., HO, T. C. & DEY, S. J. J. O. E. M. (2008), "Characteristics of steady horseshoe vortex system near junction of square cylinder and base plate", 134**,** 184-197.
LIU, X. & GARCÍA, M. H. (2008), "Three-dimensional numerical model with free water surface and mesh deformation for local sediment scour.", *Journal of waterway, port, coastal, and ocean engineering,* 134**,** 203-217.
LU, L., LIU, M., TENG, B., TANG, G. & ZHAO, M. (2015) "Numerical investigation of wave-induced local scour around a submarine pipeline". *733-740*.
LUQUE, R. F. (1974), "Erosion and Transport of Bed Load Sediment: 6 Tab".
MAHMOUD, A. H. (2020), "Effect of soil particle size in reducing the Scour around bridge Piers at the Curved Channels.", *Life Science Journal,* 17.
MARIEU, V., BONNETON, P., FOSTER, D. & ARDHUIN, F. J. J. O. G. R. O. (2008), "Modeling of vortex ripple morphodynamics", 113.
MATHIEU, A., CHAUCHAT, J., BONAMY, C. & NAGEL, T. J. W. (2019), "Two-phase flow simulation of tunnel and lee-wake erosion of scour below a submarine pipeline", 11**,** 1727.
MEHTA, A. J. (2013) *An introduction to hydraulics of fine sediment transport,* World Scientific Publishing Company.
MELVILLE, B. W. (1975), *Local scour at bridge sites.* researchspace@ auckland.
MELVILLE, B. W. & CHIEW, Y.-M. (1999), "Time scale for local scour at bridge piers", *Journal of Hydraulic Engineering,* 125**,** 59-65.
MELVILLE, B. W. & COLEMAN, S. E. (2000) *Bridge scour,* Water Resources Publication.
MENTER, F. R. (1992a), "Improved two-equation k–ω turbulence models for aerodynamic flows. NASA STI.". Recon Technical Report 93, 22809.
MENTER, F. R. (1992b), "Influence of freestream values on k-omega turbulence model predictions", *AIAA journal,* 30**,** 1657-1659.
MENTER, F. R. (1994), "Two-equation eddy-viscosity turbulence models for engineering applications", *AIAA journal,* 32**,** 1598-1605.
MENTER, F. R. (1997), "Eddy viscosity transport equations and their relation to the k-ε model".
MENTER, F. R. (2009), "Review of the shear-stress transport turbulence model experience from an industrial perspective", *International journal of computational fluid dynamics,* 23**,** 305-316.
MENTER, F. R., KUNTZ, M. & LANGTRY, R. (2003), "Ten years of industrial experience with the SST turbulence model", *Turbulence, heat and mass transfer,* 4**,** 625-632.
MIR, B. H., LONE, M. A. & RATHER, N. A. (2019), "Significance of shape factor of obstacle on local scour.", *J Iranian Journal of Science Technology, Transactions of Civil Engineering,* 43**,** 323-330.
NAGEL, T., CHAUCHAT, J., BONAMY, C., LIU, X., CHENG, Z. & HSU, T.-J. J. A. I. W. R. (2020), "Three-dimensional scour simulations with a two-phase flow model"**,** 103544.
NAJAFZADEH, M., BARANI, G.-A., AZAMATHULLA, H. M. J. N. C. & APPLICATIONS (2014), "Prediction of pipeline scour depth in clear-water and live-bed conditions using group method of data handling", 24**,** 629-635.
NAKAGAWA, H. (2017) *Turbulence in open channel flows,* Routledge.
NEZU, I. (1977), "Turbulent structure in open-channel flows", *English translation of the Japanese dissertation of Iehisa Nezu.* .
NIEMANN, S., FREDSØE, J. & JACOBSEN, N. G. J. J. O. H. E. (2011), "Sand dunes in steady flow at low Froude numbers: Dune height evolution and flow resistance", 137**,** 5-14.
NIEMANN, S. L. (2004), "Modelling of sand dunes in steady and tidal flow".
NIKURADSE, J. (1933), "Stromungsgesetze in rauhen Rohren", *VDI-Forschungsheft,* 361**,** 1.
OLSEN, N. R. B. & KJELLESVIG, H. M. (1998), "Three-dimensional numerical flow modeling for estimation of maximum local scour depth", *Journal of Hydraulic Research,* 36**,** 579-590.

OLSEN, N. R. B. & MELAAEN, M. C. (1993), "Three-dimensional calculation of scour around cylinders", *Journal of Hydraulic Engineering,* 119**,** 1048-1054.

OMARA, H., ABDEELAAL, G., NADAOKA, K. & TAWFIK, A. (2020), "Developing empirical formulas for assessing the scour of vertical and inclined piers", *Journal of Marine Georesources and Geotechnology,* 38**,** 133-143.

OMARA, H., ELSAYED, S. M., ABDEELAAL, G. M., ABD-ELHAMID, H. F. & TAWFIK, A. (2019), "Hydromorphological numerical model of the local scour process around bridge piers", *Arabian Journal for Science and Engineering,* 44**,** 4183-4199.

PAIK, J., ESCAURIAZA, C. & SOTIROPOULOS, F. (2007), "On the bimodal dynamics of the turbulent horseshoe vortex system in a wing-body junction", *Physics of Fluids,* 19**,** 045107.

PAN, J., HE, Z., SHIH, W. & CHENG, N. J. I. J. O. S. R. (2020), "Numerical modeling of scour and deposition around permeable cylindrical structures".

PARKER, G., SEMINARA, G. & SOLARI, L. (2003), "Bed load at low Shields stress on arbitrarily sloping beds: Alternative entrainment formulation", *Water resources research,* 39.

PATANKAR, S. V. & SPALDING, D. B. (1983) A calculation procedure for heat, mass and momentum transfer in three-dimensional parabolic flows. *Numerical Prediction of Flow, Heat Transfer, Turbulence and Combustion.* Elsevier.

QI, W. G., LI, Y. X., XU, K. & GAO, F. P. (2019), "Physical modelling of local scour at twin piles under combined waves and current", *J Coastal Engineering,* 143**,** 63-75.

REVIL-BAUDARD, T. & CHAUCHAT, J. (2013), "A two-phase model for sheet flow regime based on dense granular flow rheology", *Journal of Geophysical Research: Oceans,* 118**,** 619-634.

RICHARDSON, J. E. & PANCHANG, V. G. (1998), "Three-dimensional simulation of scour-inducing flow at bridge piers", *Journal of Hydraulic Engineering,* 124**,** 530-540.

RICHARDSON, J. F. & ZAKI, W. N. (1997), "Sedimentation and fluidisation: Part I", *Chemical Engineering Research and Design,* 75**,** S82-S100.

RIJN, L. C. (1987) *Mathematical modelling of morphological processes in the case of suspended sediment transport,* Waterloopkundig Laboratorium.

RIJN, L. C. V. (1984), "Sediment transport, part II: suspended load transport.", *Journal of hydraulic engineering,* 110**,** 1613-1641.

RIJN, L. C. V. (1986), "Mathematical modeling of suspended sediment in nonuniform flows", *Journal of Hydraulic Engineering,* 112**,** 433-455.

RIJN, L. C. V. (1993) *Principles of sediment transport in rivers, estuaries and coastal seas,* Aqua publications Amsterdam.

RODI, W. (1997), "Comparison of LES and RANS calculations of the flow around bluff bodies", *Journal of wind engineering and industrial aerodynamics,* 69**,** 55-75.

RODI, W., FERZIGER, J. H., BREUER, M. & POURQUIE, M. (1997), "Status of large eddy simulation: results of a workshop", *Transactions-American Society of Mechanical Engineers Journal of Fluids Engineering,* 119**,** 248-262.

ROULUND, A., SUMER, B. M., FREDSØE, J. & MICHELSEN, J. (2005), "Numerical and experimental investigation of flow and scour around a circular pile.", *Journal of Fluid Mechanics,* 534**,** 351-401.

ROUSE, H. (1938), "Nomogram for the settling velocity of spheres".

SALAHELDIN, T. M., IMRAN, J. & CHAUDHRY, M. H. (2004), "Numerical modeling of three-dimensional flow field around circular piers", *Journal of Hydraulic Engineering,* 130**,** 91-100.

SCHLICHTING, H. (1979), "Boundary Layer Theory, McGraw-Hill, New York, 1979", *FIGURE CAPTIONS solid curve displays the exact solution. The difference between the exact solution and the eighth QLM iteration for all t in the figure is less than***,** 10-10.

SCHLICHTING, H. & GERSTEN, K. (2006) *Grenzschicht-theorie,* Springer-Verlag.

SHEN, H. W., AGAWA, Y. & KARAKI, S. (1965) *Time variation of bed deformation near bridge piers,* Colorado State University.

SHI, Y.-L., LU, J., ZHAN, Y.-Z., HUANG, C. & YU, J. (2007), "Calculation of angle of repose and dry density of sediment [J]", 40**,** 14-17.
SHIELDS, A. (1936), "Anwendung der Aehnlichkeitsmechanik und der Turbulenzforschung auf die Geschiebebewegung", *PhD Thesis Technical University Berlin*.
SIMPSON, R. L. J. A. R. O. F. M. (2001), "Junction flows", 33**,** 415-443.
SINGH, N. B., DEVI, T. T. & KUMAR, B. J. I. J. O. H. E. (2020), "The local scour around bridge piers—a review of remedial techniques"**,** 1-14.
SMITH, H. D. & FOSTER, D. L. (2005), "Modeling of flow around a cylinder over a scoured bed", *Journal of waterway, port, coastal, and ocean engineering,* 131**,** 14-24.
SMITH, J. D. & MCLEAN, S. J. J. O. G. R. (1977), "Spatially averaged flow over a wavy surface", 82**,** 1735-1746.
SOULSBY, R. (1997) *Dynamics of marine sands: a manual for practical applications.,* Thomas Telford.
SOULSBY, R. & DYER, K. (1981), "The form of the near-bed velocity profile in a tidally accelerating flow", *J Journal of Geophysical Research: Oceans,* 86**,** 8067-8074.
STAHLMANN, A. (2013a), *Experimental and numerical modeling of scour at offshore wind turbines.*, Hannover: Gottfried Wilhelm Leibniz Universität Hannover.
STAHLMANN, A. (2013b) "Numerical and experimental modeling of scour at foundation structures for offshore wind turbines". *International Society of Offshore and Polar Engineers*.
STAHLMANN, A. (2013c) "Numerical and experimental modeling of scour at foundation structures for offshore wind turbines.". *International Society of Offshore and Polar Engineers*.
STAHLMANN, A. & SCHLURMANN, T. (2012), "Numerical and Experimental Modeling of Scour at Tripod Foundations for Offshore Wind Turbines.", *Proc of the 6th International Conference on Scour and Erosion, Paris, France*

SUMER, B. M. (2002) *The mechanics of scour in the marine environment.,* World Scientific.
SUMER, B. M. (2007), "Mathematical modelling of scour: A review", *Journal of Hydraulic Research,* 45**,** 723-735.
SUMER, B. M., BAYKAL, C., FUHRMAN, D. R., JACOBSEN, N. G. & FREDSØE, J. (2014) "Numerical calculation of backfilling of scour holes".
SUMER, B. M., CHRISTIANSEN, N. & FREDSØE, J. (1993), "Influence of cross section on wave scour around piles.", *Journal of waterway, port, coastal, and ocean engineering,* 119**,** 477-495.
SUMER, B. M., CHUA, L. H. C., CHENG, N. S. & FREDSØE, J. (2003), "Influence of turbulence on bed load sediment transport", *Journal of Hydraulic Engineering,* 129**,** 585-596.
SUMER, B. M., COKGOR, S. & FREDSØE, J. (2001), "Suction removal of sediment from between armor blocks", *Journal of hydraulic engineering,* 127**,** 293-306.
SUMER, B. M. & FREDSOE, J. (2002) *The mechanics of scour in the marine environment,* World Scientific.
SUMER, B. M. & FREDSØE, J. (2001a), "Scour around pile in combined waves and current", *Journal of Hydraulic Engineering,* 127**,** 403-411.
SUMER, B. M. & FREDSØE, J. (2001b), "Wave scour around a large vertical circular cylinder", *Journal of waterway, port, coastal, and ocean engineering,* 127**,** 125-134.
SUMER, B. M., FREDSØE, J. & CHRISTIANSEN, N. (1992), "Scour around vertical pile in waves", *Journal of waterway, port, coastal, and ocean engineering,* 118**,** 15-31.
SUMER, B. M., HATIPOGLU, F. & FREDSØE, J. (2007), "Wave scour around a pile in sand, medium dense, and dense silt", *Journal of waterway, port, coastal, and ocean engineering,* 133**,** 14-27.
SUMER, B. M., PETERSEN, T. U., LOCATELLI, L., FREDSØE, J., MUSUMECI, R. E. & FOTI, E. (2012), "Backfilling of a scour hole around a pile in waves and current", *Journal of Waterway, Port, Coastal, and Ocean Engineering,* 139**,** 9-23.
TALIB, A., OBEID, Z. H., HAMEED, H. K. J. I. J. O. S. & RESEARCH (2016), "New Imperial Equation for Local Scour Around Various Bridge Piers Shapes", 5**,** 654-658.

TAO, J. & LI, J. J. T. R. R. (2015), "Streamlining of bridge piers as scour countermeasures: effects of curvature of vertical profiles", 2521**,** 172-182.
TENNEKES, H. & LUMLEY, J. L. (1972) *A first course in turbulence,* MIT press.
TOWNSEND, A. (1976), "The structure of Turbulent Shear Flow (Cambridge U. Press)".
TSENG, M. H., YEN, C. L. & SONG, C. C. S. (2000), "Computation of three-dimensional flow around square and circular piers", *International journal for numerical methods in fluids,* 34**,** 207-227.
TUKOVIĆ, Ž. (2005), "Metoda kontrolnih volumena na domenama promjenjivog oblika".
UBBINK, O. & ISSA, R. (1999), "A method for capturing sharp fluid interfaces on arbitrary meshes", *Journal of computational physics,* 153**,** 26-50.
VAGHEFI, M., GHODSIAN, M., SALIMI, S. J. A. J. F. S. & ENGINEERING (2016), "Scour formation due to laterally inclined circular pier", 41**,** 1311-1318.
VAGHEFI, M., MOTLAGH, M.J.T.N., HASHEMI, S.S. AND MORADI, S. (2018), " Experimental study of bed topography variations due to placement of a triad series of vertical piers at different positions in a 180 bend", *Arabian Journal of Geosciences***,** p.102.
VERSTEEG, H. K. & MALALASEKERA, W. (2007) *An introduction to computational fluid dynamics: the finite volume method,* Pearson education.
WANG, R.-K. & HERBICH, J. B. (1983) *Combined current and wave-produced scour around a single pile,* Department of Civil Engineering, Texas Engineering Experiment Station.
WANG, S., YANG, S., HE, Z., LI, L. AND XIA, Y. (2020), "Effect of Inclination Angles on the Local Scour around a Submerged Cylinder.", *Water resources research,* 12(10)**,** p.2687.
WANG, X., YE, A. & JI, B. (2019), "Fragility-based sensitivity analysis on the seismic performance of pile-group-supported bridges in liquefiable ground undergoing scour potentials.", *J Engineering Structures,* 198**,** 109427.
WARNER, J. C., SHERWOOD, C. R., SIGNELL, R. P., HARRIS, C. K. & ARANGO, H. G. (2008), "Development of a three-dimensional, regional, coupled wave, current, and sediment-transport model", *Computers & Geosciences,* 34**,** 1284-1306.
WEILBEER, H. (2001) *Numerische Simulation von Strömung und Kolkung an Wasserbauwerken,* Inst. für Strömungsmechanik und Elektron. Rechnen im Bauwesen, Univ. Hannover.
WHITEHOUSE, R. (1998) *Scour at marine structures: A manual for practical applications,* Thomas Telford.
WILCOX, D. L., AULT, P. H. & AGEE, W. K. (2006), "Public relations: Strategies and tactics".
WILSON, K. C. (1966), "Bed-load transport at high shear stress", *Journal of the hydraulics division,* 92**,** 49-59.
WILSON, K. C. (1987), "Analysis of bed-load motion at high shear stress", *Journal of Hydraulic Engineering,* 113**,** 97-103.
WINDEUROPE (2018), "Offshore Wind in Europe: Key trends and statistics 2017".
WU, W. (2004), "Depth-averaged two-dimensional numerical modeling of unsteady flow and nonuniform sediment transport in open channels", *Journal of hydraulic engineering,* 130**,** 1013-1024.
YAGCI, O., YILDIRIM, I., CELIK, M. F., KITSIKOUDIS, V., DURAN, Z. & KIRCA, V. O. (2017), "Clear water scour around a finite array of cylinders.", *J Applied Ocean Research,* 68**,** 114-129.
YALIN, M. S. & KARAHAN, E. J. J. O. T. H. D. (1979), "Inception of sediment transport", 105**,** 1433-1443.
YANG, F.-G., LIU, X.-N., YANG, K.-J. & CAO, S.-Y. J. J. O. H., SER. B (2009), "Study on the angle of repose of nonuniform sediment", 21**,** 685-691.
YANG, L., SHI, B., GUO, Y. J. J. O. P. E. & TECHNOLOGY, P. (2012), "Study on dynamic angle of repose for submarine pipeline with spoiler on sandy seabed", 2**,** 229-236.
YANG, Y., MELVILLE, B. W., MACKY, G. H. & SHAMSELDIN, A. (2020), "Experimental study on local scour at complex bridge pier under combined waves and current", *J Coastal Engineering***,** 103730.
YAO, W., AN, H., DRAPER, S., CHENG, L. & HARRIS, J. M. (2018), "Experimental investigation of local scour around submerged piles in steady current.", *J Coastal Engineering,* 142**,** 27-41.

YIZHENG, Z. & BAOLING, X. J. I. J. H. E. (1996), "Under water angle of rest for non-cohesive sediment [J]", 1.

ZAAIJER, M. & VAN DER TEMPEL, J. (2004) "Scour protection: a necessity or a waste of money". Proceedings of the 43 IEA Topixal Expert Meeting*, 43-51*.

ZANKE, U. (1982), "Kolke am Pfeiler in richtungskonstanter Strömung und unter Welleneinfluß", *Mitteilungen des Franzius-Instituts für Wasserbau-und Küsteningenieurwesen der Universität Hannover,* 54**,** 381-416.

ZHANG, J.-S., GAO, P., ZHENG, J.-H., WU, X.-G., PENG, Y.-X., ZHANG, T.-T. J. J. O. M. S. & TECHNOLOGY (2015), "Current-Induced seabed scour around a pile-supported horizontal-axis tidal stream turbine", 23**,** 929-936.

ZHANG, Q., ZHOU, X. L. & WANG, J. H. (2017), "Numerical investigation of local scour around three adjacent piles with different arrangements under current.", *J Ocean Engineering,* 142**,** 625-638.

ZHANG, Y.-B., HAN, L.-H., ZHOU, K. & YANG, S. (2019), "Mechanical performance of hexagonal multi-cell concrete-filled steel tubular (CFST) stub columns under axial compression", *Thin-Walled Structures,* 134**,** 71-83.

ZHAO, M. & CHENG, L. J. C. E. (2010), "Numerical investigation of local scour below a vibrating pipeline under steady currents", 57**,** 397-406.

ZHOU, L. (2017), *Numerical modelling of scour in steady flows (Doctoral dissertation).*

ZYSERMAN, J. & FREDSØE, J. (1988), "Numerical simulation of concentration profiles of suspended sediment under irregular waves", *Institute of Hydrodynamics and Hydraulic Engineering, Technical University of Denmark, Progress Report,* 68**,** 15-26.

ZYSERMAN, J. A. & FREDSØE, J. (1994), "Data analysis of bed concentration of suspended sediment", *J Journal of Hydraulic Engineering,* 120**,** 1021-1042.